Electrodeposition of ZnSe, CdSe and CdTe thin film materials and optoelectronic devices.

SAMANTILLEKE, Anura P.

Sheffield Hallam University

ELECTRODEPOSITION OF ZnSe, CdSe AND CdTe THIN FILM MATERIALS AND OPTOELECTRONIC DEVICES.

Anura Priyajith Samantilleke

A thesis submitted in partial fulfilment of the requirements of
Sheffield Hallam University
for the degree of Doctor of Philosophy.

September 1998.

Materials Research Institute, Sheffield Hallam University.

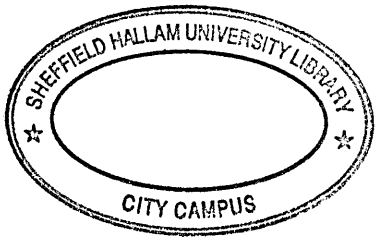
SHEFFIELD HALLAM UNIVERSITY LIBRARY
CITY CAMPUS

ABSTRACT.

II-VI semiconductors, such as ZnSe, CdSe and CdTe have been the focus of intense research during the last decade for two main reasons. Firstly, wide band gap ZnSe has been recognised as one of the best candidates for the next generation blue-green light emitting devices and secondly, CdTe has been emerged as a possible replacement for Si solar cell.

The fabrication of light emitting devices, based on ZnSe, has been partially delayed by the problems associated with metal contacts to both p-type and n-type ZnSe, and large resistances in the device structures. This work confirms, using the I-V technique, about ten Fermi level pinning positions (0.90 eV, 1.10 eV, 1.20 eV, 1.32 eV, 1.38 eV, 1.50 eV, 1.55 eV, 1.67 eV, 1.80 eV and 2.10 eV) at the metal/n-ZnSe interface, of which few have been reported in the literature. The high series resistances are in one of the 10^3 Ω, 10^6 Ω or 10^9 Ω ranges for different ZnSe epilayers grown on GaAs under different growth conditions. GDOES and C-V profiling studies show that the existence of these resistances are due to an insulating layer formed at the ZnSe/GaAs interface.

Non-conventional aqueous electrodeposition of semiconductors have recently become an attractive technique owing to its many advantages. The growth of ZnSe, CdSe and CdTe thin films on glass/ITO substrates, the fabrication of device structures, and their characterisation are presented as a part of this thesis. They were grown using electrochemical deposition technique and characterised using XRD, XPS, GDOES, PEC, SEM, EDAX and optical absorption techniques. It has been demonstrated that cubic ZnSe layers can be grown successfully using electrodeposition with (111) preferred orientation. CdSe and CdTe layers can also be grown on ZnSe (111) substrates with preferred (111) orientation.

The electrodeposition also provides a convenient method of growing both n-type and p-type ZnSe layers. It has also been shown that ZnSe layers can easily be doped with Ga or As to make the layers n-type and p-type respectively. The best p-n junction device structures, fabricated during the project with ZnSe layers, show good rectification with ~105 rectification factor at 1V, the barrier heights are in excess of 0.84 eV with ideality factors ~1.30. The glass/ITO/ZnSe/CdSe/CdTe/metal multi-layer solar cells are photovoltaic active and produce V_{OC} ~ 250 mV, J_{SC} ~ 10 $mAcm^{-2}$, FF ~ 0.7 and efficiency ~ 0.9%. Both devices show encouraging results for future developments to achieve high efficiencies.

ACKNOWLEDGEMENTS.

I would like to express my sincere gratitude to Dr.I.M.Dharmadasa, my director of studies, for his continued help, advice, guidance and encouragement throughout the course of the project and also for repeated reading of the draft version of this text. All his family members have been so kind to me since my arrival to Sheffield. My thanks also go to Dr. J. Young and Dr. M. H. Boyle, my supervisors, for their help and advice during the past three years. This thesis could not have been completed in good time without the help of Dr. M. H. Boyle for his fast editing. I am also thankful to Dr. K. Premaratne of the University of Peradeniya, for the initial inspiration for this interesting research field and also the Materials Research Institute for granting me the studentship.

I would like to extend my gratitude towards all the technical staff members of the School of Science and the Materials Research Institute of Sheffield Hallam University. These in particular being Messers K. Blake and G. France of the School of Science, P. Slingsby, and Dr. M. Ives of the Materials Research Institute for their help and expertise in instrumentation as well as Mr. K. Blake's advice, comments and suggestions in many other matters. Debts of gratitude are owed to all the secretarial staff of the School of Science and the Materials Research Institute, in particular, Ms. Angela Staniforth, Cathy Edwards, Margarette Bedingham of the school of Science and Ms. Lesley Davies of the Materials Research Institute for their enormous help and support during the project.

Dr. C. J. Blomfield, Mr. S. McGregor and Mr. J. J. McChesney are acknowledged for their invaluable support and useful discussions during the tenure of my research.

For the light entertainment and great summer times I had, which made my life at Sheffield so interesting, I thank all those belonged to cricket teams of "Hallam Lodgers" and "Sheffield Outlaws".

My friends I met in Sheffield and particularly those at Sheffield Hallam University are greatly acknowledged for all the good times I enjoyed during the course of my stay in Sheffield.

And most of all, I owe a lot to my parents for their relentless encouragement, help and support and without whom none of studies would be possible.

TABLE OF CONTENTS.

CHAPTER ONE:

INTRODUCTION.

1.1 Introduction to blue-green light emitting materials, devices, solar cells and recent achievements

In the past few years, a number of II-VI and wide band gap semiconductors have revolutionised many areas of electronics mainly for two reasons. Firstly, semiconductor light emitting devices such as light emitting diodes (LED) and lasers play a vital role in communication, control applications, optical data storage and full colour display units. Also within the optoelectronic industry, there is a need for the replacement of conventional red semiconductor lasers by short wavelength blue green lasers to increase the storage capacity. The shorter wavelength light can be focused more sharply and that would increase the storage capacity of magneto-optical and optical discs. Digital versatile discs (DVD) introduced recently to the market rely on red lasers and the capacity is about 4.7 Gbyte compared with 0.65 Gbyte for compact discs (CD). The disc capacity could be increased by nearly four times leading to about 15 Gbyte by replacing red lasers with blue lasers. Blue and green light emitting diodes based on indium gallium nitride are already being used in traffic lights and full colour displays, owing to the fact that LEDs consume only a 10% of the power consumed by electric lamps. The performances of laser printers and optical communications could also be improved with blue laser diodes. Lack of suitable blue light emitting materials has retarded fulfilling some of these areas. However after much effort, production of blue lasers from SiC, GaN and ZnSe led to major advances in the short wavelength light emitting device applications.

As far as blue light emitting photonic materials are concerned, although SiC has proven a thermal and chemical stability, it has a low efficiency due mainly to its indirect band gap, which means electrons can only recombine by scattering from lattice vibrations as electrons and holes have different momenta. SiC is proving difficult to make ohmic contacts due to high interface state densities. Otherwise it could be a leading contender for high temperature and high power laser applications. Similarly GaN which exhibits superior electronic properties and better ohmic contacts, has been suffering from lack of an ideal substrate. For optical emitters and detectors, GaN and SiC have demonstrated operation in the blue-UV region of the spectrum. GaN blue LEDs produced at Sandia National laboratories in New Mexico have been operating for 1000 hours with less than 20 mA drive current in 1996 but the group who demonstrated the first efficient blue light emitting devices in 1995, at Nichia Chemical Industries, Nakamura (1998), have recently made a blue LED with an extrapolated lifetime of about 100,000 hours and a blue laser of 10,000 hours lifetime. Blue SiC LEDs have been in the market for a few years now and blue/UV GaN LEDs joined the market recently, Morkoc et al (1994).

Despite the success of GaN in blue light emitting device fabrication, the requirement of ZnSe based blue/green light emitting devices has not been ignored in the optoelectronic industry for its role in some applications such as full colour displays. Since the successful p-doping of ZnSe, whose quality is already outstanding, realising the first blue/green laser diodes by Haase et al (1991) and the research groups at Brown and Purdue Universities, much attention has been paid to production of a high quality device by many other research groups. The laser designed by the research group at Herriot-Watt University had a peak emission of 478.8 nm at 77 K which was the shortest reported wavelength at that time. The threshold current density was relatively

low at 890 Acm^{-2} and the device had operated successfully up to 150 K. The lifetime was however limited by poor optical confinement, Prior (1996). Following a few years research, blue lasers with a fairly long lifetime have been successfully fabricated utilising ZnSe based semiconductors generating 1 mW output at 515 nm under an applied voltage of 11 V and 33 mA drive current. Currently research is concerned with producing a sufficiently durable device for practical use with an improved lifetime.

Secondly, semiconductor solar cells have been recognised as the promising contenders, to provide low cost long term renewable energy sources in the future. Decades of research to find out suitable materials for large scale, cost effective devices for terrestrial photovoltaic application are becoming a reality with the introduction of II-VI and wide band gap compounds such as ZnSe and CdS and also CdSe and CdTe. Out of all of the group, the CdS/CdTe solar cell has been studied widely following its successful fabrication with over 9% conversion efficiency by Basol (1984). In 1992, the efficiency of the same reported device was about 10% on a laboratory scale, Das and Morris (1993). Morris et al again in 1995 improved the conversion efficiency of the same cell to 12.6% by treating it with $CdCl_2$ and optimising other deposition parameters reducing the series resistance. In this particular treatment, the semiconductor layer is annealed at 400°C in air after the surface has been treated with saturated sloution of $CdCl_2$ in methanol, Morris and Vanderveen (1996). Ferekides et al (1994) developed a cell of the same structure with a much higher conversion efficiency, which was about 15.8%. A CdTe layer of 1 μm thickness absorbs over 90% of available photons ($h\nu$ >1.4eV) meaning only films of about 2 μm are sufficient for thin film solar cells.

The study of the development of a solar cell for a wider spectral region has however been limited. The ternary chalcogenide $CdS_xSe_{(1-x)}$ graded cell is widely used, mainly as a photoconductor whose band gap covers the entire visible spectrum, 2.42 eV of CdS to 1.7 eV of CdSe. Mane et al (1997), successfully attempted to use a chemical bath deposition technique to grow this device structure. However, significant improvement of the cell has not been reported.

1.2 Aims and objectives

Although there are many theories available to explain the formation of metal semiconductor junctions, the applicability of these theories to II-VI semiconductors have not been well established. Out of all the II-VI compound semiconducting materials wide and direct band gap ZnSe has been of particular interest within the semiconductor device industry for its potential use in semiconductor light emitting devices and as a window material for solar cells. Continuous wave (CW) room temperature (RT) operation of short wavelength blue-green laser diodes based on wide band gap ZnSe has been demonstrated recently with a lifetime of 100 hours, Taniguchi et al (1996). These devices were realised by improvement in ohmic contacts for the p-type material using a p-ZnTe ohmic contact layer. The specific contact resistance between the Au and p-ZnTe contact layers was reduced to $5x10^{-6}$ Ωcm^{-2} from about $3x10^{-3}$ Ωcm^{-2} which is too high for devices, by inserting a thin Pd layer in between the Au and p-ZnTe. Previous work by Blomfield et al (1995) reported discrete Fermi level pinning positions for Au/n-ZnSe contacts. They also have observed about six discrete barrier heights for metal/n-ZnSe contacts, which appeared to be independent of the metal used and correlated well with deep levels reported in the literature. Taniguchi et al

(1996) have also observed that there were no specific difference between Pd/Pt/Au contacts and Pd/Au contacts on p-ZnTe. In order to improve device operation the optical and transport properties of these materials have to be well understood. One of the aims of this project therefore was to study metal contacts to MBE grown ZnSe epilayers in order to achive a better understanding of the formation of metal/ZnSe interfaces and their properties. New experimental evidence should undoubtedly lead to improved device technologies.

Thin film technology is useful in the fabrication of low-cost photovoltaic and optoelectronic devices. The reason being that compound semiconductors, which have a direct band gap can be highly efficient even when they have a thin film structure. The fabrication of such devices on a transparent conducting glass substrate would minimise the loss of radiation due to absorption by the substrate and make characterisation easier. Utilisation of an electrochemical technique for the fabrication of thin film II-VI compounds on the other hand has been found to be promising for its attractive features mentioned elsewhere (chapter 1.7.1), especially for large scale use.

The applicability of ZnSe not only as a material for a blue-green laser diode, but also as a window material for solar cells has still to be assessed. One of the most studied solar cell structure next to Si is the CdS/CdTe solar cell, which has exhibited 15.8% conversion efficiency to date. Replacing the window material CdS (E_g=2.42 eV at RT) with wider band gap ZnSe (E_g=2.70 eV at RT) and introducing a CdSe layer with an intermediate band gap (E_g=1.7 eV) would enable the fabrication of more efficient photovoltaic devices utilising a wider spectral region. The whole aim of the project therefore fell into following categories.

1. (a) The study of the electrical properties of metal contacts formed on stoichiometric ZnSe epilayers grown by the MBE technique. The stoichiometric surfaces have been formed by wet chemical etching, using an etchant given in the literature, Dharmadasa et al (1994) and (1996). The study of interfacial properties of different metal/ZnSe properties could be related to the macroscopic behaviour of the devices.

(b) The study of ageing effects of metal/ZnSe contacts. As already mentioned, the longest lifetime of the blue-green laser reported so far is just 100 hours. It has not yet been made clear whether the short lifetime is due to the failure in structure as a result of interface mixing with time or due to any other reason. However it could be assumed that the chemical reactions that could take place in the junction would reduce device stability and lifetime. Dharmadasa et al (1996), have observed that with time the barrier heights vary showing different values reported. Studying the ageing effects of the metal/ZnSe contacts and the device structure as a whole will be helpful in understanding the cause for this failure of devices.

2. (a) Establishing an electrochemical method for the deposition of ZnSe thin films and devices. This would lead to characterisation of structural, electrical and optical properties of these films and devices and compare them with the MBE grown material.

(b) Extending the electrochemical technique to grow and characterise other relevant II-VI compound semiconductors and subsequently to fabricate multi-layer solar cell devices. Although electrochemical deposition of CdSe and CdTe has been well established, the use of ZnSe as the substrate and the device structure ITO/ZnSe/CdSe/CdTe/metal, which utilises the most effective region of the solar spectrum, has never been reported.

1.3 Approach

In order to make electrical contacts to ZnSe epilayers, a surface modification method will have to be applied to form stoichiometric surfaces. Although several methods have been reported in the past, wet chemical etching has proved to be promising for thin film semiconductors. Dharmadasa et al (1989), have shown that the etchant $NaOH/Na_2S_2O_3$ is suitable for production of stoichiometric surfaces.

Fulop and Taylor (1985), Natarajan et al (1994), Krishnan et al (1992), and some other groups have employed an electrochemical technique for the growth of ZnSe. However, they have not made significant improvement in the development of devices, more precisely there have been no detailed reports on fabrication of devices based on electrodeposited ZnSe. The semiconducting properties of the II-VI compounds appear to depend on deposition potential, solution composition, pH value and the growth temperature. Useful information has been given by Krishnan et al (1992), such as the potential-pH (Pourbaix diagram) diagram for ZnSe which could be used in electrodeposition. The knowledge gained in electrodeposition of ZnSe could be extended in growing CdSe and CdTe thin films and fabricating multi layer solar cells to utilise a wider region of the solar spectrum. The approach of the project has therefore taken the following outline.

1. (a) Stoichiometric surfaces were produced on MBE grown ZnSe epilayers using the wet chemical etching given in the literature, Dharmadasa et al (1996). The morphology, composition and also stoichiometry of the layers was studied using x-ray photoelectron spectroscopy (XPS), scanning electron microscopy (SEM) and glow discharge optical emission spectroscopy (GDOES) techniques. Bulk structure was studied using x-ray

diffraction (XRD) and optical properties were characterised using an optical absorption technique.

(b) Metal contacts were formed on to etched surfaces and characterised by conventional current-voltage (I-V) and capacitance-voltage (C-V) techniques. The devices were investigated for ageing effects using the same techniques. These results were used to relate microscopic interfacial interactions predicted by thermodynamics of the interface with the observed macroscopic properties.

(c) In order to verify the barrier heights determined using macroscopic techniques, a few samples were analysed using the microscopic ballistic electron emission microscopy (BEEM) technique with the collaboration of CNRS-Toulouse group in France. The structure of the interface could be related to electronic characteristics with this information.

(d) The deep levels within the metal/ZnSe structure and the relationship of their traps with Fermi level pinning at the interface were determined by analysing deep level transient spectroscopy (DLTS) results with the collaboration of the Warsaw group in Poland and Bio-Rad micromeasurements limited.

2. (a) An electrochemical technique was developed and established for the deposition of ZnSe thin films. Resulting films were subsequently characterised by XRD for bulk structure, SEM and EDAX for morphology and elemental composition, GDOES and XPS for elemental analysis and chemical composition. A photoelectrochemical (PEC) cell arrangement was used to determine the electrical conducting type of thin films. Optical characterisation was done by optical absorption technique, which led to determination of the band gap of the semiconducting ZnSe layer at room temperature in a fair agreement with reported values.

(b) P-n junction devices were fabricated utilising materials deposited in optimised growth conditions using the knowledge acquired from the electrical contacts to MBE grown ZnSe work in section (1).

3. The electrochemical technique developed for the growth of ZnSe was applied to the growth of CdSe and CdTe enabling subsequent fabrication of a multi layer ITO/ZnSe/CdSe/CdTe/metal solar cell structure. Thin layers and device structures were optimised following (1) and (2).

1.4 Physical properties of II-VI compound semiconductors

The II-VI compounds under consideration in this project have in recent years attracted much attention in research and in industry because of their applications in short wavelength blue lasers and in highly efficient photovoltaic device structures. In particular the fabrication of photonic devices based on ZnSe operating in the short wavelength blue green spectral region and CdS/CdTe photovoltaic devices with improved efficiency were two examples.

One of the major difficulties the device industry experiencing is the lack of suitable substrates for growing semiconducting compounds. GaAs is used as the substrate for ZnSe because of their close similarity in most physical properties except the negligible lattice mismatch (0.27%). However, as a consequence of this lattice mismatch, a GaAs/ZnSe heterostructure contains misfit dislocations with an inhomogeneous density. Colak et al (1989) showed that this inhomogeneous dislocation density is dependent on the epitaxial layer thickness. In contrast a CdS/CdTe heterostructure with a relatively

large lattice mismatch (~10% to CdTe) has exhibited a high photovoltaic output efficiency. Better performance could therefore be expected from the ZnSe/CdSe/CdTe structure with lower lattice mismatches of ~6.32% and ~6.6% at ZnSe/CdSe and CdSe/CdTe interfaces respectively (table 1.1).

Physical Quantity	ZnSe	CdSe	CdTe
Lattice Parameter (Å) at RT	5.6676	6.05	6.477
Density (kg/m^3)	5420	5674	5860
Melting Point (K)	1790	1512	1365
Band Gap (eV) at RT	2.70	1.74	1.40
Thermal Conductivity (mW/cm K) at 300K	140	90	58.5
Heat of Formation (kJ/mole) at RT.	422	---	339
Mobility - electron (cm^2/Vs) at RT	540	650	1200
- hole (cm^2/Vs) at RT	28	---	50
dE_g/dT (10^{-4} eV/°C)	-7.2	-4.6	-4.1
dE_g/dP (10^{-6} eV.cm^2/kg)	6	---	8
Molecular Mass	144.34	83.73	128.83
Specific Heat (J/kg.K) at 300K	339	255	205
Coefficient of Thermal Linear Expansion ($10^{-6}K^{-1}$ at 300K)	7.2	3.8	4.9
Index of Refraction	2.89	---	---
Ionocity	0.81	0.45	0.37
m_e/m_o	0.10	0.13	0.14

Table 1.1 Physical properties of cubic Zinc Blende ZnSe, CdSe and CdTe compounds. (CRC chemical data, 1995) Ruda (1992).

1.5 Various electronic device structures

Any electronic device falls under one of the groups of a p-n junction, a heterojunction, a Schottky diode or an MIS structure. The properties of the junctions are the basis of all semiconductor devices except the simple photoconductor, which has only one type of

carrier, either holes or electrons. LEDs, laser diodes, photodiodes and solar cells are centred around junction properties. The most common junction is the p-n junction.

1.5.1 The p-n junction (homojunction)

Homojunctions (p-n junction diodes) are basically a single material with one half rich with electrons, namely an n-semiconducting side and the other, a p-semiconducting side doped to create excess holes. The p-n junction is usually formed at the centre of the crystal structure where the p type region becomes n type. When the same material has different dopants in two regions, and the dopant concentration becomes discontinuous suddenly at the centre, the diffusion of charges takes place from one side to the other across the junction. The ionised impurities are distributed in the lattice discontinuously but the dopants are fixed in the lattice and only free carriers move across the junction. This process builds up a region of space charge in the junction region, positive on the n-side and negative on the p-side, resulting in an internal electric field opposing any further carrier motion. The initial carrier diffusion down a concentration gradient causes a diffusion current, which is balanced by the opposing drift current with all free charges having flowed out of the junction region as a result of the net field.

When the two currents are equal in magnitude, equilibrium is reached as there are no net carrier flow across the junction. A region of space charge as shown in the figure 1.1 is now formed and it is depleted of electrons and hence called the depletion region, which is in the order of 1 μm either side of the junction. Therefore the formation of the junction has no real effect on the bulk semiconductor material, which retains its original conductivity type and carrier density. Because the junction appears to have formed in the centre of one semiconducting structure and at equilibrium there is no net current

flow, the probability of finding an electron [f(E)] of any particular energy level E, must be the same throughout the crystal structure. The relationship between the probability of finding an electron [f(E)] of Energy level E and the Fermi level E_F is given by the Fermi Dirac distribution :

$$f(E) = \frac{1}{\exp(E - E_F) / kT + 1} \qquad [1.1]$$

According to equation 1.1, if the probability f(E), is the same throughout the material, the Fermi level E_F must be the same throughout both the n and p regions including the junction. To accommodate this situation, then both the conduction band and valence band have to be bent resulting in a potential difference between the conduction bands and valence bands of the two sides. This potential difference is called the diffusion potential, contact potential or built-in-potential which acts as a barrier to further electron flow from the n to p side or hole flow from the p to n side. The built-in-potential is given by

$$V_b = \left(\frac{D_p}{\mu_h}\right) \ln\left(\frac{N_A N_D}{n_i^2}\right) = \left(\frac{D_n}{\mu_e}\right) \ln\left(\frac{N_A N_D}{n_i^2}\right)$$

$$= \left(\frac{eN_A}{2\varepsilon\varepsilon_o}\right) x_p (x_p + x_n) \qquad [1.2]$$

The width of the depletion layer is given by

$$w = \left[2V_b \varepsilon\varepsilon_o \left(\frac{N_A + N_D}{eN_A N_D}\right)\right]^{1/2} \qquad [1.3]$$

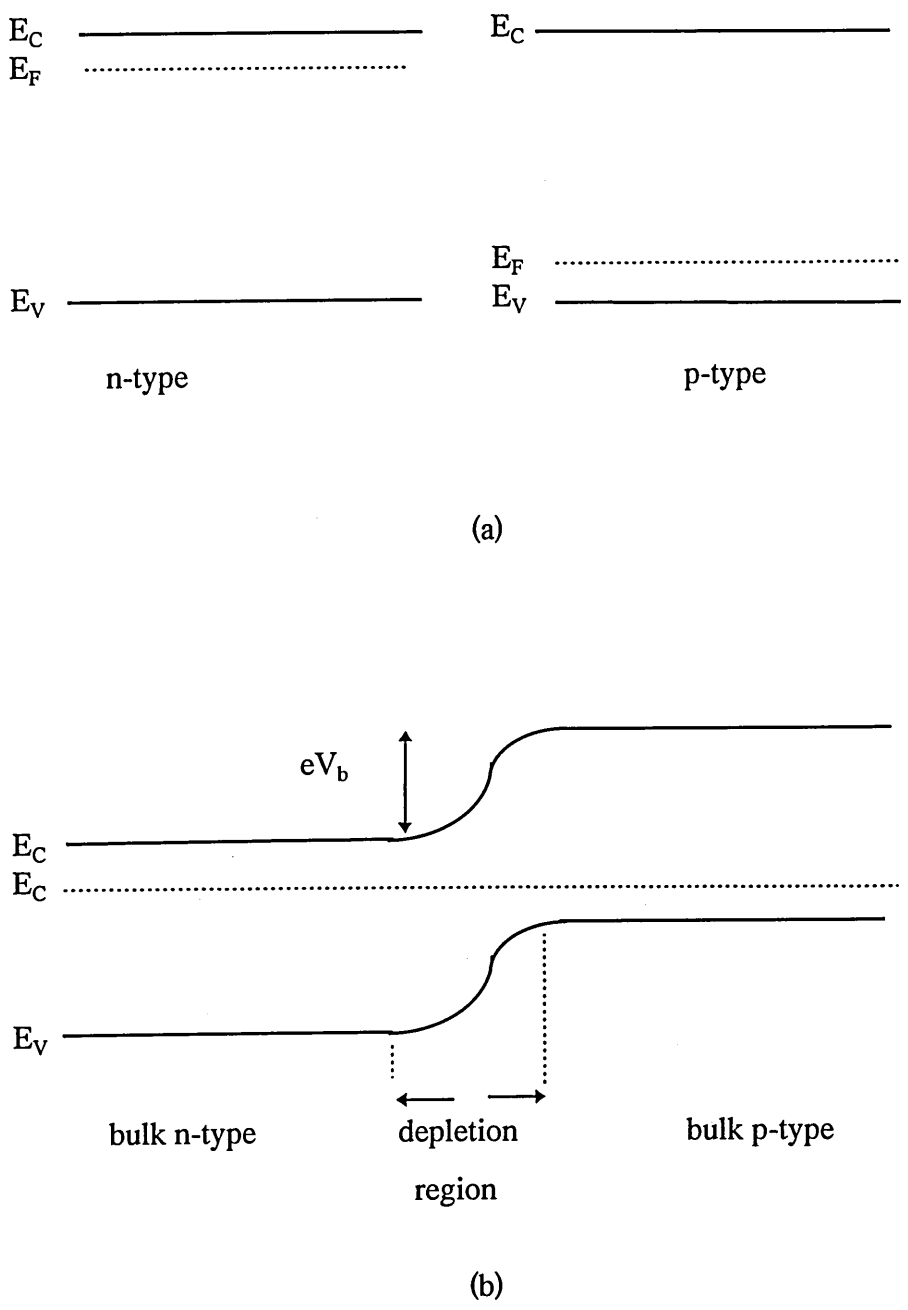

Figure 1.1: (a) Energy band diagram of two semiconductors (p and n) before the contact being made and (b) band diagram through a p-n junction.

hence 'w' is proportional to $V_b^{1/2}$ for an abrupt junction. The same analysis on a linearly graded junction would give a $V_b^{1/3}$ dependency, S.M.Sze.

The space charge distribution in an abrupt junction can be related to a parallel plate capacitor whose capacitance is given by

$$C_j = \frac{A}{2}\left(\frac{2e\varepsilon\varepsilon_o}{V_b\left(\frac{N_A N_D}{N_A + N_D}\right)}\right)^{1/2}$$

$$= \frac{\varepsilon\varepsilon_o A}{w} \qquad [1.4]$$

1.5.2 Heterojunction device structures

If the p and n semiconductors are of different materials the p-n junction device is called a heterojunction. In contrast to a homojunction, a heterojunction can have the same type of conductivity in both semiconductors, which then is called an isotype (N-n or P-p where capital letter signifies the material with the higher band gap) heterojunction or in the case of different carriers an anisotype (N-p or P-n) heterojunction. Since Schockley's proposal to use heterojunctions as efficient emitter-base junctions in bipolar transistors (1951), they have been widely studied. Many important applications have been made available with heterostructures and some of them are the room temperature injection laser, LED, photodetector and solar cells.

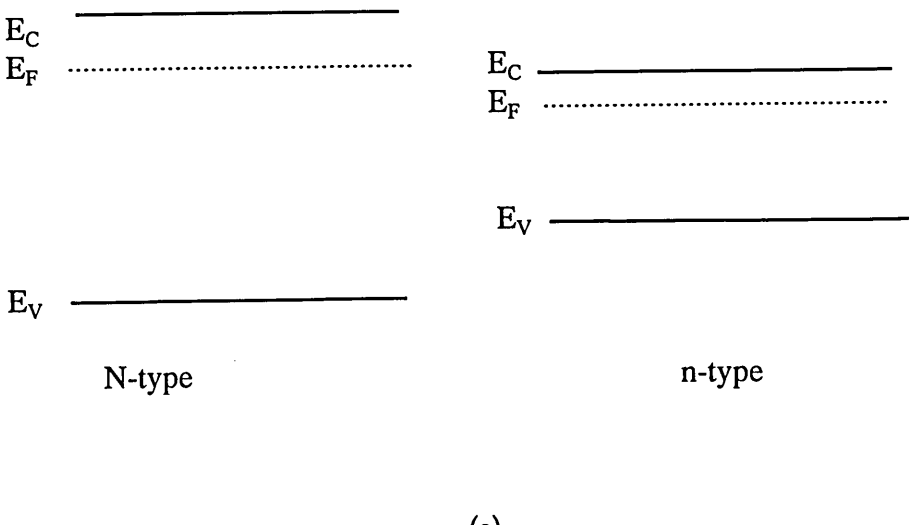

(a)

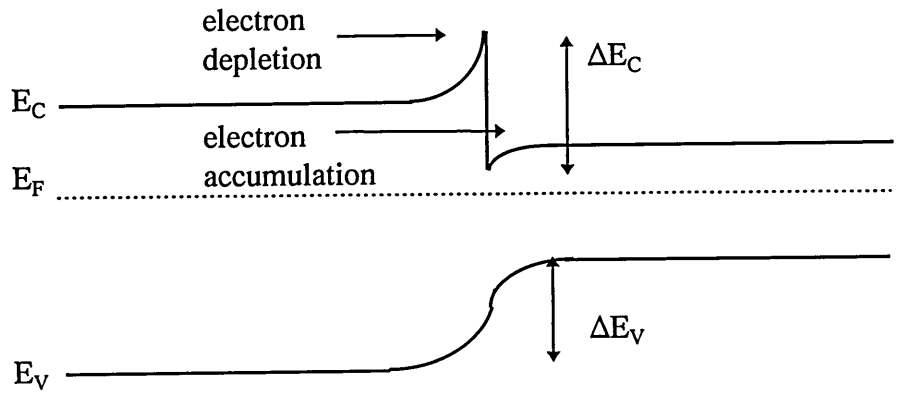

(b)

Figure 1.2: (a) Energy band diagram of two isotype semiconductors (N and n) before the contact being made and (b) band diagram through an N-n junction.

(a) Isotype (N-n or P-p) heterojunctions

When the electrons move from higher potential material (N) to the material with the lower potential (n) the conduction band bends up on N side and down on n side. As shown in figure 1.2 (b), ΔE_V is positive when moving from N to n. Therefore there is a positive discontinuity in E_V after junction formation given by ΔE_V. Similarly the negative value of ΔE_C gives a negative discontinuity in E_C after junction formation. Because the two conduction bands are moving in opposite directions, the rise in E_C on N-side appears to deplete this region of electrons and the fall in E_C on the n-side accumulates or confines electrons in the junction region. The formation of ΔE_C at equilibrium prevents further electron movement.

A band structure for a P-p junction is shown in Figure 1.3. Similar to N-n, holes transfer from P side to p side, causing a hole potential barrier at the interface hence corresponding accumulation and depletion of holes on p and P sides respectively. ΔE_C and ΔE_V can also be defined similar to the N-n structure.

(b) Anisotype heterojunction

N-p and P-n contacts at equilibrium are similar to p-n junctions, with spikes as in N-n and P-p contacts, at the rise of conduction band of N in N-p and at the fall of valence band of P in P-n structures due to the difference in energy levels of conduction and valence bands of different materials. Majority carriers are held back from moving from the wide gap material to the narrow gap material. Similarly majority carriers are held in the narrow gap material by the large difference in either E_V in N-p or E_C in P-n junctions.

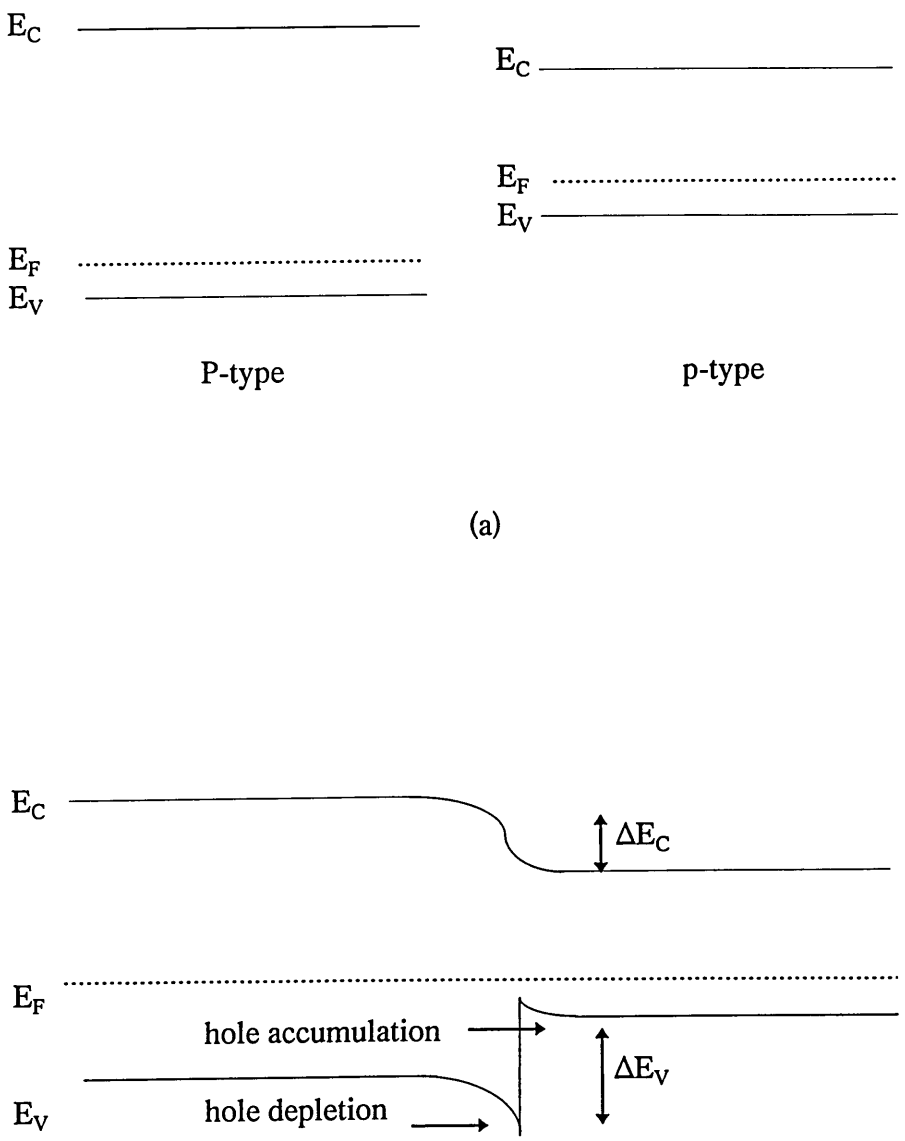

Figure 1.3: (a) Energy band diagram of two isotype semiconductors (P and p) before the contact being made and (b) band diagram through an P-p junction.

1.5.3 Metal/semiconductor junction and Schottky - Mott Theory

The metal/semiconductor system is another important structure in electronic devices. The study of metal contacts on semiconductors has a history since Braun's discovery of the asymmetric nature of electrical conduction (S.M. Sze). In 1934 Wilson formulated the transport theory of semiconductors based on the band theory of solids and four years later in 1938, Schottky suggested that a potential barrier which arises at a metal/semiconductor junction could well be due to stable space charges in the semiconductor and not the presence of a chemical layer. Mott in the same year suggested a similar idea and the model which well describes metal/semiconductor junctions based on their ideas is known as Schottky-Mott theory.

According to Schottky-Mott theory, electrons pass from the n-type semiconductor of work function ϕ_S to the metal of work function ϕ_m and the two Fermi levels (E_{Fm} and E_{Fs} of the metal and the semiconductor respectively) are forced into coincidence at thermal equilibrium, when a metal is connected electrically to a semiconductor provided $\phi_m > \phi_s$. Therefore an electric field will be formed in the direction from the semiconductor to the metal. Negative charges in the metal will be balanced by the positive charges in the semiconductor. The charge on the metal surface simply consists of extra conduction electrons contained within the Thomas-Fermi screening distance which is about 0.5Å. The charge in the semiconductor consists of uncompensated donors created by receding conduction electrons. This charge is distributed in the semiconductor over a wide range due to the lower conductivity, a region then exists depleted of conduction electrons known as the depletion region of width 'w'. Since the electron density in the metal is much higher than the donor concentration of the semiconductor, the metal Fermi level does not change when a small fraction of electrons are added. However, moving

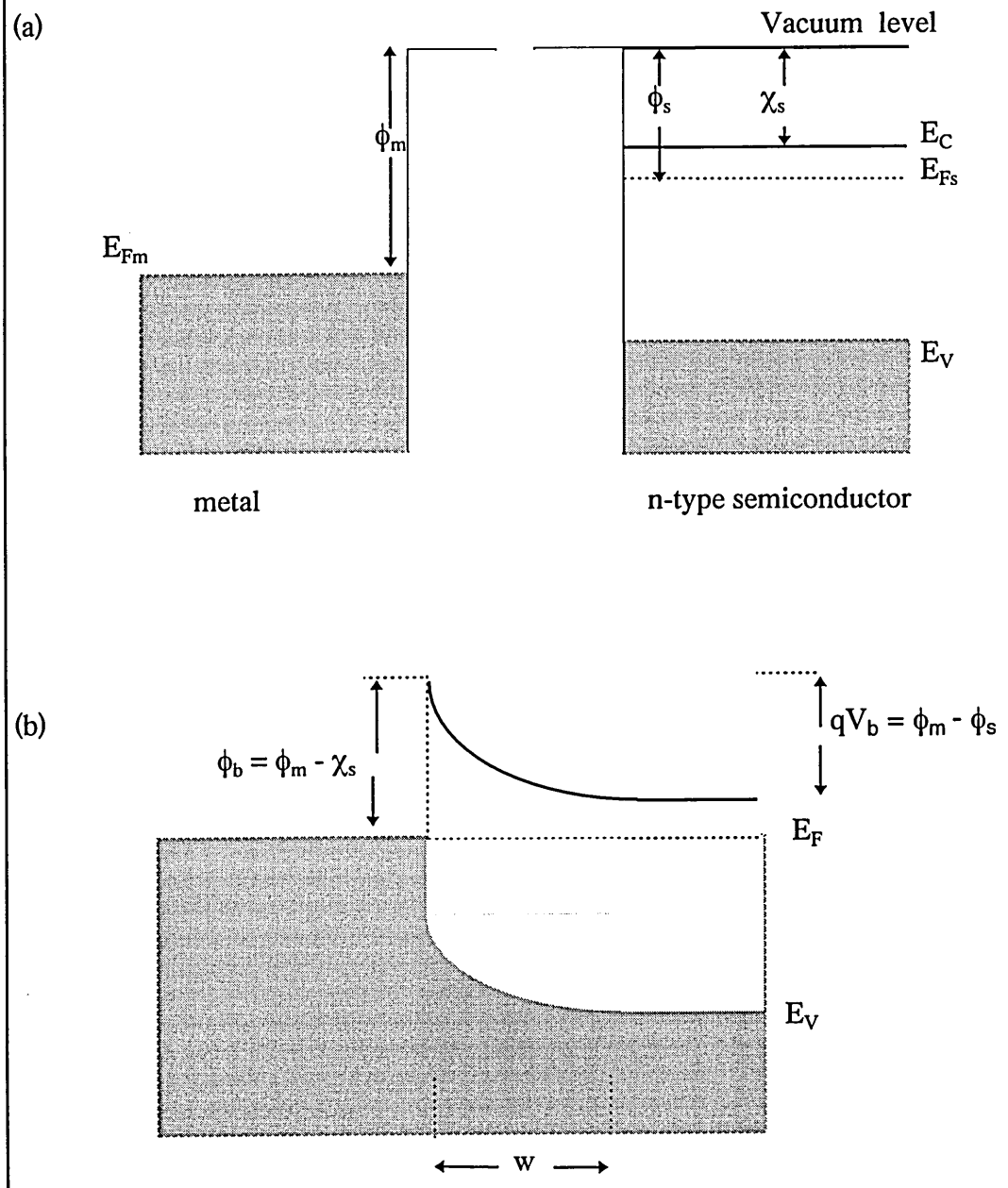

Figure 1.4 Formation of Schottky barrier (a) Different important energy levels in the metal and the semiconductor with respect to the vacuum level (b) The junction potential produced when the metal and the semiconductor are brought together. Due to the built-in potential a depletion region of width 'w' is created.

electrons from the semiconductor will leave behind positively charged fixed centres. The electric field opposes the electron flow and at equilibrium band bending is such that the Fermi level is flat in either side.

In the ideal Schottky barrier, the height of the potential barrier at the metal/semiconductor junction is,

$$\phi_b = \phi_m - \chi_s \qquad [1.5]$$

where χ_s is the electron affinity of the semiconductor.

Electrons moving from the semiconductor into the metal face a barrier denoted by V_b as shown in Figure 1.4 (b), which is called the built - in potential of the junction and is given by,

$$qV_b = \phi_m - \phi_s \qquad [1.6]$$

The height of the potential barrier can be altered by an external bias and the junction can be used for rectification. If the semiconductor is p-type with $\phi_m < \phi_s$, electrons are injected from the metal to the semiconductor causing a negative charge on the semiconductor surface. The built - in potential (V_b) then will be given by,

$$qV_b = \phi_s - \phi_m \qquad [1.7]$$

1.5.4 Metal-insulator-semiconductor (MIS) structure

A metal-insulator-semiconductor (MIS) structure is the most useful electronic device owing to its direct use in planar devices and integrated circuits. In 1959, Moll as well as Pfann and Garrett proposed MIS structures first for use as a variable capacitor, Sze (1981).

(a)

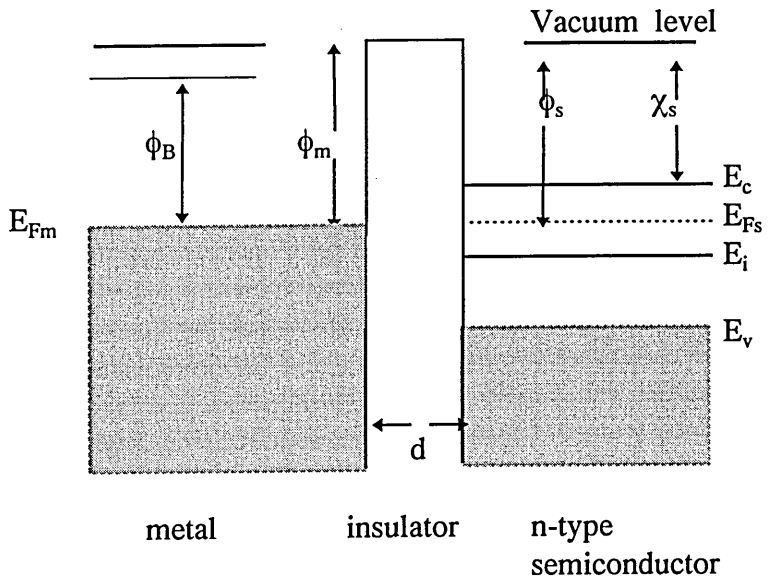

(b)

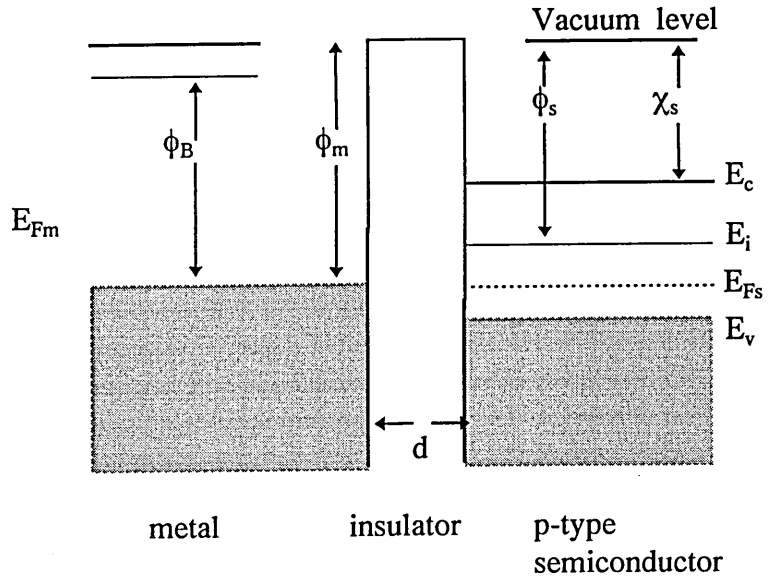

Figure 1.5 Energy band diagrams of ideal MIS diodes at V=0, (a) n-type semiconductor (b) p-type semiconductor.

Since then with an oxide layer as the insulator known as MOS used and studied widely. A charge coupled device (CCD) is a collection of MOS diodes, which can perform a wide range of electronic functions including image sensing, data storage and signal processing.

An Ideal MIS diode is defined as, at zero applied voltage (zero bias) the difference between the metal and semiconductor energy levels (ϕ_{ms}) is zero.

$$\phi_{ms} = \phi_m - (\chi + \frac{E_g}{2q} - \varphi_B) = 0 \qquad \text{For n-type} \qquad [1.8\ (a)]$$

$$= \phi_m - (\chi + \frac{E_g}{2q} + \varphi_B) = 0 \qquad \text{For p-type} \qquad [1.8\ (a)]$$

A flat band condition appears when there is no applied voltage (Figure 1.5). The resistivity of the insulator is infinity. When the device is biased with positive or negative voltages, one of the several cases may arise. When a negative voltage is applied to the metal which is in connection with p-type semiconductor, the top of the valence band bends upward and is closer to the Fermi level. The Fermi level remains constant within the semiconductor as there is no current flowing through the device. The band bending however causes a majority carrier (hole) accumulation near the semiconductor surface (Figure 1.6a). When the applied voltage is a small positive value, the band bending is in downward direction and the majority carriers are depleted (Figure 1.6b). As the positive voltage increases, the bands will bend even more downward causing the intrinsic Fermi level (E_i) of the semiconductor crossing the Fermi level (E_{Fs}) (Figure 1.6c). The situation is known as Inversion, because the minority carrier density

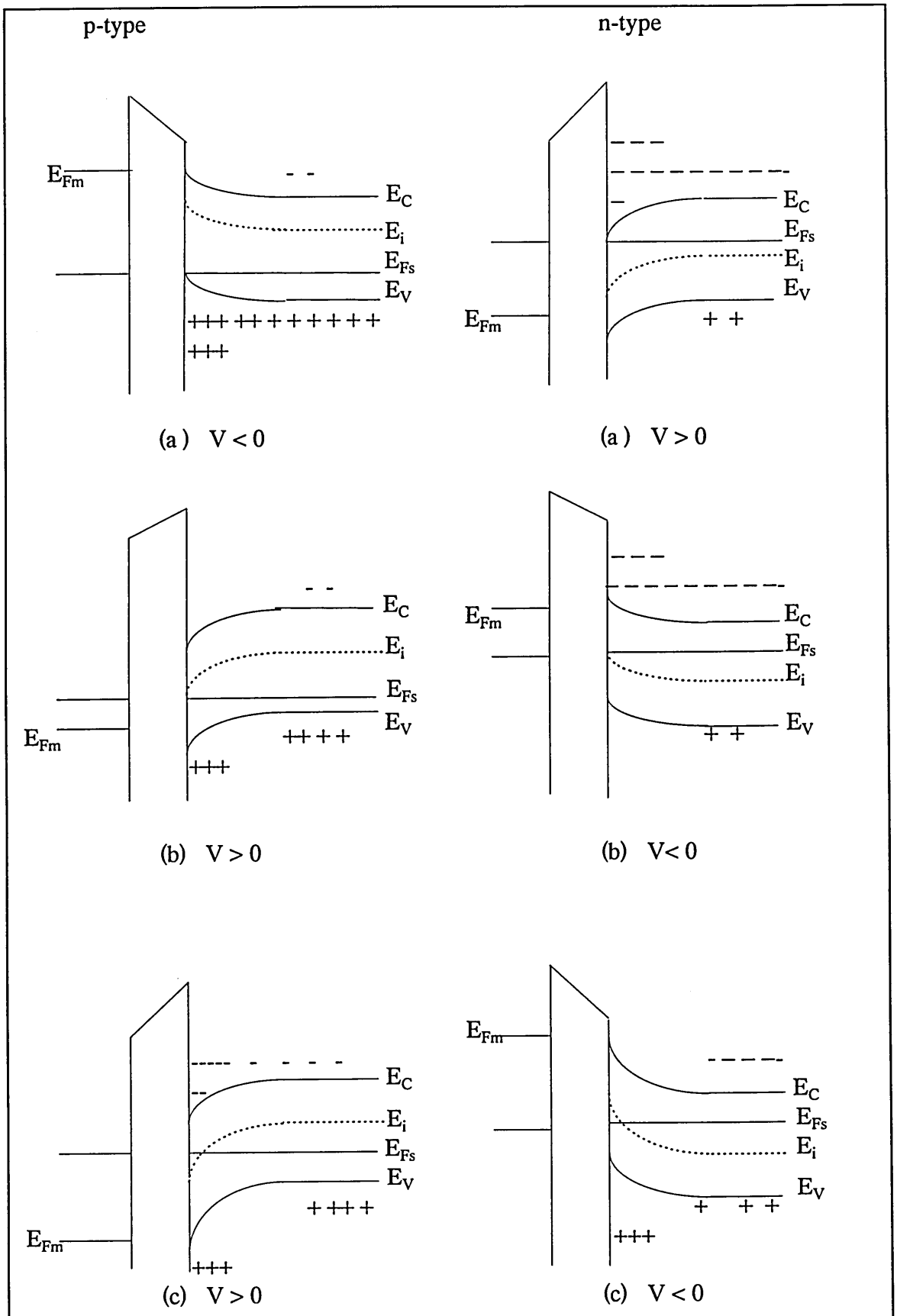

Figure 1.6 MIS diodes (a) accumulation (b) depletion and (c) inversion

becomes larger than the majority carrier density. Similar results can be obtained for the n-type semiconductor as shown in figure 1.6.

1.6 Applications of ZnSe, CdSe, CdTe and other II-VI compound semiconductors, devices and associated problems.

1.6.1 Light emitting devices

Despite the fact that the first ever blue-laser was based on ZnSe, its development has so far not been a great success. In the early stages, defects in the active region caused device failure within seconds. Defect levels have continuously been reduced through better control of material growth. However, a marketable light emitting device utilising ZnSe is still not a reality owing to its poor reliability and low productivity. Utilisation of wide band gap semiconductors such as ZnSe (E_g=2.70 eV) and GaN (E_g=3.34 eV), would enable higher density storage in optical disks as their output wavelengths are shorter. Long term feasibility of II-VI LEDs and lasers has been concerned with the question of reliability. Although the operating voltage has been reduced to a very low value of 4.2 V, Han et al 1994, using semi-metallic HgSe, defect formation and device degradation in ZnSe systems is still a problem.

Allen et al (1972) produced an electroluminescent device using ZnSe performing under reverse biased conditions. The luminescence was described as being associated with luminescent impurities. Radiation occurs when electrons recombine with luminescent centres after they are impact-ionised. The process requires electrons to have kinetic energy of 2-3 eV. The operation under forward bias was found difficult as the metal used to make the ohmic contact was Au, because the electrons can never attain 2-3 eV

kinetic energy as the highest Schottky barrier reported for Au/ZnSe has been 1.5 eV. However the same group (1973) developed a device to be operated under forward bias, Livingston et al (1973), introducing a ZnO insulating layer by etching ZnSe layer in a solution of bromine in methanol. Yellow to blue-green light was emitted from an metal-insulator-semiconductor (MIS) structure. However, since then there has been no report on any improvement to this device. Robinson (1975) fabricated a series of LEDs to cover a spectral region from 340 nm to 490 nm using a ZnSe/ZnS combination. Progress in these devices were not significant. Difficulty in p doping of ZnSe delayed the progress of making devices. Only in 1991, Haase et al in 3M laboratories demonstrated the first pulsed operation of blue/green laser diodes based on ZnSe following the successful p-doping of ZnSe using Nitrogen in 1990. Research groups at Brown and Purdue universities demonstrated the blue laser action in the same year with a very similar crystal structure, Jeon et al (1991). These devices were not very stable and had a very short lifetime. The problems were basically associated with metal contacts which are of fundamental importance to the operation of all semiconductor devices. This problem has been partially overcome using a heavily doped p-ZnTe ohmic contact layer. Nakayama et al (1993) reported the specific contact resistance between the Au electrode and p-ZnTe was about $10^{-3}\Omega cm^{-2}$ but in a few months time, Ozawa et al (1994) demonstrated the blue laser with a lower specific contact resistance ($10^{-6}\Omega cm^{-2}$) by introducing a Pd layer in between Au and p-ZnTe. Takeo Ohtsuka (1995) explained it as a possible breakage of high resistance bonds or native oxide layers between Au and p-ZnTe by Pd. Fermi level pinning has been well accepted and much work has been done to establish Fermi level pinning positions and to explain the mechanism. It has not been made clear in the literature how far ZnTe would be successful with different Fermi level pinning positions. Although nitrogen appears to be the most effective p

ZnSe BASED BLUE-GREEN LASER STRUCTURE

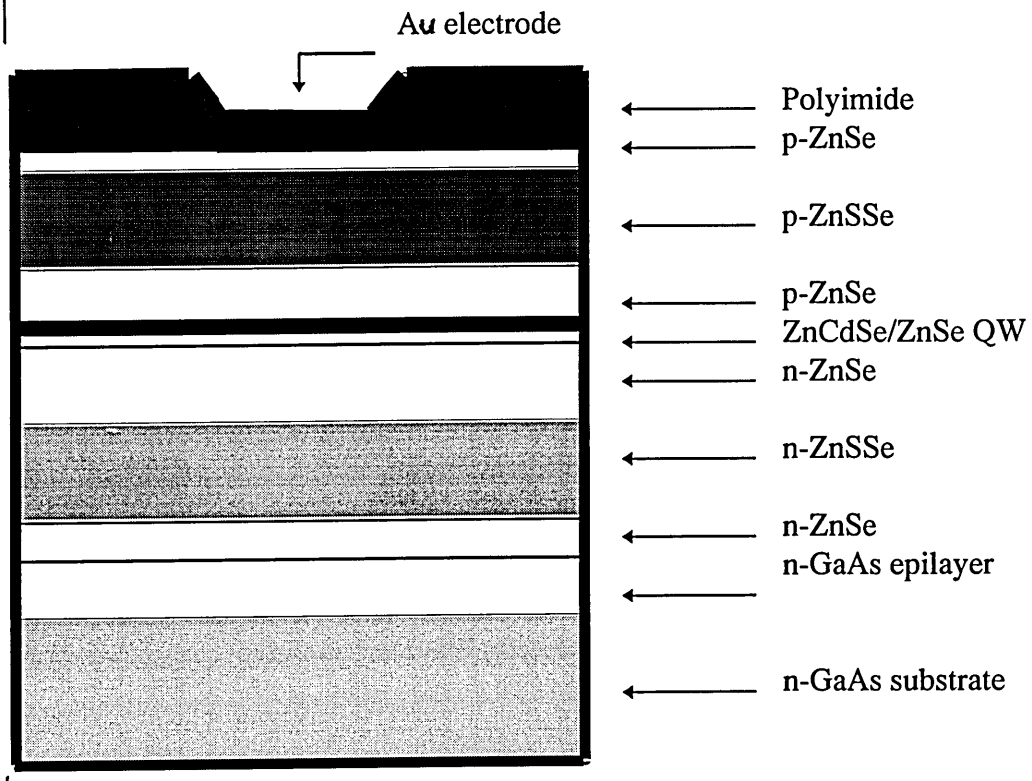

- This LASER device consists of one or more quantum wells between ZnSe or ZnSSe barriers, those provide carrier confinement.

- A larger number of quantum wells produces a higher gain at a given current well above threshold, and is the choice for systems with a large amount of loss.

- Gain guiding is provided by the cladding layers of ZnSSe which have a lower refractive index than the ZnSe guiding layers and are lattice matched to the GaAs substrate, reducing the number of mismatch dislocations.

Figure 1.7: Laser structure developed by Hasse et al in 1991.

dopant and the resistance of the p-layer seems to be decreasing with increasing band gap, the minimum conductivity of p-type ZnSe is limited.

Basically light emission takes place in the junction region of a p-n junction diode when excess electrons and excess holes are injected into the n-layer and p-layer respectively. The excess carrier concentrations are made by forward biasing the diode and light is emitted during the recombination of electron-hole pairs. The first ever blue laser based on ZnSe produced by 3M, Haase et al (1991) group is of the structure as shown in the figure 1.7. The structure is different from a simple p-n junction and $Zn_xCd_{(1-x)}Se$ quantum wells confine the charge carriers. ZnSe guiding layers were about half of the width of $ZnS_ySe_{(1-y)}$ cladding layers whose refractive indices are much lower than those of ZnSe. Although the control of the thickness of the cladding layers are given less consideration, the guiding layers are carefully determined by the refractive indices of the material and the working wavelength. In order to minimise the absorption of the emitted light by the substrate, a GaAs layer of a higher refractive index and lower band gap, the lower cladding layer is made thicker than the upper cladding layer. The other layers are there to optimise the surface morphology and to minimise the defect concentration. The device worked at 77 K with about 300-1000 Acm^{-2} threshold current density and under an operating voltage of 20-35 V. As the temperature increased towards room temperature the threshold current density increased to about 400-1500 Acm^{-2} moving the wavelength of the emitted light from 481 nm to 502 nm. This shift is explained as due to a thermally induced shrinking of the band gap. This is also said to have an effect of turning blue lasers at cryogenic temperature into blue-green at room temperature or at higher temperatures. Lattice mismatch between GaAs and ZnSe layers

in the structure develops dislocations. These dislocations then propagate through the active layer causing device failure.

The structure of light emitting devices is still not well established. The further development of light emitting devices utilising ZnSe ultimately depend on improvement of the low resistance ohmic contacts to ZnSe, reduction of defects and improvement of the graded structure preventing the generation of dislocations.

1.6.2 Light detecting devices based on ZnSe, CdSe and CdTe

Since the development of the Si p-n junction solar cell in 1954 by Chapin et al followed by a CdS based structure by Raynolds et al, much effort has been made to fabricate a highly efficient solar cell structure using different semiconductor compounds, Sze (1981). The CdS/CdTe anisotype heterostructure with over 9% conversion efficiency reported by Basol (1984) proved that it was an important candidate for the fabrication of high efficiency solar cells. To date Ferekides et al (1994), have improved the conversion efficiency of that same structure to 15.8%. ZnSe/CdSe and CdS/CdSe anisotype and isotype device structures have also been studied but significant improvements have not yet been reported.

The development of II-VI semiconductor based solar cell structures, mainly CdS/CdTe solar cells has been limited by several factors. Fermi level pinning has been identified as a limiting factor for the ITO/CdS/CdTe/metal solar cell. Five levels of Fermi level pinning of a metal/CdTe Schottky junction has so far been reported, Dharmadasa et al (1998). In a similar manner to the metal/ZnSe structure Fermi level pinning occurs in this device structure depending on the device manufacturing process and also with time.

Degradation of the device and short lifetimes have been identified as due mainly to the high series resistance of the metal/CdTe contact. Te-Au and Te-Sb contacts, Uda et al (1994), Au/Cu contacts, Chou et al (1995), were tested on CdTe but there has been no significant change in series resistance. Mondal et al (1992) used a ZnTe ohmic contact yet the conversion efficiency was about 8%. However, the major problem as described by Singh et al (1995), is the diffusion of oxygen through the metal contact forming a $CdTeO_3$ interface layer making the device an MIS structure.

Ferekides et al (1994), decreased the thickness of the CdS layer from 1000Å to 650Å, but, there is a critical thickness. For optimum characteristics of the cell, the CdTe films have to be heated at 400°C in air as pointed out in the literature, Morris and Vanderveen (1996). Although Wei and Rajashwar (1992) fabricated a ZnSe/CdSe multi layer super lattice structure successfully with no Cd contamination in ZnSe layers, $Zn_{(1-x)}Cd_xSe$ grown by Natarajan et al (1995) using electrochemical deposition technique found excess Cd in the films, destroying the crystalline orientation.

Solar cells in the laboratory scale of about 19% conversion efficiency would be needed to make 15% efficient commercial modules. The thin film technology next closest to commercial use is based on CdTe. Although 15.8% efficient laboratory based cells have been produced, the commercial module efficiencies could expected to be in the range of 10%.

Fermi level pinning of CdTe has been studied by several groups, Williams et al (1986) and Dharmadasa et al (1998). In general it is accepted in the literature that for the more ionic material the Schottky barriers are highly metal dependents whereas for Si or

GaAs, contact formed with covalent materials, the barrier is relatively independent of the metal, Fowell et al (1990). Electronic properties of CdTe are not well controlled, the treatments use in fabrication cause deviation. Tomitori et al (1987) observed six electron trap levels in n-CdTe. The main majority carrier trap levels were associated with Te and Cd vacancies and Cd interstitials, Lee (1988) and Isett et al (1984). Electron traps in CdS were reported by Grill et al (1979).

Electrical barriers to clean and chemically treated CdTe crystals show large variations of the order of 1 eV for different metals, Dharmadasa et al (1987). It has also been shown using XPS and SXPS that CdTe surfaces react with many metals. In contrast, metals which do not strongly react with CdTe such as Au and Sb are highly irreproducible, Dharmadasa et al (1989).

Another problem with CdSe compared to CdTe when using an electrochemical deposition technique is, Te reduction occurs at more positive potentials than Se, that highly reduced Te species such as H_2Te may not be expected to play a key role in CdTe deposition chemistry relative to the CdSe system.

1.7 II-VI semiconductor growth techniques

1.7.1 Conventional semiconductor growth techniques

One of the most exciting developments in modern semiconductor electronics is the capability of engineering the band structure and the optical properties by growing multi layers. With the advanced semiconductor growth techniques such as molecular beam epitaxy (MBE) and metal organic vapour phase epitaxy (MOVPE) methods, much of

modern compound semiconductor device fabrication now involves quite precise multi layer structures.

(a) Molecular beam epitaxy (MBE)

After a slow start in 1960's MBE became established rapidly as the technique to grow thin films, especially those containing multi layers. Although the evaporation of individual elements onto a glass substrate to give polycrystalline material and subsequent condensation was described in 1958, this technique was used to give monocrystalline layers only in 1968. The MBE technique began to receive a lot of attention with the growth of III-V compound semiconductors such as AlGaAs/GaAs structures. In this technique, substrates are loaded into the growth chamber, via a vacuum load lock system which prevents opening the chamber to air. In certain applications, there are sputter cleaning and high temperature heating stages, before the beginning of the growth process. The epitaxial sample growth process is done under ultra high vacuum condition of the order 10^{-10}-10^{-11} torr. The growth rate is about one monolayer per second and in situ monitoring is done by the reflection high-energy electron diffraction (RHEED) technique. The substrate is heated and rotated to improve deposition uniformity. The chemical composition, including any doping of the epilayer, can be varied via the temperature of the effusion cell or the apertures of the shutters.

Although the technique has been experiencing competition from the MOVPE technique, all successful fabrications of ZnSe based light emitting devices have been made using the MBE technique. ZnSe epilayers grown at Herriot Watt University have been used for electrical contact work in this project.

(b) Metal organic vapour phase epitaxy (MOVPE)

Metal-organic vapour phase epitaxy (MOVPE) is often referred to as metal-organic chemical vapour deposition (MOCVD). This epitaxial growth technique was first described in 1969 and mostly used to grow III-V semiconducting compounds. The process is a highly successful, basic technology used in the formation of advanced semiconductor devices. Since its further development in the 1980's, MOVPE has been applied to the growth of all major classes of heterojunction devices. The precursors used in the production of semiconductors are organic compounds and usually liquid at room temperature. They are transformed to the wafer surface by bubbling hydrogen carrier gas through the liquid. Dopant carrier gases may also be added to the reaction tube to produce conducting materials. MOVPE now produce epitaxial layers of excellent electrical and morphological characteristics over a large area of multi layered structures. Direct flow control, convenient handling of volatile elements like sulphur and nitrogen by using appropriate organic compounds, reproducible homogeneity of composition and quick access to the sample are some of the advantages of this technique. However, the MOVPE technique still has to overcome problems such as lack of in situ growth control to reach the quality of material growth by MBE. In addition the toxic nature of the precursors use in the technique is still under debate.

(c) Summary of conventional growth techniques

Although epitaxial thin semiconducting films of ZnSe and light emitting devices have been grown using the MBE technique, a photovoltaic device has not so far been developed to compete with Si technology.

ZnSe grown using MBE and MOCVD showed a high density of extended defects in the early stage. This was due to poor nucleation on the GaAs substrate, Prior (1996). Because of the smaller energy of formation of this type of defects in ZnSe which is about 2.12 $kJ.mol^{-1}$, compared to III-V compounds, (for GaAs it is 9.08 $kJ.mol^{-1}$) they are very easily formed in ZnSe. These defects are stacking faults and cause a loss in the crystallinity of the material. However, Gunshor et al (1997) showed that better quality ZnSe could be grown by using a GaAs substrate grown in a different chamber with an As cap instead of a clean GaAs layer. Closed space vapour transport (CSVT), liquid phase epitaxy, elemental co-evaporation and radio frequency sputtering techniques have also been used to grow ZnSe and other II-VI semiconductors.

To date few groups have reported significantly efficient CdS/CdTe thin film solar cells made using different other techniques. Chu et al (1992) achieved over 15% efficiency using the closed space sublimation (CSS) technique. Nishitani et al (1994) reported CdS/CdTe heterostructure made on ITO substrate with about 10% efficiency using a hot wall vacuum evaporation technique (HWVE). In order to achieve high efficiency, a ZnO thin layer was formed on ITO before CdS deposition, as ZnO can suppress the interdiffusion of indium and tin from ITO to the CdS layer. In addition ohmic contacts to the CdTe layer were made by doping acceptor impurities such as Cu, Ag, P.

1.7.2 Electrochemical deposition (ECD)

During the past several years, the electrochemical deposition technique has extensively been employed for the growth of semiconductors in the fields of solar cells and other optoelectronic devices. High solar energy conversion efficiencies of 17.5% for $CuInSe_2$ and 15.8% for CdS/CdTe and also values such as 8% for CdS/$CuInSe_2$ and 10.6% for

CdS/HgCdTe have been observed for thin film structures made using the electrochemical deposition technique. Photovoltaic cells for large scale terrestrial use require high efficiencies, long lifetime, stability and low cost which could be met with the electrodeposition technique. Low cost, minimum waste and simplicity are some of the advantages that this technique has over some of the other chemical and physical semiconductor growth methods. Primarily ECD offers the following attractive features for the manufacture of thin optoelectronic materials.

(a) It is an isothermal process, operating usually at low temperatures, usually below 200°C. The thin films can be deposited at low temperature with sharper junctions and minimum contamination, dopant redistribution and interdiffusion effects, which are typical of high temperature growth and fabrication. The purification and controlled doping are far easier than many other techniques.

(b) The film thickness and other properties such as morphology and stoichiometry can easily be controlled as they are dependants of electrical parameters such as cell voltage and current density.

(c) This technique is particularly suitable for the fabrication of large area heterojunction and multi layer optoelectronic devices, simply by changing the deposition electrolyte.

Potentiostatic electrochemical deposition has been proved to give stoichiometric ZnSe (Natarajan et al-1994), ZnTe (Neumann-Spallart et al-1995) and many other II-VI semiconducting compounds (Mishra et al -1989) than the galvanostatic electrochemical method. However there are some problems associated with compound semiconductor electro chemical deposition. Stoichiometric and non degenerate material deposition has been found to be relatively difficult, Engelken et al (1985). Achieving large grains and non amorphous deposits has also been found difficult specially in II-VI compound

semiconductors such as CdTe and ZnSe deposition. The work done by Wei and Rajashwar (1992), in electrodepositing nanomodulated layers of CdSe and ZnSe is noteworthy. The ratios Cd:Se and Zn:Se were remarkably even as proved by XPS results and also ZnSe layers were free of Cd contamination, in contrast to the fact that Cd contamination is a commonly identified problem in electrodeposited ZnSe layers under a Cd environment.

The electrochemical cell for the deposition of semiconductors almost always consists of three electrodes (figure 1.8), namely cathode or the working electrode on which the deposition takes place, anode or the counter electrode and the reference electrode. The electrode chosen as the universal standard is the reversible hydrogen reference electrode, which is the most important of the reference electrodes available for use with aqueous solutions. This is due to the fact that this electrode, set up in a solution of hydrogen ions at unit activity, exhibits a potential which is arbitrarily taken as zero at any temperature. The other available reference electrodes have been made with their potentials fixed with respect to hydrogen electrode. One very commonly used reference electrode is the silver-silver chloride electrode whose potential with respect to hydrogen electrode is given at 65°C by:

$$E_{Ag/AgCl} = 0.1969 + \left(\frac{2.303RT}{F}\right)pH \qquad [1.9]$$

This is prepared by immersing an electrode consisting of a noble metal (Pt) coated with Ag and AgCl in hydrochloric acid of known concentration, which is highly reproducible. The counter electrode keeps the potential difference between the cathode

ZnSe ELECTRODEPOSITION CELL

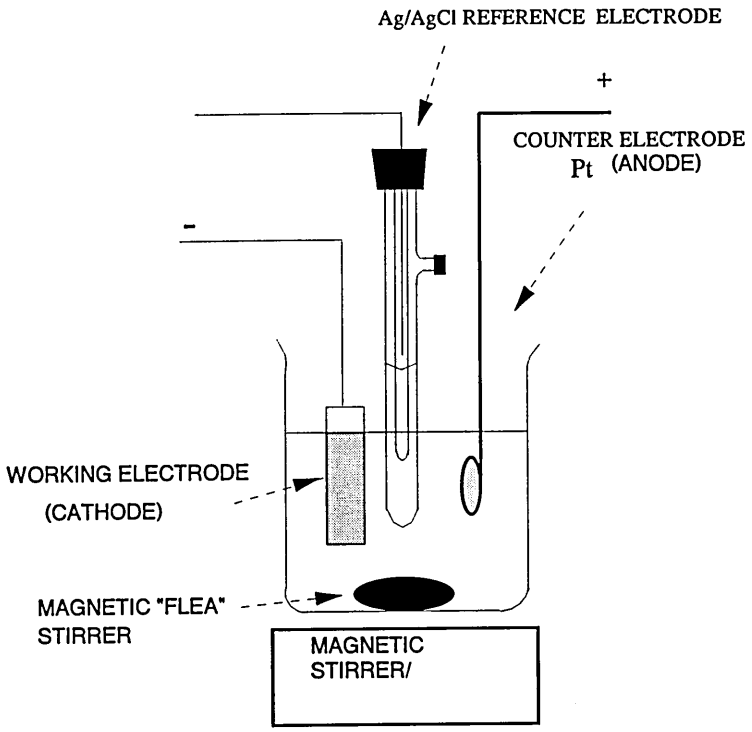

Cathodic electrosynthesis of MX [M=Zn, Cd and X = Se, Te] in aqueous medium involves the co-deposition of M^{2+} from $MCl_2(aq)$ (or $MSO_4(aq)$) and X^{2-} from $H_2SeO_3(aq)$ or XO_2. Deposition of ZnSe involves the following steps.

$$Zn^{2+} + 2e^- \longrightarrow Zn^o$$

$$H_2SeO_3 + 4H^+ + 4e^- \longrightarrow Se^o + H_2O$$

$$Zn^o + Se^o \longrightarrow ZnSe$$

Figure 1.8 Schematic Diagram of Electrodeposition Cell

and the reference electrodes unchanged. From thermodynamics, the maximum electrical energy available from such a cell is proportional to the change in Gibbs free energy:

$$\Delta G = -nFE \qquad [1.10]$$

where n is the number of electrons participating in the reaction and F is Faraday's constant. If the Gibbs free energy change is negative for a reaction, then the reaction is thermodynamically favoured to proceed in the forward direction. The formation of II-VI semiconductors has been found rather difficult, the reason being the large potential difference between group II-VI species. In order to achieve cathodic deposition, the deposition potential of the less noble component (group II species) must be shifted relative to the noble component (group VI species) by the free energy gained from compound formation. Therefore the gain in Gibbs free energy must be able to balance the potential difference between the species. Out of all II-VI semiconductor compounds, CdTe, the least difference in standard potentials of components and ZnSe, the widest gap between the potentials of components have been found relatively difficult to deposit in the literature. This is because, for these two compounds, CdTe and ZnSe, the difference in standard potentials between Zn and Se as well as Cd and Te is greater than the shift in potential due to the change in free energy of formation of the compound. The shift of potential is a constant value for the formation of a compound. When the experiments are operating at normal laboratory conditions (not standard conditions) the deposition potential is given by the Nernst equation, which is

$$E_M = E_M^{\circ} + \frac{RT}{nF} \ln\left(\frac{a_M^{m+}}{a_M}\right) \qquad [1.11]$$

where E_M is the potential of the metal electrode m in a given situation, E_M° is the standard potential for the reduction to form M, R is the gas constant, T the absolute temperature, n the number of electrons required for the reduction, F the Faraday constant and a_M^{m+} and a_M are the activities of M^{m+} metal ions in the electrolyte and of m in the deposit respectively.

Electrodeposition of M can occur at potentials more negative than the equilibrium potential due to the neglect of interactions of the solute M^{m+} ion with the solvent or with other complexing legends in the above equation. They are known as overpotentials. The condition for the simultaneous deposition of two different metals at the cathode can be written as ,

$$E_M + \eta^m = E_X + \eta^X \qquad [1.12]$$

Here E_M and E_X are the equilibrium potentials for the elements M and X respectively and η^M and η^X are their respective overpotentials.

Codeposition requires the equilibrium potentials of the two ions to be close (<200 mV) to each other. The activities of M and X in the compound are determined by their concentrations, and by the thermodynamic stability of the deposit. The reversible potential of a metal M alloyed with a component should be more positive than that of the pure metal. This is because of the free energy of formation of the alloy or compound.

One common method of representing the Nernst equation is to plot reversible potential against pH values of the solution known as Pourbaix diagram, Marcel Pourbaix (1966). Pourbaix diagrams for ZnSe, CdSe and CdTe are shown and discussed in chapter 3. These diagrams are very useful in the determination of the most stable potential region of the compound for the deposition.

The approximate thickness of electrodeposited films can be determined using Faraday's law of electrolysis which has been derived assuming that the amount of the deposition formed is directly proportional to the electric charge passed through the system and the masses of products formed are proportional to the electrochemical equivalent weights of the products.

$$m = \frac{sMIt}{nF} \qquad [1.13]$$

where m is the mass of the deposit, s is the stoichiometric coefficient of the species of the deposit, M is the atomic or molecular weight, I is the current and t is the deposition time.

CHAPTER TWO:

THEORIES AND MODELS OF OPTOELECTRONIC DEVICES

2.1 Introduction

Any electronic device requires a front and a back electrical contact to connect it to external circuits. Their electrical contacts, known as ohmic or Schottky contacts depending on their electrical properties, are usually metal contacts formed on the semiconducting device surfaces. These electrical properties mainly depend on the potential barrier height present at the metal/semiconductor interface. As far as Schottky contacts are concerned, according to the Schottky - Mott theory, barrier height for n-type or p-type semiconductors depends on the metal and the semiconductor properties. However, the dependence of the Schottky barrier height on metal work function, specifically of metal/II-VI semiconductors has not been proved convincingly. During the days when the Schottky model was introduced only electrical measurements such as I-V and C-V were the main experimental tools available giving macroscopic information. Later developments in analytical techniques led to the study of Schottky barriers microscopically as well. These advances led to the development of a number of models using data that was ignored in deriving Schottky model.

The different models attempting to describe the formation of Schottky barriers, Fermi level pinning mechanisms and transport processes across the interfaces are discussed in this chapter. The device structures where these theories are applied are also discussed towards the end of the chapter.

2.2 Summary of models of Schottky barrier formation and Fermi level pinning.

The band bending of a Schottky barrier is given by the classical expression;

$$qV_B = \phi_m - \phi_{SC} \qquad [2.1]$$

and Schottky barrier by

$$\phi_B = \phi_m - \chi_S. \qquad [2.2]$$

In general, band bending does not follow these simple theories. The band bending has shown a little dependence on the metal work function in the literature, Brillson (1994), Blomfield et al (1995). Brillson (1978 and 1979) observed that the sensitivity of band bending to different metals varies with the way that semiconductor molecules are bonded. The band bending is high for ionically bonded and low for covalently bonded semiconductors.

2.2.1 Models of Schottky barrier formation

(a) The Bardeen model

According to the Schottky model, the height of a Schottky barrier must have a linear relationship with the metal work function. However, experimentally measured values in the literature indicates little agreement with this theory. In order to understand this relative insensitivity, Bardeen (1947) proposed his model explaining the role that electronic states localised at the semiconductor surface play in the contact rectification.

In this model interface states which may arise due to various defects are taken into account. A number of interface states or electronic levels are distributed in

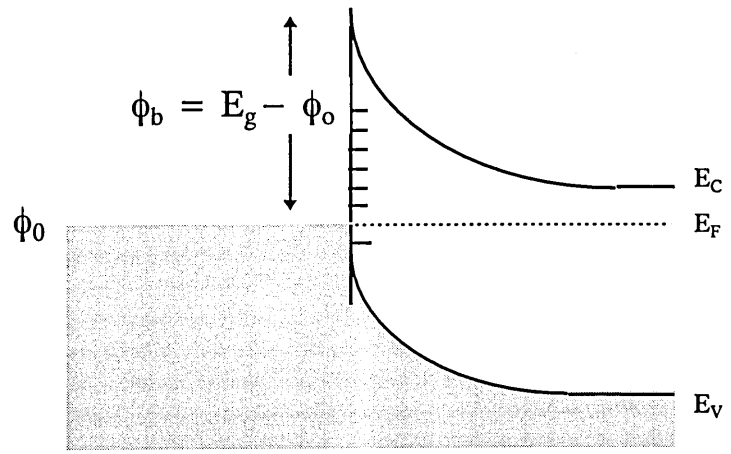

Fig 2.1 A practical metal-semiconductor interface, there are large number of interface states in the band gap region.

the band gap at the interface. A neutral level ϕ_o (Figure 2.1) is selected having the properties that states below it are neutral if filled and above it are neutral if empty. If the density of states is very large near ϕ_o then the Fermi level will not alter if electrons are added or depleted to the semiconductor. The Fermi level is then said to be pinned, and the Schottky barrier height which is almost independent from the metal used is;

$$\phi_b = E_g - \phi_o \qquad [2.3]$$

This model gives only a qualitative explanation of the Schottky barrier heights.

(b) The Linear Model

Kurtin et al (1969) introduced a parameter called "the index of interface behaviour (S)" in an attempt to combine both the Schottky and Bardeen models. Then the relationship for the barrier height becomes

$$\phi_b = S\ (\chi_m - \chi_s) + C \qquad [2.4]$$

where C is a constant and χ_m, χ_s are the electronegativities of the metal and semiconductor respectively.

This model will obey the Schottky model for S=1 (and C=0) and when S=0 it obeys the Bardeen model in determination of the barrier height. The value of S is close to unity for ionic materials because of their low density of interface states and they therefore obey the Schottky model whereas covalent materials have a high density of interface states and obey the Bardeen model. The behaviour of the materials in the transition between the two regions was explained by the presence of sufficient surface states to pin the Fermi level to some extent, but not enough to make the barrier height independent of metal work function. II-VI semiconductors such as ZnSe and CdS occupy the transition region between ionic and covalent materials (Fig.2.2).

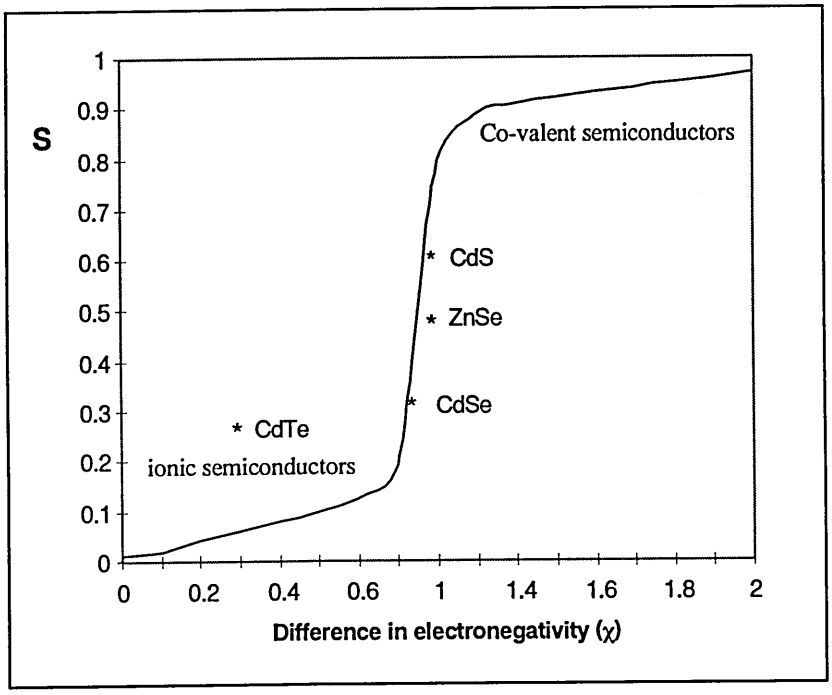

Figure 2.2 Interface behaviour (S) against electronegativity after Kurtin et al in 1969.

(c) The Effective Work Function Model

Freeouf and Woodall (1981) assumed that microclusters at the interface, non-stoichiometry, metal semiconductor interaction, oxide species and different phases formed due to chemical interactions were also contributors to the Schottky barrier formation. Therefore the Schottky model was accepted but an average work function of different interface phases or an effective work function (ϕ_{eff}) was introduced to replace simple metal work function (ϕ_m) in the Schottky theory giving,

$$\phi_b = \phi_{eff} - \chi_s. \qquad [2.5]$$

Thus the measured ϕ_b can depend on the effective work function of the intermediate phase and also on the measurement technique, e.g. I-V or C-V. For many semiconductor compounds, effective work function (ϕ_{eff}) is mainly due to the work function of the anion (ϕ_{anion}) of the semiconducting compound.

2.2.2 Models of Fermi level pinning

Fermi level pinning has been observed and discussed in detail for metal/II-VI semiconductor systems in the literature, Blomfield et al (1995). The mechanism by which the pinning occur has been discussed by several groups following Bardeen's theory.

(a) Metal Induced Gap States (MIGS) Model

Heine (1965) suggested that a continuous distribution of surface states may exist within the semiconductor band gap due to the exponentially decaying metal wave functions which could be responsible for Fermi level pinning. Apart from penetrated wave

functions from metal to semiconductor when making contacts, there is a possibility that any localised states may change into broadened resonances. This may result in generating additional interface states. Williams (1990) described the possibility of new states appearing in the band gap. The existence of MIGS has been studied by various research groups during the last two decades. However, there is now strong evidence that they do exist and play a major role in the formation of electrical barriers.

Tejedor et al (1977) applied the model to a metal/Si (111) junction and developed the relationship:

$$\phi_b = \left(\frac{1}{1+\alpha N_{VS}}\right)\left[\phi_m - \chi - D_j + \alpha N_{VS}(E_g - \phi_o)\right] \quad [2.6]$$

where N_{VS} is the density of states of interface states, α is a complicated function of all the parameters of the charges and D_j is the lattice constant of the metal. All three of these parameters depend on the metal, in line with experimental evidence. Interestingly, two classical limits, Bardeen and Schottky, can be studied with this model. The Bardeen model can be explained considering a high density of states. For the case of high density of states or when N_{VS} reaches very high values (N_{VS} -----> α), the barrier height will be given by;

$$\phi_b = E_g - \phi_o, \quad [2.7]$$

explaining the Bardeen limit. When there are no interface states N_{VS} would be negligibly small (N_{VS} ----->0) and the equation reduces to;

$$\phi_b = \phi_M - \chi + D_j \qquad [2.8]$$

which has an additional term, D_j to the Schottky model. The significance of D_j however has not been evaluated.

Tersoff (1984) discussed the MIGS model and described it as an appropriate model for bulk MS interfaces and also suggested the continuum nature of gap states and the resulting locally metallic character of the semiconductor near the interface.

(b) The Unified Defect Model

This model was proposed, based on the Fermi level pinning by defect levels, by Spicer et al (1979). As Bardeen suggested, at the free surface a very small number of states in the gap can pin the Fermi level. Tersoff (1984) experimentally observed evidence for defect related pinning of the Fermi level on surfaces with submonolayer metal coverage. However, results of these experiments are inconsistent with bulk barrier height measurements. In particular submonolayer metal coverage neither serves the defect charge effectively nor provides a continuum of states in the gap.

Spicer et al (1986) found experimentally that non-metals, as well as a bare GaAs surface, produced pinning at the energy levels predicted by the unified defect model, which was hard to explain using MIGS or EWF model. As a further improvement to the model, it was suggested that the most likely defects in III-V semiconductors were of the antisite type where a cation site is occupied by an anion and vice versa. The antisite defect As on Ga was identified as being responsible for deep levels, at 0.74 eV above

the valence band maximum for GaAs in the advanced unified defect model, by the same group in 1988.

(c) The Disorder Induced Gap States (DIGS) model

Hasegawa et al (1986) assumed that oxidation, chemical etching process or diffusion may cause the formation of disordered layers in a metal/semiconductor junction interface which may uniformly be distributed throughout the band gap. E_{HO} is a neutral position between bonding and anti-bonding states at which Fermi level will be pinned. The calculated values using this model coincide very often with E_b, the corresponding energy value for ϕ_b, which makes it difficult to distinguish between the two. However, it was calculated that E_{HO} would occur about 5eV below the vacuum level and the barrier height would be given by;

$$\phi_b = 5.0 - \chi_s \qquad [2.9]$$

This equation shows that the Fermi level pinning is independent of the metal and the surface preparation procedure, but not the semiconductor material.

(d) Pinch off Model

Another significant model which was based upon inhomogeneities proposed by Ohdomari and Tu (1980) at the metal/semiconductor interface, is the 'pinch off model'. Freeouf et al (1982) assumed that interfacial inhomogeneities would lead to the formation of a number of diodes under one metal contact. The current transport properties of these devices can be assumed as those of a number of parallel diodes. Tung et al (1992) suggested that previous models of parallel conduction were in significant

error when the inhomogeneities of the Schottky barrier height were on a scale less than or comparable to the depletion width. This error arises as a result of the model failing to take the effect of pinch off into account. An area is said to be pinched off if majority carriers originating from outside the space charge region need to go over a potential barrier, higher than the band edge position at the MS interface, in order to reach the interface. The pinch-off model was used by Tung to explain such effects as greater than unity ideality factors, temperature dependence of the ideality factor and differences in Schottky barrier height depending upon the measurement technique used.

2.2.3 Summary of models

The models mentioned above are some of the main attempts found in the literature to explain the formation of the Schottky barrier. Many of these models have been applied to Si and III-V semiconductor systems but the applications to II-VI systems have not been studied in detail. Real systems may well be explicable by using more than one of these models as proposed by Williams (1991).

2.3 Current transport mechanism across semiconductor devices

In p-n junction diodes, majority carriers as well as minority carriers take part in current transport process, whereas in MS junctions only majority carriers are held responsible. The current flow across a Schottky barrier can involve a number of different mechanisms. The most important mechanism is thermionic emission in which electrons having energy greater than the barrier height [$e(V_b-V)$ when forward biased] can pass across the junction, and diodes whose current transport mechanism is predominantly thermionic emission are known as "Ideal diodes". In addition to thermionic emission, if the semiconductor is heavily doped so that the depletion width is very small, electrons

can tunnel through the barrier generating a current. There are also other mechanisms, as shown in figure 2.3, in high quality Schottky barriers such as minority carrier injection and trap related recombination, which are less important.

All the mechanisms except thermionic emission make devices deviate from ideal behaviour. In general the transport of electrons over the potential barrier for a high-mobility semiconductor can be described by thermionic emission theory. Diffusion theory and generalised thermionic-diffusion theory are applicable to low-mobility semiconductors.

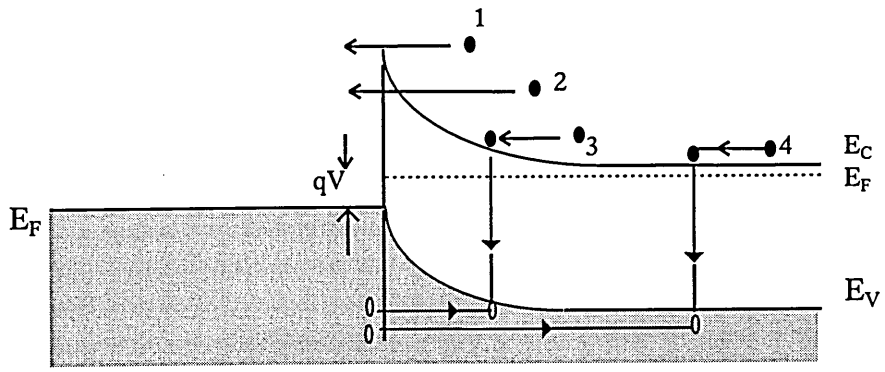

Figure 2.3 Four basic transport processes under forward bias. 1. thermionic emission 2. quantum mechanical tunnelling of electrons through the barrier (important for heavily doped semiconductors and responsible for ohmic contacts) 3. recombination in the space charge region 4. minority carrier (hole in this case) injection from the metal to the semiconductor.

In thermionic emission theory the mechanism is the emission of carriers over the potential barrier. In diffusion theory it is diffusion through the depletion region and in the combined theory it is the combination of these two mechanisms.

2.3.1 Thermionic emission theory diffusion theory and combined thermionic and diffusion theory

(a) Thermionic emission theory

Bethe (1942) derived thermionic emission theory assuming

i. barrier height ϕ_b is very much greater than the thermal energy kT and

$\varepsilon(x_m) > kT/q\lambda$, where $\varepsilon(x_m)$ is the electric field at the boundary of the interface within the semiconductor and λ is the carrier mean free path.

ii. thermal equilibrium, which is not affected by the existence of net current flow, is established at the plane that determines emission.

The current flow depends solely on the barrier height ϕ_b and does not depend on the barrier profile because of these assumptions. The electron concentration on the semiconductor side of the barrier is given by

$$n = N_c \exp\{-q(\phi_b - V)/kT\} \qquad [2.10]$$

where $N_c = 2(2\pi m^* kT/h^2)^{3/2}$ is the density of states in the conduction band whose m^* is the effective mass, q is the electronic charge, V the applied voltage across the semiconductor, k is the Boltzmann constant, T is absolute temperature and ϕ_b is the barrier height of the metal/semiconductor interface. The current density flowing from semiconductor to metal is $J_{s-m} = nqv/4$ according to kinetic theory, and $v = (8kT/\pi m^*)^{1/2}$. Therefore the current density is given by

$$J_{s-m} = (N_c qv/4).\exp\{-q(\phi_b - V)/kT\} \qquad [2.11]$$

Also we have to consider the thermionic emission from the metal to the semiconductor, these electrons always see the same potential such that

$$J_{m\text{-}s} = (qN_c v/4). \exp\{-q\phi_b/kT\} \qquad [2.12]$$

Hence the net current density J across the barrier should be

$$J = J_{s\text{-}m} - J_{m\text{-}s}$$

$$J = qN_c v/4.\exp(-q\phi_b/kT).\{\exp(qV/kT)-1\} \qquad [2.13]$$

substituting known values

$$J = A^*T^2\exp(-q\phi_b/kT).\{\exp(qV/kT)-1\} \qquad [2.14]$$

where $A^* = 4\pi m^* qk^2/h^3$ gives the current through the barrier due to the thermionic emission.

(b) Diffusion theory

Diffusion theory is mainly applicable to low mobility semiconductors. Schottky (1938) derived this theory assuming;

1. barrier height is very much larger than the thermal energy
2. electron collision within the depletion region is considered
3. carrier concentration at the ends of the depletion region is not affected by the current flow
4. impurity concentration of the semiconductor is non-degenerate

The current in the depletion region is dependent on the electric field created at the interface (local field). Therefore the current density (J_n) for an n-type semiconductor can be given using Maxwell's equation ;

$$J_n = q\left[n(x)\mu E + D_n \frac{\partial n}{\partial x}\right] \qquad [2.15]$$

where D_n is the diffusion coefficient, μ is the mobility of electrons and E is the electric field at the interface.

Using Einstein's relationship $D_n = \frac{kT}{q}\mu$, J_n can be expressed as,

$$J_n = qD_n\left[-q\frac{n(x)}{kT}\frac{\partial V(x)}{\partial x} + \frac{\partial n}{\partial x}\right] \qquad [2.16]$$

which can be integrated over the whole depletion region to take the form

$$J_n = J_D\left[\exp\left(\frac{qV}{kT}\right) - 1\right] \qquad [2.17]$$

where

$$J_D = \frac{q^2 D_n N_C}{kT}\left[\frac{q(V_b - V)2N_D}{\varepsilon_S}\right]^{1/2} \exp\left(\frac{-q\phi_b}{kT}\right) \qquad [2.18]$$

This relationship for J_n is similar to the current transport expression for thermionic emission (as well as that of p-n junctions), however, the saturation current density is more sensitive to voltage variations and less sensitive to temperature variations compared with the saturation current density for thermionic emission. This indicates the diffusion theory's applicability to low mobility semiconductors.

(c) Combined thermionic emission and diffusion theory

Thermionic emission and diffusion combined theory was described by Crowell and Sze (1966). Taking the image force lowering [chapter 2.3.2(a)] also into account, the current density J was expressed as

$$J = \frac{qN_C v_R}{1+\left(\frac{v_R}{v_D}\right)} \exp\left(-\frac{q\phi_{Bn}}{kT}\right)\left[\exp\left(-\frac{qV}{kT}\right)-1\right] \qquad [2.19]$$

where v_D is the effective diffusion velocity associated with the transport of electrons from the edge of the depletion layer at 'w' to the potential energy maximum and v_R is the thermionic recombination velocity near the metal/semiconductor interface. If $v_D >> v_R$, the current density is dominated by v_R and hence the thermionic emission is dominant whereas if $v_R >> v_D$ the diffusion process is dominant according to the equation. If the electron mobility is independent of the electric field, and if the image force lowering effects are neglected, $v_D = \mu\varepsilon$, where ε is the electric field in the semiconductor near the boundary. Combined with this result, equation 2.19 gives the relationship for diffusion when $v_D >> v_R$ and it agrees with the thermionic emission theory when $\mu\varepsilon(x_m) > v_R$. This condition is in agreement with Bethe's $\varepsilon(x_m) > kT/q\lambda$. It can also be simplified to $J = J_S(e^{qV/kT} - 1)$, where $J_S = A^{**}T^2\exp(-q\phi_{Bn}/kT)$. Here A^{**} is the effective Richardson constant. However the current transport mechanism in most semiconductor Schottky barrier diodes is due to thermionic emission of majority carriers.

2.3.2 Deviation from ideal thermionic emission theory

(a) Image force lowering

As described by Rhoderick and Williams (1988), intimate metal/semiconductor contacts tend to reduce the barrier height depending on the bias due to the image force as shown in the figure 2.4.

The effective barrier height can then be given as,

$$\phi_e = \phi_b - \Delta\phi_I \qquad [2.20]$$

If ϕ_e varies linearly with the bias voltage, $\frac{\delta\phi e}{\delta V} = \beta$, where β is a constant. Therefore ϕ_e can be given as

$$\phi_e = (\phi_b)_o - (\Delta\phi_i)_o + \beta V \qquad [2.21]$$

Thermionic emission theory can be altered using this relationship to

$$J = J_o \exp\left(\frac{qV}{nkT}\right)\left[1 - \exp\left(\frac{-qV}{kT}\right)\right] \qquad [2.22]$$

with a modified J_o,

$$J_o = A^* T^2 \exp\left[-q\left(\frac{(\phi_b)_o - (\Delta\phi_i)_o}{k'T}\right)\right] \qquad [2.23]$$

The diode quality factor, 'n' is defined as $\frac{1}{n} = 1-\beta$.

In fact n is a value representing the bias dependence of the Schottky barrier height.

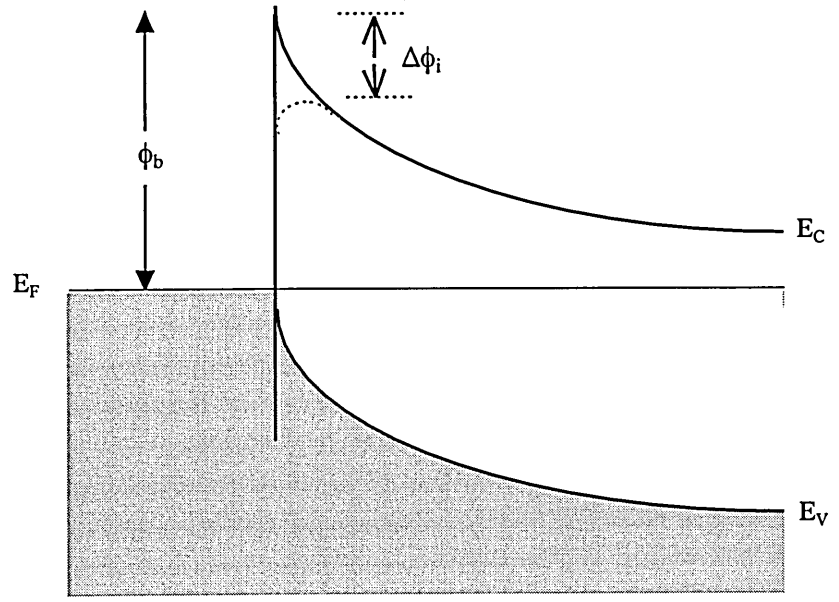

Figure 2.4 image force lowering by $\Delta\phi_i$

(b) Quantum Mechanical Tunnelling

Field emission and thermionic field emission are the two possible mechanisms of quantum mechanical tunnelling in Schottky barriers. For a heavily doped semiconductor or one at low temperatures, the tunnelling current may become the dominant transport process. Field emission involves electrons tunnelling through the barrier in the region close to the semiconductor Fermi level and is more likely to occur at low temperatures. Thermionic field emission occurs when electrons tunnel through the narrow barrier at higher energies. This is more likely to occur at high temperatures and in heavily doped materials as there are more electrons at higher energy. However, for an Au-Si barrier when the donor concentration $N_d \leq 10^{17}cm^{-3}$ and $T \geq 300K$ the ratio of the tunnelling current to the thermionic current is very much less than unity and thus the tunnelling component can usually be neglected. In general, the current density will have to be

modified to include both thermionic emission and tunnelling currents. When the tunnelling current is proportional to the product of the quantum transmission coefficient and either the occupation probability in the semiconductor or the unoccupied probability in the metal.

If the tunnelling current determines the current flow, as in the case of a high carrier concentration or low temperature, the transmission coefficient will be of the form;

$$T(\eta) \approx \exp\left(\frac{-q\phi_b}{E_{oo}}\right) \qquad [2.24]$$

where $E_{oo} = \frac{qh}{4\Pi}\sqrt{\frac{N_D}{\varepsilon_S m^*}}$

Tunnelling current too has a similar expression;

$$J_t \approx \exp\left(\frac{-q\phi_b}{E_{oo}}\right) \qquad [2.25]$$

which indicates that the tunnelling current increases exponentially with the square root of the carrier concentration.

(c) Generation and Recombination theory

Generation and recombination can occur either in the neutral region or in the depletion region of a Schottky barrier and recombination in the depletion region can influence electron transport characteristics. This is the main process by which electron hole pairs

are generated or recombined across the band gap. The recombination and generation current density at low forward bias is given by;

$$J_I = J_{IO} \exp\left(\frac{qV}{2kT}\right)\left[1 - \exp\left(\frac{-qV}{kT}\right)\right] \qquad [2.26]$$

where $J_{IO} = \frac{qn_i w}{2\tau_r}$

n_i = intrinsic carrier concentration

w = width of the depletion region

τ_r = carrier lifetime in the depletion region

When the MS junction is forward biased, the major recombination-generation processes in the depletion region are the capture processes, also we have a recombination current and diffusion current as well. The experimental results for the total forward current in general has been represented by S.M.Sze (1981) by the empirical form,

$$J_F \sim \exp\left(\frac{qV}{nkT}\right) \qquad [2.27]$$

where the factor n equals 2 when the recombination current dominates and n equals 1 when the diffusion current dominates. When both currents are comparable n has a value between 1 and 2.

(d) Minority carrier injection ratio

Under low injection conditions a Schottky barrier diode is mainly a majority carrier device. At sufficiently large forward voltages the minority carrier injection ratio γ , which is defined as the ratio between the currents due to the minority carriers to the total

current, increases with current. This is due to the enhancement of the drift field component, which becomes much larger than diffusion current at high forward voltages. For low injection conditions, minority carrier drift is negligible in comparison with diffusion. However for sufficiently large forward bias voltage the electrical field causes significant carrier drift current. This eventually dominates the minority carrier current.

In order to reduce the minority carrier injection ratio in device applications, semiconductors with large N_D, which corresponds to a low resistivity, large J_s which corresponds to small barrier height and small n_i which corresponds to large band gap, must be used.

(e) Interfacial layers

The presence of an insulating layer between metal and semiconductor in an MS junction is inevitable in practical devices. Very thin oxide layers are commonly associated with MS structures making them MIS (or MOS) devices. Card and Rhoderick (1971) pointed out that these layers on Si contained charges which affect the semiconductor surface potential. They have also observed experimentally that these charges were ionic and positive. Therefore in the presence of these charges the diffusion potential would reduce in n-type semiconductors and increase in p-type semiconductors thus increasing their barrier height. Oxide charge is expected to increase with film thickness. The I-V relationship of the device can be understood by a modified 'n' in the presence of interfacial layers. Card and Rhoderick (1971)derived a relationship for n, which is,

$$n = 1 + \frac{\left(\frac{\delta}{\varepsilon_1}\right)\left[\left(\frac{\varepsilon_S}{w}\right) + qD_{sb}\right]}{1 + \left(\frac{\delta}{\varepsilon_1}\right)qD_{sa}} \qquad [2.28]$$

2.3.3 Capacitance of a Schottky barrier

Similar to a p-n junction, the depletion region of a Schottky barrier can be considered as a voltage dependent capacitor. In the ideal situation minority carrier transport across the junction can be neglected, hence the effect of minority carriers can be neglected if the barrier height is over 3kT/q. The induced band bending V_r for a reverse bias will be equal to the diffusion voltage V_d. The maximum electric field due to uncompensated donors is,

$$E^2{}_{max} = \frac{2qN_d}{\varepsilon_S}\left(V_d - \frac{kT}{q}\right) \qquad [2.29]$$

The charge due to uncompensated donors is given by the Gauss' theorem

$$Q_d = \varepsilon_S E_{max}$$

Therefore

$$Q_d = \left(2q\varepsilon_S N_d\right)^{1/2}\left(V_d - \frac{kT}{q}\right)^{1/2} \qquad [2.30]$$

The capacitance of the Schottky barrier is the partial derivative of the charge (Q_d) with respect to the applied reverse potential (V_r).

$$C = \frac{\partial Q_d}{\partial V_r},$$

However,

$V_d = V_r + V_{do}$ where V_{do} is the band bending at reverse bias which is given by;

$$V_{do} = \phi_b - \zeta$$

and can be regarded as a constant to a large extent. Therefore the capacitance can be given as the partial derivative with respect to V_d.

$$C = \frac{\partial Q_d}{\partial V_d}$$

which in turn can be given by

$$C = \left(\frac{q\varepsilon_s N_d}{2}\right)^{1/2} \left(\phi_b - \varsigma + V_r - \frac{kT}{q}\right)^{-1/2} \qquad [2.31]$$

The capacitance studies of a Schottky barrier can be used to determine the carrier concentration, barrier height and also parameters of deep traps as described in chapter 3. The carrier concentrations are found to be of the right order when using the capacitance studies in the literature, by Dharmadasa (review article-in press) and Wang et al (1995). However, the barrier heights deviated from values determined for the same devices using other techniques. This deviation is attributed mainly to the interfacial layers present in the MS interface and deep electron traps in the bulk of the semiconductor.

(a) Effects due to interfacial layers

Cowley (1966) discussed the effects of interfacial layers. The plot of C^{-2} against V_r remains linear with the gradient $2/q\varepsilon_S N_A$ but the intercept was interfacial layer dependent. If the interfacial layer is sufficiently thin, the occupancy of interface states is predominantly governed by the electrons tunnelling from the metal.

(b) Effects due to deep traps

Figure 2.5 shows a Schottky junction with a deep impurity level and a shallow doping level.

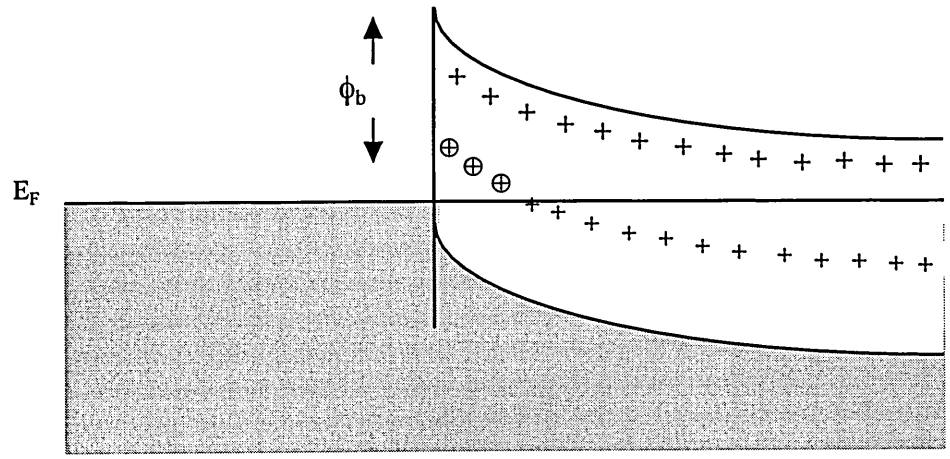

Figure 2.5 A Schottky barrier with a shallow doping level and a deep electron trap.

When a voltage is applied to the device, all donors above the Fermi level will be ionised giving a higher doping concentration near the interface. In capacitance measurements, a small AC signal is superimposed on the DC bias voltage. A deep level can follow this signal giving an additional contribution to the capacitance.

2.4 Light emitting devices

Conventional light sources emit light as a result of their high temperature. In this case most of the energy is supplied results in heat rather than light, so as a light source the process is relatively inefficient. Semiconductor light emitting devices operate in a different way, known as luminescence. This is a result of electronic excitation or generation and recombination. Electrons at higher energy levels fall to available lower energy state emitting photons having an energy equal to the energy difference of the two levels. The two types of semiconductor light emitting devices are isotropically light emitting LED's and lasers with intense monochromatic light beams.

2.4.1 Light emitting diodes (LED)

The basic structure of an LED is a p-n junction. The depletion region of a p-n junction emits light when a current is passed through the device under forward bias. This is known as injection electroluminescence. Electrons and holes are injected from n-side and from p-side respectively of a p-n junction under forward bias. The injected carriers pass across the junction and become excess minority carriers in the region of opposite conductivity. For an LED the excess carriers must be aimed to recombine quickly. The material should have a short minority carrier lifetime and diffusion length for this process to happen. When they recombine, photons with the energy ($h\nu$) equal to the band gap (E_g) of the material are emitted. In fact photon energy is given by;

$$h\nu = E_g + kT \qquad [2.32]$$

For practical purposes the 'kT' term can be ignored, therefore ;

$$h\nu \approx E_g \qquad [2.33]$$

A direct band gap semiconductor has a high transition probability and a short minority carrier lifetime. For an indirect band gap semiconductor, the probability of occurrence is low as phonon scattering is involved in the transition process in order to conserve momentum.

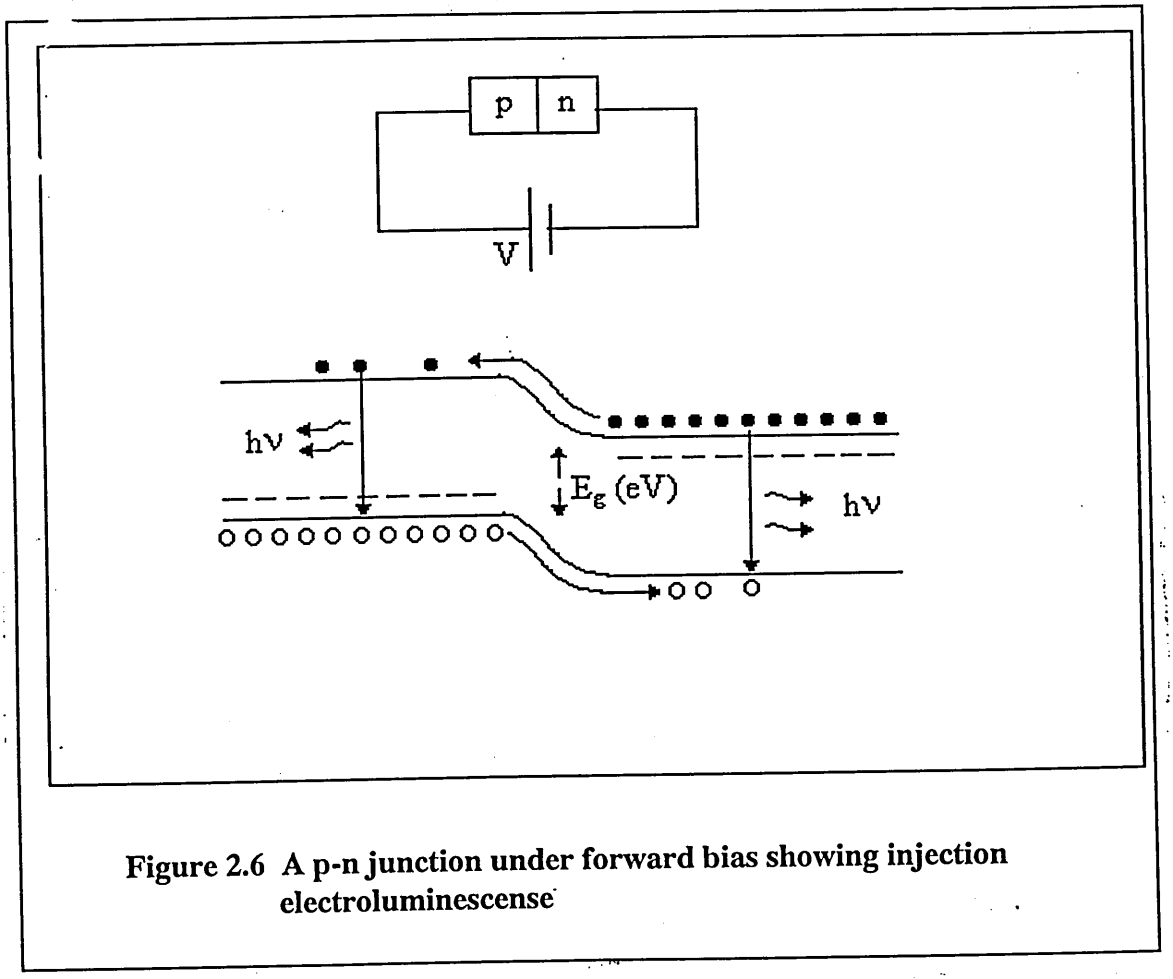

Figure 2.6 A p-n junction under forward bias showing injection electroluminescense

This spontaneous emission is the main transition process in an LED. Each recombination is independent of any other. The transition process in a semiconductor laser is different from spontaneous emission of radiation and known as stimulated emission.

2.4.2 Semiconductor lasers

LED and a semiconductor laser have a lot of similarities in their physical construction. The fundamental difference in transition is the spontaneous emission and stimulated emission.

As in the case of spontaneous emission, a photon is incident on a semiconductor and interacts with a valence band electron, it will be absorbed and the energy will be used to create an electron-hole pair.

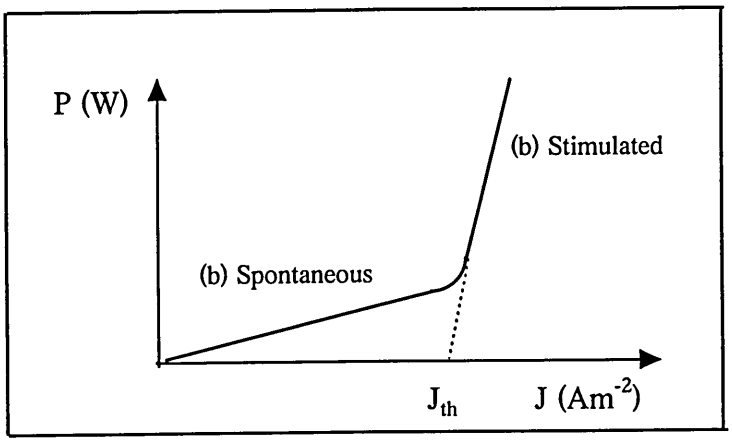

Figure 2.7 Power output vs current input characteristic of a semiconductor laser

However, if it interacts with an electron in the conduction band while in the excited state, then the electron is stimulated immediately to make its transition to the ground state and gives off a second photon. These two photons consequently produce more photons and the process is called stimulated emission. The emitted photons are experimentally found to be in phase with the stimulating photon.

An LED works by spontaneous emission, so does a laser up to the threshold current. Above the threshold current density, stimulated emission becomes the dominant mechanism for photon production increasing the forward current linearly. The stimulated process is much more efficient and hence the power-current curve in figure 2.7 is much steeper.

Laser light is strongly collimated as a result of the method of generation in a long narrow cavity. The mirror like end faces of the laser device causes light reflection many times between them making it a narrower beam. Any photon which is not closely parallel to the axis of the cavity is soon absorbed leaving only those with low divergence. In comparison with an LED emitting spontaneous radiation which is broad in its nature and incoherent, a laser emits stimulated radiation which is a narrower beam and coherent. However LEDs can give an output power as same as a semiconductor laser up to the threshold current, but an individual laser gives more output in stimulated mode.

2.5 Solar cells

At present solar cells are the most important long duration energy supply for satellites and space vehicles and in addition solar cells are also being used in terrestrial applications. The first ever solar cell was a Si p-n junction developed by Chapin et al (1954). Raynolds et al in the same year developed the first CdS based solar cell, Sze (1981). Since then, many other semiconductor systems have been tested but only the Si solar cell has shown a considerable marketable efficiency. Recently isotype heterojunctions or graded junctions have been used instead of p-n junctions for greater

efficiencies. The action of a solar cell, the conversion efficiency and other essential parameters are explained in this section.

2.5.1 Theory of solar cells

When a p-n junction solar cell, as shown in figure 2.8(a), is exposed to solar radiation, photons with energy greater than the band gap (E_g) are absorbed by the cell and electron-hole pairs are produced continuously. The photons with energy less than the band gap do not contribute to the cell output. Photogenerated charge carriers are separated to produce a current in the external circuit as shown in the band diagram (figure 2.8 (a)). The equivalent circuit for a solar cell is shown in figure 2.8 (b) and the current source I_L results from the excitation of excess carriers by solar radiation.

The I-V characteristics of such a device can be given by;

$$I = I_D - I_L$$

$$I = I_S(e^{qV/kT} - 1) - I_L \qquad [2.34]$$

where I_S is the diode saturation current and the characteristics are shown in figure 2.9.

This equation can be re-arranged to take the form;

$$\frac{kT}{q}\log_e\left(\frac{I+I_L}{I_S}+1\right) = V \qquad [2.35]$$

$V = V_{OC}$ (open-circuit voltage) when $I = 0$

$$V_{OC} = \frac{kT}{q} \ln\left(\frac{I_L}{I_S}\right) \qquad [2.36]$$

Also $I = I_{SC}$ (closed-circuit current) $= I_L$ when $V = 0$.

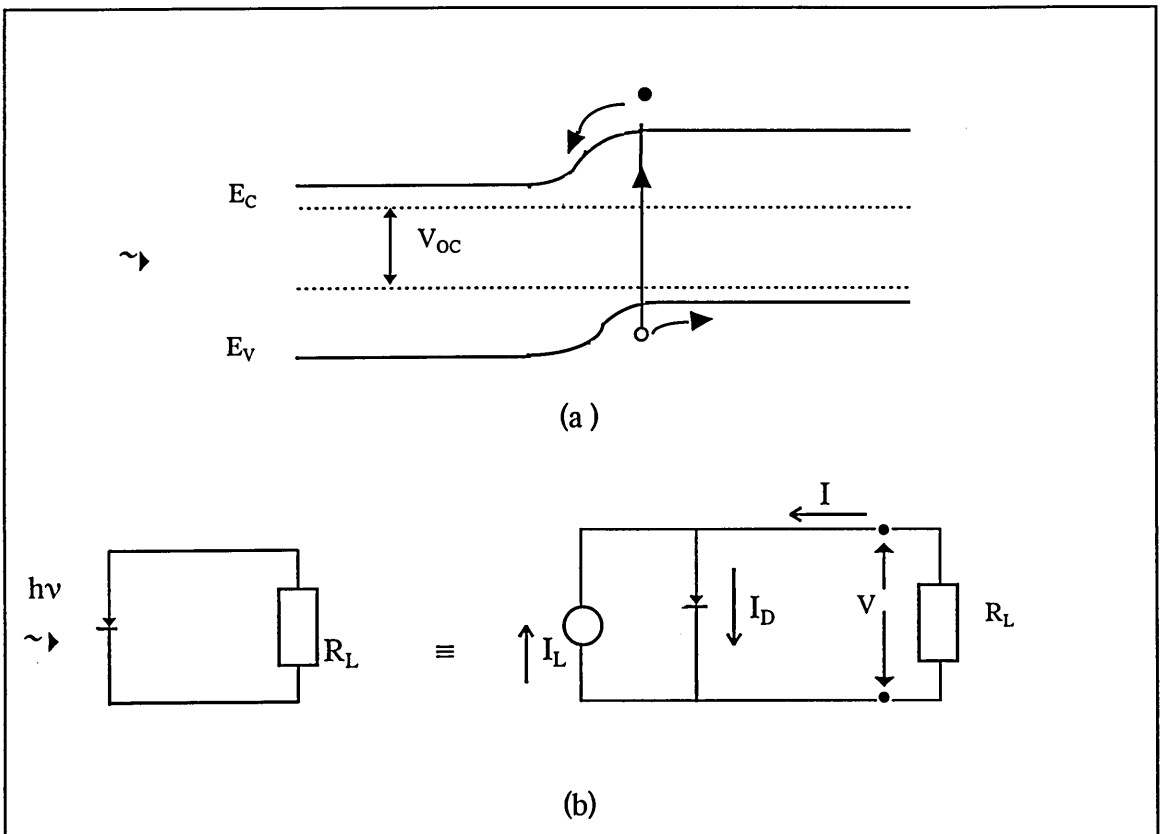

Figure 2.8 (a) Energy band diagram of a p-n junction solar cell under solar irradiation (b) Idealised equivalent circuit of a solar cell.

The shaded area in the curve is the maximum power rectangle and the maximum power is given by;

$$P_m = I_m V_m \qquad [2.37]$$

Power output is given by;

$$P = IV$$

$$= I_S V(e^{qV/kT} - 1) - I_L V \qquad [2.38]$$

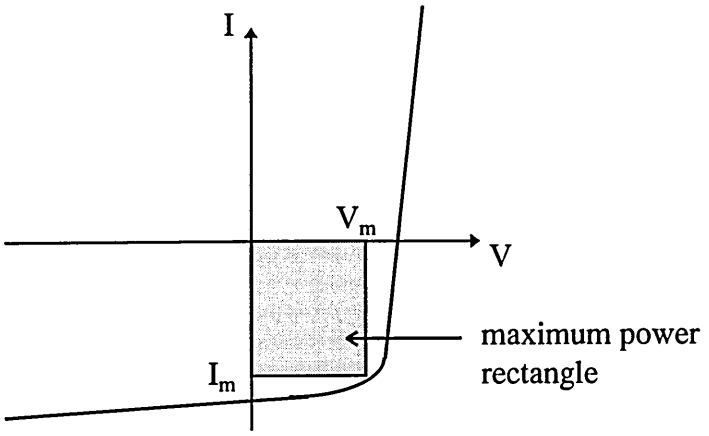

Figure 2.9 Current-voltage characteristics of a solar cell under illumination

Condition for maximum power can be obtained when $\frac{dP}{dV} = 0$

$$\therefore I_m = I_S \beta V_m e^{\beta V_m} \approx I_L \left(1 - \frac{1}{\beta V_m}\right) \qquad [2.39]$$

$$V_m = \frac{1}{\beta} \ln\left(\frac{I_L / I_S + 1}{1 + \beta V_m}\right) \approx Voc - \frac{1}{\beta} \ln(1 + \beta V_m) \qquad [2.39\ (a)]$$

where $\beta = \frac{q}{kT}$

Maximum power output $P_m = I_L \left(Voc - \frac{1}{\beta} \ln(1 + \beta V_m) - \frac{1}{\beta} \right)$

$$= I_L (E_m / q) \qquad [2.40]$$

$$E_m = q\left(Voc - \frac{1}{\beta}\ln(1+\beta V_m) - \frac{1}{\beta} \right) \qquad [2.41]$$

This energy E_m corresponds to the energy per photon delivered to the load at the maximum power point. E_m depends on material properties, such as, τ, D and doping levels. The ideal efficiency corresponds to an optimum choice of material property that minimise J_S.

$$\text{ideal conversion efficiency} = \frac{\text{maximum power output}}{\text{incident power}}$$

$$\eta = \frac{P_m}{P_{in}} = I_L\left(\frac{E_m / q}{P_{in}}\right)$$

$$\eta = \left(\frac{V_m^2 I_S (q/kT) e^{qV/kT}}{P_{in}}\right) \qquad [2.42]$$

Increase in η is caused by increase in V_{OC}, which in turn causes an increase in E_m.

$$\eta = \frac{V_m I_m}{P_{in}} = \frac{FFV_{OC}I_{SC}}{P_{in}} \qquad [2.43]$$

$$FF = \frac{V_m I_m}{I_{SC}V_{OC}} = \frac{P_m}{I_{SC}V_{OC}} \qquad [2.44]$$

FF is a measure of the squareness of the I-V characteristics. To maximise efficiency (η), all three parameters V_{OC}, I_{SC} and FF must be increased.

CHAPTER THREE:

EXPERIMENTAL TECHNIQUES

3.1 Introduction to electrochemical deposition of semiconductors

The successful preparation of semiconductors by electrochemical means would mainly depend on controllable electrical parameters, such as current density and deposition voltage and also kinetics and thermodynamics. Engelken (1985) described the major problems associated with compound semiconductor electrodeposition as producing stoichiometric non-degenerate material and achieving large grained non-amorphous deposits. Depending on the purity of the precursors, the change in kinetics of the electrolyte causes changes in stoichiometry and the rate of electron transfer reaction, which means redox kinetics influences the nature and morphology of the deposits.

The relationship between the deposition potential (E) and the temperature is given by the Nernst equation, section 1.7.2. That is the potential required for the deposition of the II-VI semiconducting thin film, as represented by;

$$M + X \rightarrow MX, \qquad [3.1]$$

where M is either Zn or Cd and X is either Se or Te.

This is however not a straight forward reaction, and is in fact the final step of the series of three reactions as suggested for CdTe by Panicker et al (1978).

In the first step, X^{4+}(Se^{4+} or Te^{4+} ions) reduce to elemental form X(Se or Te):

$$HXO^{2+} + 3H^{+} + 4e^{-} \rightarrow X + 2H_2O \qquad [3.1\ (a)]$$

$$M^{2+} + 2e^{-} \rightarrow M \qquad [3.1\ (b)]$$

These M and X then react as given in the equation 3.1 to form the semiconducting compound MX.

The compound formation and their crystallinity is highly dependent on the pH (<3.0) of the electrolyte. The production of H_2X has been observed to be inevitable in an acidic medium at more negative potentials. This H_2X may then react with the acidic medium giving excess elemental X species in the compound. These X can then react with M species forming a less crystalline compound and this indirect process of formation of semiconducting compound would also be expected in acidic baths. Fulop and Taylor (1985) observed the rate of electron transfer reaction, that is the redox kinetics, influences the nature and morphology of the deposit. This rate is usually higher for X species and considerably lower for M species. The bath should essentially contain a higher M concentration and a lower X concentration.

The primary difficulty for decades in fabricating devices based on ZnSe has been the p-doping. Since the first report (1990), only nitrogen is used for p-doping in the device industry utilising MBE and MOVPE technology. II-VI compounds can be expected to have p-type conductivity when doped with group I or V elements and n-type when doped with elements from group III or VII. Some strange but successful p-doping of

ZnSe using Li, In and As and n-doping with Cd were reported by Berezovskii et al (1997).

3.1.1 Electrochemical deposition of ZnSe

A few attempts have been made in the literature to describe electrosynthesis of ZnSe in an aqueous medium, Natarajan et al (1994), Mishra et al (1989). The electrodeposited polycrystalline thin ZnSe films have not however been of high quality, also as described above, the reduction of Zn^{2+} well above the standard potential is made possible due to the gain in free energy upon compound formation. Although ZnSe is reported to appear frequently as n-type, some research groups have been able to electrodeposit p-type thin films, Natarajan et al (1994), Singh et al (1987 and 1989). In ZnSe electrodeposition, it has been suggested the three steps of the reaction mechanism are:

$$H_2SeO_3 + 4H^+ + 4e^- \rightarrow Se^0 + 3H_2O. \quad \text{at } 0.54\ V \qquad [3.2\ (a)]$$

$$Zn^{2+} + 2e^- \rightarrow Zn^0 \qquad \text{at } -0.96\ V \qquad [3.2\ (b)]$$

$$Zn^0 + Se^0 \rightarrow ZnSe \qquad [3.2]$$

The deposition potentials are with respect to Ag/AgCl reference electrode.

The ZnSe deposition potential or quasi rest potential as described by Kröger (1978), is -0.078 V against a Ag/AgCl reference electrode at room temperature, Krishnan et al

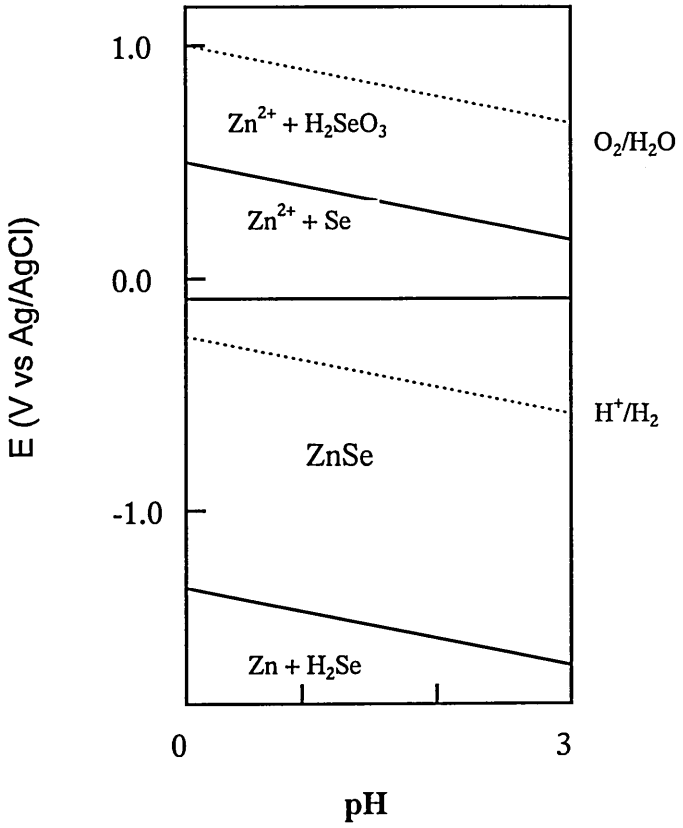

Figure 3.1 (a): Pourbaix diagram for ZnSe

(1992). Wei and Rajeshwar in the same year found it to be -0.76 V probably at an elevated temperature, which is not given. However, Natarajan et al (1994) deposited good quality thin ZnSe layers in a potential range from -0.07 V to -0.9 V with respect to SCE. The detailed publication by Natarajan et al (1994) found the optimum temperature for ZnSe deposition at -0.9 V was ~ 65°C. The films deposited at lower temperatures (25°C) and at more negative potentials (-1 V) were amorphous and around 85°C, even though the films were well crystallined, they were non stoichiometric. The crystal structure of electrodeposited ZnSe layers has often been reported as polycrystalline zinc blende cubic.

ZnSe is normally known to be an n-type semiconductor but electrodeposited ZnSe was found to have p-type conductivity, Singh et al (1987), Mishra et al (1989) and Krishanan et al (1992). Interestingly, doping was done using an impurity source by Singh et al (1989) and Rai (1993). A considerably large amount (0.001M $TlNO_3$ solution) of Tl was added to the bath containing 0.01M $ZnSO_4$ and SeO_2. However p-ZnSe layers were reasonably stable with an acceptor concentration of 4.22×10^{17} cm^{-3} and reproducible.

3.1.2 Electrochemical deposition of CdSe

CdSe exists in hexagonal wurtzite and cubic zinc blende structures and electrodeposited thin layers have been stable in either structure, Lade et al (in press), Islam et al (1997), Natarajan et al (1995). Mane and Lokhande (1997) found that electrochemically deposited thin films can be of either cubic, hexagonal or even of mixed crystal structure depending upon deposition conditions. The three steps for CdSe deposition against an Ag/AgCl reference electrode are:

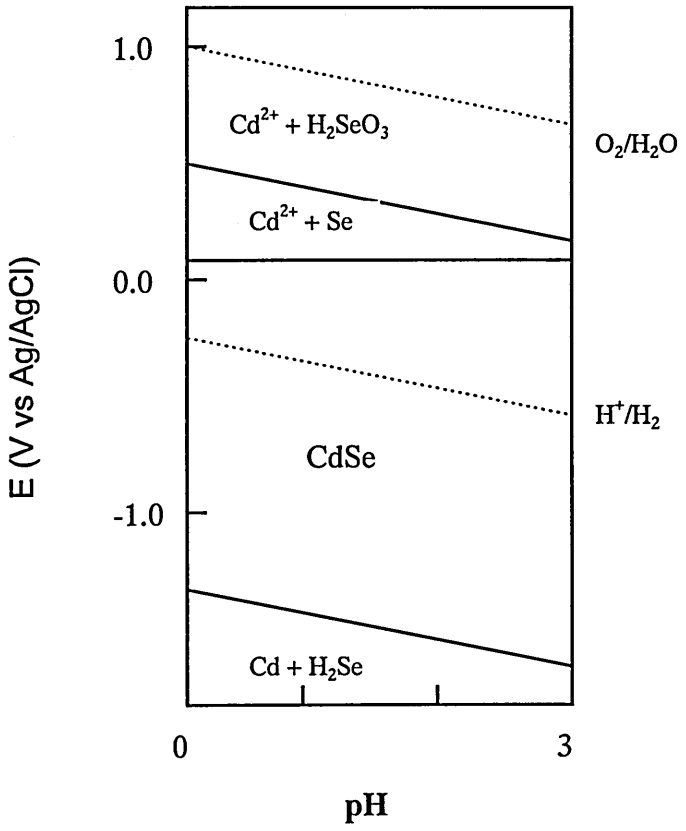

Figure 3.1 (b) Pourbaix diagram for CdSe

$$H_2SeO_3 + 4H^+ + 4e^- \rightarrow Se^0 + 3H_2O. \text{ at } 0.546 \text{ V} \quad [3.3\ (a)]$$

$$Cd^{2+} + 2e^- \rightarrow Cd^0 \quad \text{at } -0.602 \text{ V} \quad [3.3\ (b)]$$

$$Cd^0 + Se^0 \rightarrow CdSe \quad [3.3]$$

Natarajan et al (1995) electrodeposited CdSe in a (111) highly preferred orientation in a potential range from -0.5 V to -0.7 V against an SCE electrode. A wide deposition potential range from about -0.2 V to -1.2 V is given in the Pourbaix diagram against a Ag/AgCl reference electrode (Figure 3.1b) by Pourbaix (1966) and Krishnan et al (1992).

CdSe has been deposited in a wide temperature range from 30°C to 90°C with minimal potential variation being observed, Lade et al (1997). The pH value does not seem to affect the deposition conditions or the material characteristics.

3.1.3 Electrochemical deposition of CdTe

The usual method of electrodeposition of CdTe is deposition from aqueous solution. The basis of all research on cathodic electrodeposition of CdTe from aqueous solutions is the work done by Panicker et al (1978). Similar to the growth of ZnSe and CdSe, Cd^{2+} and Te^{4+} can be reduced simultaneously from an aqueous solution to grow CdTe. The three major steps for CdTe deposition against an Ag/AgCl reference electrode are:

$$H_2TeO_3 + 4H^+ + 4e^- \rightarrow Te^0 + 3H_2O \quad \text{at } 0.751 \text{ V} \quad [3.4\ (a)]$$

$$Cd^{2+} + 2e^- \rightarrow Cd^0 \qquad \text{at } -0.602 \text{ V} \quad [3.4\ (b)]$$

$$Cd^0 + Te^0 \rightarrow CdTe \qquad [3.4]$$

Lokhande et al (1989) deposited CdTe in a temperature range from 25°C to 100°C and in a potential range -0.2 V to -0.5 V against SCE. Sella et al (1986) found that the deposits formed in basic solutions were powdery and those formed in acidic media were adhesive. Their deposition potential range was 0 V to -0.5 V against a standard hydrogen electrode (SHE). Meulenkamp et al (1996) showed that unlike many other II-VI semiconductors, near stoichiometric growth of CdTe is possible by selecting appropriate choices for Te^{4+} and Cd^{2+} concentration and deposition potential. Many researchers claimed to have found that as deposited layers were n-type and that annealing at 400°C for 15 minutes made it p-type, Das et al (1993), Engelken et al (1985). However, Lockhande et al (1989) found the films deposited at potentials $\geq$ -0.3 V were n-type and p-type with potential $\leq$ -0.3 V. A few researchers have sought to overcome the problem of low rate of solubility of TeO_2 in H_2O. Panicker et al (1978) deposited CdTe with hexagonal single phase with (111) as preferred orientation.

Cowache et al (1989) reported that films with thickness $\leq$ 5000 Å were found to be adhesive and crystallined whereas those with thickness $\geq$ 5000 Å were powdery with excess Te on it. Contrary to this finding, highly crystalline thin layers of CdTe were grown by McGregor et al (1996) with 1-2 μm thickness. Annealing at a temperature above 400°C seem to improve the crystallinity as well as make it p-type.

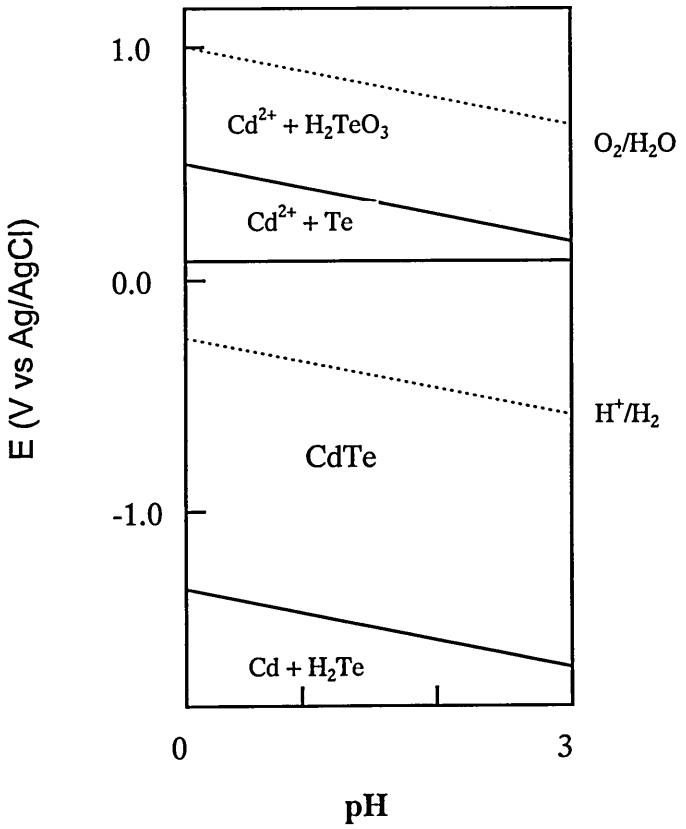

Figure 3.1 (c): Pourbaix diagram for CdTe

3.2 Material Characterisation

3.2.1 Introduction

Thin semiconducting layers were characterised to investigate their crystallinity, morphology, stoichiometry and optical properties. An X-ray diffraction (XRD) technique was employed to study both bulk structure and thin semiconducting layers. Scanning electron microscopy (SEM) with energy dispersive X-ray detectors (EDX) mounted within and X-ray photoelectron spectroscopy (XPS) techniques were used to characterise surface layers, their morphology, stoichiometry and cleanliness of the surfaces.

Optical absorption and photo-electrochemical (PEC) cells were used to determine band gap and conduction types of the materials. Elemental analysis and uniformity of films were observed using a glow discharge optical emission spectroscopy (GDOES) technique.

3.2.2 X-ray diffraction (XRD)

X-ray diffraction is a tool for the investigation of the structure and texture of matter and a reliable technique for the characterisation of thin semiconducting layers. The beginning of the technique dates back to the discovery of X-rays by Rontgen in 1895, Von Laue's discovery of X-ray diffraction from solid crystals and the further development of its physical equations by W.H. and W.L. Bragg. Von Laue realised that if crystals were composed of regularly spaced atoms which might act as scattering centres for X-rays, and if the X-ray wavelength was comparable to interatomic distance, then it is possible to diffract X-rays by means of the crystal. Bragg showed that if an X-

ray beam is incident on an atomic array of interplanar spacing *d* and is diffracted at an angle θ by two atomic planes as in figure 3.2, then the path difference between the diffracted rays may be given by:

$$AB + BC = 2d\sin\theta \qquad [3.5]$$

Hence the two rays will be completely in phase if the Bragg condition is satisfied. The Bragg condition is:

$$2d\sin\theta = n\lambda \qquad [3.5\ (a)]$$

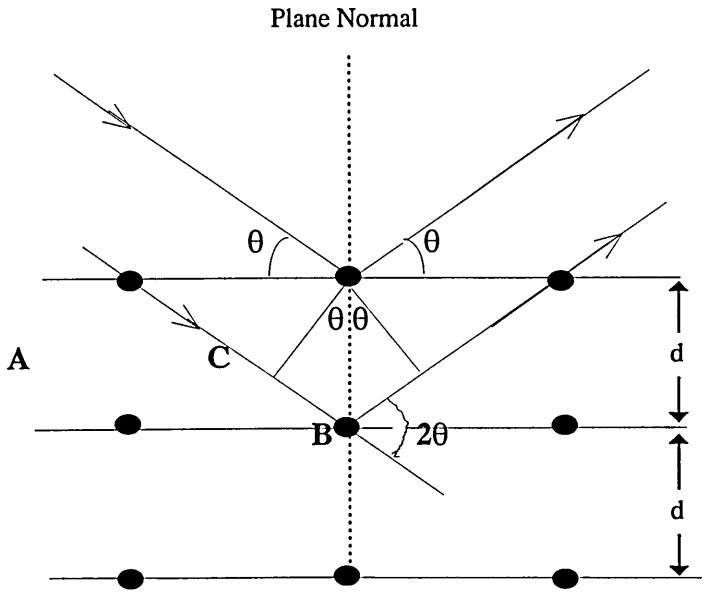

Figure 3.2 Schematic of the X-ray diffraction of by a crystal lattice

Therefore, the incident beam, the normal to the reflecting plane and the diffracted beam are always co-planar, and the angle between the diffracted beam and the transmitted beam is always 2θ.

X-ray diffractometer methods have been developed to take advantage of the above relationships for the examination of crystal structure and for studies of thin semiconductor films. Diffractometer techniques essentially measure the intensity of a diffracted beam directly by means of a movable electronic counter and its main features are shown in figure 3.3.

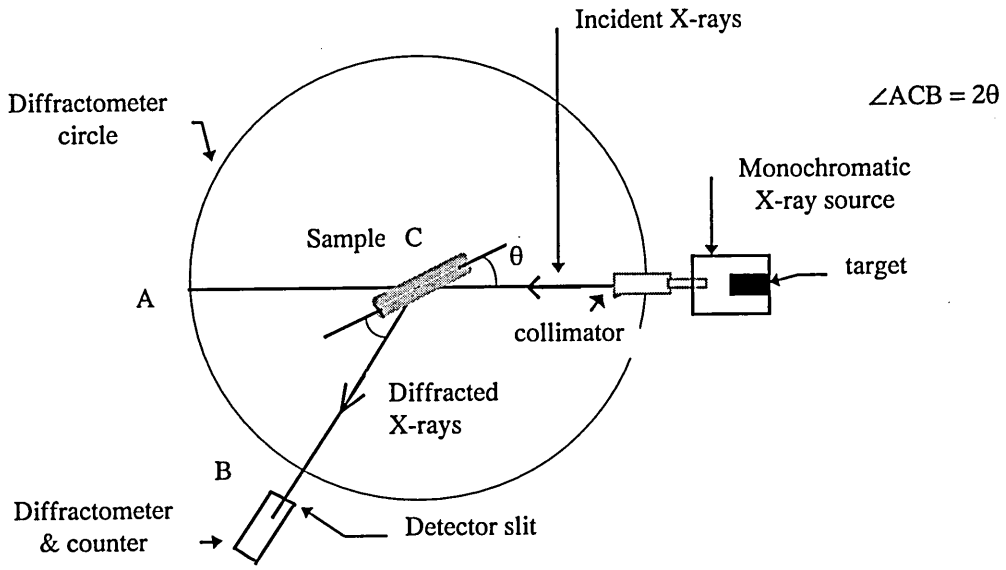

Figure 3.3 Schematic diagram of an X-ray diffractometer

Monochromatic X-rays of a known wavelength are generated and allowed to diverge from the source and irradiate a flat plate sample supported in the centre of a table. The table can rotate about its axis through an angle θ. The X-rays are diffracted by the

sample to form a convergent beam, which comes to a focus at a collimation slit at the front of the constant angular velocity counter. This is mechanically coupled to the specimen to cause rotation about the same axis through an angle 2θ to maintain the Bragg condition. The detector senses a succession of current pulses at a given angle of 2θ and gives an output of number of counts or X-ray intensity over a selected scan period. The output is a plot of a series of peaks of the number of X-ray counts as a function of diffraction angle 2θ. These peaks and their intensities are characteristics of the unit cells of each phase present in the crystalline solid. Analysis of full width at half maximum (FWHM) of the individual X-ray peaks can also yield information on the film grain size, lattice strain and the extent of peak shift, Dawar et al (1989). Examination of the peak position and intensity provides data on the film preferred orientation, unit cell dimensions and the atomic arrangement within the crystalline lattice.

All X-ray diffraction analysis performed during this project was carried out on a PW 1710 Phillips horizontal axis powder diffractometer. The counter movements are set in the vertical plane. The instrument is fully computer controlled via automated powder diffraction software, utilising monochromatic Cu $K\alpha$ radiation whose wavelength is 1.5406 Å.

3.2.3 X-ray photoelectron spectroscopy (XPS)

X-ray photoelectron spectroscopy (XPS) has been used extensively in the recent past in many areas of surface and materials analysis. The origins of the technique goes back to the discovery of the photo-electric effect by Hertz in 1887, in which X-rays were used as the exciting photon source. XPS involves the removal of a core electron by an incident X-ray photon as shown in figure 3.4(a). Auger electrons are produced in XPS

along with photoelectrons. Auger electrons are emitted following reorganisation of the atom after the ejection of the photo-electron.

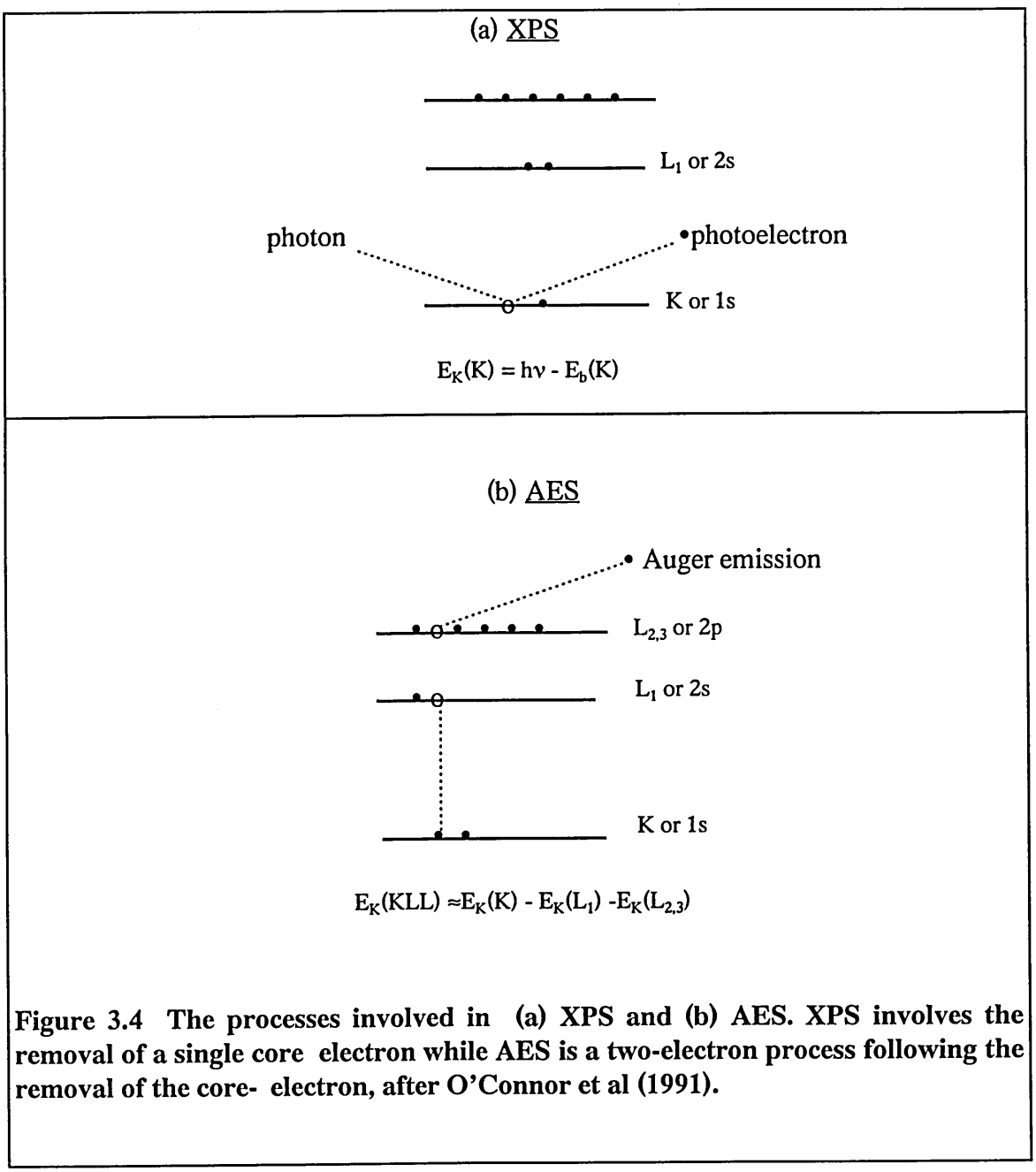

Figure 3.4 The processes involved in (a) XPS and (b) AES. XPS involves the removal of a single core electron while AES is a two-electron process following the removal of the core- electron, after O'Connor et al (1991).

In the photoemission process as shown in 3.4(a), when the sample is irradiated with X-rays of energy hν, electrons of binding energy (BE), $E_b < h\nu$, are emitted. The kinetic energy of the emitted electron E_k can be given by,

$$E_k = h\nu - E_b \qquad [3.6]$$

Thus by measuring the kinetic energy of the photoelectrons, equation 3.6 can be used to translate this energy into BE of the electrons.

(a) Typical X-ray photoelectron spectrum

The spectrum is generated by plotting the measured photo-electron intensity as a function of BE. Figure 3.5 is a typical Mg K_α spectrum of an MOCVD grown CdTe film. The binding energies of these intensity lines are characteristic for each element, and also they represent the atomic orbital energies. Reported values of photoelectron binding energies for different elements may be used to assist in elemental analysis. As shown in figure 3.5, various p, d and f orbitals produce two lines due to spin-orbit splitting and C 1s line appears always as a single one.

Apart from elemental identification, this technique is used to monitor surface cleanliness, stoichiometry and the chemical nature of elements as will be discussed in detail in the next chapters.

(b) Surface Sensitivity

The main region of interest for XPS is electron energies from 100 - 1200 eV, which corresponds to a mean free path (λ_m) of 0.5 to 2.0 nm. However, the actual escape depth, λ, of photoelectrons depends on their travel direction within the solid and is given by;

$$\lambda = \lambda_m \cos\theta \qquad [3.7]$$

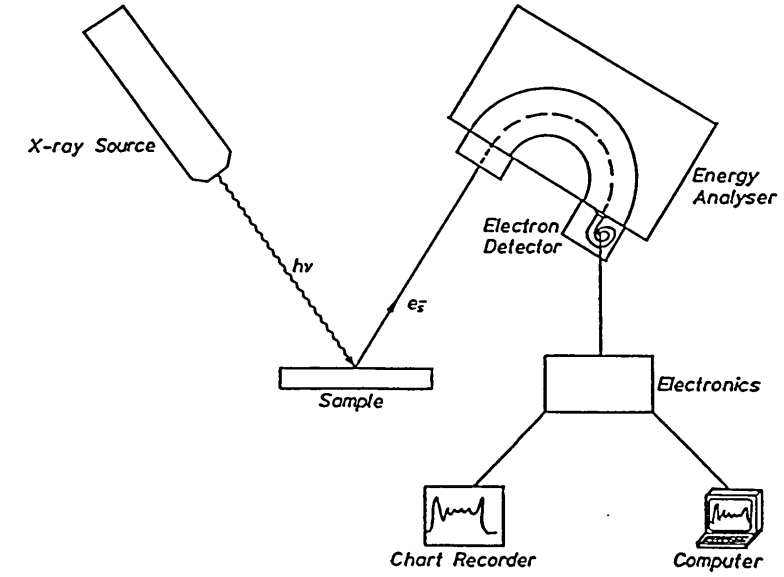

Figure 3.4 (c) Schematic representation of components for performing XPS.

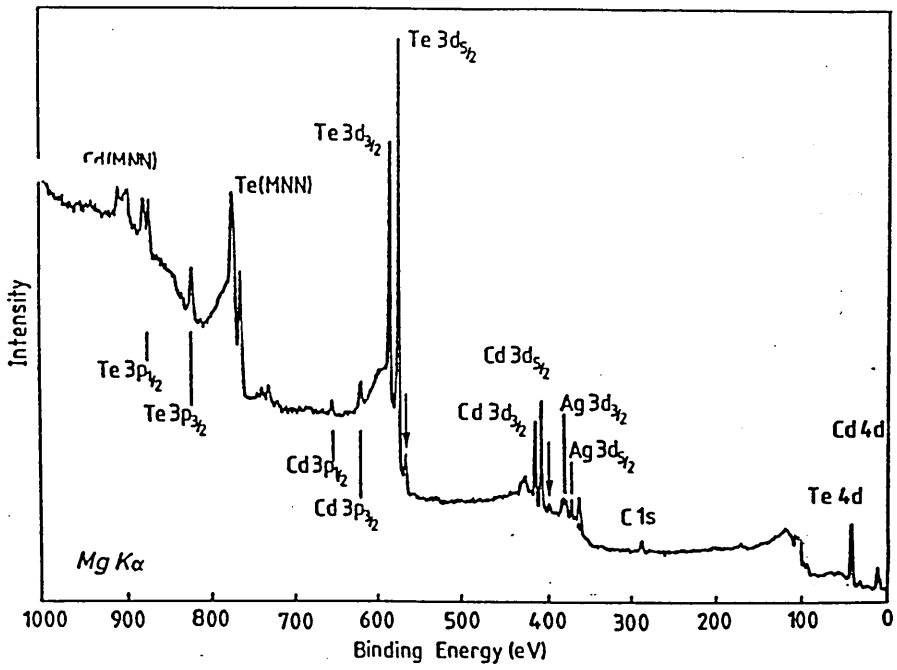

Figure 3.5 Mg K_α XPS spectrum of MOCVD grown CdTe, after O'Connor et al in 1991.

where θ is the angle of emission to the surface normal. Thus electrons from the maximum depth will be emitted perpendicular to the surface (θ = 0°) whereas electrons from the outermost layer of the material will be emitted nearly parallel to the surface (θ = 90°). XPS is therefore a surface sensitive technique and the sensitivity can be enhanced by varying the angle of detection during the experiment.

(c) Instrumentation

A VG microlab instrument was used in XPS studies in this project. Figure 3.4(c) is a schematic representation of the essential components necessary for XPS performance. This consists of an X-ray source, a sample mounting system, an electron energy analyser and an electron detector/multiplier, all of which are maintained under ultra high vacuum. The detector is connected to suitable electronics to convert the detected current into a suitable spectrum.

(i) X-ray source

An ideal photon source must be sufficiently energetic to access core electron states of the solid and intense enough to produce a detectable electron flux. It also has to have a narrow line width and be simple to use and maintain. Therefore sufficiently energetic Al K_α , Mg K_α or a combination of both is commonly used as the X-ray source (table 3.1).

In the VG microlab, the source consists of a thin film of either material on a Cu substrate. A high energy electron beam incident on the anode causes emission of core-level electrons. The photon energy distribution from an X-ray anode is dominated by characteristic X-rays resulting from core-level transition. However, in addition to

characteristic radiation, continuous radiation known as Bremsstrahlung radiation is also produced. Bremsstralung radiation is inherent in non-monochromatic X-ray sources.

Table 3.1: Common X-ray sources

X-ray line	Energy (eV)	Line width (eV)	Comments
Mg K_α	1253.6	0.70	narrow line; stable
Al K_α	1486.6	0.85	narrow line; stable
Cu K_α	8048.0	2.6	source; wide line

Removing unwanted components and eliminating continuum radiation is done by monochromatization by means of a diffraction grating. However, monochromatized radiation will be greatly reduced in intensity due to dispersion.

(ii) Electron energy analyser and detector

Once the photoelectrons are produced, they will be separated according to their energy and subsequently converted into a spectrum. The electron energy analyser is the critical component in determining sensitivity and resolution.

There are several types of analyser that have been used in XPS. The concentric hemispherical analyser (CHA) is commonly used. The resolution of the analyser can be defined in two ways. One is the absolute resolution, ΔE, measured at FWHM of a peak and the other is the relative resolution (ϱ) of the peak at $KE = E_o$

$$\varrho = \frac{E_o}{\Delta E} \qquad [3.8]$$

Absolute resolution is independent of the peak position but relative resolution is related to the kinetic energy of the peak.

An electron multiplier is used as the pulse counting detector, as the current reaching the analyser exit slit following photoionisation is about 10^{-16} - 10^{-14} A, which is well below any current measuring technique.

(d) Other advantages of X-ray photoelectron spectrum

(i) Spin orbit splitting

If an unpaired electron in a degenerate state with spin and orbital angular momenta being S and L respectively, combine they will to produce new states given by the total angular momentum;

$$J = |L \pm S| \qquad [3.9]$$

J can have values 1/2, 3/2, 5/2, ... and we can therefore investigate how identical different samples of the same material are. The degeneracies of the states is 2J+1. Relative intensities of the split peaks is given by the ratio of these degeneracies. For example the intensity ratio between Cd $3p_{1/2}$ and Cd $3p_{3/2}$ is: $2x\frac{1}{2}+1 : 2x\frac{3}{2}+1 = 2:3$.

(ii) Chemical shifts

As will be discussed in chapter 5, additional peaks for $3d_{1/2}$ and $3d_{3/2}$ peaks of Te can very often be observed in a shifted BE position of the spectrum, when TeO_2 is present in the material. It has been observed very often that by etching the semiconducting layer and thereby removing oxide in the material, these additional peaks can be removed, O'Connor et al (1991). The reason being, these peaks tend to move towards higher binding energies as the oxidation number of Te increases. This information can be of substantial aid in determining the chemical nature of an element from a given spectrum.

(iii) X-ray line satellites

As mentioned earlier, X-rays produce a series consisting of a main line with some minor components at higher photon energies. These minor lines can cause small satellite peaks to occur for each major photoelectric peak.

In addition, a few ghost lines may appear in the spectrum as a result of X-radiation from foreign material. For example, common ghost lines may arise from a Mg impurity in Al source or vice-versa in a dual anode source.

(iv) Quantitative analysis

Assuming constant photon flux and fixed geometry, the number of photoelectrons per second in a given peak is given by;

$$I = KN\lambda\sigma AT \qquad [3.10]$$

where K = constant, N = number of atoms of the element per cm^3, σ = photoionisation cross section for element, λ = intrinsic mean free path length for photoelectrons, A = area of the sample responsible for phototelectron emission, T = analyser transmission function.

The relative amounts of elements (N) in the sample can be determined using the intensities (peak areas) of the elements and the sensitivity factors (S), which are given by the relationship;

$$S = K\lambda\sigma AT \qquad [3.11]$$

Therefore :

$$N = I/S \qquad [3.12]$$

S values determined for several instruments are tabled in Briggs and Seah (1990).

(e) Samples

All materials were etched and washed using acetone and distilled water before loading them into the chamber in order to minimise contamination and preserve the vacuum. Samples were mounted on metal studs using conducting Ag dag and the semiconducting surfaces were connected to the metal stud to avoid any charging effect during the experiments, as all the samples studied in the project were semiconductors and had no conducting path to the stud.

3.2.4 Scanning electron microscopy (SEM)

The microscope consists of a gun with a filament (usually W) heated to incandescence at around 2850 K to become a thermionic electron emitter which operates most efficiently when it is saturated. Electrons are emitted by the gun and are affected by an electrostatic field provided by a Wehnelt grid which has a small negative bias applied to it as shown in figure 3.6. This causes the electron beam to be deflected in such a way that they are focused at a point just before an anode with a cross-over diameter of about 50 μm. The electron beam is then passed through the microscope column under a vacuum of pressure 10^{-9} bar. This should produce a beam of coherent electrons focused to a very fine probe at the specimen surface. There are several electromagnetic condenser lenses and scanning coils to cause collimation, deflection, de-magnification, focusing and synchronisation of the electron beam in two orthogonal directions.

A signal is generated at every point of the scanned sample. Contrast is developed as the surface will differ in its efficiency at producing the signal, hence an image will be

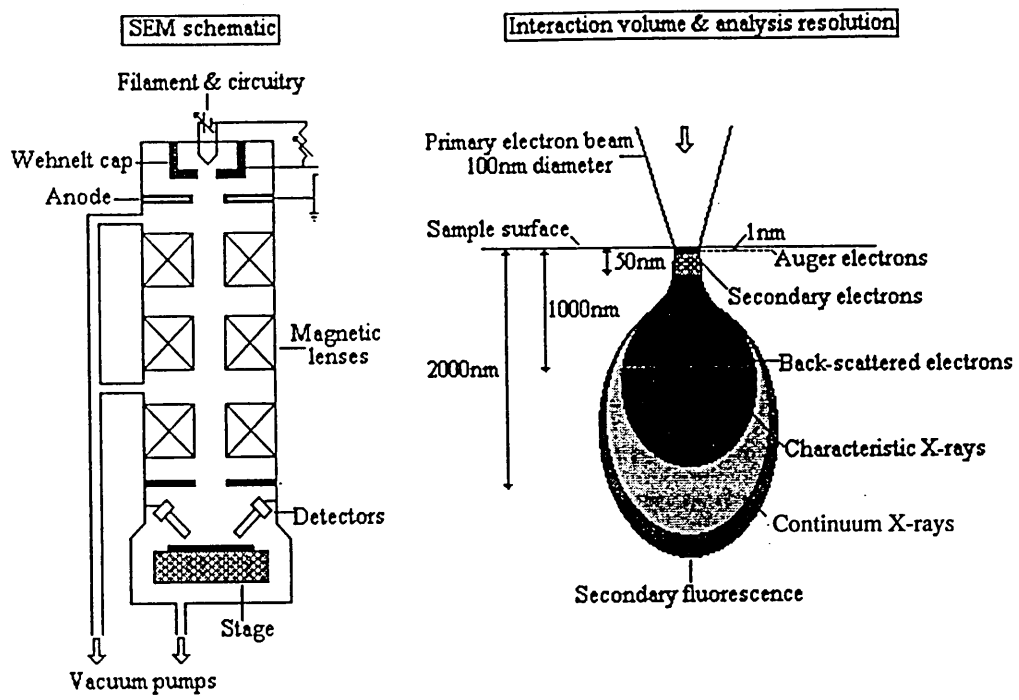

Figure 3.6 Schematic of the SEM and its typical interaction volume.

produced. The signals generated in scanning are detected and converted into electrical pulses, which can be used to control the intensity of output of the electron gun in a cathode ray tube.

The most common mode used for imaging utilises the secondary electron signal reflecting from the sample. The secondary electron detector consists of a positively biased grid connected to a photomultiplier and aimed at an acute angle to the specimen. The fact that secondary electrons are not energetic and they can be considered to drift from the specimen can be considered in explaining contrast in secondary electron images. They will only be accelerated towards the detector if they experience a field on the grid. This field will strongly be affected by topographical effects on the specimen surface. Therefore regions of the specimen which are in the shadow of the field are not attracted into the detector and signals from such areas are low and appear dark in the image. Thus a secondary electron image provides information relating to surface topography. There are other interaction events that may take place when an electron beam impinges on the surface of a sample. These include back-scattering of energetic primary electrons and the emission of characteristic X-rays. Back-scatter detectors are placed above the sample close to the final condenser lens. The contrast is developed from the fact that different elements have different back-scattering efficiencies. Therefore back-scattered images are sensitive to elemental composition variations and fine scale topographical details.

If a high energy primary electron from the incident beam collides with an atom in the sample, an electron from an inner shell may be removed causing excitation and a vacancy may be created. The atom can return to ground state by an electron transition

from a high energy shell to fill the vacancy generating X-rays. The X-ray energy is defined by the energy gap between the energy levels in the atom and is characteristic of the type of the atom. The energy of the X-ray photon is specific to the element and provides information about the elemental composition of the sample. Therefore energy dispersive X-ray detectors (EDX) are also mounted within the equipment enabling elemental analysis in parallel to imaging. The equipment used for analytical scanning electron microscopy was a Phillips XL40 series ASEM with a Link eXL EDX and back-scatter facility.

3.2.5 Optical absorption

Optical absorption technique have been widely used to determine band gap of semiconducting materials. As schematically shown in the figure 3.7(a) the lowest point of the conduction band occurs at the same momentum k_o as the highest point of the valence band for direct band gap photonic materials such as ZnSe. When the semiconductor is illuminated a direct optical transition can be observed from the valence band to the conduction band with no significant change in the momentum vector k_o. The threshold frequency ν_g for absorption by the direct transition determines the energy gap. If no impurity levels are present within the forbidden gap, as the frequency of the illuminated light is increased an abrupt change in the absorption can be observed due to the absorption of photons in the transition of electrons from the valence to the conduction band.

$$E_g = h\nu_g \qquad [3.6]$$

$$E_g = hc/\lambda_g \qquad [3.6\ (a)]$$

where λ_g is the associated wavelength of the transition. Substituting known values for h and c;

$$E_g = 1240/\lambda_g \text{ eV} \qquad [3.6 \text{ (b)}]$$

λ_g is in nm.

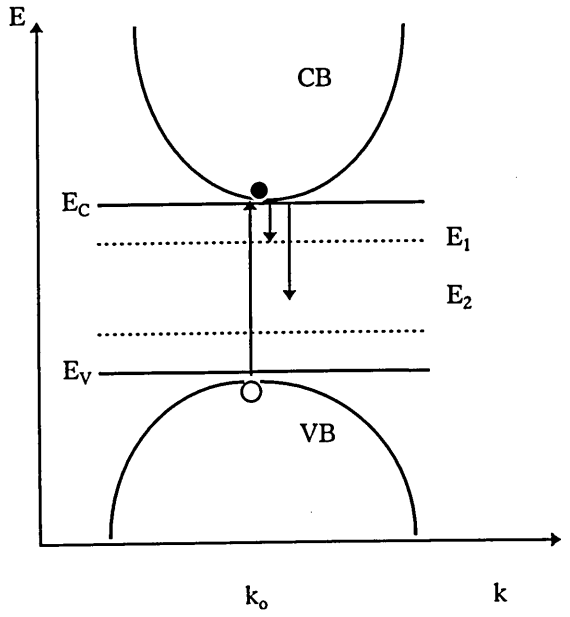

Figure 3.7 (a) E-k diagram of a direct band gap semiconducting material. The k (k_o) is the same at the bottom of the conduction band as at the top of the valence band. When illuminated, electrons jump to the conduction band from the valence band by absorbing photons. At the same time light emitting materials such as ZnSe emit light causing transitions of electrons from the conduction band to levels present within the band gap.

The absorption spectrum would be a curve similar to one shown in the figure 3.7(b). The corresponding wavelength, λ_g can be determined by means of the absorption curve as it is the value corresponding to the abrupt change in the curve. Absorbance (A) can be given in terms of the intensity of light incident (I_O) on the semiconductor and light transmitted (I) through the semiconductor by the relation,

$$A = \log_{10}(I_O/I) \qquad [3.7]$$

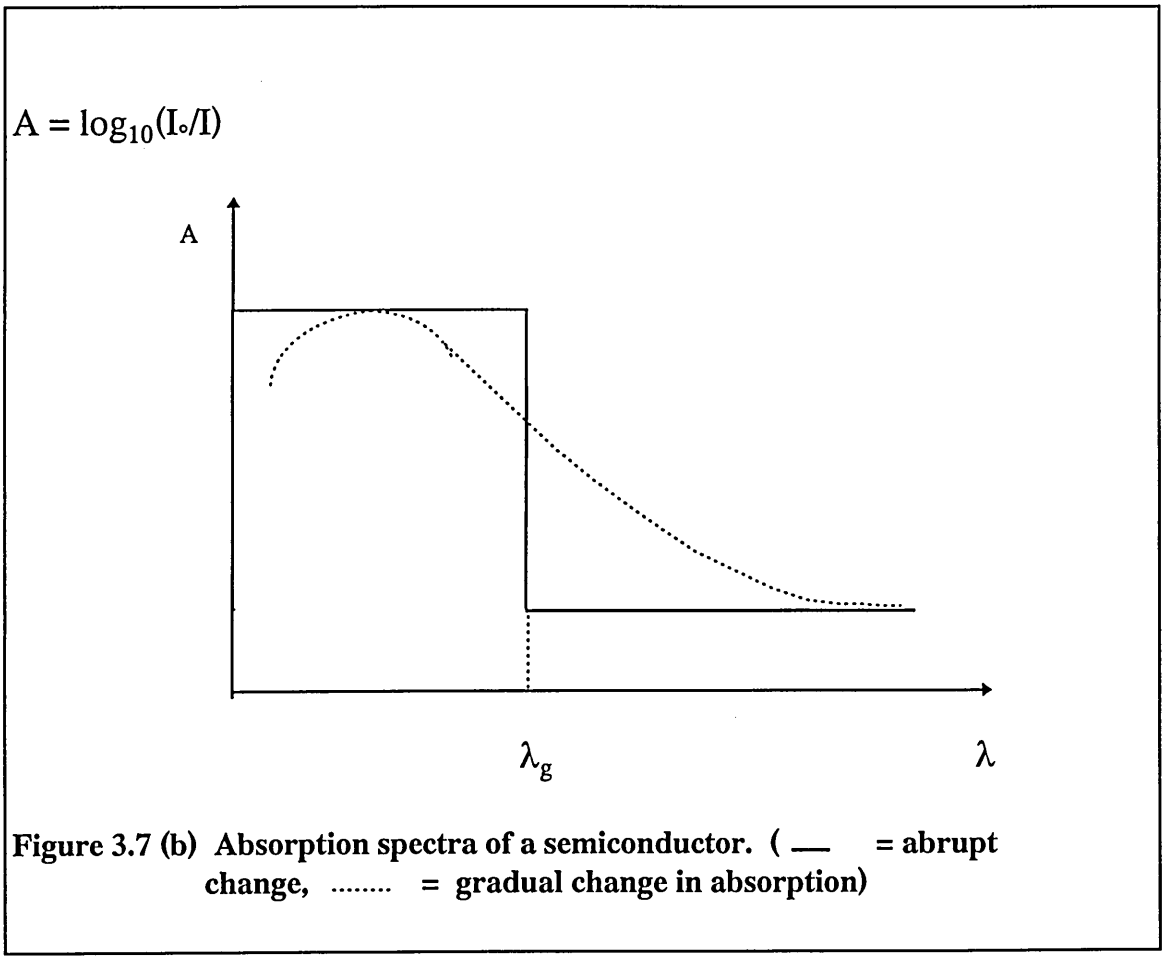

Figure 3.7 (b) Absorption spectra of a semiconductor. (___ = abrupt change, ... = gradual change in absorption)

The impurity levels present within the forbidden band gap (E_1 and E_2 as shown in the figure 3.7(a)) may absorb photons, therefore instead of the abrupt change in absorption, it will produce a gradual change in absorption. Since materials such as ZnSe are capable of emitting light by transfer of electrons from the conduction band to the valence band, the absorption would probably have a fall at short wavelengths as shown in figure 3.7 (b).The equipment used in these measurements was a UNICAM model UV2 uv-visible spectrophotometer.

3.2.6 Photo electrochemical cell (PEC) arrangement

The PEC cell arrangement is primarily a solar energy conversion device, which can also be used as a semiconductor characterisation technique. The cell arrangement used consisted of a 0.1M KI electrolyte, semiconducting sample and a Pt electrode (figure 3.8a). Electron-hole pairs are produced within the depletion region created at the liquid/solid junction upon irradiation (figure 3.8b). Holes will move towards the surface of the semiconductor and absorb an electron from the electrolyte if the semiconductor is n-type. The following reaction then takes place on the semiconductor surface:

$$I^{-1} \rightarrow I + e \qquad [3.8]$$

the photo-generated electrons will move towards the back contact of the semiconductor, generating a current in the external circuit. Eventually those electrons will reach the electrolyte causing reduction at the Pt electrode.

$$I + e \rightarrow I^{-1} \qquad [3.8\ (a)]$$

Thus the PEC cell acts as a solar energy converter, if the photon energy is greater than the band gap of the semiconducting material. The direction of the current or the polarity of the voltage measured in the external circuit gives the conductivity type of the semiconductor.

3.2.7 Glow discharge optical emission spectroscopy (GDOES)

The glow discharge optical emission spectroscopy (GDOES) technique has been designed to utilise an argon glow discharge to depth profile the sample and allow compositional analysis. Measurements include qualitative and quantitative

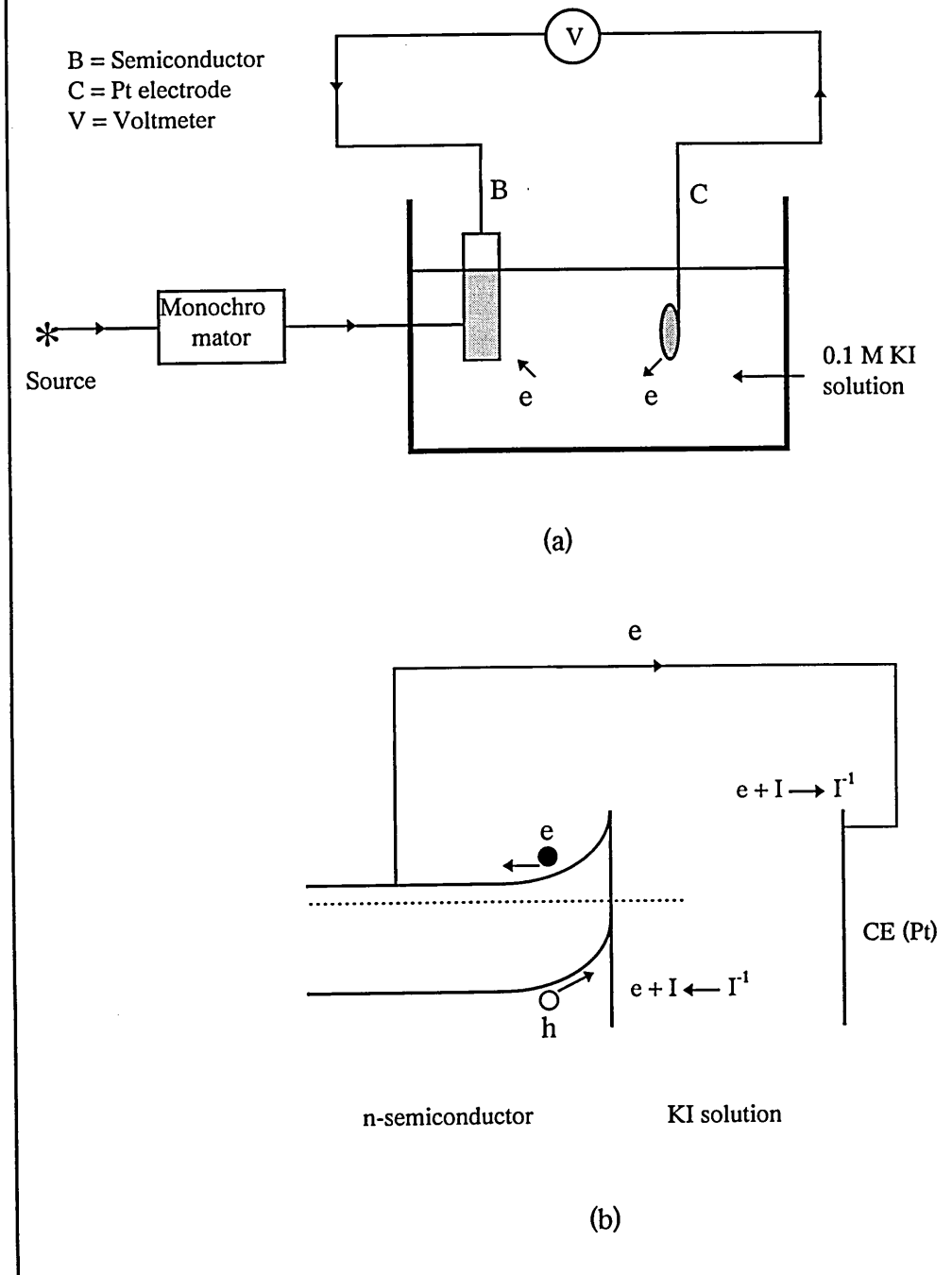

Figure 3.8: (a) PEC cell arrangement and (b) Energy band diagram of the liquid/semiconductor junction.

determination of the metal and non-metal elemental composition as a function of depth. The plasma created next to the sample surface will remove atoms from the surface and some will be excited into their higher atomic energy levels. The excited atom will then relax back to the ground state by the transition of an electron between relevant energy levels with emission of a photon of wavelength:

$$\lambda = \frac{hc}{E_1 - E_2} \qquad [3.9]$$

where E_1 & E_2 = energy states

h = Planck's constant

c = speed of light and λ = wavelength of the emitted photon.

Because each element has different electron orbital energy levels, the wavelength of the photon emissions will be characteristic of the elements present within the sample. Also the intensities of the emission lines will be proportional to the number of emission quanta and hence elemental concentration.

The atom must be in the form of a low pressure gas, volatilised from a solid within a vacuum chamber. Then it can produce a clean line spectra without contributions from continuum energy in the form of thermal radiation or lattice vibration. The glow discharge naturally separates atoms from the solid surface and we can expect no subsequent excitation and ionisations. Thus there is no sample to sample inconsistencies and it is ideally suited for this process.

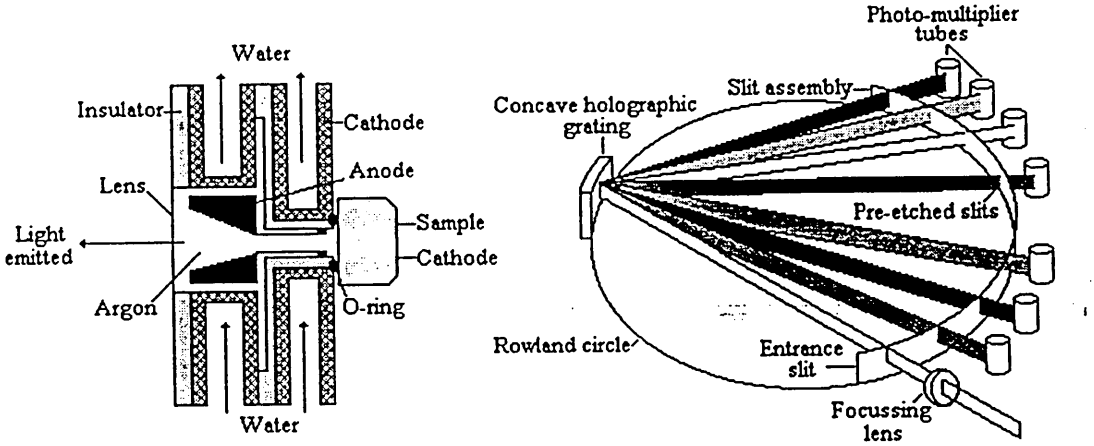

Figure 3.9 The glow discharge lamp and polychromator.

The GDOES equipment used was a Leco 750-GDS which consisted of a water cooled glow discharge source with a standard 4 mm diameter aperture and a hollow cylindrical anode under vacuum. The cathodic sputtering process is created by applying a voltage between the wall of the cylinder and the sample. Surface atoms are removed by the sputtering process and diffuse into the argon plasma where excitation and photon emission occurs (figure 3.9). Separation of the removed atom and excitation provides a spectrum with a linear relationship between element concentration and spectral intensity. A focusing lens is fixed at the end of the glow discharge lamp and entrance slit to the polychromator through which the emitted light passes. The polychromator of the spectrometer can detect up to 44 elements through a series of photo-multiplier tubes accurately fixed around the spectrometer perimeter.

3.3 Fabrication of devices

3.3.1 Introduction

The final step in the fabrication of devices is the formation of ohmic contacts to semiconducting surfaces and a rectifying contact to photovoltaic structures. Criteria for ohmic contact formation were established by Sze in the early 1970s, S.M.Sze (1981). In this project, MBE grown ZnSe epilayers, electrochemically deposited ZnSe p-n junctions and ZnSe/CdSe/CdTe multi layer structures were chemically etched using 0.1M NaOH/0.1M $Na_2S_2O_3$ etchant, as this etchant has been shown to produce stoichiometric surfaces in the literature, Dharmadasa et al (1994). Au, Ag, Al and Cu metal contacts were formed on etched surfaces for electrical characterisation.

3.3.2 Wet chemical etching and annealing

Often there exist surface oxide layers on semiconductors and surfaces of different compositions depending on the growth technique, the precursors used and the way the samples are stored. These insulating layers or surfaces of uneven stoichiometries would result in high contact resistances. Much work has been done on wet chemical etching of ZnSe and CdTe surfaces in the literature by Dharmadasa et al (1994) and some etchants have been found to produce stoichiometric surfaces. Both ZnSe and CdTe appear to display similar characteristics to the etchants used in their work (table 3.1).

Acidic etchants (etchant 1 and 2, table 3.2) would cause depletion of the semiconductor cation, M (Cd, Zn) species, leaving the surface rich of anion, the X (Se, Te) species. Strong acids would release Zn^{2+} from ZnSe and Cd^{2+} from CdSe and CdTe forming H_2Se (or H_2Te in CdTe case). This would lead to Se or Te rich surfaces. In an alkaline medium (etchant 7), high concentration of OH^- ions would cause anion to dissolve leaving a cation (M species) rich surface. Careful application of etchants 5 and 6, which are acidic etchants followed by alkaline etchants, would ideally produce stoichiometric surfaces. It has however been observed that oxide layers form or non-stoichiometric surfaces when etchants 5 or 6 were used. This was suggested as being due to the uneven etching durations in acidic and alkaline media. In this respect, etchant 5 has been observed in the literature as the most suitable and controllable etchant to be used to produce stoichiometric and oxide free surfaces, Dharmadasa (1994 and 1994). Thus only etchant 4 was used in this work for the preparation of stoichiometric semiconductor surfaces free of oxides to be able to make low resistance electrical contacts.

Table 3.2 Summary of chemical etchants used in the literature (Dharmadasa et al 1997)

Etchant	*Etchant composition*
1	1% Bromine in methanol
2	1 g of $K_2Cr_2O_7$ in 10 ml H_2SO_4 + 20 ml H_2O
3	Ar-ion sputtered cleaned ZnSe surface
4	0.5 g of NaOH, 0.5 g of $Na_2S_2O_3$ in 100 ml H_2O
5	Etchant 2 followed by etchant 4
6	Etchant 1 followed by a wash in hot NaOH (80-90°C)
7	1 g of NaOH in 20 ml H_2O + 1 ml H_2O_2

3.3.3 Metal contact formation

Several techniques have been described in the literature for metallizing compound semiconductors, Wood (1994), such as thermal evaporation, electron beam evaporation, sputtering, plasma enhanced chemical vapour deposition (PECVD) and laser enhanced deposition. Although the control of film stress and resistivity is limited, neither is usually a problem for devices. Also a tall vacuum chamber is needed in this technique, however, thermal evaporation also has advantages in metallization. It is a high purity technique and coating is directional which is ideal for a lift off process. The technique is applicable to all metals, but some with high melting points must be handled with care. The uniformity of the metal layer depends on the system design and the thickness can be measured in situ.

Thermal evaporation involves heating a small evaporation boat (usually made out of tungsten) containing the material to be evaporated. The equipment, an Edwards

metalizer, consisted of a rotary and diffusion pumps. Etched samples were washed thoroughly and masked with a mesh containing holes of diameter 0.5 mm,1.00 mm or 1.2 mm. The masked samples were transferred to the vacuum chamber and pure Au (99.999%), Ag, Al or Cu evaporated under a vacuum pressure of about 10^{-6} mbar. Ohmic contacts were formed on the back of each sample using In/Ga alloy and electrical contacts were made using conductive Ag paint.

3.4 Device Characterisation

3.4.1 Introduction

The completed diodes were then characterised in order to understand the electrical properties of the Schottky barrier or the heterostructure. The Schottky barrier heights were measured using current-voltage (I-V) and capacitance-voltage (C-V) techniques. Photoluminescense experiments were performed with the collaboration of the research group at Warsaw university in Poland. Ballistic electron emission microscopy (BEEM) using a scanning tunelling microscopy (STM) was carried out with the collaboration of Toulouse group in France.

3.4.2 Current - voltage (I-V) characteristics

The more general form of the current - voltage relationship for a Schottky diode provided by thermionic emission theory [chapter 2.3.1(a)] is;

$$J = J_o\left[\exp\left(\frac{qV}{nkT}\right) - 1\right] \qquad [2.14]$$

where J_o is known as the saturation current density and is given by

$$J_o = A^*T^2 \exp\left(\frac{-q\phi_b}{kT}\right)$$

Therefore the current through the junction will be

$$I = I_o\left[\exp\left(\frac{qV}{nkT}\right) - 1\right] \text{ in which } I_o = J_oS \qquad [3.10]$$

where S is the contact area and n is the diode quality factor, which has the value 1.00 for pure thermionic emission as described in chapter 2.3.1. A* is the effective Richardson constant which is about 1.2×10^4 AKm^{-2}.

For applied voltages, $V \geq 0.075$ V, the above equation reduces to

$$I = I_o . \text{Exp}\left(\frac{qV}{nkT}\right) \qquad [3.11]$$

which can be re arranged to

$$\log_{10} I = \left(\frac{q}{2.303nkT}\right) V + \log_{10} I_o \qquad [3.12]$$

The quality factor n can be evaluated from the gradient and the intercept provides a value for ϕ_b in a plot of $\log_{10} I$ versus V (Figure 3.10). Ohdomari (1979) showed the routines for the determination of correct n and ϕ_b values from forward I-V relationships extracting the effects of recombination and generation. In practical terms, a device is

considered to be ideal if n is less than 1.1, as for practical devices there are numerous deviations from ideal thermionic emission as described in chapter 2. In addition, the series resistance R_s, the shunt resistance R_{sh} can also be deduced using I-V relationships.

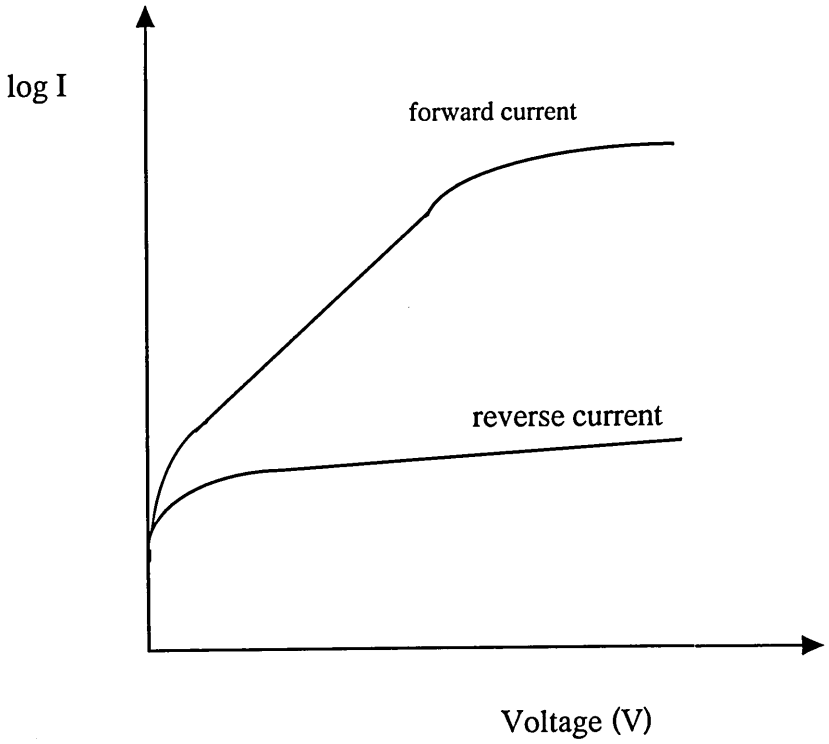

Figure 3.10 I-V characteristics of a Schottky diode.

The I-V measurements were made using a fully automated Keithley 619 system under PC control via GPIB interface. Dark I-V characteristics were monitored to minimise any photocurrents as II-VI compounds are relatively more sensitive to light. Metal contacts were normally of diameter 0.5 mm but those with a diameter of 1.0 mm and 1.2 mm were also characterised.

3.4.3 Capacitance - voltage (C -V) characteristics

When a small ac voltage is superimposed upon a dc bias, charges of one sign are induced on the metal surface and charges of the opposite sign in the semiconductor, this dipole then has the properties of a capacitor. The capacitance voltage relationship of a Schottky junction is given by equation 2.31 (chapter 2.3.3):

$$C = \left(\frac{q\varepsilon_S N_d}{2}\right)^{1/2}\left(\phi_b - \varsigma + V_r - \frac{kT}{q}\right)^{-1/2} \qquad [2.31]$$

This relationship can be rearranged to the form

$$\frac{1}{C^2} = \frac{2}{qN_d\varepsilon A^2}\left(V_b - V - \frac{kT}{q}\right) \qquad [3.13]$$

The plot of a graph of $1/C^2$ versus V is a straight line with the gradient providing a value for the doping concentration (N_d) and the intercept a value for V_b (diffusion voltage). The barrier height is then

$$\phi_b = V_b + \xi \qquad [3.14]$$

where ξ is the energy difference between the conduction band and the Fermi level of the semiconductor.

C-V measurements were performed using Wayne Kerr 6425 analyser, a four terminal bridge capacitance meter. Measurements were taken in the parallel resistor-capacitor configuration and a test signal of 30 mV was applied with a maximum frequency of 300

kHz. A dc bias voltage was applied externally. The accuracy of the results was a dependent on whether the leads were trimmed correctly both in open and short circuits.

There are however numerous other mechanisms which cause deviation from the ideal capacitance as described in chapter 2.3.3. High frequency can minimise the effect of traps on the capacitance characteristics. Cowley (1966) reported very reliable capacitance measurements but his operating frequency was in MHz range. The maximum available frequency in the experiments which is 300 kHz may not be sufficient for accurate results. Barrier heights determined using a C-V method by Tyagi and Arora (1975) with an operating frequency of 100 kHz, had considerable deviations from those measured using an I-V technique for a range of metal contacts on ZnSe.

3.4.4 Ballistic electron emission microscopy (BEEM)

The size of the metal contacts to measure conventional I-V characteristics is typically a diameter of over 0.5 mm, whereas the low-barrier patches may exist on a very much smaller scale. There has been a need, therefore, for methods which can probe the variation of electrical barriers of contacts on a much smaller scale. The BEEM technique, which relies upon scanning tunnelling microscopy (STM) can determine the Schottky barrier height at a very high spatial resolution, < 2nm.

The STM relies upon the tunnelling of an electron from the end of a point probe terminated by a single atom on to the sample surface. When the tip potential is at a specific value, a current exist between the tip and the sample, known as the 'tunnelling current' (I_T). This tunnelling current is dependent on the gap between the tip and the sample surface. The tip will follow a scan of the sample surface if the tunnelling

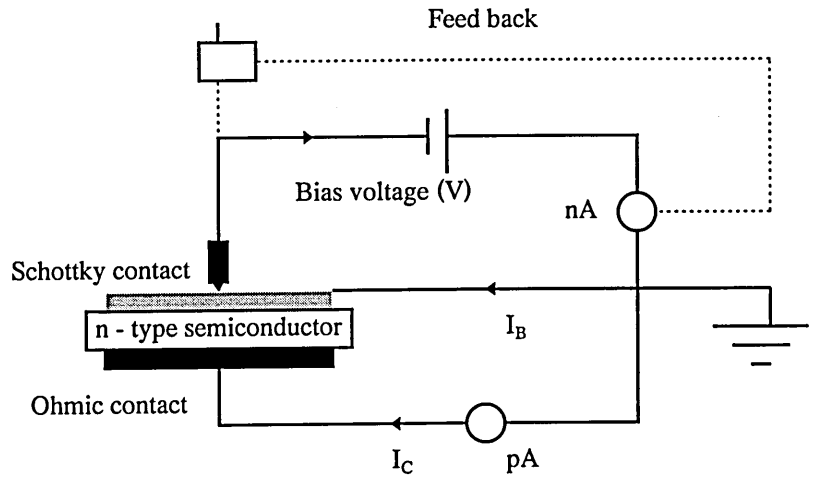

(a)

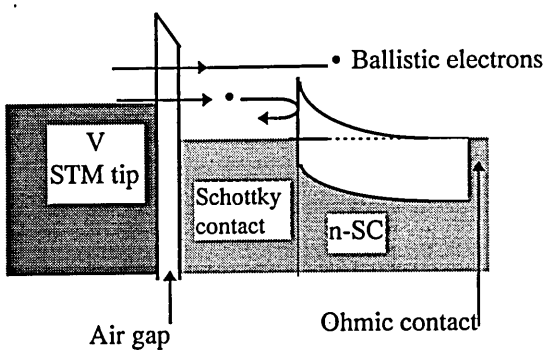

(b)

Figure 3.11: (a) Schematic diagram of the experimental set up used for determining the Schottky barrier height by BEEM using an STM (b) Energy band diagram showing the ballistic electron emission over the Schottky barrier, after Bell and Kaiser in 1978 and Dharmadasa et al in 1997.

current is maintained through a feed back system. As first introduced by Kaiser and Bell (1988), three terminal BEEM arrangement (figure 3.11) has an electron emitter injecting electrons into the metal overlayer, which acts as the base. When the tip bias voltage (V_T) exceeds the Schottky barrier height, electrons will enter the semiconductor surface and it acts as the collector. In order to maximise the BEEM current, I_B, the thickness of the metal layer has to be comparable with the mean free path of electrons in the metal. Crowell and Sze (1966) observed that this value is practically < 100 nm for most metals. Electrons with a momentum component parallel to the interface ($k_{//}$) will lead to a critical angle θ_c. Those incident on the semiconductor surface with a higher angle than θ_c will be reflected back into the metal layer and hence the resolution at the MS interface will be about 2 nm. BEEM spectra is usually obtained by sweeping the tip bias and by measuring I_C as a function of tip bias voltage. The threshold voltage of the I_C versus tip bias provide the local Schottky barrier height for the metal/semiconductor interface. I_B was given as a function of V_T by Kaiser and Bell (1988).

$$I_B(V) = RI_T \int dE[f(E) - f(E - eV)]x\vartheta[E - E_F - eV + eV_T] \quad [3.15]$$

Bias dependent R is a constant and measures the attenuation due to scattering in the metal layer. The Fermi function f(E) is given by:

$$f(E) = \left[1 + \exp\left(\frac{E - E_F}{kT}\right)\right]^{-1} \quad [3.16]$$

BEEM studies were performed by the Toulouse group in France using the equipment described by Coratger et al (1991).

CHAPTER FOUR:

MATERIALS CHARACTERISATION AND ELECTRICAL CONTACTS TO MBE GROWN ZnSe EPILAYERS.

4.1 Introduction

This chapter presents the results of various investigations on the characterisation of ZnSe thin films grown by the MBE technique at Heriot-Watt University and electrical contacts made on them. The intention of the study was to investigate the structure of the material and electrical properties of the metal/ZnSe interfaces. The section also presents issues related to the device manufacture such as low resistance ohmic contacts and ageing effects on the metal/ZnSe interfaces.

4.2 Material Characterisation

4.2.1 XRD results

X-ray diffraction traces developed using Cu K_α radiation in 2θ range 20° - 70°, showed that all the MBE grown ZnSe thin layers of thickness ~ 3 μm, were epitaxial and oriented in <100> direction (figure 4.1). XRD experiments which were carried out a few months after they were made, showed that the compound structure and epitaxial nature of the top layers had not been affected by the ageing of the whole sample. As marked in the figure, Ga_2Se_3 (111) and (222) peaks were also identified, which is in consistent with the observation of Ga_2Se_3 in Raman spectroscopy by Wolverson (1997). All layers were found to exhibit a single phase, cubic zinc-blende crystal structure. Full width at half maximum (400) reflections were always about 0.08°, which is far more higher than some values reported in the literature.

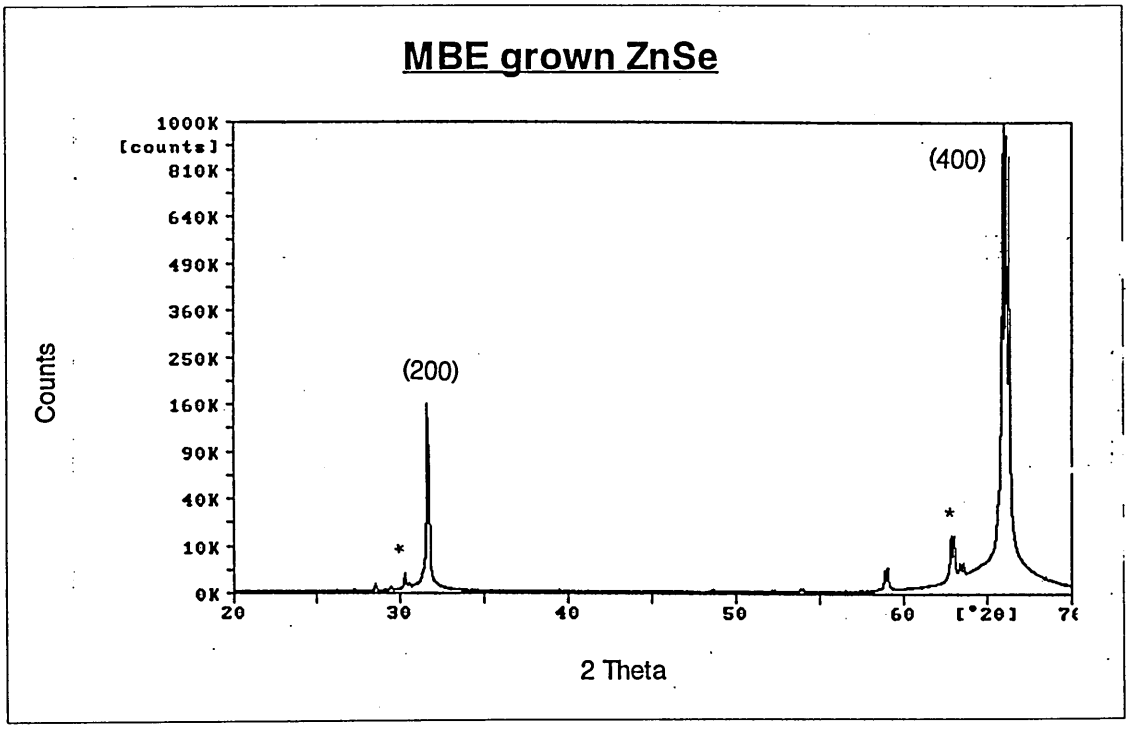

Figure 4.1 X-ray diffractogram of MBE grown ZnSe on GaAs (100) planes. ZnSe (200) and (400) peaks are shown. Peaks labelled with * are Ga_2Se_3 (111) at 30° and (222) at 64° indicating the existence of an intermediate insulating layer.

For an example, Dawar et al (1989), deposited ZnSe layers using a closed space vapour transport technique with the layers preferentially oriented in <111> direction and the FWHM was about 0.007°. These higher values of FWHM, meaning smaller grain sizes, may have been due to the strain resulting from the difference in lattice constants between ZnSe and GaAs. However, XRD data were in good agreement with the JCPDS unstressed powder standard data.

4.2.2 XPS results

Analysis was performed on air exposed chemically etched and Ar ion etched MBE grown ZnSe samples, all grown by the MBE method. Initially the chemically etched but air exposed materials were investigated after leaving them overnight under a high vacuum and a typical spectrum is given in figure 4.2 (a). The Ar ion etched samples were then studied in order to compare the above results with a contaminant free surface. Figure 4.2 (b) is a typical spectrum of an Ar ion etched surface. The obvious difference between the two spectra is that the chemically etched surface displays a C or an O peak whereas Ar ion etched surface shows only Zn and Se peaks. The oxide content is such that the 3d peak of Se did not show any SeO_2 peaks in any of the Ar etched surfaces, but on all chemically etched surfaces (figure 4.2 (c)).

The oxygen Auger peak KL1 as shown in figure 4.2 (a) is not seen in the spectrum of the Ar ion etched sample (figure 4.2 (b)). The oxygen content of the surface layer of the chemically etched surface is evidenced by the presence of an oxygen peak around 532 eV and SeO_2 3d peak at 60 eV. Even though ZnO peaks are not well resolved in the spectrum, figure 4.2 (e) shows the association of ZnO peaks within Zn peaks.

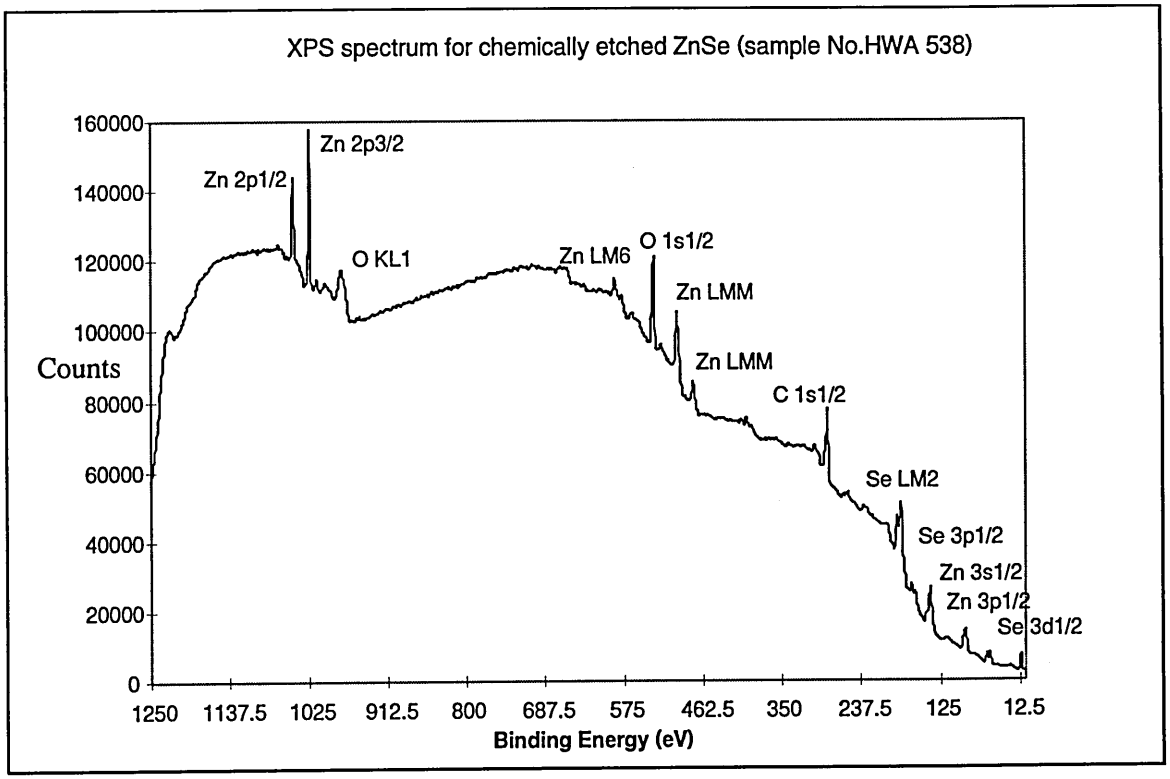

Figure 4.2 (a) XPS spectrum of chemically etched MBE grown ZnSe sample no. HWA 538. XPS peak O $1s_{1/2}$ and Auger peak O KL1 from oxygen and also XPS peak C $1s_{1/2}$ from carbon are always present in chemically etched surfaces.

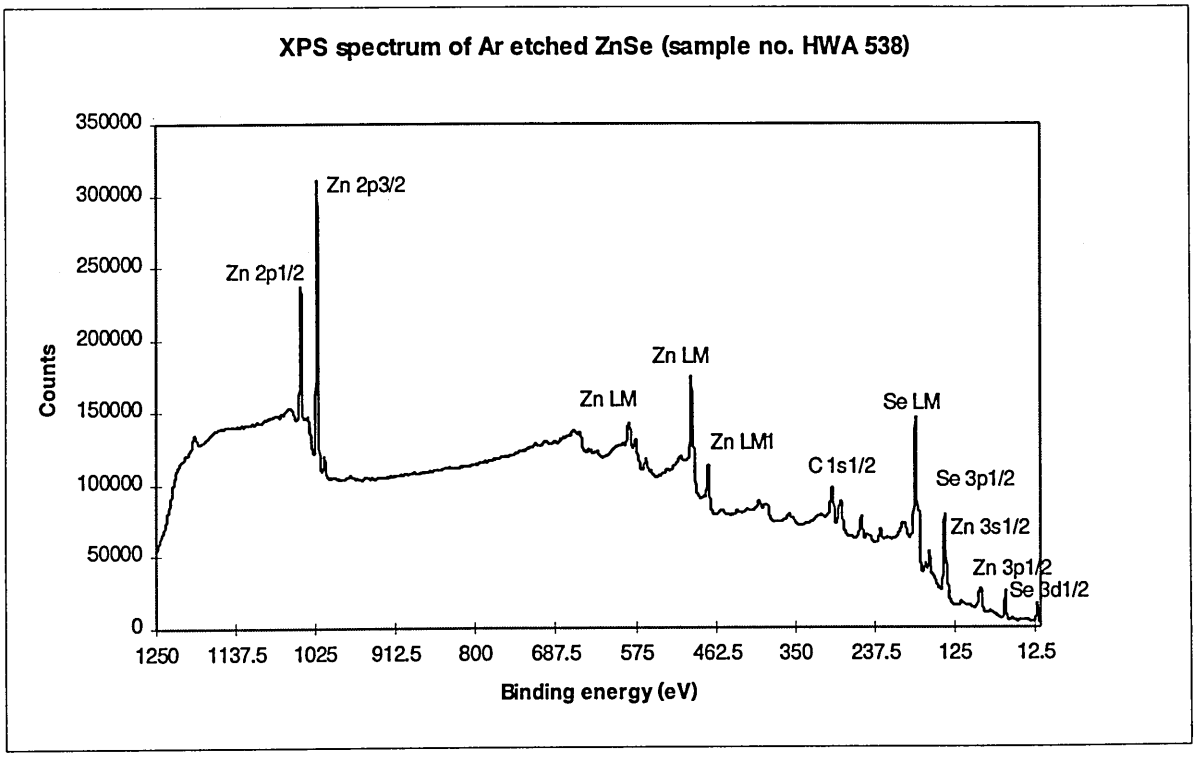

Figure 4.2 (b) Ar etched MBE grown ZnSe sample no. HWA 538. Note the complete disappearance of oxygen peaks and low intensity of carbon XPS peak.

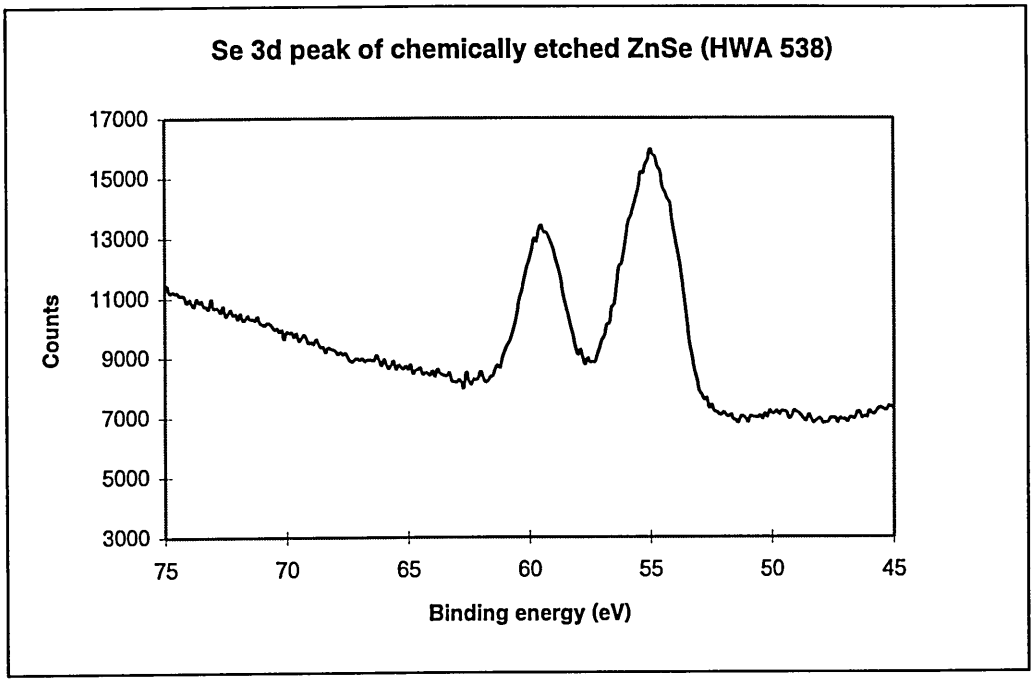

(i)

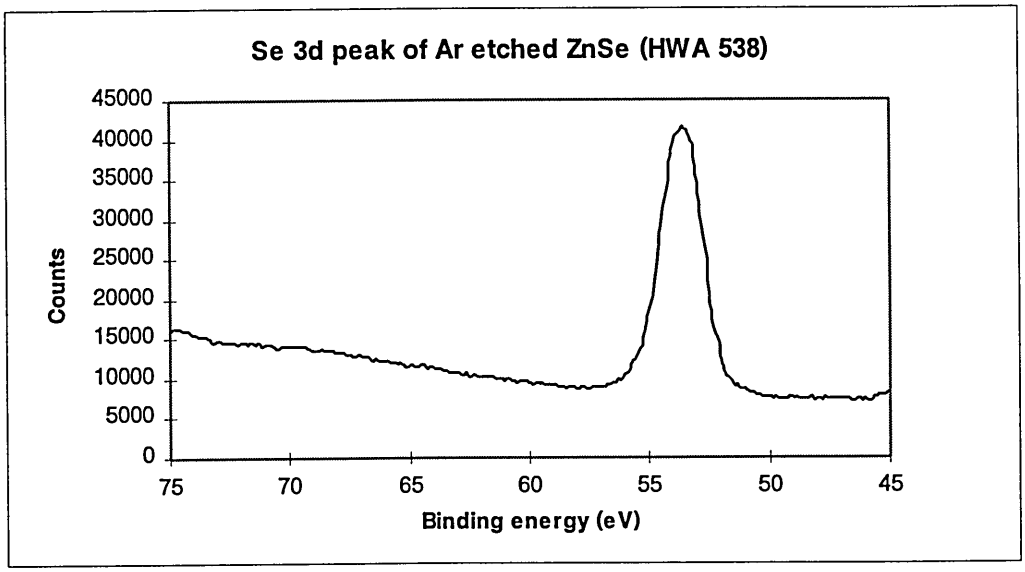

(ii)

Figure 4.2 (c) Expanded Se 3d peak of (i) chemically etched ZnSe sample indicating the presence of oxide species of selenium. The peak at BE = 54 eV and 59.0 eV are due to Se and SeO_2 respectively. (ii) After Ar etching, SeO_2 peak is no longer present and Se 3d peak is sharper. Ar etching is the way to get rid of oxides and some of the carbon on the surface.

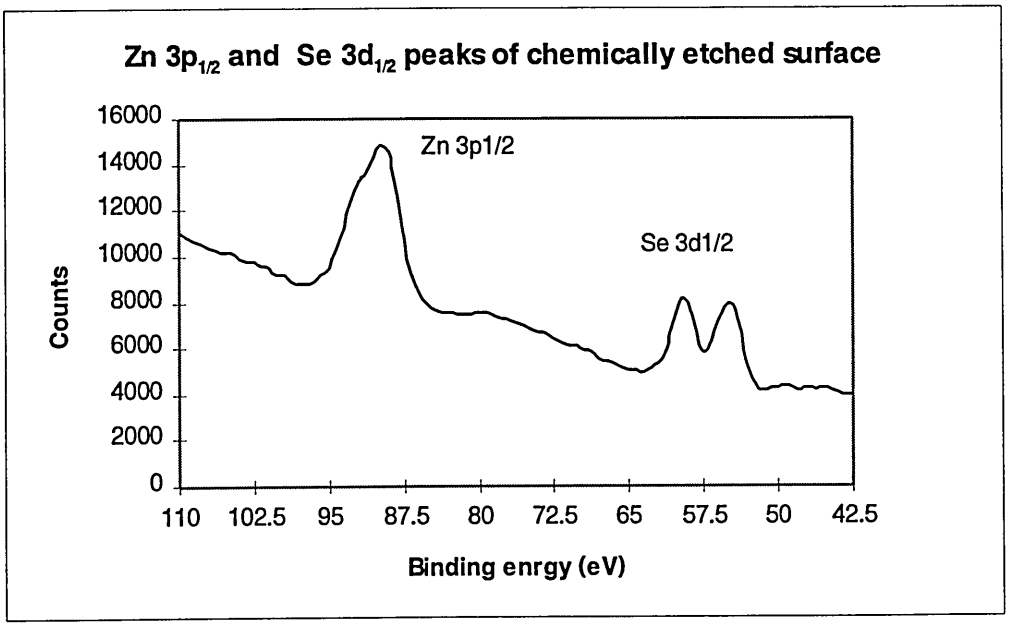

(i)

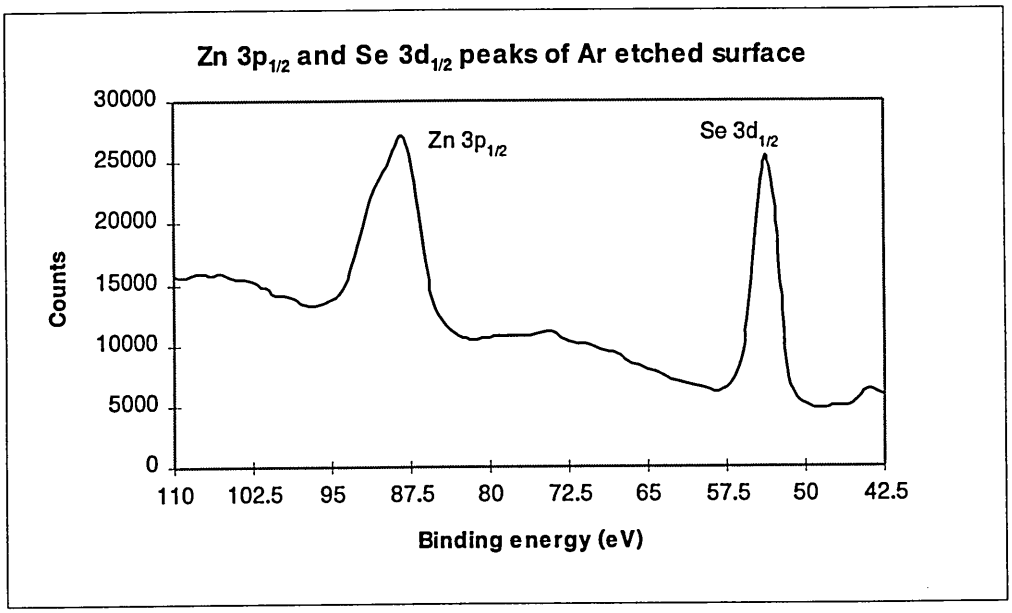

(ii)

Figure 4.2 (d) Qualitative comparison of chemical nature and stoichiometry of ZnSe. (i) Chemically etched surface showing the existence of SeO_2 and non-stoichiometric surface and (ii) Ar etched surface showing nearly stoichiometric surface.

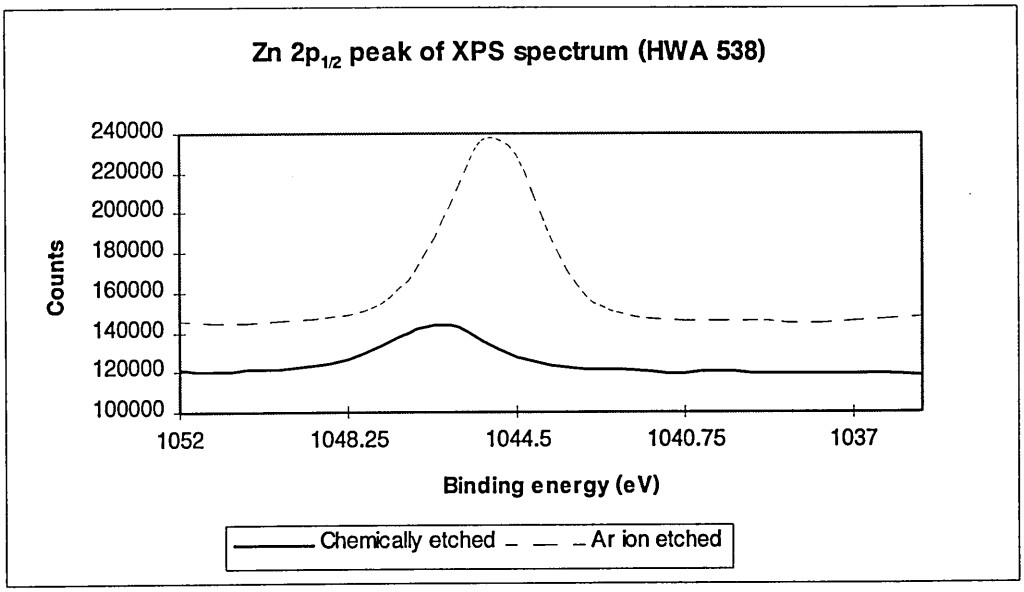

(i)

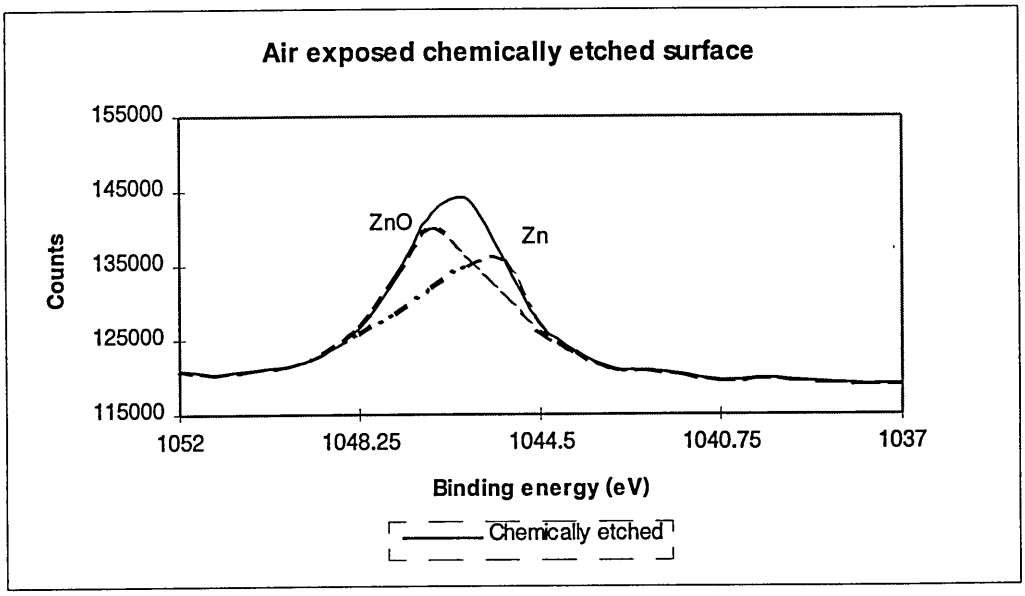

(ii)

Figure 4.2 (e) (i) Ar ion etched surface shows a peak at the binding energy of 1045.25 eV, which arises from Zn $2p_{1/2}$ whereas the corresponding peak in the spectrum of air exposed chemically etched surface is at the binding energy 1046.0 eV. In fact this peak is a resultant of both Zn and ZnO peaks as depicted in the figure (ii). The peak arising from Zn is at 1045.25 eV and the peak due to ZnO is shifted to 1046.75 eV.

4.2.3 SEM and EDAX results

The SEM and EDAX techniques were used to analyse the surface topography and the elemental composition of the thin films respectively. The samples were chemically etched and washed prior to the experiments. Figure 4.3 (a) shows a typical micrograph of a ZnSe sample and all the samples showed an identical nature. SEM micrographs show uniform background indicating epitaxial growth without any grain boundaries.

Back scattered electron images were focused and EDAX spectra were observed. The back scattered electrons are sensitive to elemental composition variations and fine scale topographical details. EDAX spectra showed slight variations at different focusing points of the back scattered spectra. However, they were very close in appearance to each other and a typical spectrum is shown in figure 4.3 (b). All the peaks in the EDAX spectrum were either Zn or Se and the spectra of different samples were identical to each other. The low sensitivity of EDAX in comparison with XPS is such that the peaks from C and O present on ZnSe surfaces, as observed in XPS, were not observed in EDAX.

4.2.4 GDOES results

GDOES technique was employed to study the elemental composition and the uniformity of elements distribution in qualitative terms. Figure 4.4 shows an unsmoothed GDOES profile through Au/n-ZnSe/n^+-GaAs structure. The plasma penetrated through both the Au layer and the ZnSe layer but switched off when it reached the ZnSe/GaAs interface. The insulation property at the interface is such that the same plasma source is capable of profiling through highly insulating layers such as SiO_2. This indicates the presence of a very high resistance at the interface and the resistance of this intermediate layer will

qualitatively be assessed using C-V profiling and I-V results.

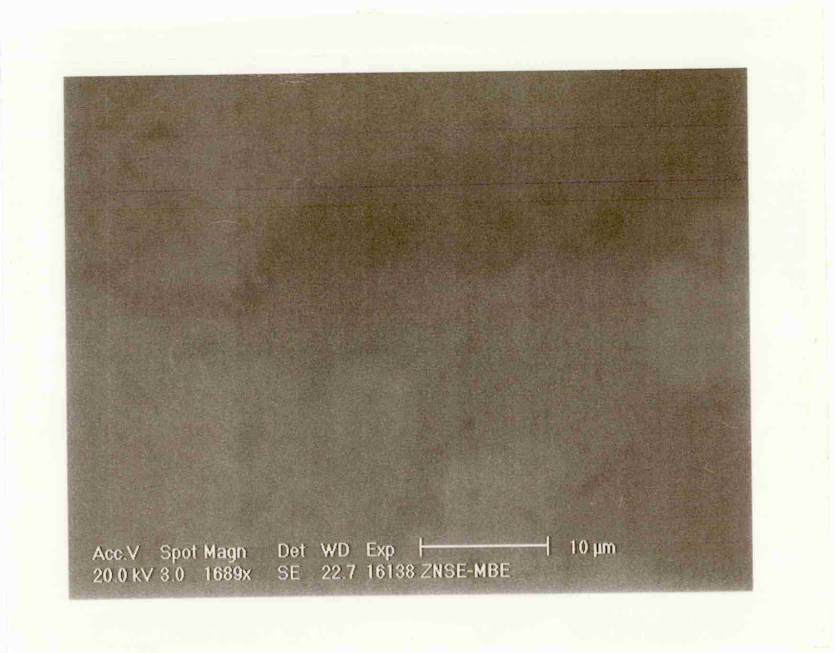

Figure 4.3 (a) A typical scanning electron micrograph of MBE grown ZnSe (100) layers. The layers are epitaxial and no grain boundaries can be observed.

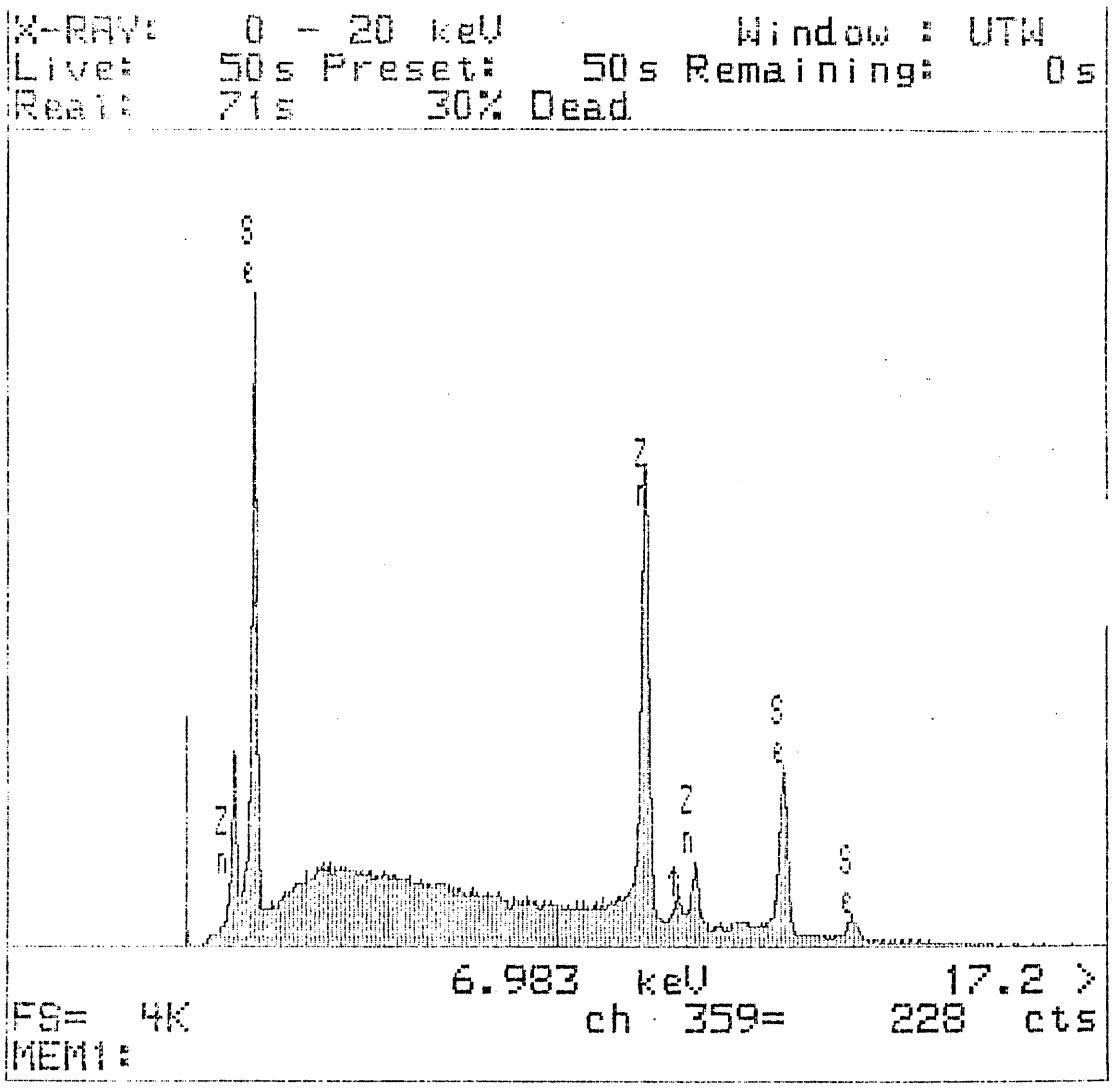

Figure 4.3 (b) EDAX spectrum of MBE grown ZnSe. All peaks are either Zn or Se.

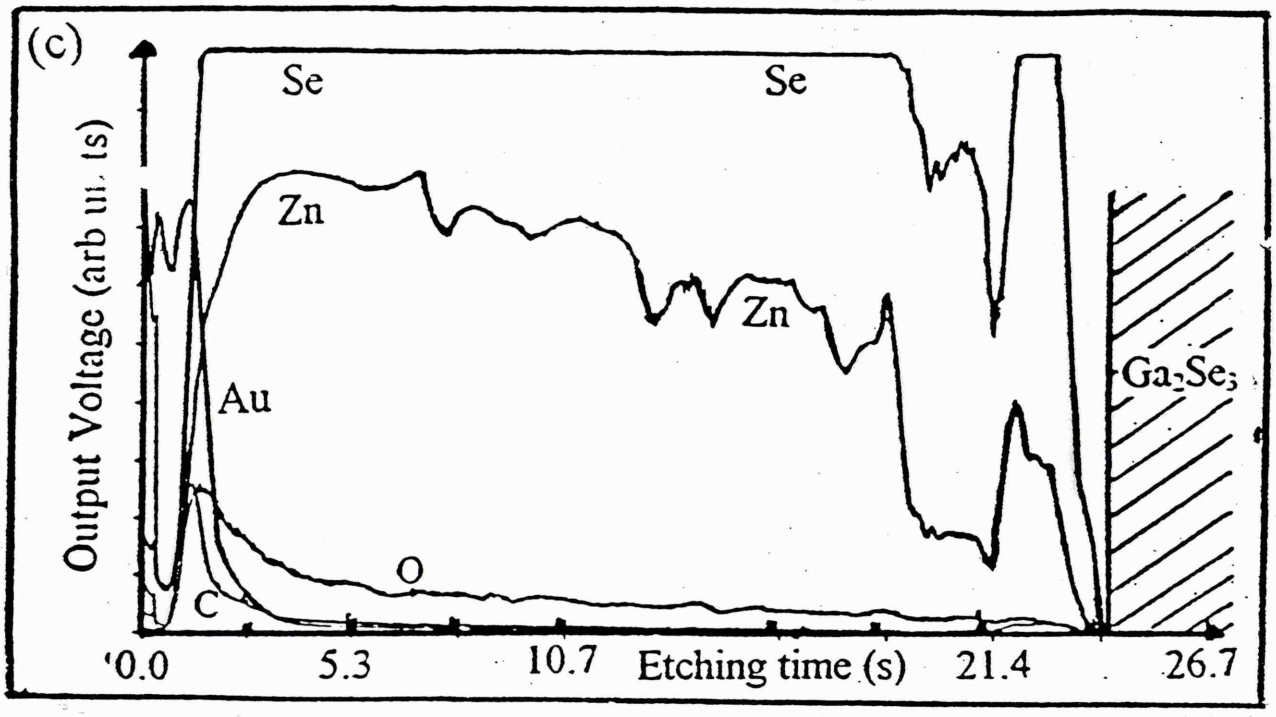

Figure 4.4 GDOES depth profile of Au/ZnSe/GaAs structure. The plasma switched off at the ZnSe/GaAs interface indicating the existence of a high resistance at the interface.

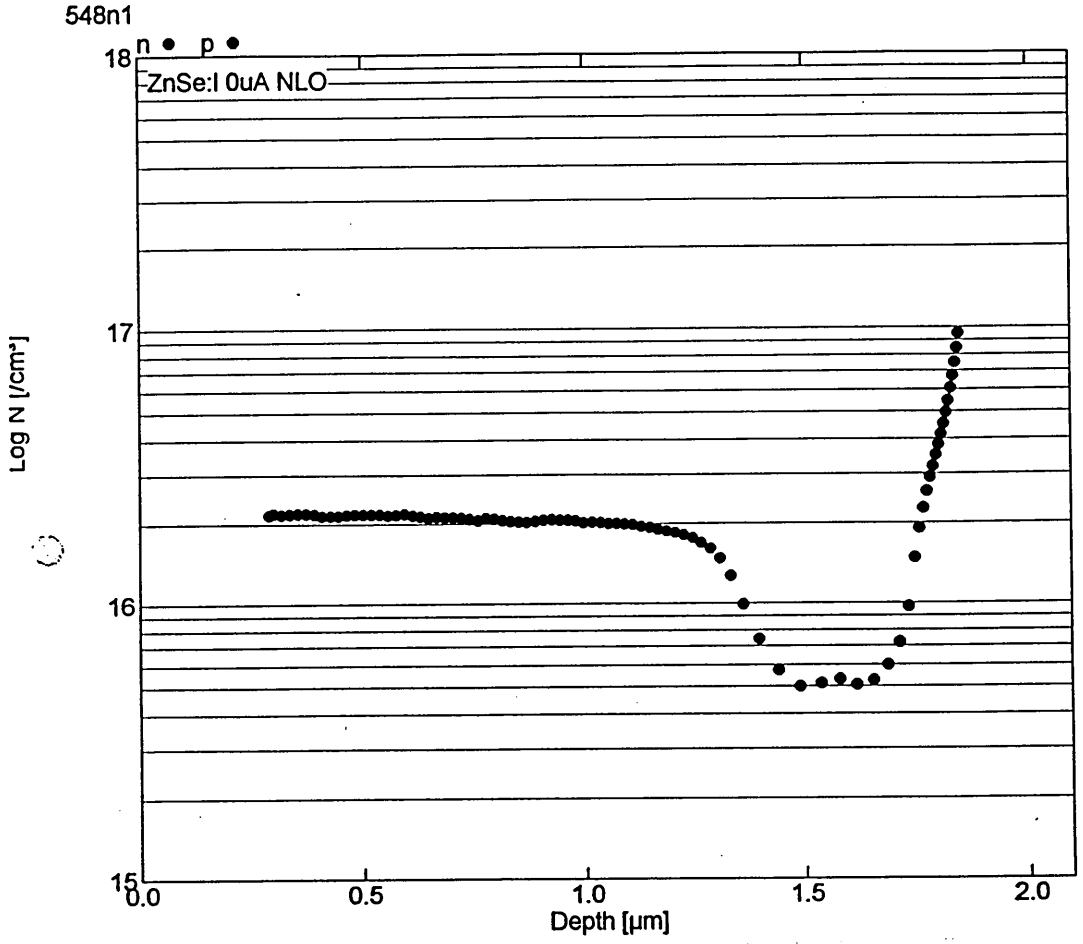

Figure 4.5 A typical C-V profiles of n-ZnSe/n$^+$-GaAs structures grown by MBE method. The dip with a relatively low carrier concentration indicates a different phase or a differently doped layer at the interface (These were measured at HW laboratories).

4.2.5 C-V depth profiling

The C-V profiling experiments were performed by the research group at Heriot-Watt University, UK and figure 4.5 is a typical electrochemical C-V profile of a ZnSe/GaAs structure. The results indicate that both ZnSe and GaAs are n-type with doping concentrations of ~1.2 x 10^{16} cm^{-3} for ZnSe and over 10^{17} cm^{-3} for GaAs, which are in close agreement with the suppliers information. As shown in figure 4.5, typical C-V profiles consist of three main regions, namely a ~3 μm thick ZnSe layer (~1.4 μm for this particular sample), a ~ 0.4 μm thick intermediate layer and the GaAs layer. The intermediate region is of a low doping concentration, which is ~ 5 x 10^{15} cm^{-3} for this particular sample and it indicates the formation of a different phase or a differently doped layer at the ZnSe/GaAs interface. This behaviour is consistent with the GDOES results which showed a high resistance at the interface, although the resistivity indicated by C-V profiling is not much different to that of the ZnSe layer.

4.2.6 Discussion of material characterisation

X-ray diffraction analysis has shown that the ZnSe layers grown on GaAs (100) were highly epitaxial and oriented preferentially in a <100> direction, Dharmadasa et al (1994). The spectra observed in this work for several epilayers showed similar characteristics, however, the appearance of the peaks of Ga_2Se_3, which is an insulator also grown in a preferential <111> direction, is useful in understanding the ZnSe/GaAs interface structure. Even though there is a 0.027% difference in lattice constants between ZnSe and GaAs, the peak positions were in good agreement with standard JCPDS unstressed powder diffraction data. The reason for not showing strain effects in the XRD spectrum may be the large thickness of the epilayers which were ~ 3 μm thick.

XPS spectra as shown in figures 4.2 (a) and (b) indicate the necessity of careful cleaning of material surfaces before contact formation or any further studies. Figure 4.2 (b), which is the spectrum obtained after Ar etching contains only lower intensity C $1s_{1/2}$ and O $1s_{1/2}$ XPS peaks and no Auger peaks in comparison with the non-Ar etched surface as shown in figure 4.2 (a). The sample was etched in an Ar stream for nearly five minutes, which is the minimum time required to remove O and C. Chemical etching and subsequently leaving the sample in air would certainly oxidise the surface. As clearly shown in figure 4.2 (c)-i, SeO_2 appears at the binding energy 59 eV in addition to the Se $3d_{1/2}$ peak at 54 eV, whereas the Ar etched surface does not contain a SeO_2 peak (figure 4.2 (c)-ii). This indicates that Ar etching has been able to remove oxygen but not all carbon. Complete removal of C could be done by increasing the etching time. Surface oxide and carbon layers may make a contribution to the short durability of the ZnSe based devices. Stoichiometry of the surface can be determined using the intensities of Se $3d_{1/2}$ and Zn $3p_{1/2}$ peaks as they both have similar binding energies and are separated only by about 36 eV, indicating similar escape depths. Figure 4.2 (d)-i, which is the spectrum of the non-Ar etched surface shows the uneven stoichiometry in comparison with the Ar etched surface as shown in figure 4.2 (d)-ii.

Analysis of GDOES results indicated the presence of only Zn and Se in the ZnSe layer. The very high resistance of the intermediate layer would stop the plasma and this same resistive layer could be the reason for the requirement of high voltages (~ 11 V) and short lifetimes of light emitting devices based on n-ZnSe/n^+-GaAs structure. This can further be explained using C-V profiling results. The uniform ZnSe layer of about 1.2 x 10^{16} cm^{-3} carrier density, which is about ~3 μm thick, has a dip of a lower charge density at its edge. This intermediate layer which is about 0.4 μm thick may be the

highly resistive layer, which appeared in GDOES profiling and gave two peaks in XRD spectra. The attribution of the dip to the intermediate insulating layer may be explained as follows. When the electrolyte penetrates the ZnSe layer and meets the Ga_2Se_3 containing intermediate layer, the doping concentration profile would drop down to a very low value but at the GaAs layer, the value shoots up to a high value of 5×10^{18} cm^{-3}. However, the instrument would smooth out these results combining high carrier concentrations of ZnSe and GaAs layers with the low carrier concentration of intermediate layer, leaving a smaller dip at the interface position.

4.2.7 Summary of material characterisation

ZnSe layers grown using the MBE technique are epitaxial and preferentially oriented in a (100) direction. Ga_2Se_3 phases have been observed at the ZnSe/GaAs interface. Air exposed and chemically etched surfaces contain carbon and oxygen. Oxygen is in the form of SeO_2 but ZnO may also be there as well, as ZnO peaks are not detectable using XPS due to limitations in the resolution of the XPS spectrometer. SEM shows no grain boundaries confirming the epitaxial nature of ZnSe. GDOES and C-V profiling indicate the presence of a highly resistive layer at the n-ZnSe/p^+-GaAs interface.

4.3 Electrical characterisation of metal/n-ZnSe Schottky junctions.

Electrical characterisation of metal/ZnSe interfaces was performed mainly using conventional current-voltage (I-V) and capacitance-voltage (C-V) techniques. The ageing effects of the contacts were observed for about 3 months until the contacts showed considerable changes. Ballistic electron emission microscopy (BEEM) studies were carried by the research group at CEMES-LEO/CNRS, Toulouse, France via a well

established research collaboration. Analysis of I-V results provides the magnitude of the Schottky barrier and the diode quality factor and C-V results can be used to determine the carrier concentration. In addition, C-V results provide values for built-in-potential and hence the barrier height. Finally ballistic electron emission microscopy results are summarised to support the explanation given for macroscopic I-V results, on a microscopic scale.

4.3.1 I-V results

The degreased ZnSe epilayers grown on GaAs substrates by MBE were etched in an etchant 4 of the table 3.2 prepared using 0.6g NaOH, 1.0g $Na_2S_2O_7$ and 75 ml H_2O which should produce a stoichiometric surface. Circular metal contacts were made on ZnSe surfaces by thermal evaporation through shadow masks under high vacuum conditions, about 10^{-6} Torr. Au, Ag, Sb and Al were investigated by the I-V technique. Only the forward currents of many contacts were monitored as the reverse currents were below the detection limit of the instrument.

(a) Discrete barrier heights

Many ideal diodes and a few non-ideal diodes were found in almost all n-ZnSe/n^+-GaAs epilayers on which Au, Ag and Sb contacts were made. Al contacts made on the same material etched using the same etchant showed non-ideal behaviour with very large n values in all occasions.

As depicted in the figure 4.6.1, ideal Schottky diodes ($n < 1.1$) with barrier heights of 0.9, 1.1, 1.2, 1.38, 1.47 , 1.55, 1.67 and 1.80 eV were observed frequently. These values, which were independent of each other were observed for different contacts not only on

different samples but also on the same sample. Similar work done by Blomfield et al (1996) reported a comprehensive set of ϕ_b values for Au, Ag and Sb contacts including all the values observed in this work except 1.1 eV and 1.38 eV. The value 1.47 eV has been observed often in the literature, among them were Blomfield et al (1996) and Vos et al (1989). In this project, Au/n-ZnSe/n^+-GaAs contacts were commonly found to have barrier heights of 1.2, 1.47 and 1.55 eV but occasional appearance of the values 1.1, 1.67 and 1.80 eV was observed as well (figure 4.6.2 (a)). Ag/n-ZnSe/n^+-GaAs contacts were in general of the barrier heights 1.38, 1.47 and 1.55 eV with occasional appearance of 0.9 eV (figure 4.6.3 (a)).

Tyagi and Arora (1975) reported the barrier height 1.47 eV and Nedeoglo et al (1977) have reported 1.2 and 1.49 eV as the average barrier height for a Ag/n-ZnSe contact formed on etched surfaces using 1% bromine methanol solution followed by a wash in hot aqueous NaOH solution. Dharmadasa et al (1996) reported this etchant as an oxidising agent which leaves a Zn rich surface after etching. Tarricone (1980) followed by Blomfield et al (1996) reported a different value which is 1.67 eV for Au and Sb contacts on n-ZnSe/n^+-GaAs epilayers, which was one of the commonly observed barrier heights in this work. Almost all ideal ($n < 1.1$) Sb contacts were of the barrier heights 1.38 or 1.55 eV (figure 4.6.4).

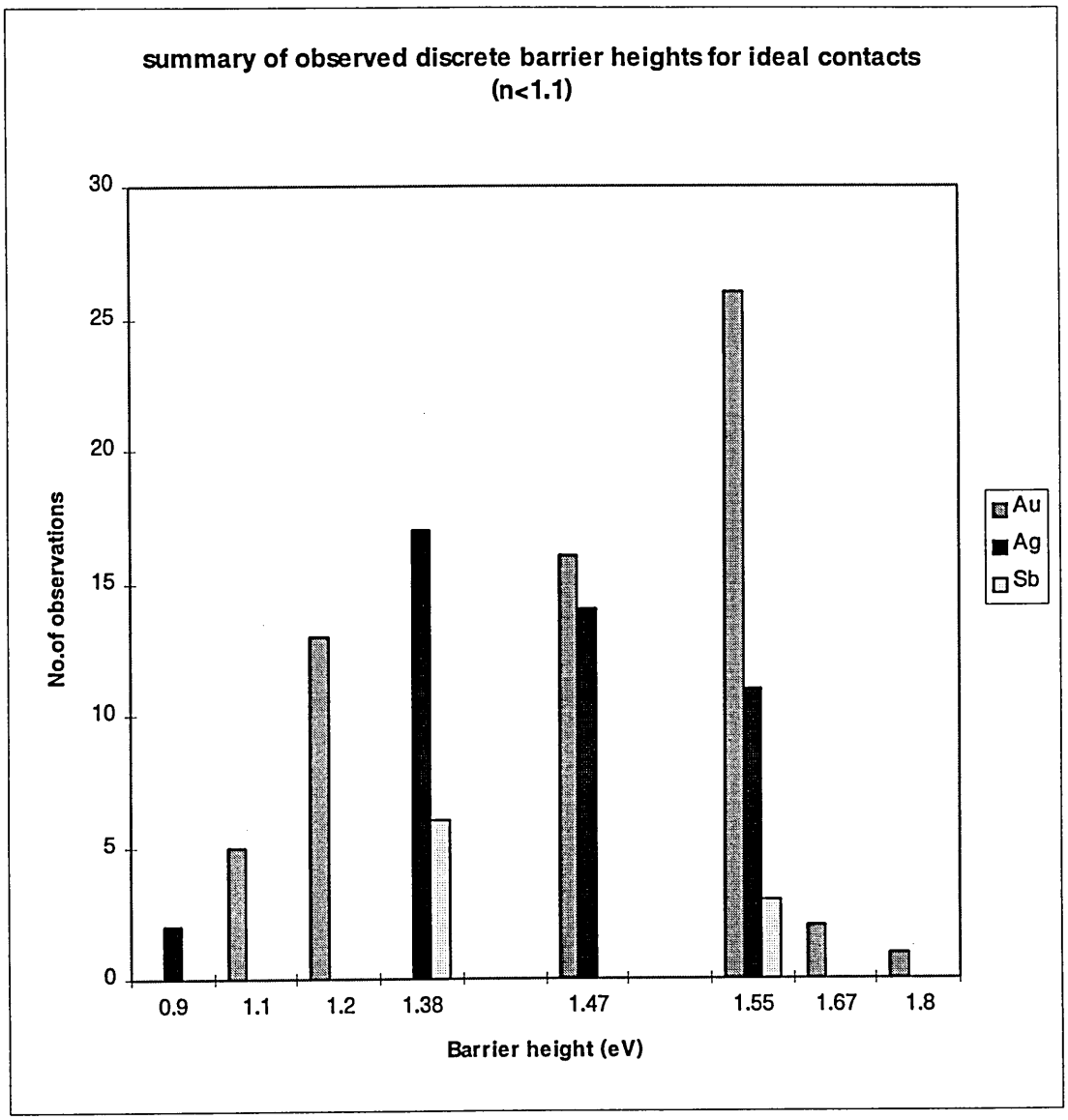

Figure 4.6.1 : Observed discrete barrier heights for Au, Sb and Ag contacts on n-ZnSe/n^+-GaAs heterostructure.

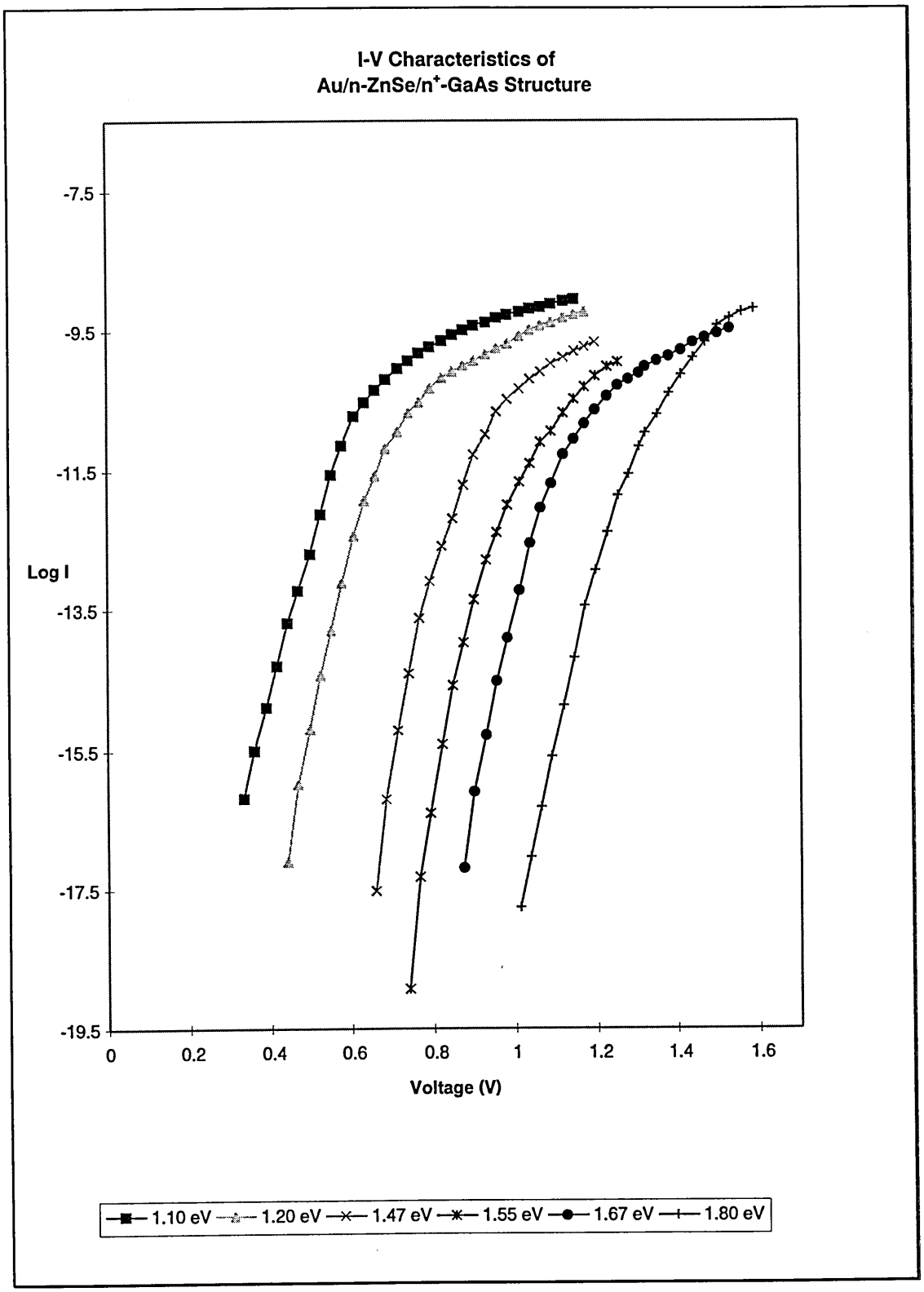

Figure 4.6.2 (a): Discrete barrier heights frequently observed for ideal Au/n-ZnSe/n^+-GaAs structure. ϕ_b = 1.2, 1.47 and 1.55 eV were observed for many of the contacts.

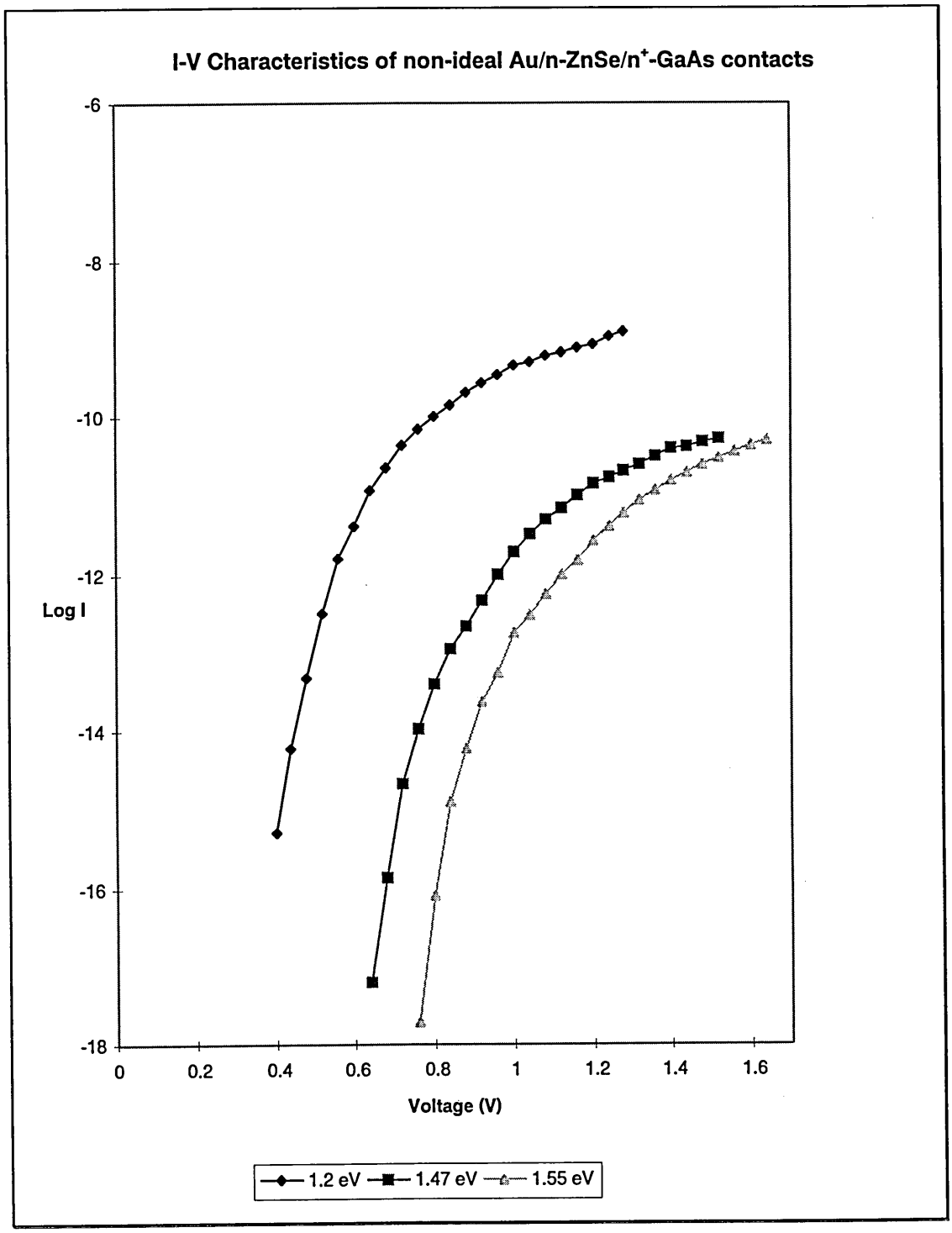

Figure 4.6.2 (b): Discrete barrier heights frequently observed for non-ideal Au/n-ZnSe/n^+-GaAs contacts. Barrier heights 1.2 eV and 1.47 eV are from contacts with n = 1.24 whereas 1.55 eV barrier height is from a contact with n=1.35.

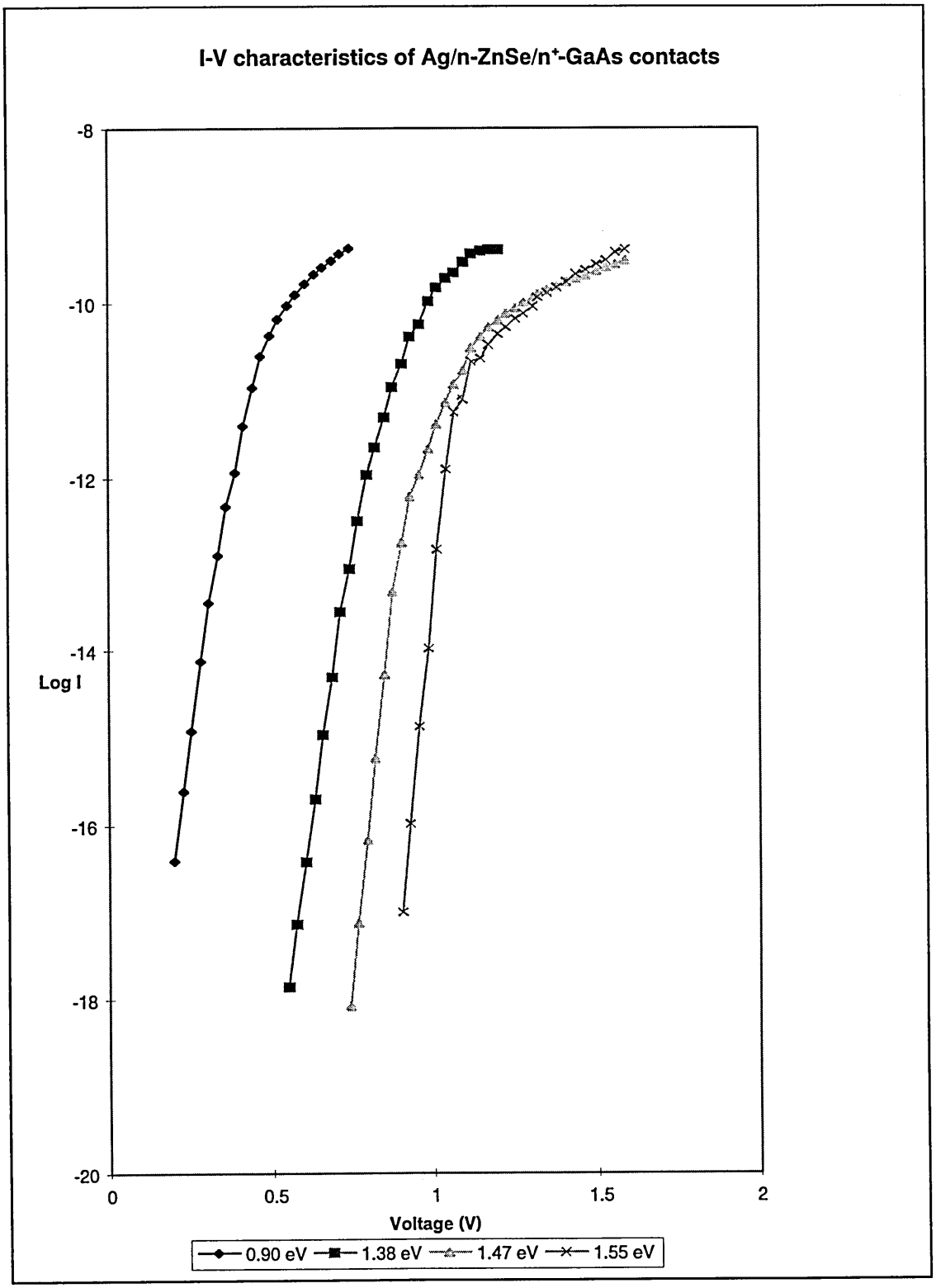

Figure 4.6.3 (a): Discrete barrier heights observed for ideal Ag/n-ZnSe/n^+-GaAs structure.

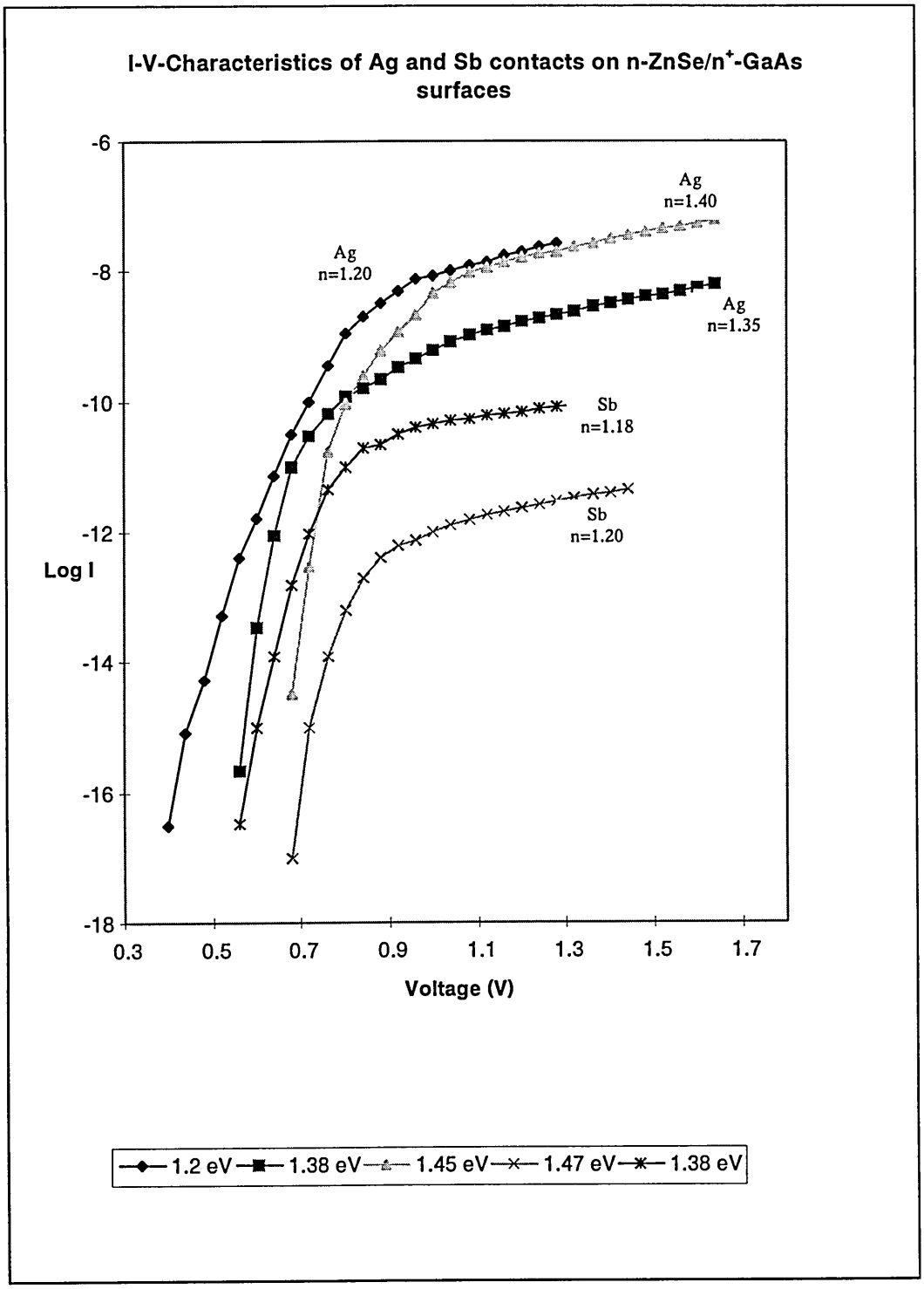

Figure 4.6.3 (b): Barrier heights observed for non-ideal contacts on n-ZnSe/n^+-GaAs. Barrier heights are similar to those observed for ideal diodes. In general n-values range was from 1.2 to 1.5.

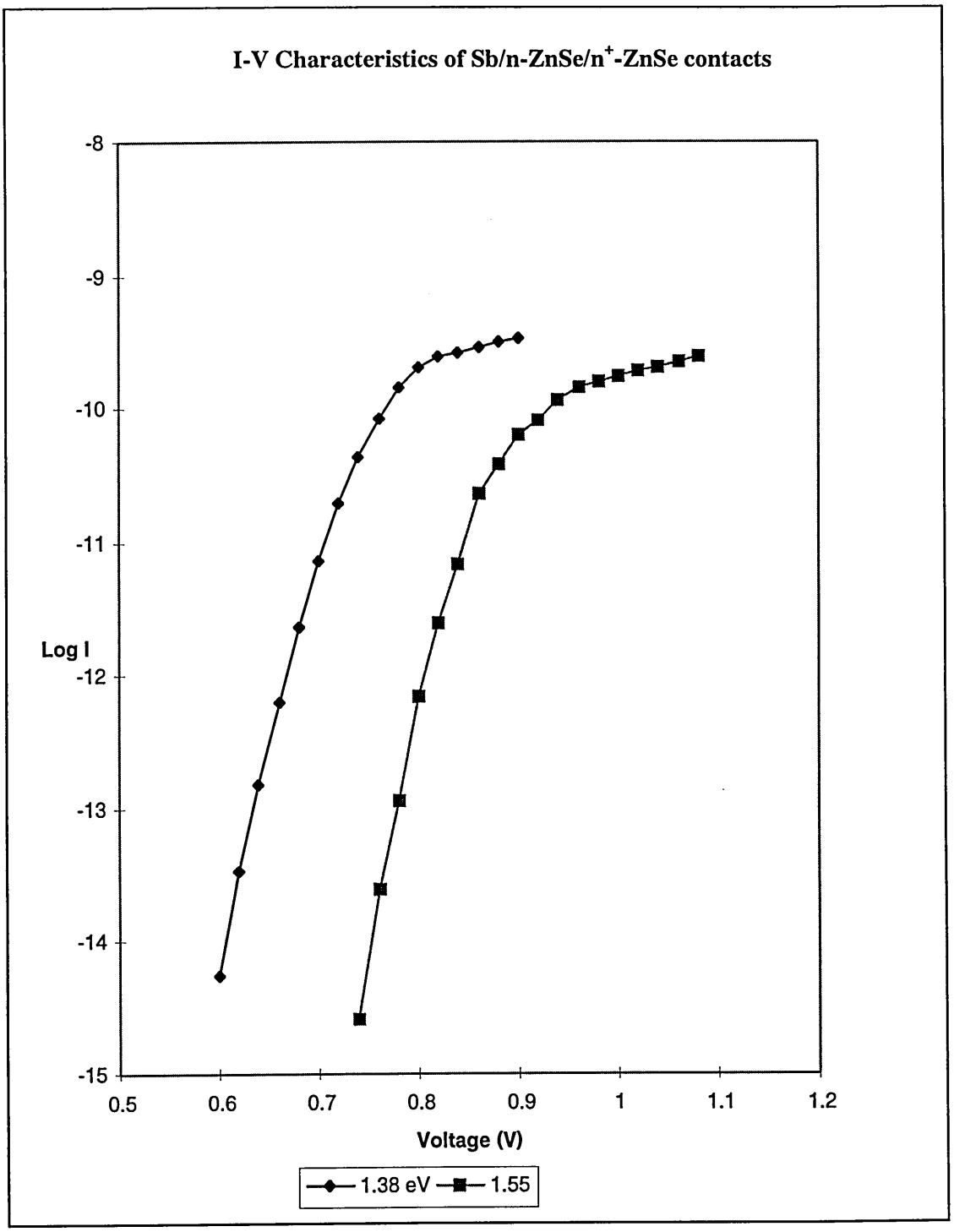

Figure 4.6.4: Almost all ideal Sb/n-ZnSe/n^+-GaAs contacts were of the barrier heights 1.38 eV or 1.55 eV.

Several non-ideal Au (figure 4.6.2 (a)) and Ag (figure 4.6.3 (b)) contacts were observed to have n values ranging from 1.2 to 1.5 as the contacts were made. They were of the barrier heights 1.2, 1.47 and 1.55 eV for Au contacts and 1.2, 1.38 and 1.45 eV for Ag contacts. Non-ideal (n ~ 1.25 - 1.45) Sb contacts showed 1.38 and 1.47 eV barrier heights (figure 4.6.2 (a)).

(b) Series resistance

As shown in figure 4.6.5, for a forward biased device, forward current can be divided into two regions. In region (i), the current is limited mainly by the thermionic emission over the barrier height ϕ_b, but in region (ii), the series resistance, R_S, has a greater contribution to the current. This series resistance is for the device structure as a whole. The same ϕ_b values were observed in this project in different devices with various R_S values (figure 4.6.5) which were mainly in three different regions namely, $10^3\ \Omega$, $10^6\ \Omega$ and $10^9\ \Omega$. These different resistances were observed for diodes made on different ZnSe layers, which were grown under different conditions and it is often observed that the series resistance decreases with time (figure 4.6.6).

(c) Ageing effects

The devices were investigated for durability and stability over a period of several months. The ideality factor ($n < 1.1$) for ideal diodes remained the same for a few weeks but ϕ_b changed jumped from one value to the other in the series (figure 4.6.6). However, starting from about 2 months time, the devices began to exhibit higher ideality factors and lower R_S values. The estimated barrier heights then appeared to be low due to higher n values. Some devices would remain at the same barrier height

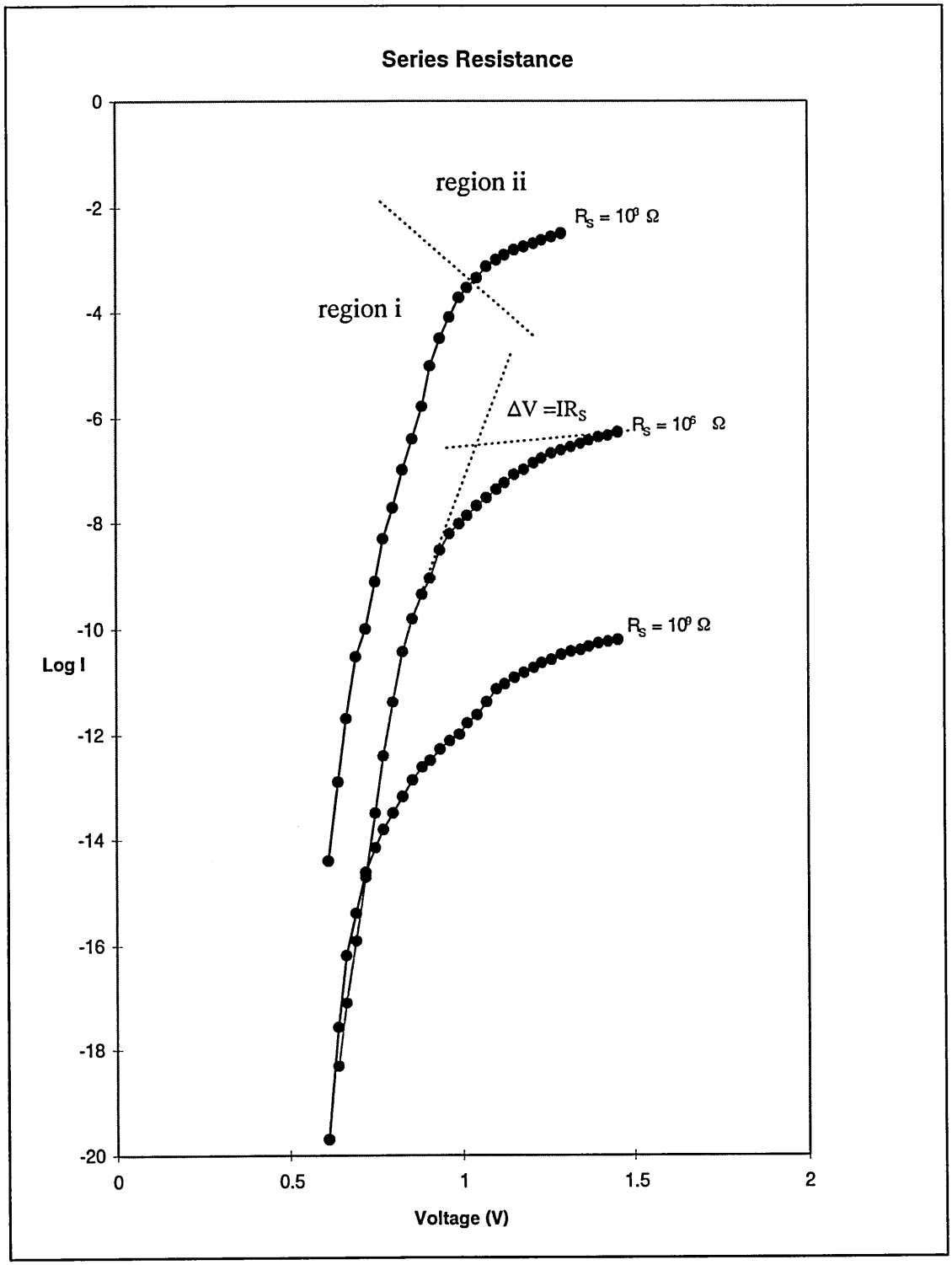

Figure 4.6.5: I-V characteristics of different ideal Au/n-ZnSe/n^+-GaAs contacts. Series resistances were mainly in 10^3, 10^6 or 10^9 Ω regions. These different series resistances were observed for ZnSe layers grown with different MBE growth conditions.

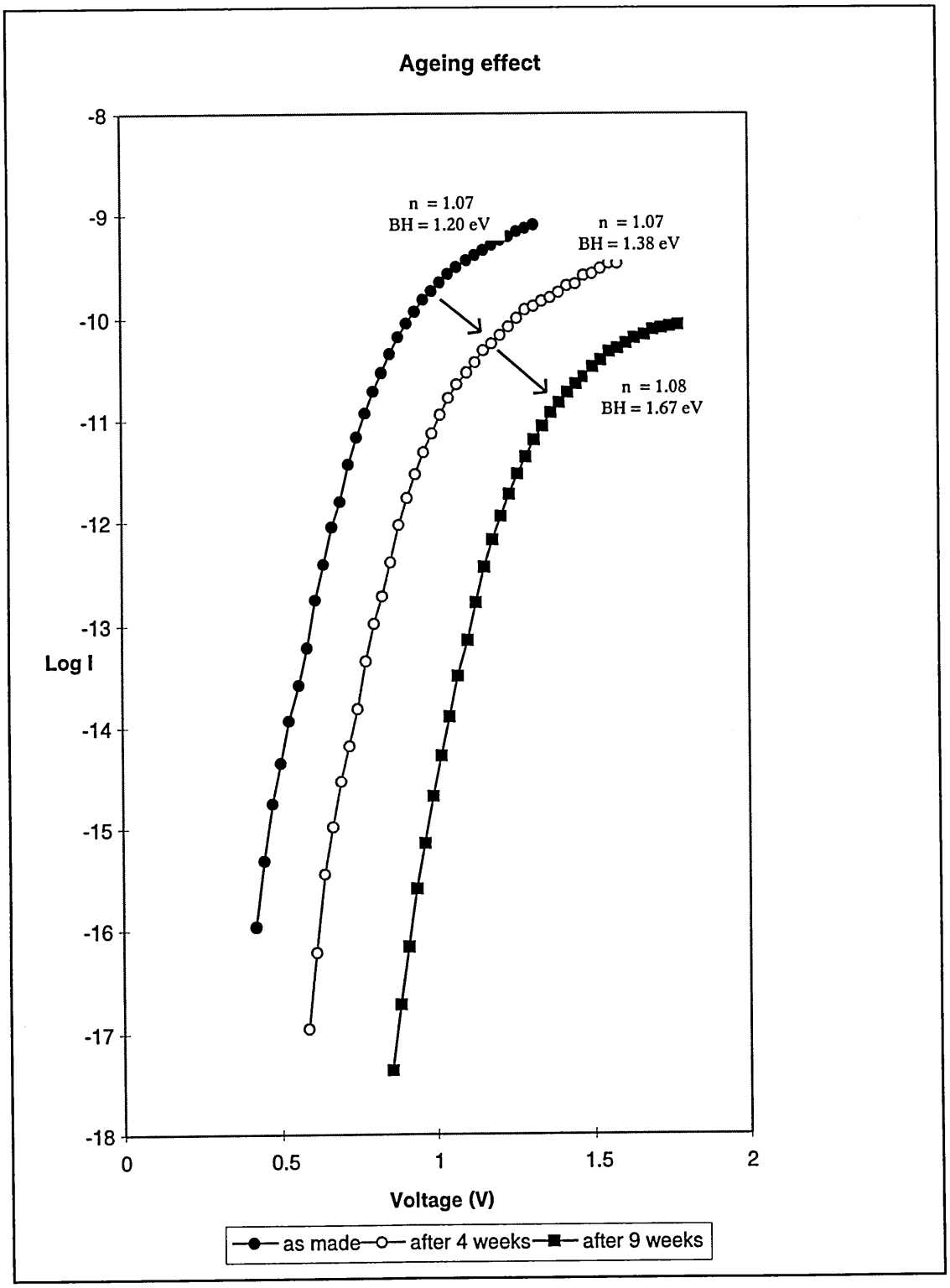

Figure 4.6.6: Many ideal metal contacts changed from one barrier height into another one in the series with time keeping n value approximately the same.

over a period of four to five months before the forward current started to decrease resulting in an increase in n values.

(d) Metal contacts on p-ZnSe/n^+-GaAs

As far as metal/p-ZnSe contacts are concerned, the initial resistance was in the 10^9 Ω range and the same as a metal/n-type structure, but decreased to 10^2 Ω range in two to three weeks time. Similar observations were reported by Dharmadasa et al (1996). The barrier heights were observed to be quite low ($\phi_b < 0.80$ eV) and the diodes were non-ideal with very high n values ($n > 2$).

(e) Summary of I-V results

The high series resistance of the metal/n-ZnSe/n^+-GaAs structure is one of the prominent features found from the I-V measurements. As seen from the XPS results, oxides on the surface would not exist after Ar ion etching in vacuum. However, the main feature displayed by the I-V results was the independence of barrier height from the metal used for contacts on n-ZnSe. The results do not necessarily obey Schottky theory as shown in figure 4.6.7. Also with time, barrier heights change into another value found in the series keeping n value approximately the same. The initial high series resistance of metal/p-ZnSe/n^+-GaAs decreases within a few weeks from the fabrication of the device.

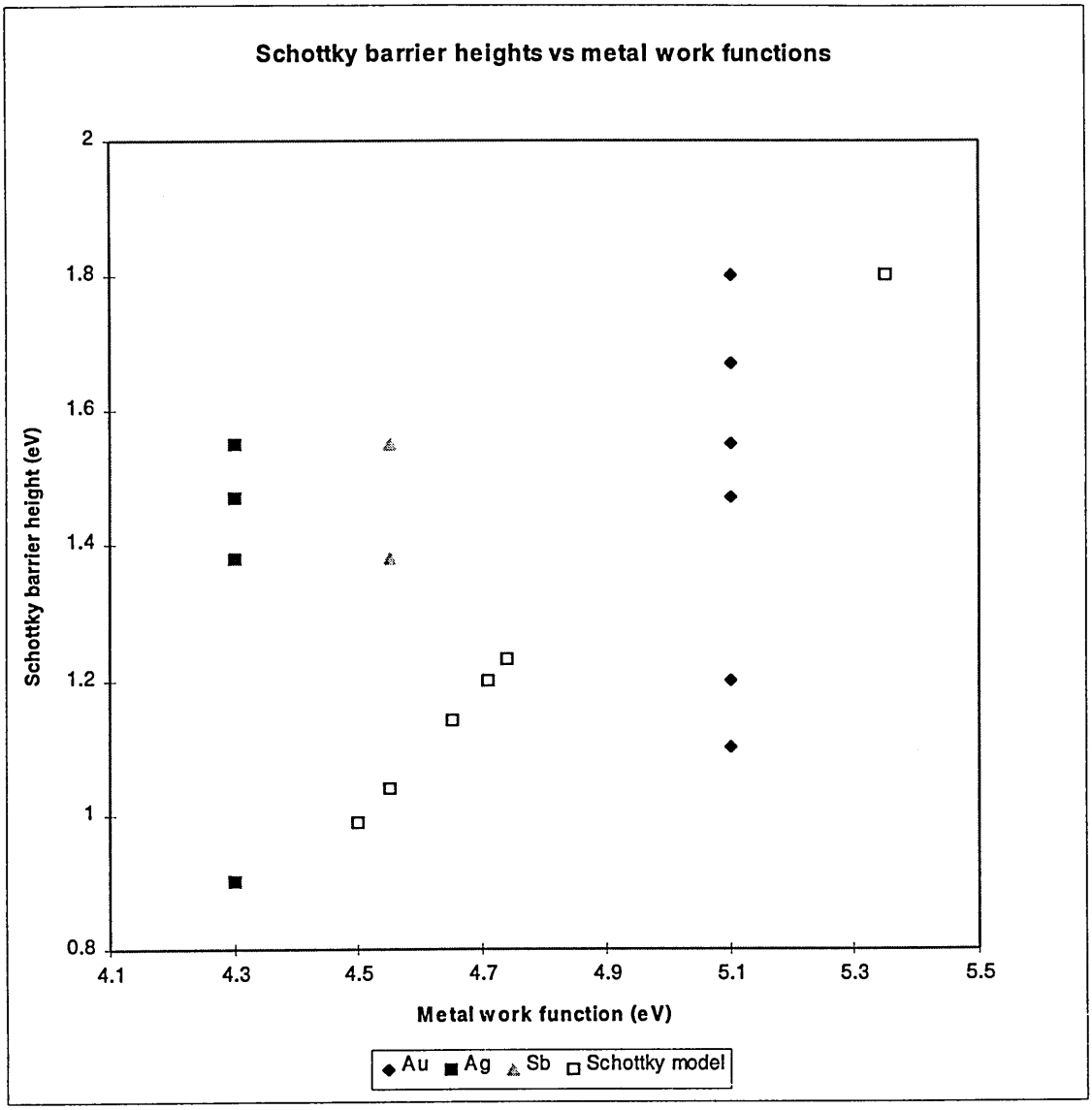

Figure 4.6.7 Summary of discrete Schottky barriers observed for Ag, Sb and Au contacts on n-ZnSe (100) layers and the values predicted by Schottky model.

4.3.2 C-V results

A few metal contacts were selected for C-V studies, and typical observations are shown in figures 4.7.1, 4.7.2 and 4.7.3. All the curves are linear indicating uniformity in dopant distribution within the material. Table 4.1 shows the barrier heights (ϕ_b) and carrier concentration (N_d) values obtained from the C-V analysis. As can be seen from the table, N_d values were in good agreement with the information provided by the supplier and the values derived from the C-V profiling technique, but ϕ_b was in excess of the values obtained from I-V results. Cowley (1966) explained the difference in results in terms of interfacial layers.

Table 4.1 Summary of C-V analysis

Figure	N_d cm-3	$\phi_{b\ (C\text{-}V)}$	n value	$\phi_{b\ (I\text{-}V)}$
4.7.1	6×10^{16}	1.58	1.08	1.38
4.7.2	2×10^{16}	1.77	1.10	1.47
	2.5×10^{16}	1.93	1.07	1.55
4.7.3	5.0×10^{17}	1.54	1.34	1.38

The barrier heights were calculated using the equation 3.14. The energy difference between the conduction band and the Fermi level, ξ of ZnSe was taken in the calculation as 0.10 eV.

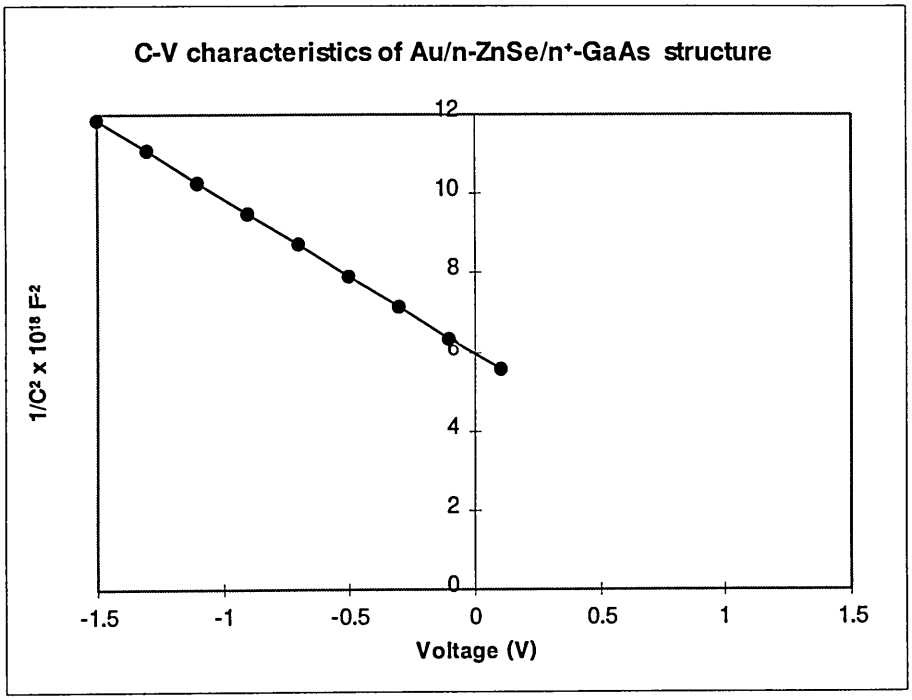

Figure 4.7.1 C-V characteristics of an ideal (n=1.08) Au/n-ZnSe/n^+-GaAs structure. The barrier height observed from I-V technique is 1.38 eV and the extrapolated $\frac{1}{C^2}$ vs V curve gives ϕ_b = 1.58 eV.

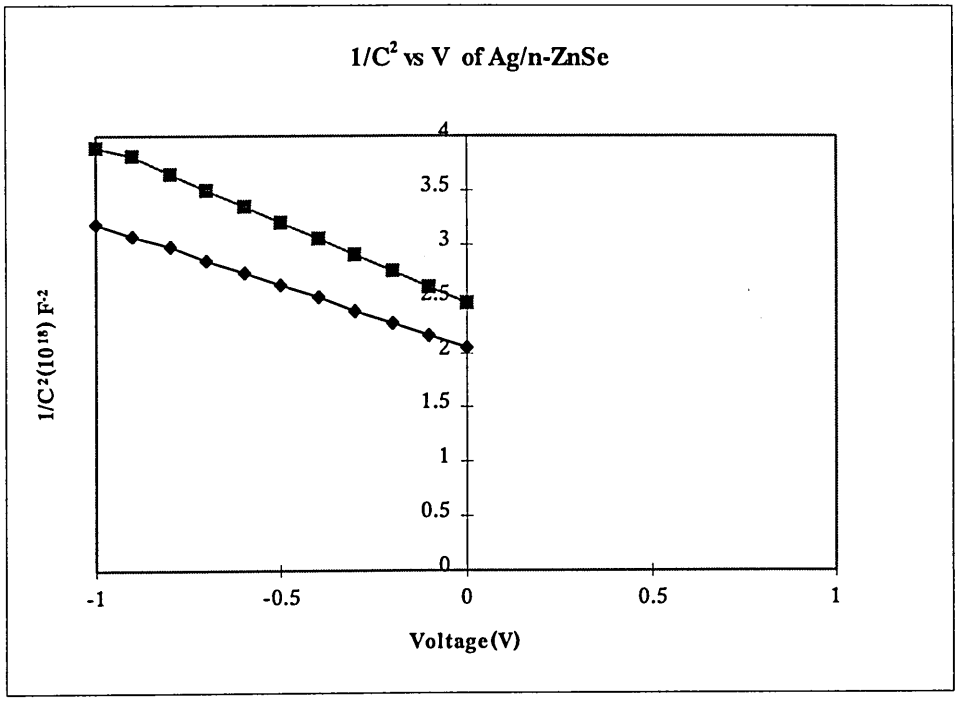

Figure 4.7.2 C-V characteristics of two ideal (n < 1.1) Ag/n-ZnSe/n^+-GaAs structures. The barrier height observed from I-V technique for the two devices represented by the curves are 1.47 eV and 1.55 eV whereas these two curves give values of 1.77 eV and 1.93 eV respectively.

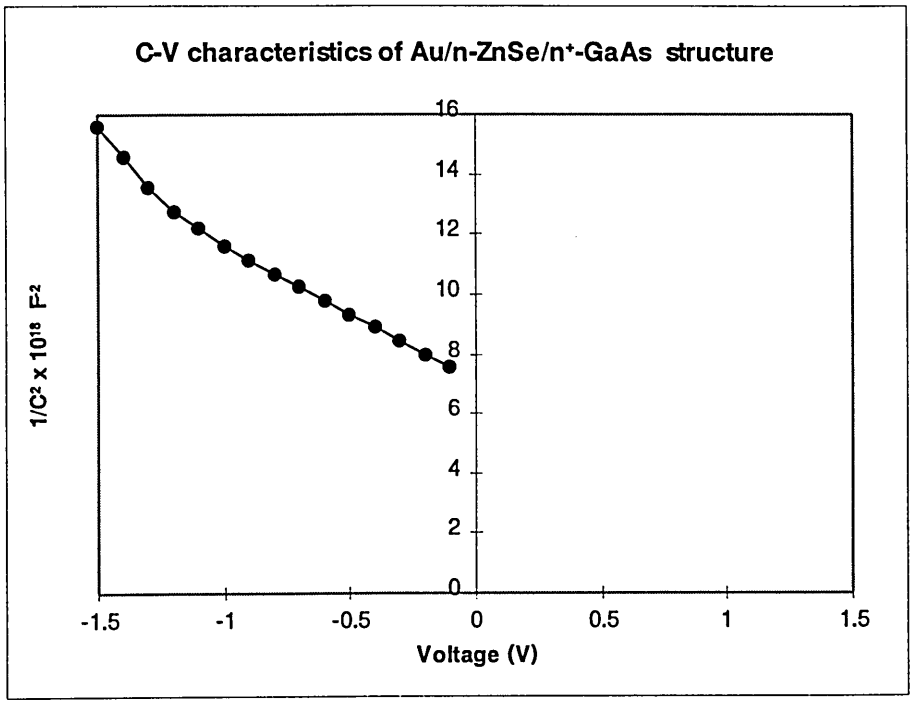

Figure 4.7.3 C-V characteristics of a non-ideal Au/n-ZnSe/n^+-GaAs structure. The barrier height measured from I-V results was 1.38 eV with an n value of 1.34, whereas extrapolation of this graph gives a V_b value of 1.44 eV leading to a ϕ_b value of 1.54 eV. However, the curve is no longer a straight line for reverse voltage below -1 V indicating various other influences.

4.3.3 BEEM results

A few ideal contacts as seen from I-V results were sent to be studied by the BEEM technique. Four out of the seven discrete barrier heights reported for metal/n-ZnSe Schottky barrier using I-V technique has so far been identified using BEEM work in the literature. BEEM experiments performed on Au/n-ZnSe Schottky diodes by Morgan et al (1996) have identified ϕ_b = 1.32 eV level and by Coratger et al (1995) have identified ϕ_b = 1.50 eV, 1.67 eV and 1.80 eV to date.

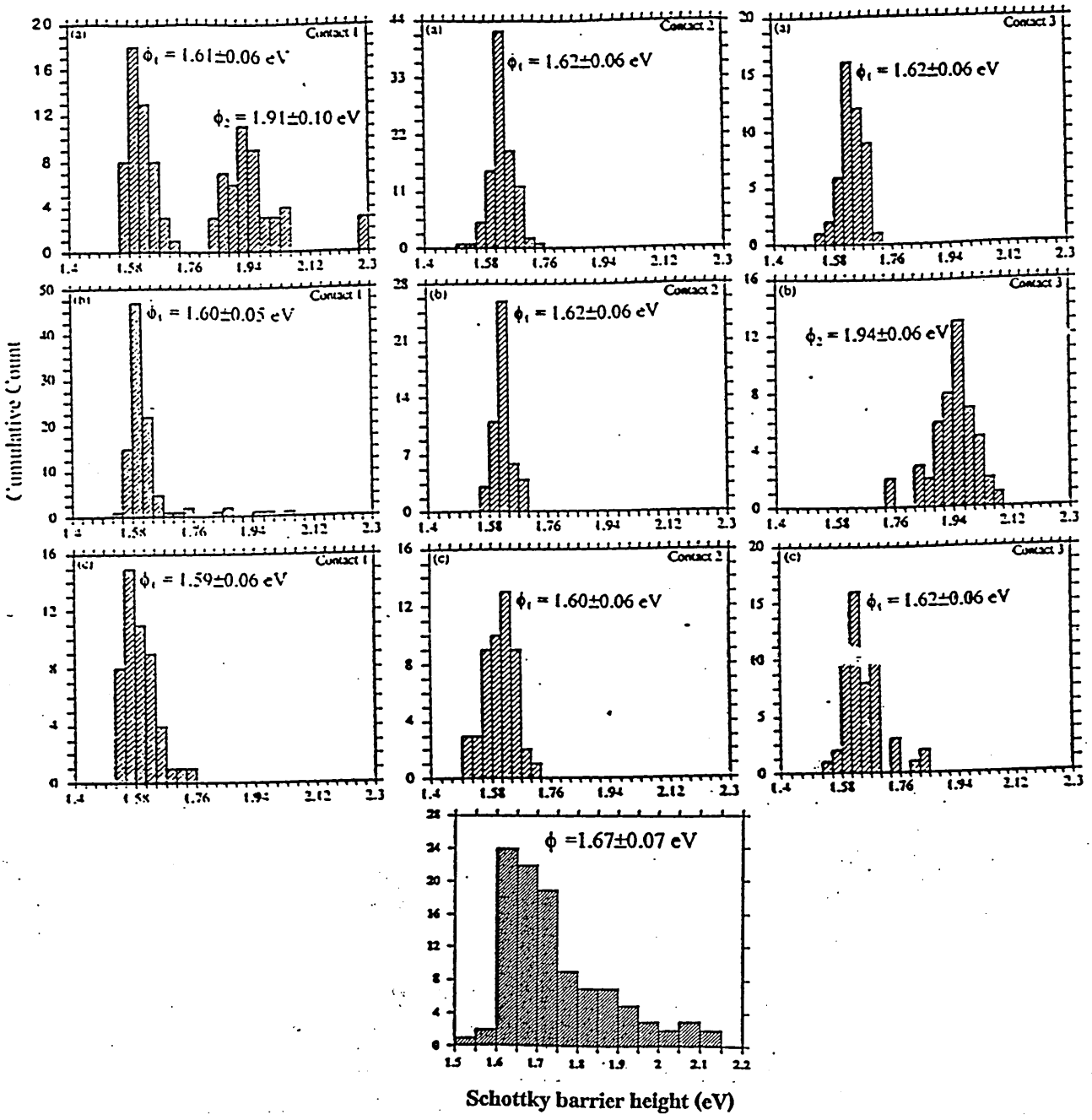

Figure 4.8 BEEM spectra of Au/n-ZnSe/n$^+$-GaAs Schottky diodes having different barrier heights 1.61 eV, 1.67 eV and 1.92 eV as found by I-V technique.

The devices investigated here were all ideal and were prepared in the same way as for I-V measurements. The barrier heights and n values were measured using the I-V technique before they were sent for BEEM work.

Table 4.2 Summary of barrier heights measured from I-V and BEEM techniques

ϕ_B as measured from I-V (eV)	ϕ_b as measured from BEEM (eV) (average values from histograms)
0.90 ± 0.04	.....
1.10 ± 0.04	.....
1.20 ± 0.04	.....
1.32 ± 0.04[a]	.....
1.38 ± 0.04	1.37 ± 0.05[b]
1.50 ± 0.04[a]	.....
1.55 ± 0.04	1.61 ± 0.06
1.67 ± 0.04	1.67
1.80 ± 0.04	1.92 ± 0.06
2.10 ± 0.04[a]	.....

a Coratger et al (1997)
b Morgan et al (1996)

The seven barrier heights found utilising all the techniques have been summarised by Coratger et al (1997). The barrier height pairs 1.1 eV /1.2 eV, 1.32 eV/1.38 eV and 1.47 eV/ 1.50 eV may be the same levels as they were measured at different places. However, even after that reduction, there are seven discrete barrier heights observed to date for the metal/ZnSe system.

Figure 4.8 shows BEEM spectra obtained for three different ideal Au/n-ZnSe/n^+-GaAs diodes of ϕ_b = 1.61 eV, 1.67 eV and 1.92 eV as measured using the I-V technique. All spectra show saturation of I_b (ballistic current) at high voltages. The Schottky barrier heights deduced from each of the spectrum by using the Kaiser and Bell model for the

ballistic current are ϕ_b = 1.61 eV, 1.67 eV and 1.92 eV within the experimental error of ± 0.06 eV. The ϕ_b values obtained from I-V and BEEM results and those found in the literature are summarised in table 4.2.

4.3.4 Discussion of electrical characterisation

I-V characteristics have shown a set of ϕ_b values for metal/n-ZnSe/n^+-GaAs structures and these values of ϕ_b = 0.9, 1.1, 1.2, 1.38, 1.47, 1.55 and 1.80 eV, are almost independent of the nature of the metal used in the contact formation. It has been claimed that the range of ϕ_b values measured for ZnSe can be accounted for using a model based on ZnSe defect levels, Dharmadasa et al (1996), Blomfield et al (1996), Wolfframm et al (1998). However, the ZnSe surfaces used in BEEM and I-V measurements were chemically treated prior to metal contact formation. It is thus possible that the pinning positions are generated by the processing steps rather than during metal deposition.

The models available to date, including the Schottky model are not capable of adequately explaining the multi Fermi level pinning situation seen in this work. The barrier height variation for different metal contacts should have a linear relationship with metal work function according to the Schottky model. This implies the barrier heights for Ag, Sb and Au metal contacts on ZnSe are ϕ_b = 0.75 eV, 1.04 eV and 1.59 eV (figure 4.6.7). Even though some of the values found in this work are close enough to these values, these results show the inability of the model to recognise discrete Fermi level pinning situations and also its inability to explain of the role of surface states and deep levels in practical devices. Ageing effects which showed ϕ_b changes from one value to another contradict many of the theories. The other models available have

similar tendencies. Kurtin et al (1969) in the linear model predicted that ZnSe is an ionic material which may behave as a weak acid or a strong base depending on the etchant used prior to contact formation. The model further suggests a value for the index of interface behaviour (S) as 0.5 for ZnSe. S was given by the equation 2.4 (a);

$$S = \frac{d\phi_b}{d\chi_m} \qquad [2.4\ (a)]$$

which implies that for a particular metal, barrier height can have no more than a single value. The theory is unsuccessful in attempting to explain multi Fermi level situations.

The effective work function (EWF) model indicates the possibility of the occurrence of multiple Schottky barriers without Fermi level pinning. The type of etching process and subsequent exposure to air would slightly modify the surface of ZnSe as observed from XPS results. Chemical reactions and intermixing at the metal/ZnSe interface also create numerous phases with different properties. The work function would therefore be modified to an effective work function. The barrier height of a pure Se/ZnSe contact would be 2.17 eV, which is one of the highest values a Schottky barrier can have according to Schottky model as the work function for Se (ϕ_{Se}) is 5.68 eV and the electron affinity of ZnSe (χ_{ZnSe}) is 3.51 eV. If the metal used for the contact is Zn, the barrier height would be 0.82 eV as ϕ_{Zn} = 4.33 eV. Interestingly, all the barrier heights observed fall within these two limits, and this can be due to the fact the work functions of all three metals considered in the project lie within the limits of Zn and Se. This model therefore can be used to explain the observed multiple Schottky barriers in terms of mixed phase or modified work functions. However, the various reactions that may occur between different metals and surfaces rich with either Se or Zn can be different and hence explanation using this model is limited. As observed by Blomfield et al

(1996), even though the barrier heights observed fell within the limits of EWF model, their discrete nature was inexplicable.

The most likely cause of multiple barrier heights is considered to be Fermi level pinning. The MIGS model presented by Heine (1965) described the decaying wavefunctions of the metal that would cause states within the band gap, with the possibility of pinning of E_F to a fixed position. However, numerical explanations cannot be given due to the non-availability of data in the literature. Similarly, the DIGS model presented by Hasegawa et al (1986) predicted only one pinning position due to disorder at the interface. Chemical etching, subsequent air exposure and chemical reactions during metallisation would certainly change the nature of the metal/ZnSe interface, causing disorder on the metal surface. Considering the pinning position E_{HO} as given in the MIGS model, only one value for the barrier height would be evaluated. However, the existence of multiple barrier heights would not be predictable using this model.

The UDM of Spicer et al (1979) predicts the pinning of E_F by extrinsic states introduced by the metal overlayer induced defects. Intrinsic or extrinsic defect involvement in Fermi level pinning as described by this model can be reasonably accepted. The ionic nature of II-VI compounds in general is more favourable for anion or cation vacancies to be created within the crystal structure. There is a remarkable agreement between the defect associated deep levels reported in the literature and the Schottky barrier heights observed. As suggested by Blomfield et al (1996), there are some apparent correlations between observed Schottky barrier heights and deep levels assigned to simple Se or Zn vacancies or As impurities. Therefore this model shows

reasonable agreement with the multi Fermi level pinning situation.

As suggested by Blomfield et al (1996), the semiconductor ZnSe may have a distribution of native defects resulting in a natural distribution of discrete states occurring in sufficient concentrations to pin E_F. The concentration of these states varies in the bulk depending on the growth conditions. The chemical etching process would have an influence on the density of states near the surface and the natural distribution of these native defects. Similar to Bardeen model, it can be suggested that in certain cases, one defect level may cause pinning of the Fermi level leading to domination over the other levels. This would result in a unique Schottky barrier height independent of the metal. As suggested by Blomfield et al (1996), impurity-defect complexes may play an important role in pinning the Fermi level to discrete values within the band gap. The ideal contacts as shown in 4.6.2 (a), 4.6.3 (a) and 4.6.4 show the similar nature of the barrier heights with different metal contacts. Figures 4.6.2 (b) and 4.6.3 (b) show non-ideal contacts, indicating the effect of deep levels on Fermi level pinning is hardly affected by the parameters that cause non-ideal behaviour.

Barrier heights deduced using C-V results are always greater than with those determined from I-V results for the investigated set of contacts. The differences can be explained in terms of interfacial layers and defect levels. Cowley (1966) discussed the effects of interfacial layers where as described in section 2.3.3 (a), the plot of C^{-2} against V_r remains linear but the intercept is interfacial layer dependent. Also a Schottky junction with deep impurity levels can follow the signal give an additional contribution to the capacitance. Deep traps would have played a role in deviation from the ideal capacitance as the frequency used in this work was relatively low, which was 3 kHz. In

the literature high frequencies such as 3 MHz have been used to minimise the effect of deep traps in capacitance studies. In addition to the interfacial layers and defect levels, inconsistency of the donor concentration throughout the depletion region and the existence of interface layers may have contributed to these deviations as well. These explanations go in parallel with the discrete barrier heights observed in I-V results. It is evident that all these four values are larger than values obtained from the I-V technique. However, figure 4.8, the histogrammes of 1.61 eV, 1.67 eV and 1.92 eV barrier heights have their lower limit at values matching those values from the I-V technique, namely 1.50 eV, 1.65 eV and 1.80 eV.

So far four barrier heights observed from I-V have been identified by the BEEM technique in the literature, Coratger et al (1997) and Morgan et al (1996). The values measured in this work show another three (1.61 eV, 1.67 eV and 1.92 eV) out of the seven discrete Fermi level pinning positions. It has been suggested that interface states and bulk defects are responsible for this multi Fermi level pinning situation, Coratger et al (1997). BEEM investigations have not only confirmed the Fermi level pinning situation observed from I-V results but indicate the formation of non-uniform Schottky barriers at metal/n-ZnSe interfaces.

Besides the Fermi level pinning situation, I-V results indicate a high resistance in the order of 10^6 Ω - 10^9 Ω in the metal/n-ZnSe structure. The bulk resistance of the material (ZnSe/GaAs) can be calculated using the known values of the carrier densities (N_{ZnSe}=1.5 x $10^{16}cm^{-3}$, N_{GaAs}=5 x $10^{18}cm^{-3}$), sample thicknesses (t_{ZnSe}=3μm, t_{GaAs}=3mm), electron mobilities (μ_{ZnSe}=540 cm^2/Vs, μ_{GaAs}= 8500 cm^2/Vs) and the area of the electrical contact made on ZnSe surface (2.0 x 10^3cm^{-2}). The calculated resistance

(R_S) of the bulk material, ($R_S=R_{ZnSe}+R_{GaAs}$) would be 1.49 Ω, which is far lower than the resistance shown by the I-V technique. From the material characterisation work it has been proved that the high resistance is associated not with the bulk of ZnSe or GaAs, but `with the Ga_2Se_3 intermediate phase formed at the interface. When forming Ga_2Se_3, GaAs would release As at the interface during growth using the MBE technique. As would then affect the n-dopants in ZnSe leaving a compensated insulating layer at the interface. This insulating layer of the thickness < 0.4 μm as observed from GDOES and C-V profiling studies would possibly be the cause for the high series resistance limiting performances, in the light emitting device structures based on ZnSe. This information suggests that the growth of n-ZnSe layers on GaAs should be avoided in order to eliminate the formation of this resistive layer. In contrast, the growth of p-ZnSe layers on GaAs should not be affected by the release of As and therefore the resistive layer will not exist in p-ZnSe/GaAs structures. Schull et al (1997) produced indium tin oxide (ITO) ohmic contacts with a lowest specific resistance of $9x10^{-3}$ Ωcm^2, to n-ZnSe layers of the thickness 0.28 μm and doping levels of $2x10^{17}$ cm^{-3}. These contacts had been made by evaporating ITO at a pressure of $< 5 \times 10^{-5}$ Torr on the epilayer and annealing it at 260°C for 15 minutes. However, the ZnSe device industry appear to concentrate on metal contacts to p-ZnSe. Improved growth conditions are such that the lowest contact resistance value reported to date is 1.1×10^{-4} Ωcm^2 for a Ti/Au/Au multi layer contact on an etched p-ZnSe surface for a doping level of 2×10^{19} cm^{-3}, Miyajma et al (1990).

In most cases, the forward current seems to saturate in the nanoampere or microampere region, and on a few occasions it was in the milliampere region (figure 4.6.5). This phenomenon would be a consequence of the highly insulating layer observed in this

work. In addition, there is another contributing factor, as explained by means of the back to back diode model by Colak et al (1989). As shown in the figure 4.9, this model incorporates both the metal/n-ZnSe barrier, ϕ_b and an n-ZnSe/GaAs heterojunction barrier, ϕ_{hj}. They were considered as two back to back diodes. When the Schottky barrier (ϕ_b) is forward biased, the current is limited by the reverse current of ϕ_{hj}. Similarly when ϕ_b is reverse biased, ϕ_{hj} will be a forward biased diode, thus the reverse current of the Schottky diode will be very small. This fact would certainly contribute to the high series resistance, hence as low current as in the nanoampere or microampere region, in the device structure. If the insulating Ga_2Se_3 is considered, the ϕ_{hj} structure would be a semiconductor-Insulator-semiconductor structure leading to a higher resistance.

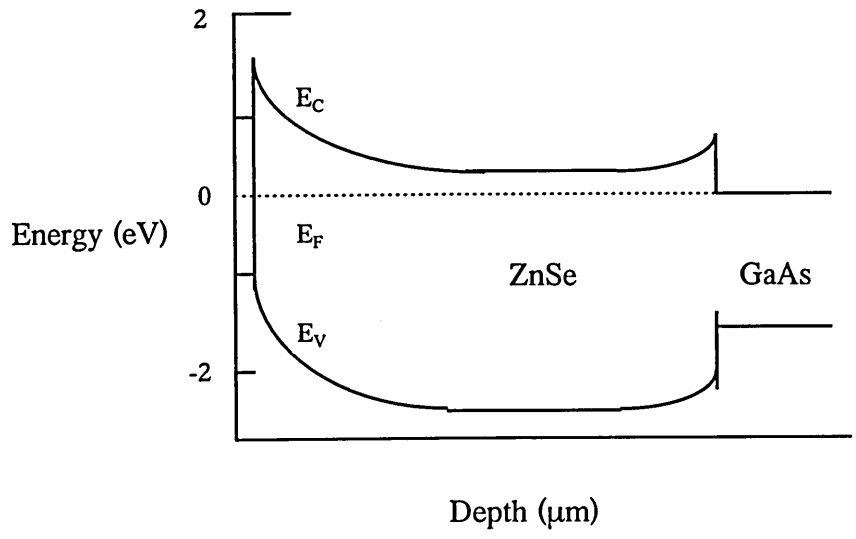

Figure 4.9 Energy band profile for a Au/n-ZnSe/n^+-GaAs heterojunction, after Colak et al (1989).

In addition, this work was focused more on practical chemically etched surfaces and therefore contain native oxide layers such as ZnO and SeO_2 and also other residual layers. These oxide containing layers are usually resistive and form MIS type structures introducing high resistance. However, with ageing, these layers would merge with the metal contact exhibiting a gradual decrease of series resistance.

4.3.5 Summary of electrical characterisation

Discrete barrier heights are observed for metal contacts on MBE grown ZnSe epilayers. The barrier heights do not behave according to the Schottky model as they are independent of the metal used. The series resistances of device structures are in one of $10^3\Omega$, $10^6\Omega$ or $10^9\Omega$ ranges for different ZnSe epilayers grown under different growth conditions. However, this resistance decreases with time as the devices become non-ideal.

CHAPTER FIVE:

ELECTROCHEMICAL DEPOSITION AND CHARACTERISATION OF ZnSe, CdSe AND CdTe THIN SEMICONDUCTING LAYERS IN AQUEOUS MEDIA.

5.1 Introduction

Observations of a non-conventional aqueous method of growing ZnSe and other II-VI semiconducting materials and appropriate characterisation are presented in this section. The effect of thermodynamic conditions on the growth of ZnSe, doping of layers of ZnSe, deposition of CdSe, CdTe and their characterisation are discussed. The mechanism and kinetics of electrodeposition are discussed too.

Non-aqueous electrochemical deposition at high temperature of Cd chalcogenides has been a great success, Premaratne et al-in press. Even though Se compounds such as SeO_2, H_2SeO_3 and Zn compounds such as $ZnSO_4$, $ZnCl_2$ are soluble in aqueous media, the deposition of ZnSe in an aqueous medium has not been studied in detail. The brief reports by a few groups, Natarajan et al (1994), Rai et al (1993), were not a great success. The results of this new work are compared with those found in the literature in this chapter. The electrodeposition of CdSe and CdTe has not been found difficult in the literature in comparison with that of ZnSe. $CdSO_4$, which is soluble in aqueous solutions was used as the Cd source in the deposition of either material. Even though TeO_2 is hardly soluble in water, the aqueous electrodeposition of CdTe has been a great success in the recent past.

In all the experiments, thoroughly cleaned glass/ITO using detergents followed by rinsing in organic solvents was used as the substrate for deposition of these films. Cyclic voltammograms were obtained during the experiments by connecting the electrodes to an X-Y chart recorder.

5.2 Electrodeposition of thin ZnSe layers

The chemicals used in the experiments were analytical grade and preserved under normal laboratory conditions. The experimental set up utilised a standard three electrode cell geometry (figure 1.8). The cell contained a cathode, known as the working electrode which was an ITO/glass electrode, an anode or the counter electrode which was a Pt disk or a carbon rod and a reference electrode, which was a Ag/AgCl standard electrode. All the potentials measured were with respect to this reference electrode unless otherwise stated.

5.2.1 Effect of change in deposition parameters

The experiments were carried out in an aqueous media over a range of potentials, a range of concentration combinations and a range of temperatures (table 5.1). $ZnCl_2$ or $ZnSO_4$ was used as the Zn precursor and SeO_2 or H_2SeO_3 was used as the Se precursor. The possible deposition potential range and pH combination was determined using the Pourbaix diagram for ZnSe (figure 3.1). The pH value of the solution was adjusted using diluted (0.1M) HCl or H_2SO_4 to be in the acidic medium, depending on the Se precursor used in the bath.

As shown in table 5.1, the first set of experiments were performed in order to determine the proper set of deposition conditions.

Table 5.1: Results of different combinations

Sample No.	Zn^{2+}: SeO_2 (H_2SeO_3) in the bath	colour of the film	PEC response (V)	deposition time	potential (V)
1.	$0.1:10^{-1}$	red	0	2 minutes	-
2.	$0.1:10^{-2}$	red	0	5 minutes	-
3.	$0.1:10^{-3}$	reddish-orange	0	10 minutes	-
4.	$0.1:10^{-4}$	orange-red	0	30 minutes	-0.4
5.	$0.1:10^{-5}$	yellow	0 for $ZnSO_4$ and -0.07 for $ZnCl_2$	1 hour	-0.5 to -0.6
			0	1 hour	-0.75 to -0.8
6.	$0.1:10^{-6}$	dark	0	15 minutes	-0.6

Although the experiments were started with even Zn^{2+} and SeO_2 concentrations, only the concentration ratio $Zn^{2+}:SeO_2 = 0.1:10^{-5}$ at 65°C with -0.5 V to -0.6 V applied voltages showed a response to a PEC cell indicating semiconducting properties. The temperature was varied from room temperature (RT) to 80°C in steps of 5°. Each experiment was repeated for different potentials within the potential range -0.3 V to -0.9 V at 0.1 V steps. Pourbaix diagrams were used to determine the potential range and pH values. The deposition rate and film colour were similar for the pH value range 2-3 under all different conditions. When the parameters were determined, the process was optimised by means of a cyclic voltammogram to give precise conditions. The results are given in table 5.2 for a 2 cm^2 substrate.

Table 5.2: Optimised deposition parameters

V_{ref} (V)	V_{cell} (V)	I (μA)	t (hours)	T°C
-0.54	1.78	60.0	2	65
-0.78	2.10	76.0	1.5	65

The current density J = 30 μA cm^{-2} and film thickness was about 0.2 μm. The rate of deposition was approximately 0.1 μm per hour.

Thoroughly cleaned Ti and Cu plates were also tested as substrates and the results are given in table 5.3.

Table 5.3: Suitability of different substrates for electrodeposition of ZnSe.

Substrate	Time taken	Potential range (V)	Temperature (°C)	Colour of film
Cu	5 minutes	-0.2 to -0.6	30-60	dark
Ti	2 hours	-0.2 to -0.8	30-60	dark
ITO	2 hours	-0.54	~65	yellow

Cu plates began to react in the acidic medium evolving hydrogen and showed no sign of a ZnSe deposition. Ti did not react with the solution but the deposition was a powdery dark film.

5.2.2 Cyclic voltammogram studies

Cyclic voltammograms were obtained while the experiments were in progress. This was mainly done to determine the exact deposition conditions. Figure 5.1.1 shows a

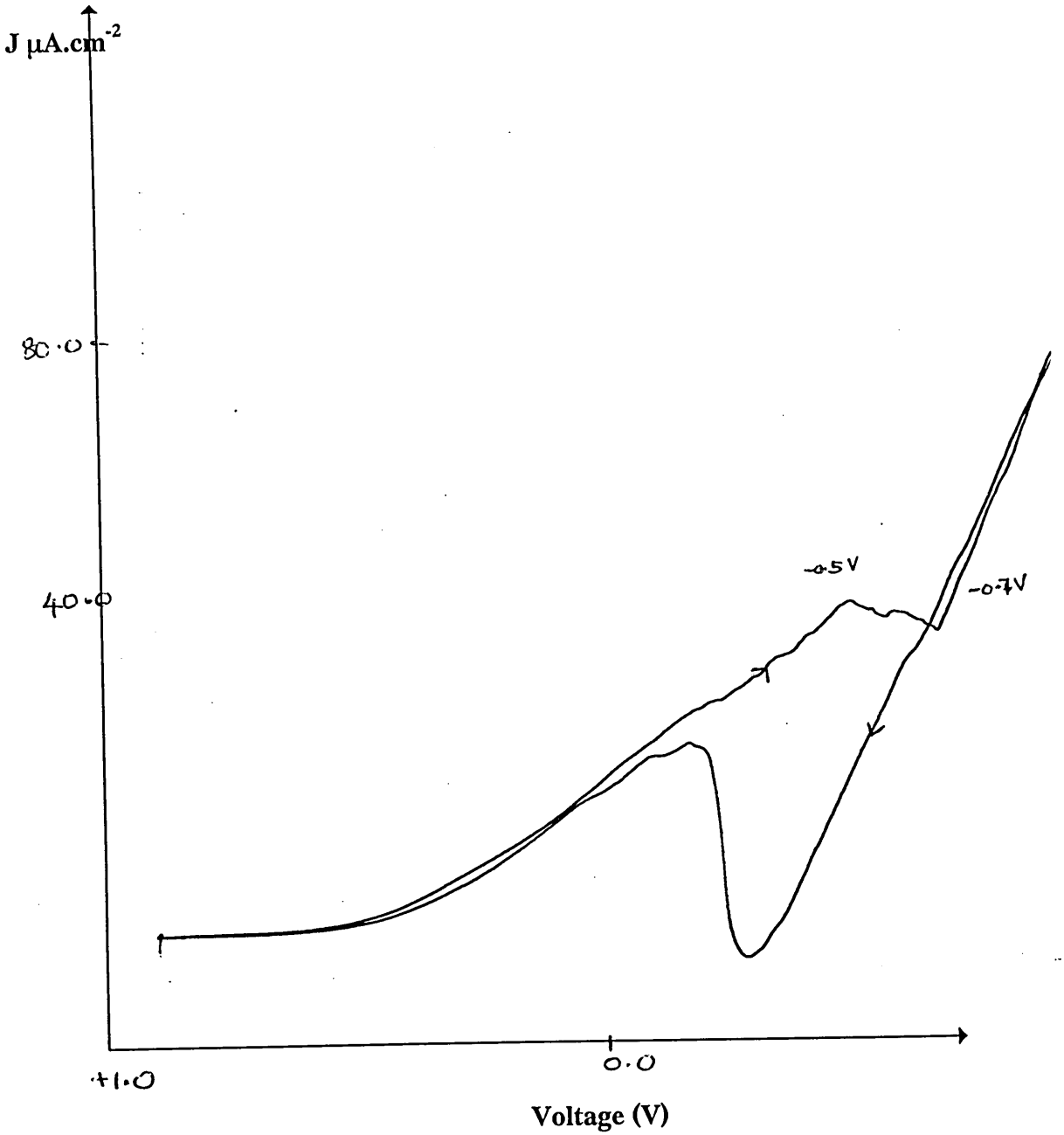

Figure 5.1 Cyclic voiltammogram for the electrodeposition of ZnSe. The plateau region below -0.5 V is identified as the possible ZnSe deposition region. The cathodic onsets below and above -0.5 V are Se and Zn deposition regions respectively. The excess Zn deposited on top of ZnSe corrodes during the reverse sweep.

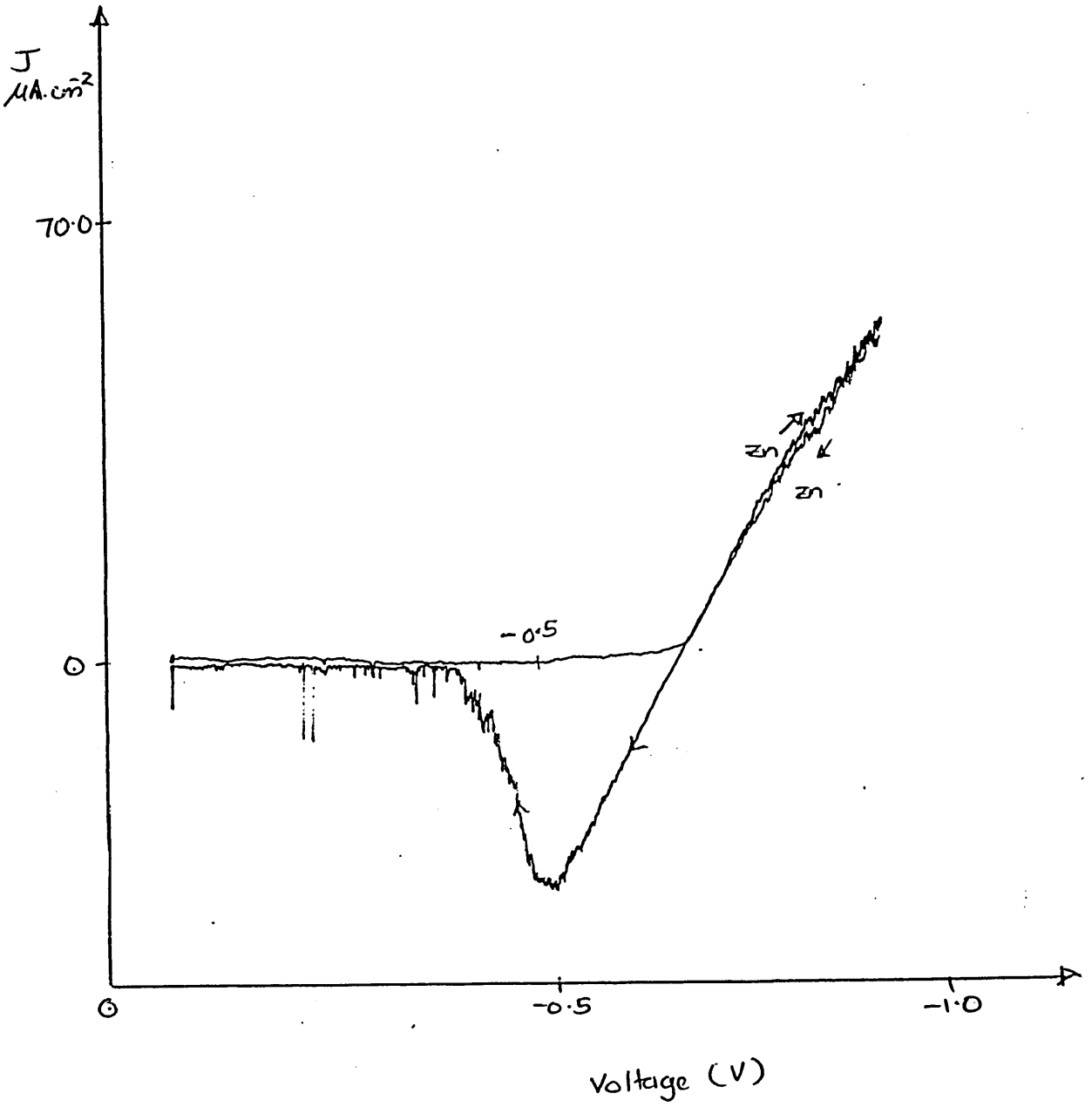

Figure 5.2 Cyclic voltammogram for an electrodeposition of Zn in the absence of Se. Unstable Zn layer corrodes during the reverse sweep.

cyclic voltammogram which was swept between +1.0 V and -1.0 V, for a cell containing solution with a concentration similar to the solution in No.5 of the table 5.1. This was the approximate potential range for the deposition of ZnSe given by Pourbaix diagram (figure 3.1). Figure 5.2 shows the deposition of Zn alone at higher negative potentials in an electrolyte free of Se.

5.2.3 XRD results

XRD studies were carried out in order to identify the composition, crystallinity and phases of the thin films. Figure 5.3.1 to 5.3.4 show the XRD spectra obtained for different deposition conditions. As shown in figure 5.3.1, the spectrum for the films deposited at high negative voltages showed only ITO substrate peaks and the annealing did not make any difference. A spectrum of a sample grown at -0.45 V is shown in figure 5.3.2, whose main peak arises from Se and SeO_2 (111) plane. The figure 5.3.3 (a) is of a film deposited at 0.54 V, whose major peaks arise from the planes (111) and (222) of cubic ZnSe. The small peaks arise due to Se_2O_5 (120) and ZnO_2 (200), $ZnSeO_3$ (023) or ZnSe hexagonal structures as marked in the figure. The four small peaks marked with * are arising from ITO substrate. After annealing at 250°C in air for 15 minutes, substrate peaks almost disappeared (figure 5.3.3 (b)). An XRD spectrum of a film deposited at -0.6 V is shown in figure 5.3.4. There is no peak corresponding to ZnSe but the peak at 22° arises from the (101) plane of $ZnSeO_4$. All the other peaks arise due to the reflections from the substrate. Figure 5.3.5 represent a sample grown at -0.7 V which has its strongest peak from the plane (111) of ZnO and the film has an amorphous hump due to the glass substrate and four peaks marked with * are due to the ITO layer.

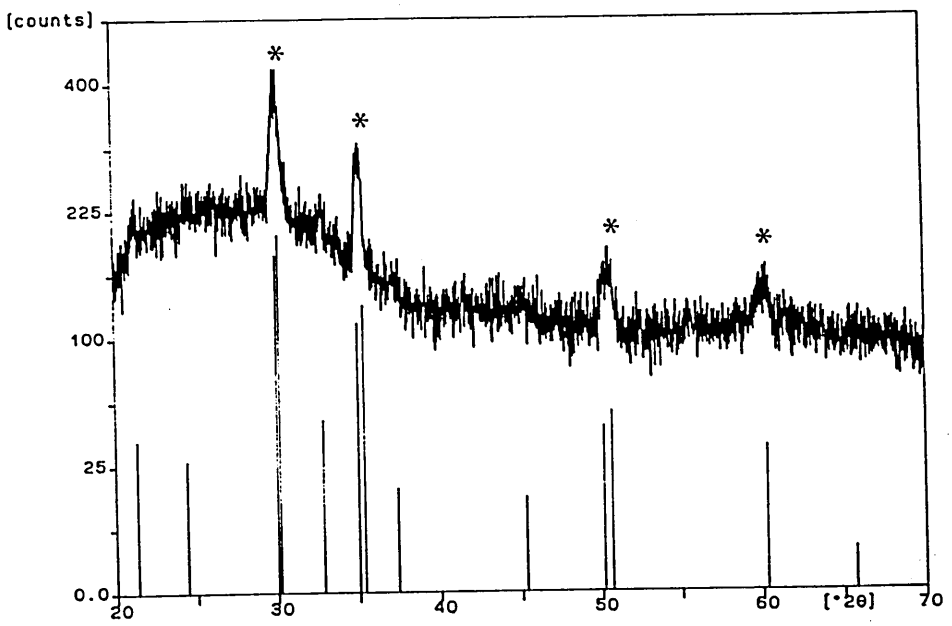

Figure 5.3.1 XRD spectrum of the sample no. 23ZS4S1, deposited at 65°C under an applied voltage of -0.6 V. All the peaks are arising from ITO planes indicating an amorphous Zn layer.

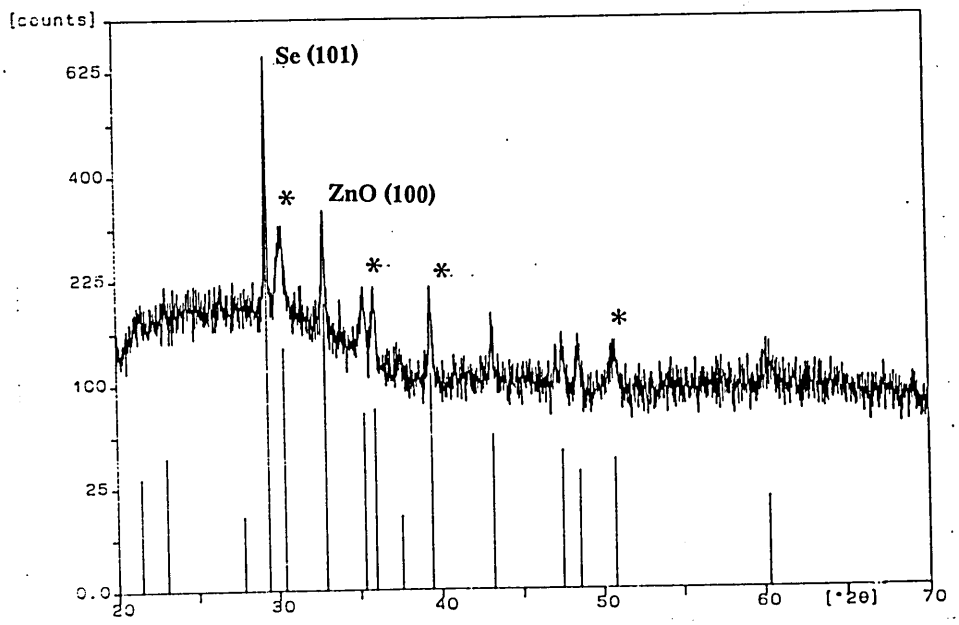

Figure 5.3.2 A sample (23ZS4S4) deposited at the voltage -0.45 V. The peak at 29.2° is due to the reflections from (101) plane of Hexagonal Se.

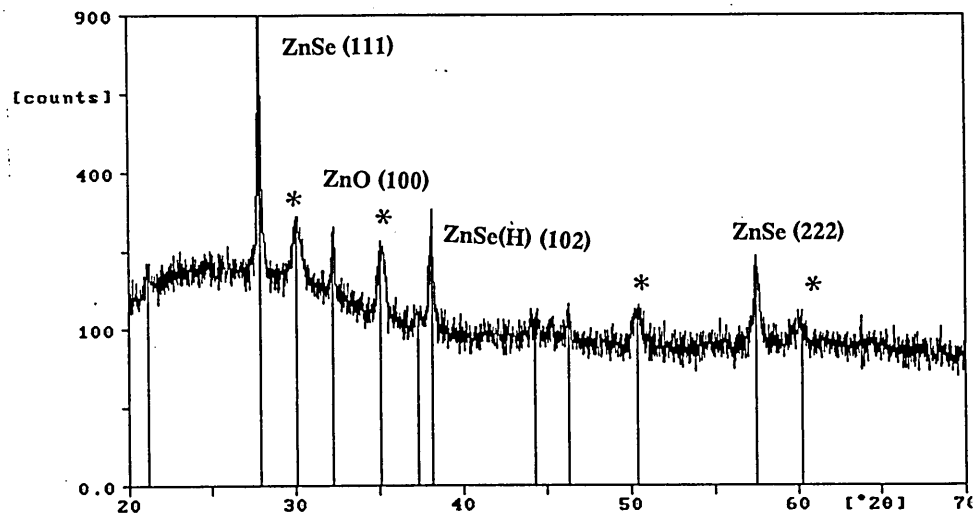

(a)

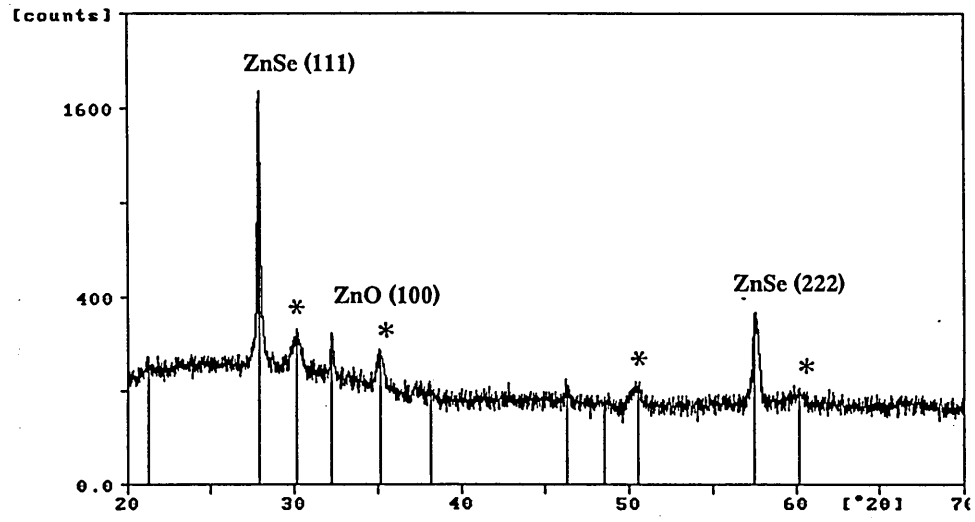

(b)

Figure 5.3.3 (a) A typical spectrum of an unannealed ZnSe layer, deposited at -0.54 V. The two major peaks are (111) and (222) of cubic ZnSe and (b) the spectrum for post annealing ZnSe layer, which shows an increase in intensities of the two peaks and decrease in the substrate peaks which are marked *. The intensity ratio of the two peaks (111):(222) was 100:14 and after annealing it was 100:9. The peak at 32° due to reflections from (100) peak of ZnO and at 37.96° due to (102) plane of hexagonal ZnSe are not to be seen in the post annealed spectrum.

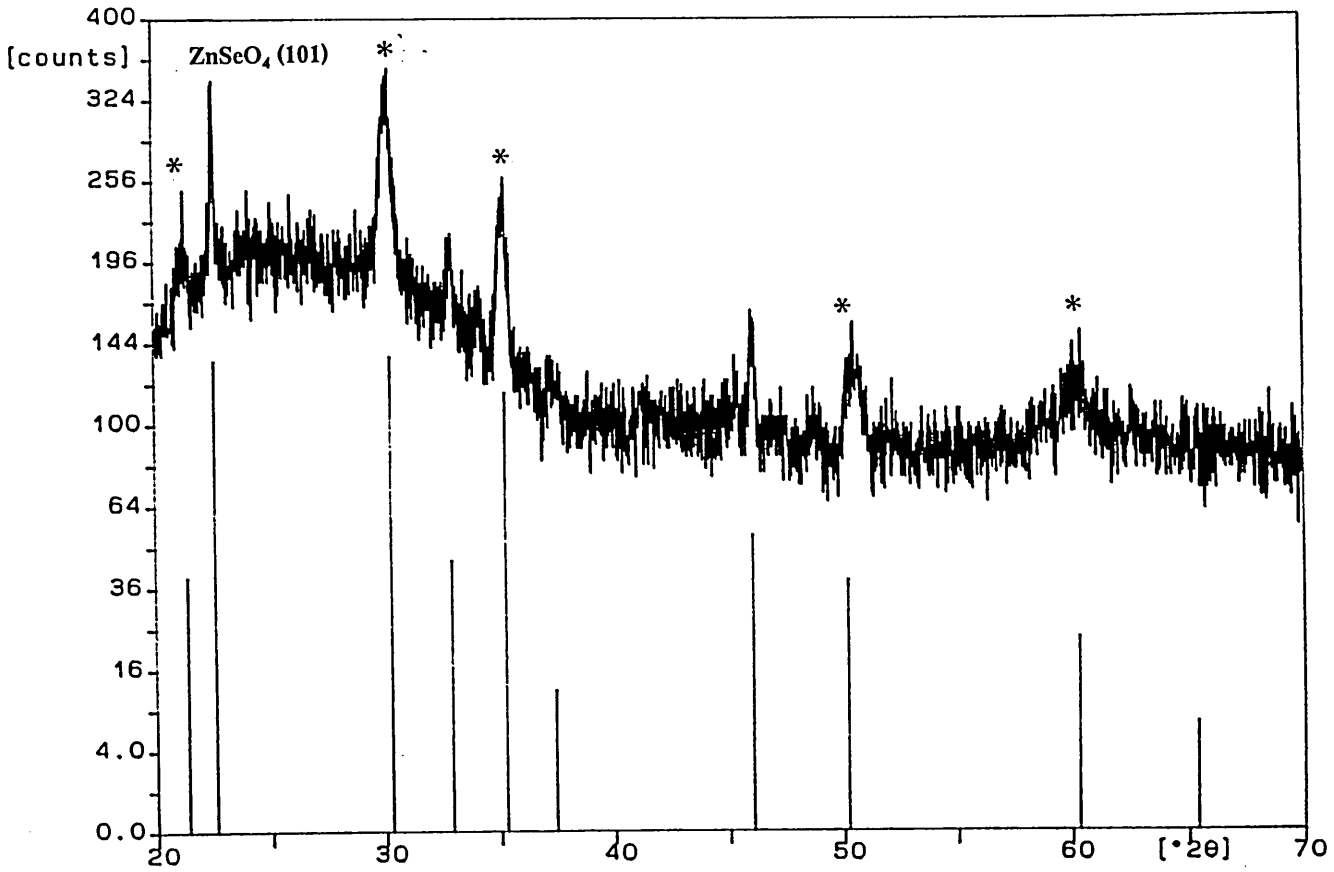

Figure 5.3.4 A typical XRD spectrum for a film which was grown at cathodic voltage -0.60 V. The peak at $2\theta = 22.2°$ is arising from the crystal plane (101) of $ZnSeO_4$ and the peaks marked with * are from ITO surface.

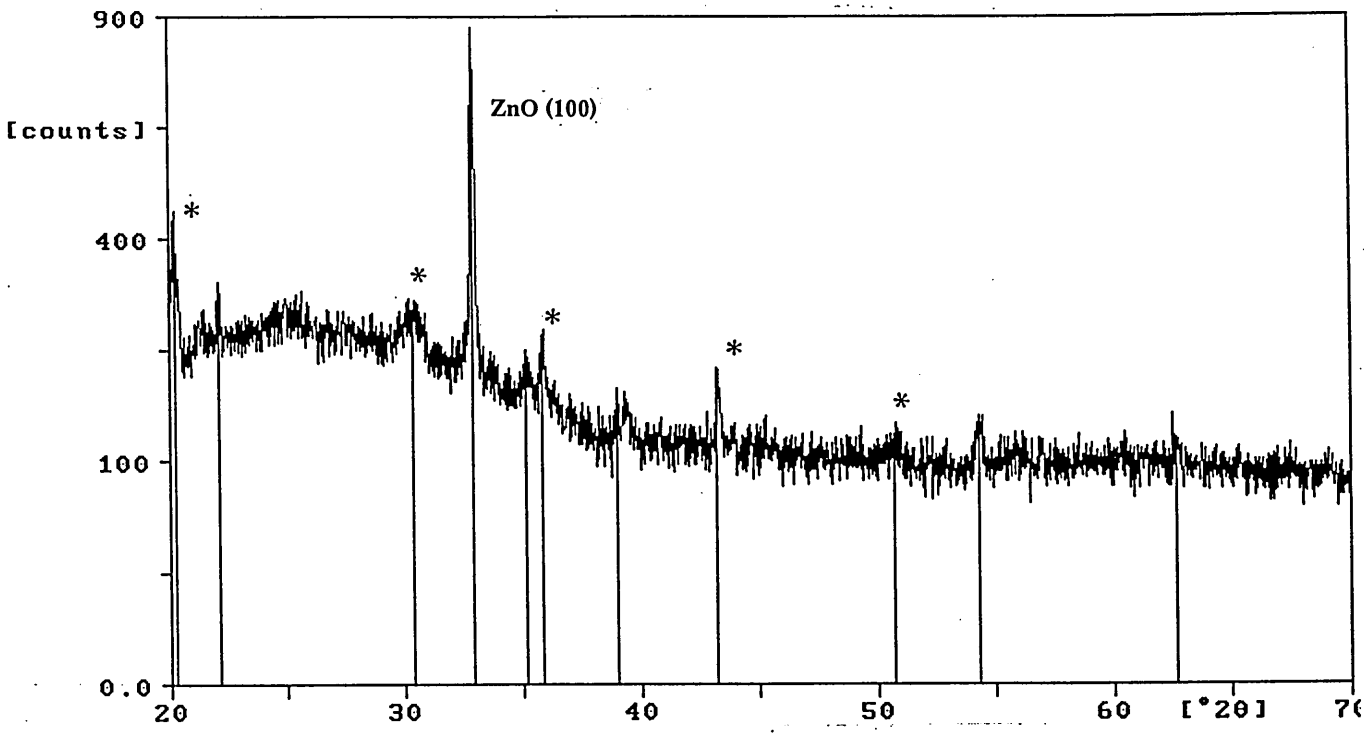

Figure 5.3.5 An XRD spectrum of a sample grown at -0.70 V. The peak at 2θ = 32° is arising from the crystal plane (100) of ZnO.

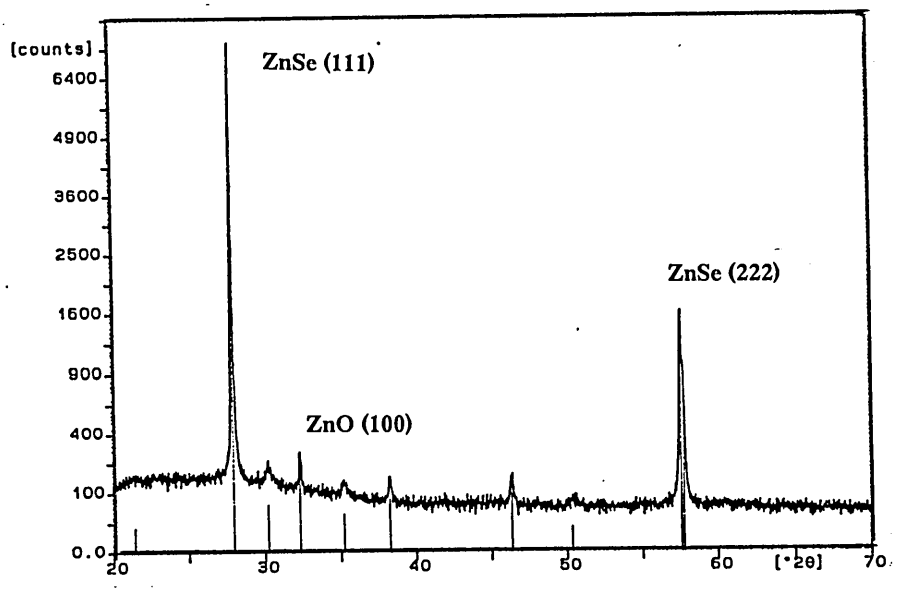

(a)

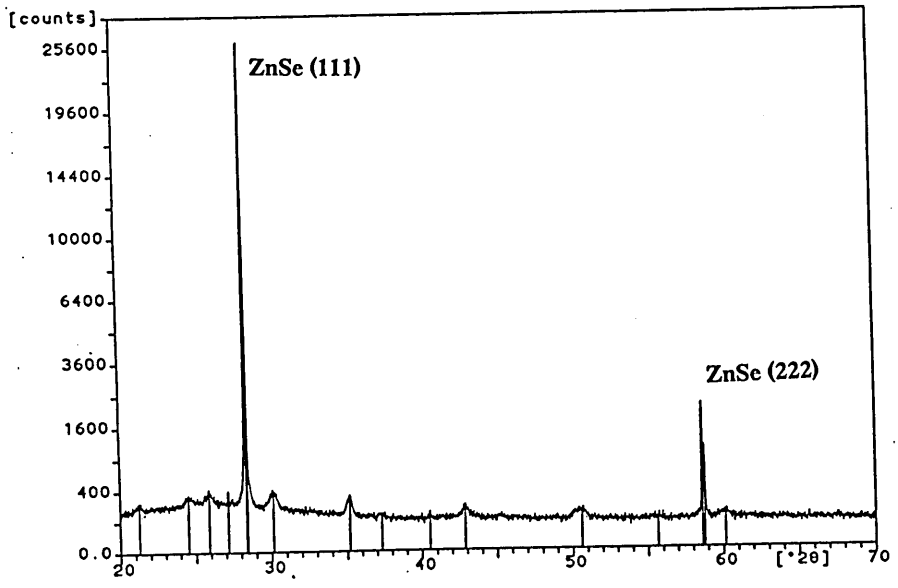

(b)

Figure 5.3.6 (a) A typical spectrum of an unannealed ZnSe sample grown using pure precursors (99.99% $ZnCl_2$ and 99% H_2SeO_3). (b) The same sample after annealed at 250°C for 15 minutes.

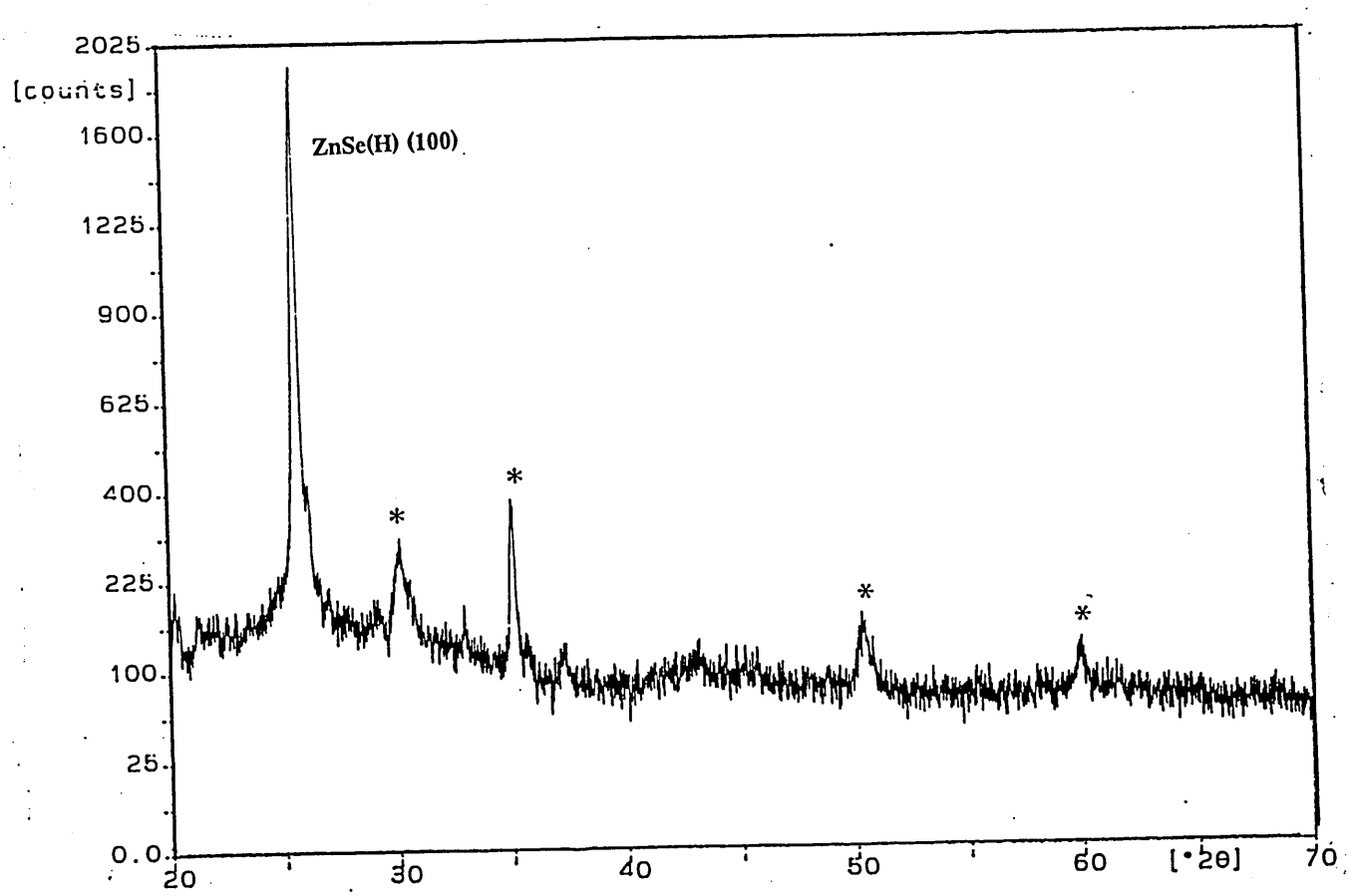

Figure 5.3.7 A spectrum of a sample grown applying a potential -0.78 V. The major peak of the spectrum at 25° is due to the crystal plane (100) of hexagonal ZnSe.

Figure 5.3.6 (a) is a spectrum of a sample grown under the same conditions as those employed for the sample represented by the figure 5.3.3 but with purer starting materials. In comparison to the 98% $ZnCl_2$ and 98% H_2SeO_3 used at the beginning, in this growth, 99.99% $ZnCl_2$ and 99% H_2SeO_3 were used. The substrate peaks are no longer seen in the spectrum of the annealed sample (figure 5.3.6 (b)). Also, an increase in the intensity of (111) peak and an increase in the ratio of the two peaks can be observed after annealing.

A remarkably different result was observed from a film deposited at -0.78 V . As shown in figure 5.3.7, a fairly amorphous structure with (100) peak arising from hexagonal ZnSe can be seen in the spectrum. However, there was no change in the peak intensities after annealing. In all the cases, annealing beyond 250°C caused a decrease in intensities.

5.2.4 SEM and EDAX results

An SEM micrograph of a ZnSe layer annealed at 250°C for 15 minutes with good XRD peaks is shown in figure 5.4.1. Apart from the crystals identified as Zn, Se, Si and KCl, in the EDAX studies no other features such as grain boundaries were seen, as shown in the figure, even after thorough cleaning with acetone and distilled water. Figure 5.4.2 is a micrograph obtained on a similar sample treated with Br_2 in methanol, which has no KCl peaks, but all the other features are similar to the figure 5.4.1. The samples annealed beyond 250°C (figure 5.4.3 a & b) showed cracked surfaces.

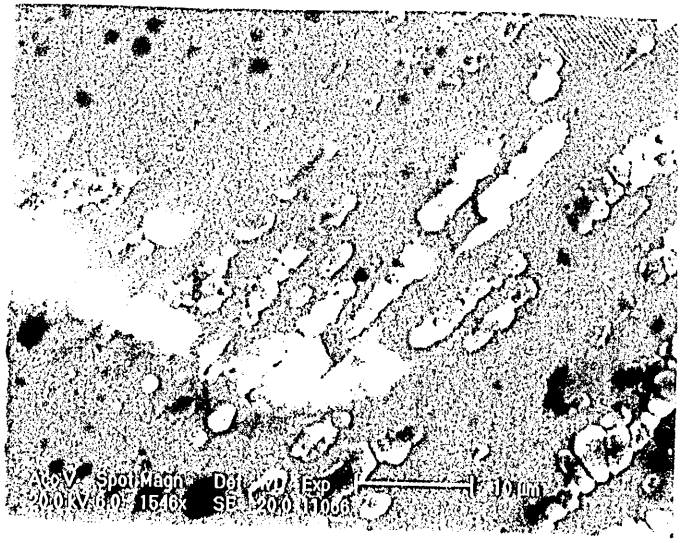

(a)

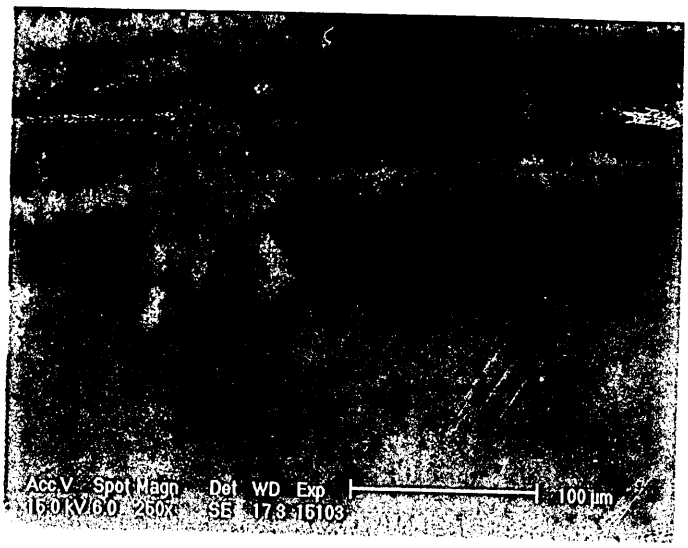

(b)

Figure 5.4.1 Two SEM micrographs of an electrodeposited ZnSe layer (14ZS5S3). Except KCl crystals in (a) and some dust in (b), no any other features such as grain boundaries can be seen.

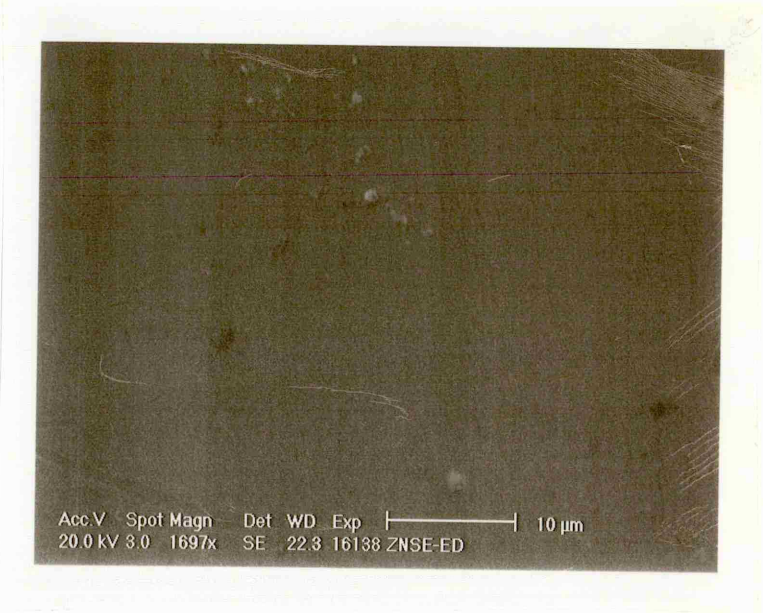

Figure 5.4.2 After Br_2 in ethanol treatment, the layer does not seem to contain KCl crystals and no extra features are found.

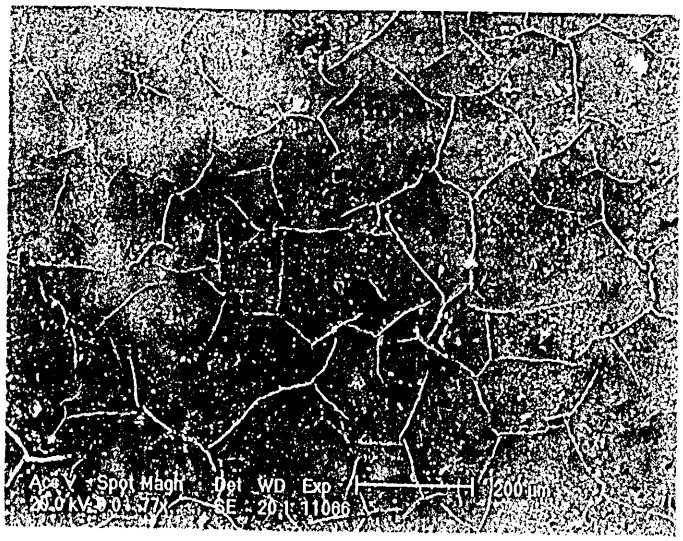

(a)

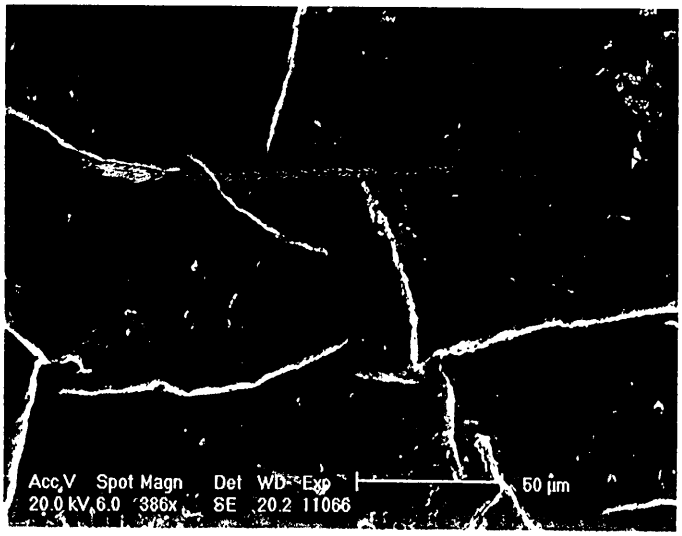

(b)

Figure 5.4.3 A ZnSe layer (21ZS2S3) after annealing at 350°C for 20 minutes. The samples show cracked surfaces in SEM studies.

(a)

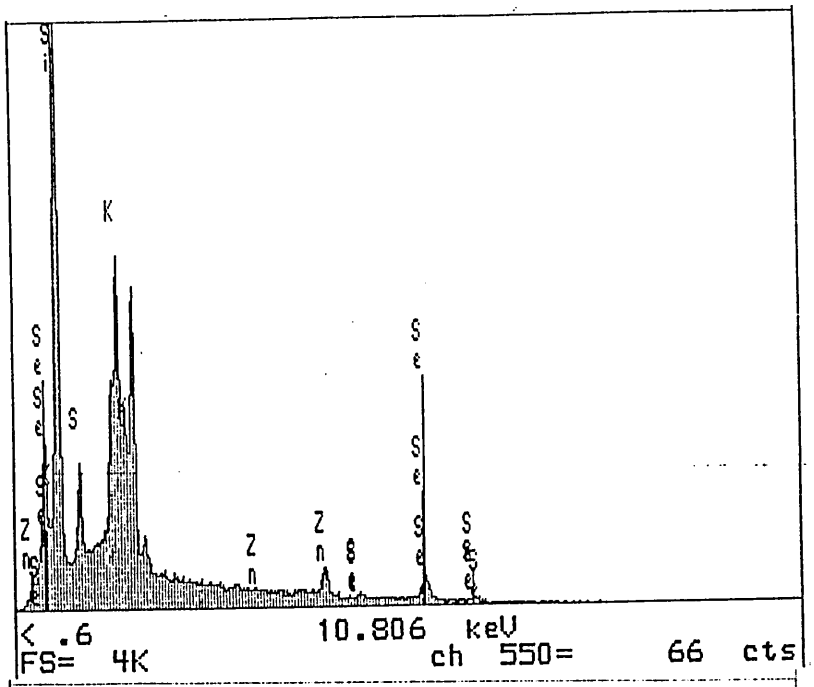

(b)

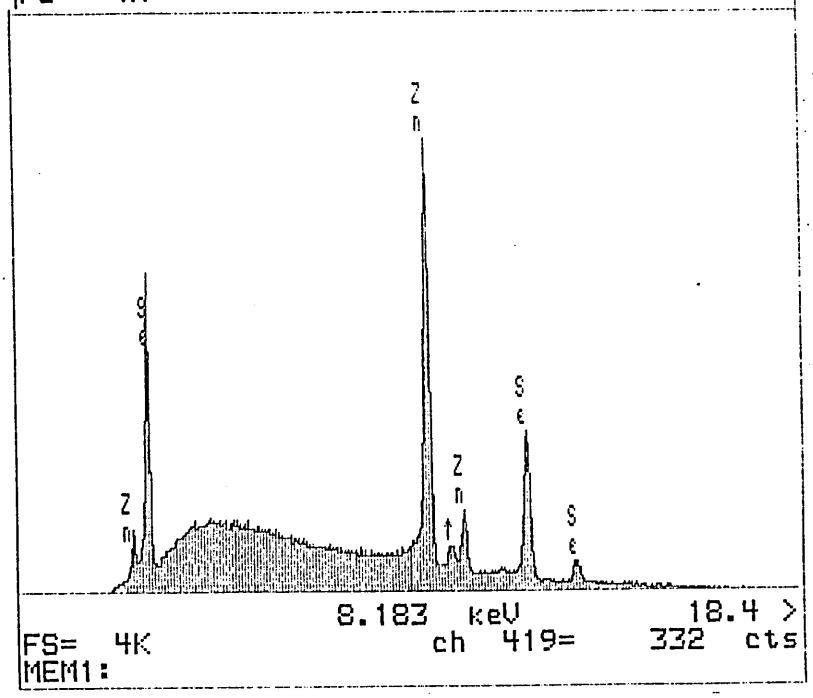

Figure 5.4.4 (a) EDAX spectrum of an electrodeposited ZnSe layer (12ZS1S3) at bias voltage of 20 kV. Zn and Se peaks are less prominent due to more intense peaks of K and Si from the substrate. (b) When the bias voltage was dropped down to 15 kV, the substrate peaks disappeared leaving only Zn and Se peaks in the spectrum. The spectrum is similar to the spectrum of MBE grown ZnSe layers.

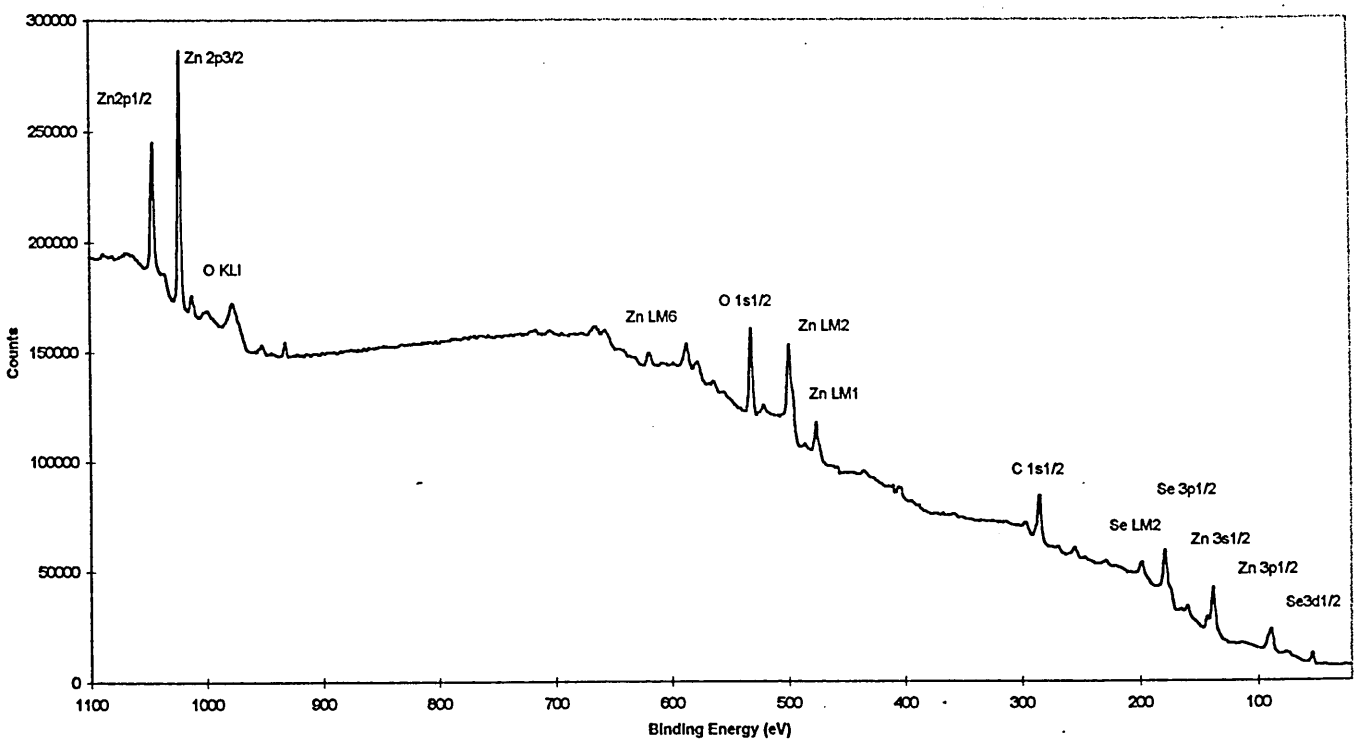

Figure 5.5.1 A typical XPS spectrum of an annealed cubic ZnSe layer. All the peaks are either Zn or Se except the three peaks due to C $1S_{1/2}$, O $1S_{1/2}$ and oxygen Auger emission.

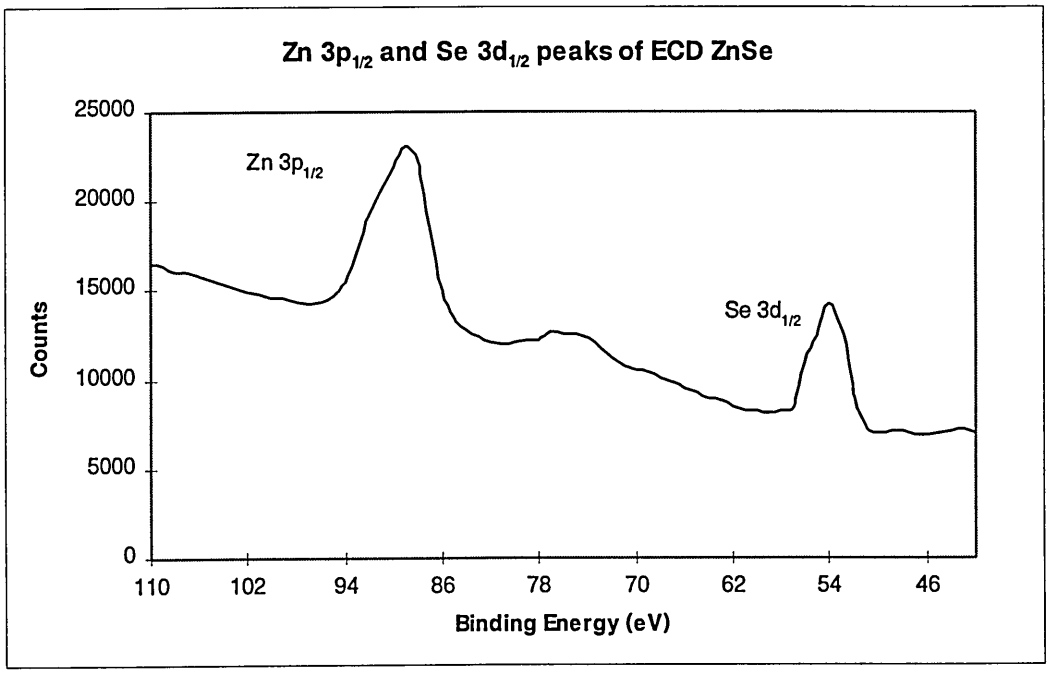

Figure 5.5.2 Qualitative comparison of chemical nature of electrodeposited ZnSe.

The intensity ratio, Zn $3p_{1/2}$:Se $3d_{1/2}$ is 60:40.

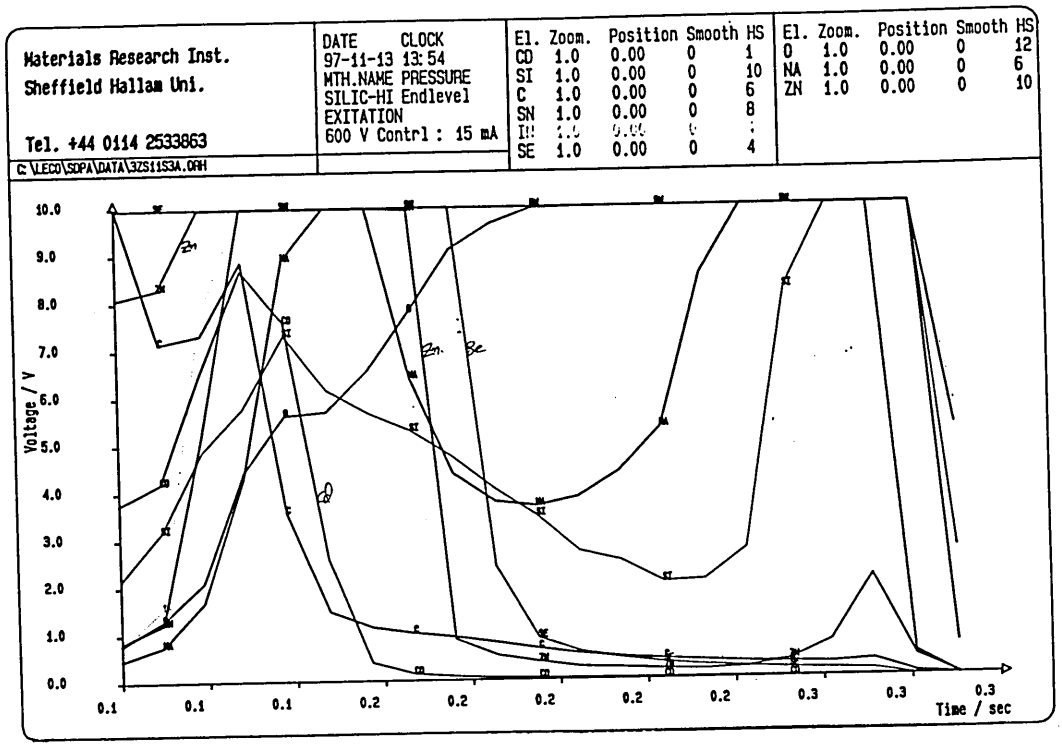

Figure 5.6.1 A GDOES profile of an early stage ZnSe layer electrodeposited in a glass beaker. Apart from Zn and Se signals, the presence of Na and Si in the sample is evident.

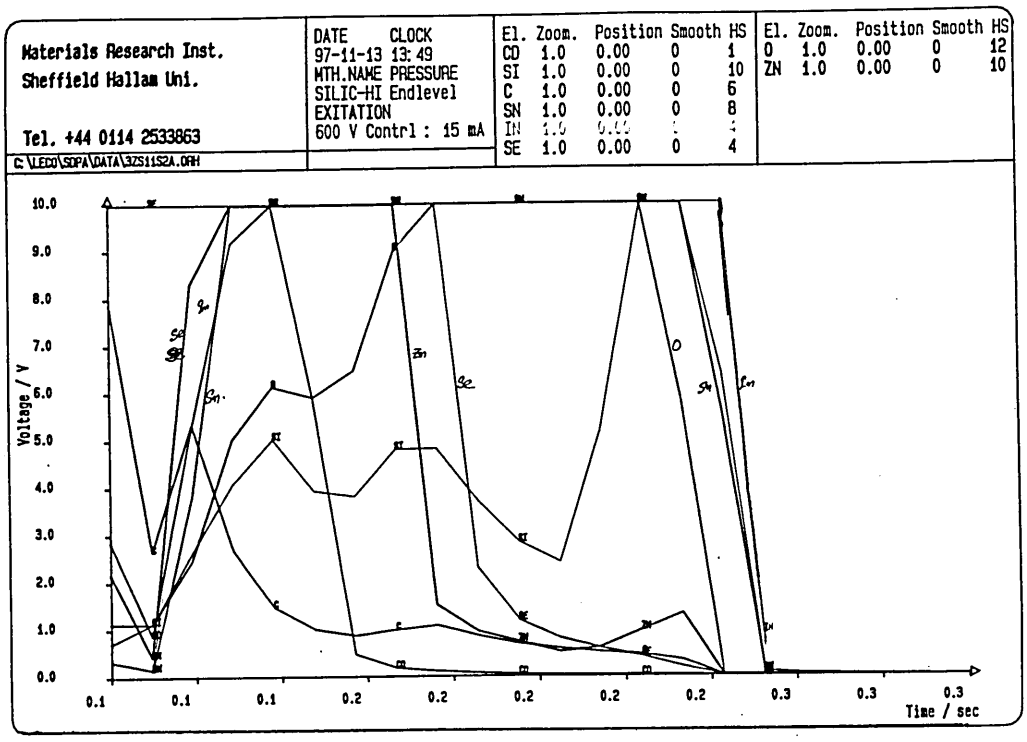

Figure 5.6.2 A GDOES profile of an early stage ZnSe layer electrodeposited in a teflon beaker. Although some Si is still present in the sample, there is no indication of Na in it. .

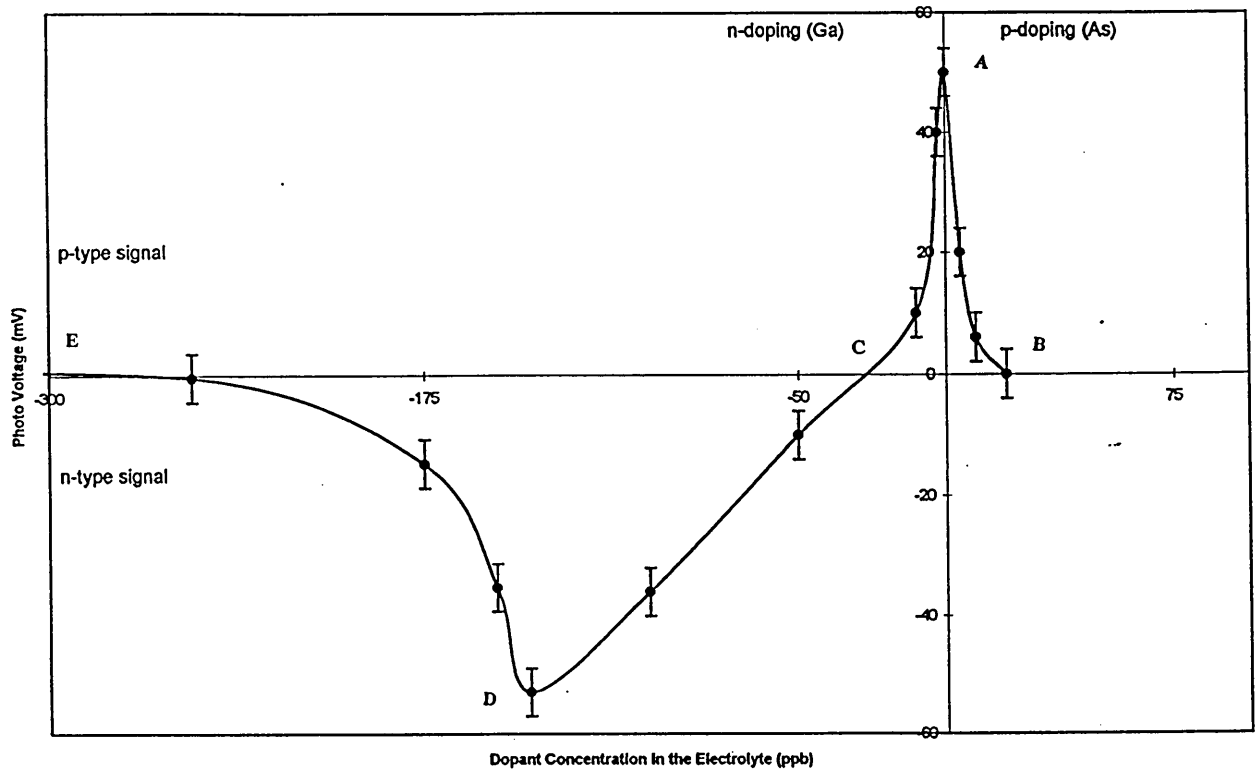

Figure 5.7 The variation of open circuit voltage of the liquid/ZnSe Schottky junction upon illumination. The undoped material is p-type (A) and As doping makes the layer p^+ (AB). Doping with Ga compensates the material first (AC) and then converts it to n-doped (CD). Further doping with Ga makes the layer n^+-doped (DE). All the measurements were done on samples annealed at 200°C for 15 minutes.

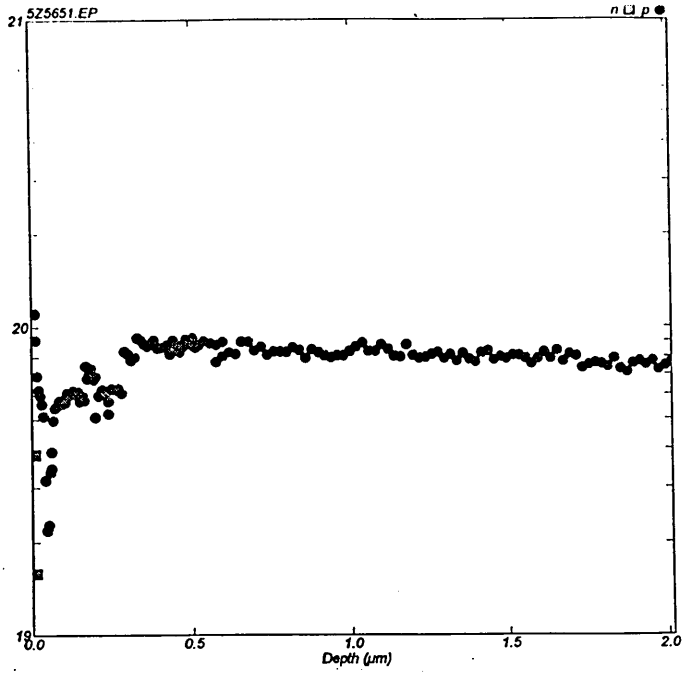

(a) n-type

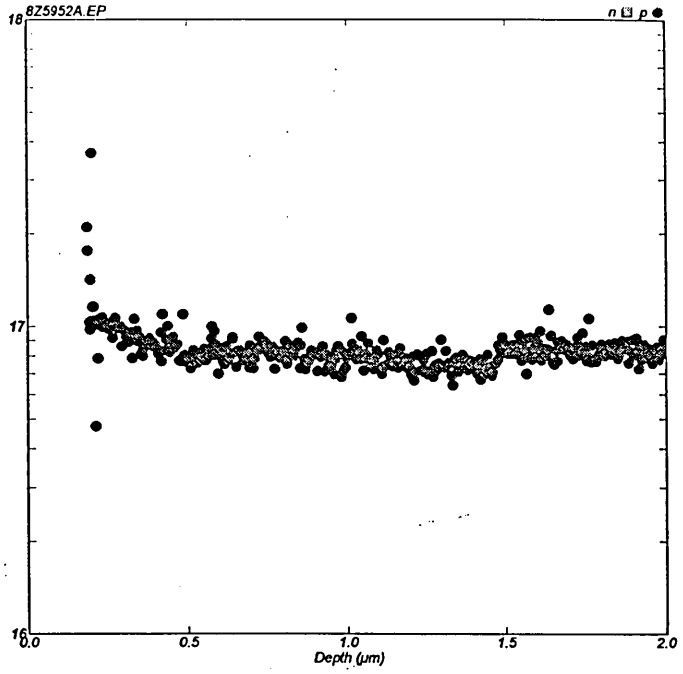

(b) p-type

Figure 5.8 C-V profiles of two electrodeposited ZnSe layers (a) n type sample 5ZS6S1 and (b) p type sample 8ZS9S2A. n- type sample shows a relatively high carrier concentration ($10^{19\pm1}cm^{-3}$) whereas p type sample shows a reasonable carrier concentration for a semiconductor ($10^{17\pm1}cm^{-3}$).

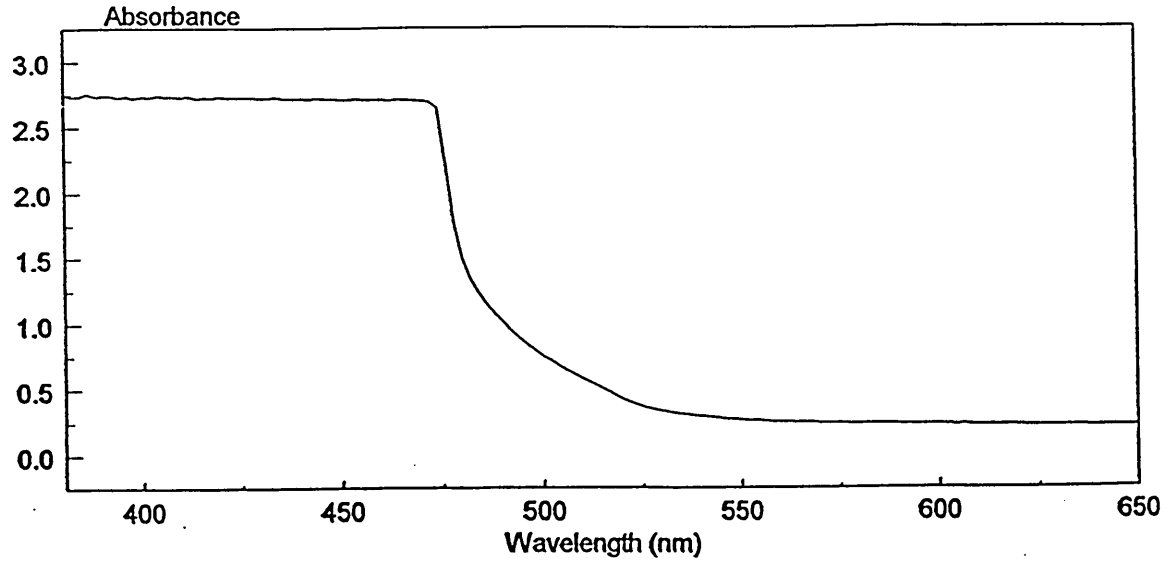

(a)

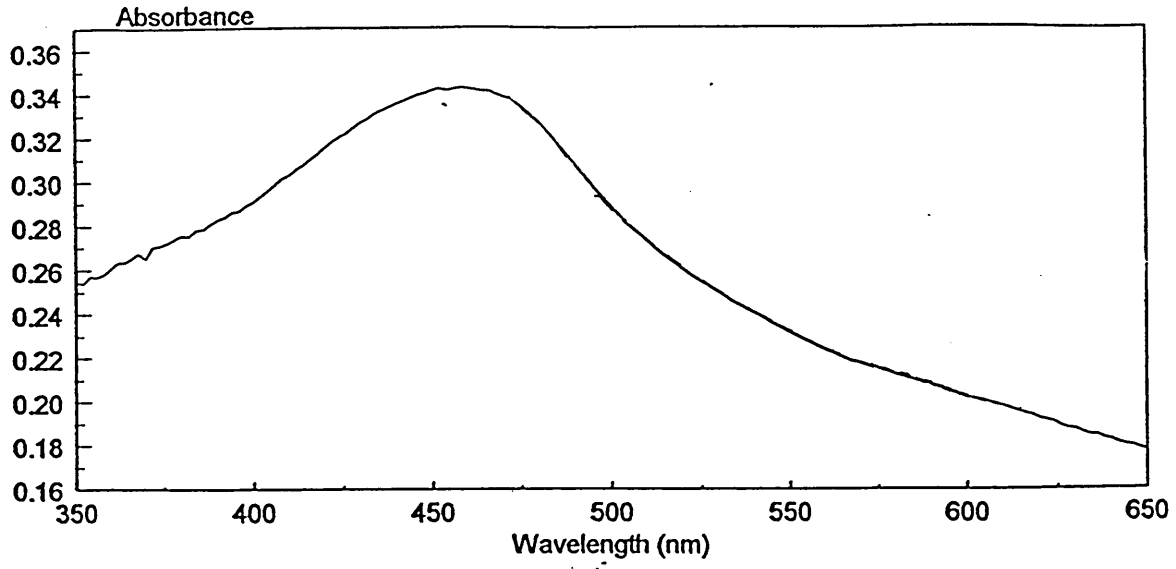

(b)

Figure 5.9 Optical absorption of commercially available (a) ZnSe sample shows a sharp absorption edge at 460 nm indicating the band gap of 2.7 eV. The electrodeposited ZnSe layer (b) has an absorption variation from about 440 nm to about 470 nm.

When the applied voltage was 20 kV, EDAX spectrum [Figures 5.4.4 (a) and (b)] showed large Si peaks, but when the voltage dropped down to 15 kV, the Si peak disappeared leaving only Zn and Se peaks in the spectrum.

5.2.5 XPS results

Electrodeposited samples were left in a vacuum chamber under a pressure of 10^{-6} Torr prior to experiments as the creation of a vacuum was found to be difficult with chemically etched samples due to outgassing. XPS spectra were obtained for heat treated ZnSe layers in the energy range 0-1100 eV. Spectra for electrodeposited ZnSe were almost identical to those for MBE grown samples (figure 5.5.1). Intensities of the peaks and FWHM were the same as those for MBE grown samples. In addition to Zn and Se, only oxygen and carbon peaks appeared in both spectra.

The compositional ratio was determined using $Zn3p_{1/2}$ and Se $3d_{1/2}$ peaks (figure 5.5.2). The two peaks are close enough in terms of energy and only about 40 eV away from each other, so the escape depths of the two elements should be similar. The intensity ratio, $Zn3p_{1/2}$:Se $3d_{1/2}$ is 60:40 and this is similar to Ar etched MBE grown sample whose spectrum is given in figure 4.2 (d).

5.2.6 GDOES results

Preliminary GDOES studies were carried out in order to test the adhesion qualitatively determine the stoichiometry and the elemental distribution within the ZnSe layer. It has been found that the samples were not adhesive enough nor thick enough for the plasma to initiate the profiling process. However, the indications were that apart from Zn and Se, the materials contain Na and Si as well (Figure 5.6.1). This observation led the

experiments to be moved to teflon beakers as glass beakers were the main sources contributing Si and Na to the acidic bath. Figure 5.6.2 shows a GDOES profile of a sample grown in a teflon beaker, which does not contain any Si or Na.

5.2.7 Doping and PEC results

The PEC cell arrangement shown in figure 3.8 was employed to determine the conductivity type of ZnSe layers. A weak KCl or KI solution was used as the electrolyte and a liquid/solid Schottky junction was formed at the KI solution/ZnSe interface.

Table 5.4: Photo-voltage produced at different liquid/solid Schottky junctions during white light illumination.

Material	V_{dark}(mV)	$V_{illumination}$ (mV)	V_{photo} (mV)	conductivity type
ITO	-604	-604	0	metallic
CdS	-308	-390	-082	n-type
n-InP	-252	-460	-208	n-type
n-GaAs	-357	-497	-140	n-type
p-Si	-360	-320	+040	p-type
n-Si	-390	-530	-140	n-type
ECD-ZnSe† (undoped)	-092	-015	+077	p-type
ECD-ZnSe† (undoped)	-469	-423	+046	p-type
ECD-ZnSe* (undoped)	-412	-418	-006	n-type
ECD-ZnSe† (Ga doped)	-765	-822	-057	n-type
ECD-ZnSe† (As doped)	-624	-592	+032	p-type

(† $ZnSO_4$ as the Zn source and * $ZnCl_2$ as the Zn source)

Monitoring of the open circuit voltage produced at this interface, during white light illumination, indicates the conductivity type as described in the section 3.2.6. The cell was calibrated using standard n- and p-type semiconductors prior to each measurement.

The data presented in table 5.4 clearly identifies the type of electrical conductivity for the samples.

As deposited ZnSe layers were almost always p-type provided $ZnSO_4$ was used as the Zn source. When $ZnCl_2$ was used as the Zn source, the samples showed n-type conductivity. However $ZnSO_4$ was used in most of the experiments as it was more controllable in comparison with $ZnCl_2$. Adding Ga^{2+} ions into the deposition bath converts the conductivity type into n- whereas As^{2-} doping makes the sample p-type as shown in the table. Figure 5.7 shows the variation of the PEC signal (open circuit voltage) as a function of doping of the material.The x-axis of figure 5.7 shows the amount of dopant added to the electrolyte in ppb level and this quantity is used only as a guide for doping. However, the amounts incorporated in the material can vary according to the electrochemical conditions used. Undoped materials indicate p-type conductivity ($ZnSO_4$ was the Zn precursor) showing ~50 mV as shown in the figure which is the optimum p-type conductivity found in the experiment. Doping with Ga made the sample n type with an optimum value at the doping level of ~150 ppb level, whereas doping with As showed a further p-type conductivity and when the doping level was about 75 ppb level, it showed almost no photo signal due to the production of p^+-material.

5.2.8 C-V profiling results

Selected samples were sent to Heriot-Watt University to do C-V profiling studies on them. Figure 5.8 (a) and (b) show the profiles of two samples n-type (5ZS6S1) and p-type (8ZS9S2A). The n-type layer shows a high carrier concentration, which is about $9 \times 10^{19\pm1}$ cm^{-3} whereas p-type sample shows a reasonable charge carrier

concentration for a semiconductor, $10^{17\pm1}$ cm^{-3}. In these studies, $NaOH+Na_2S_2O_3$ solution had been used as the electrolyte in the measurements.

The studies had been done without calibrating the depth scale, thus the thickness in the figure could not be estimated accurately. However, the samples were estimated to be of the thickness 0.3 μm from the growth parameters.

5.2.9 Optical absorption results

The band gap of the semiconducting ZnSe layers were studied using an optical absorption technique. A typical optical absorption spectrum of an annealed ZnSe sample, is shown in figure 5.9 (b). All these samples showed ZnSe peaks in XRD and XPS spectra confirming the layers consisted of ZnSe. A considerably high absorption occurs at ~460 nm, corresponding to the band gap of ZnSe, which is 2.7 eV. The commercially available single crystal ZnSe (3 mm thick) shows a sharp abrupt absorption at 460 nm (figure 5.9 (a)) for comparison. The electrodeposited samples did not show any distinguishable absorption for the samples deposited using chemicals with less purity in the early stage of the project. Only those deposited with high purity material shows a reasonably high absorption at 450 nm. It should be noted that difficulties arose in absorption measurements from these layers (~ 0.3 μm) when compared to thick samples (~ 3 mm).

5.2.10 Discussion of electrodeposition of ZnSe

It has been reported that the electrodeposition of ZnSe at room temperature is amorphous and for crystalline layers, the deposition has to be done at high temperatures, Natarajan et al (1994). This is to overcome the kinetic barrier from the sources to the

product ZnSe. The deposition at low temperature (close to RT) was found to be difficult on ITO/glass electrodes but the high temperature (60°C-80°C) deposition seem to work well with ZnSe. Cu electrodes started to react in the acidic medium at all temperatures and the deposit was always dark in colour. This deposit may be CuO formed evolving H_2 in an acidic medium.

$$Cu + H_2O \rightarrow CuO + H_2 \qquad [5.1]$$

Ti substrate showed various peaks at different temperatures and different potentials in XRD spectra but none of the peaks were ZnSe. An ITO/glass substrate was found to be appropriate for the electrodeposition of compounds such as ZnSe.

As described by KrÖger, Zn is the potential determining species for all possible compositions of Se in the deposit. Nobler species Se and less noble species Zn can be co-deposited, if the electrolyte contains Se at a low concentration and Zn at a high concentration. The equation 3.2 (a) is not in fact a straight forward reaction, even though it represents the formation of Se^0.

$$H_2SeO_3 + 4H^+ + 4e^- \rightarrow Se^0 + 3H_2O. \quad \text{at } 0.546 \text{ V} \qquad [3.2\ (a)]$$

Initially H_2SeO_3 reacts with H^+ ions to form positive ions of $HSeO^{2+}$. These ions then reacts and discharge to form Se^0 at the cathode-electrolyte interface.

$$H_2SeO_3 + H^+ \rightarrow HSeO_2^+ + H_2O \qquad [5.2\ (a)]$$

$$HSeO_2^+ + 3H^+ + 4e^- \rightarrow Se^0 + 2H_2O \qquad [5.2\ (b)]$$

The equation 3.2 (a) represents both of these reactions. For only under the conditions mentioned above, is it possible to reduce the concentration of $HSeO_2^+$ ions relative to that of Zn^{2+} ions at the cathode-electrolyte interface and make co-deposition of ZnSe possible. For this reason, ZnSe deposition was observed only when the Zn:Se concentration ratio was $0.1:10^{-5}$ (table 5.1).

The cyclic voltammogram (figure 5.1 and 5.2) can be explained in the same way as KrÖger, who in 1978 described such a diagram for a general MX compound. As shown in figure 5.1, deposition of Se can be expected at low electrode potentials. The gradual increase of the current until the voltage was about -0.4 volts should therefore represent the deposition of Se. Applying a potential to the cathode more positive than that which is required to deposit Zn in the absence of Se, prefers to deposit Se. The deposit may vary from Se to Zn as the cathodic applied voltage is increased. At more negative potentials than that which would be required to deposit Se in the absence of Zn, will prefer to deposit Zn. In the intermediate voltages, Zn_rSe_s would deposit with r=s=1 at a particular voltage. The deposition of Se would result in reducing the concentration and activity of the $HSeO_2^+$ species in the electrolyte. As the activity E_X^{n+} as described in section 1.7.2, is gradually reduced a plateau region is reached where ZnSe deposits. The plateau region -0.5 V to -0.6 V in figure 5.1 would therefore be the deposition potential region for ZnSe, which is a shining yellow coloured deposit as mentioned in table 5.1. According to this explanation, reddish films deposited at more positive voltages than -0.5 V as given in table 5.1 should be Se.

A sharp increase of the current occurs as the potential increases towards the standard potential of Zn, indicating the deposition of Zn. This is highly possible due to the very

high concentration of Zn^{2+} in the electrolyte. The dark films deposited at higher negative voltages as mentioned in table 5.1 can be suggested as a mixture of amorphous Zn and polycrystalline ZnO as there were ZnO peaks in the XRD spectra of such films deposited at -0.7 V (figure 5.3.5). It can further be suggested that the deposition of ZnO occurs at relatively higher negative potentials with hydrogen evolution.

$$Zn^{2+} + H_2O + 2e^- \rightarrow ZnO + H_2 \qquad [5.3]$$

The figure 5.2 shows the deposition of Zn or ZnO at higher negative potentials According to the Pourbaix diagram, Zn is stable at higher voltages as the standard potential of Zn in the absence of Se is -0.760 V with respect to standard hydrogen electrode. Underpotential deposition of ZnO is possible, as it has been predicted in the literature even though Zn^{2+} ions are stable in the electrolyte only at high positive potentials, as shown in the Pourbaix diagram.

In the figure 5.2, in the reverse sweep, the deposition process becomes unstable and the deposited Zn would begin to strip off giving rise to a reverse current in the circuit.

The optimised voltage of -0.54 V was found to be the best deposition voltage for ZnSe in an aqueous medium together with the other conditions of 65°C as the temperature, 2.25 as pH value and $0.1:10^{-5}$ as the Zn:Se concentration ratio. The reactions for the deposition of ZnSe are given in section 3.1.1

$$H_2SeO_3 + 4H^+ + 4e^- \rightarrow Se^0 + 3H_2O. \quad \text{at } 0.54 \text{ V} \qquad [3.2\ (a)]$$

$$Zn^{2+} + 2e^- \rightarrow Zn^0 \qquad \text{at } -0.96 \text{ V} \qquad [3.2\ (b)]$$

$$Zn^0 + Se^0 \rightarrow ZnSe \qquad [3.2]$$

As described in section 1.7.2, the reduction of the less noble component, Zn^{2+}, well above its standard potential or the formation of ZnSe even when there is a large difference in standard potentials of Zn ($E_{Zn}° = -0.760$ V vs SHE) and Se ($E_{Se}° = 0.403$ V vs SHE), is made possible due to the gain in free energy upon compound formation as given in the equation 1.10.

$$\Delta G = -nFE \qquad [1.10]$$

The standard free energy change ($\Delta G°$) in the formation of ZnSe is -163 $kJmol^{-1}$, Mishra and Rajeshwar (1989), which gives a value -0.28 V for the standard deposition potential of ZnSe with respect to the standard hydrogen electrode (SHE). The non-standard deposition potential under normal laboratory conditions can be calculated using equations 1.1 and 1.2. The potential at which ZnSe was deposited was -0.54 V with respect to the Ag/AgCl reference electrode whose potential with respect to SHE is given by equation 1.9,

$$E_{Ag/AgCl} = 0.1969 + \left(\frac{2.303RT}{F}\right)pH \qquad [1.9]$$

which is 0.22369 V at 65°C and pH of 2.25, which were the conditions that ZnSe was deposited.

The deposition of ZnSe at high negative potentials, -0.78 V in this work, as evidenced in XRD studies (figure 5.3.7), is suggested in the literature, Natarajan et al (1994). At sufficiently negative potentials, instead of the above reactions, the formation of a soluble compound H_2Se (at -0.6 V with respect to SHE) can be expected. This soluble compound can then react with Zn^{2+} leading to the precipitation of ZnSe.

$$Se + 2e^- + 2H^+ \rightarrow H_2Se\ (aq) \qquad \text{at -0.6 V} \qquad [5.4\ (a)]$$

$$Zn^{2+} + H_2Se \rightarrow ZnSe + 2H^+ \qquad \text{at -0.78 V} \qquad [5.4\ (b)]$$

At the same time, H_2Se may react with the acidic medium and form elemental Se.

$$2H_2Se + H_2SeO_3 \rightarrow 3Se + 3H_2O \qquad [5.5]$$

This ZnSe layer is loosely bound to the substrate and is incorporated with Se. Hence the XRD spectrum shows an amorphous hump and no improvement even after annealing. H_2Se can be expected to react with elemental Zn to form $ZnSeO_4$ as discovered in XRD analysis (figure 5.3.4). The deposition at -0.6 V, which showed $ZnSeO_4$ peaks in figure 5.3.4, can be suggested to take place via the reaction 5.6.

$$H_2Se + Zn + 4H_2O \rightarrow ZnSeO_4 + 5H_2 \qquad [5.6]$$

The thin films were found to be of cubic zinc blende structure whose close packing direction is (111). The two main peaks which appear in the XRD spectra shown in the figures 5.33 (a), 5.33 (b), 5.36 (a) and 5.36 (b) are (111) and (222) of cubic zinc blende ZnSe. The substrate peaks which appear in the spectra are mainly due to low film

thickness and the high power applied in the experiments, which was 1.6 kW (40 kV x 40 mA). Application of a lower power would have reduced the X-Ray penetration depth reducing the intensities of substrate peaks. However, the substrate peaks were not seen in the spectrum (figure 5.3.6 (b)) of the annealed sample grown with high purity chemicals. In addition to the power, the impurities, which would have been in ppb levels in the sample, seem to destroy the preferential orientation of the film. Annealing may increase the intensities of the material peaks making relatively low intensive ITO peaks less visible in the figure 5.3.6 (a).

The XPS spectrum (figure 5.5.1) indicates that the electrodeposited ZnSe layer is of good quality as it is almost identical to the spectrum of the MBE grown sample. The stoichiometry of the sample was found to be Zn:Se = 60:40, using the two peaks $Zn3p_{1/2}$ and Se $3d_{1/2}$ which are close enough in terms of energy and only 36 eV away from each other, indicating similar escape depths. The stoichiometric ratio was similar to that of MBE grown material, as shown in figure 4.2 (d). Even though $Zn3p_{1/2}$ and Se $3d_{1/2}$ have only about 36 eV gap between them, this energy difference may have produced a difference in the calculation of stoichiometric ratio.

FWHM of the (111) peak of ZnSe spectrum is ~ 0.06°, which indicates the grain size of 260 nm as calculated using Scherrer formula. However, the grain boundaries could not be seen in the SEM micrographs even after Br_2/methanol etching. It can be suggested that the reason for this observation is the existence of a Se overlayer on top of the ZnSe layer. Even the Br_2/methanol treatment might not be strong enough to remove the layer if it is in the form of an oxide. KCl crystals found on the surface in SEM studies should be in a very low concentration in the samples. KCl is the electrolytic solution in

the Ag/AgCl reference electrode, which has a porous wall open to the electrolyte. The small atomic percentage of KCl may leak out in to the electrolyte through this porous wall and may eventually deposit on the thin layer. This process is highly possible as the deposition of ZnSe is usually done over a long duration. However, KCl is not adhesive to the thin layer and it can easily be dissolved in a weak acidic solution (diluted Br_2/methanol solution) or in acetone or perhaps using some hot water. Si which appeared in the EDAX spectra was assumed to be an impurity source from the beaker at the beginning but later it was realised that it is a result of X-rays penetrating through the sample and picking Si from the substrate. Thus the power input was reduced to 15 kV from 20 kV and the Si peak disappeared. However, a small percentage of Si can be added to the electrolyte from the glass beaker. Although the detection of this Si is not possible using EDAX technique, GDOES profiling indicates the presence of Si in the ZnSe layer. In fact, GDOES not only showed the existence of a low concentration of Si, but showed the existence of Na as well, which again is an impurity added by the glass beaker. Nevertheless, these impurities may exist in negligible amounts, as the substrate is a glass which is kept in the acidic beaker for a long period during the deposition. This amount may be too small to be detected by these techniques but may drastically affect electrical properties.

The second observation from GDOES profiling is the poor adhesion of the sample to the substrate. This may either be a result of the very thin layer (~ 0.3 μm) or lack of cleanliness of the substrate.

The C-V profiling done by the group at Heriot-Watt University on the electrodeposited samples, whose thickness were about 0.3 μm, are shown in figures 5.8 (a) and 5.8 (b).

The carrier concentration of the p-type layer, which is about $\sim 10^{17\pm1} cm^{-3}$ indicates the success of As doping whereas the Ga doped n-type shows a higher value for the carrier concentration, which is $\sim 9 \times 10^{19\pm1}$ cm^{-3}. These results are for materials grown at early stages, but the indications from this preliminary C-V profiling results are encouraging.

Although doping of ZnSe has been a difficult task for decades, electrochemically grown ZnSe appears to be easily controllable. The data presented in table 5.4 shows that as deposited layers were p-type if $ZnSO_4$ was used as the Zn source and they were n-type if $ZnCl_2$ was used as the Zn source. Incorporation of group VII chlorine atoms within the ZnSe lattice in ppb levels can be suggested for the n-type behaviour when $ZnCl_2$ is used in the deposition bath. However, the growth utilising $ZnCl_2$ is less controllable compared to the growth utilising $ZnSO_4$. The stability is such that the photovoltage lies within 50 and 70 mV for all undoped, Ga doped or As doped ZnSe grown utilising $ZnSO_4$ as the Zn precursor, whereas the photovoltaic signal varied from about 10 mV to 147 mV.

Further table 5.4 shows that the Ga doped ZnSe is n-type whereas, the As doped layers are p-type. This behaviour could be expected as Ga is a group III element and As is a group V element. When doped with Ga or As, Zn atoms may be replaced by Ga in ppb levels converting ZnSe into n-type and similarly, Se may be replaced by As in ppb levels making it a p-type semiconductor. As shown in figure 5.7, As doping increase the conductivity of the p-type sample and drops down the PEC signal to zero due to p^+-doping. This would result in thinning the depletion layer of the liquid/solid junction reducing the open circuit voltage as shown by the curve AB. When the doping level was about 20 ppb levels, there was almost no signal in the circuit, meaning a highly

conducting structure. Ga doping first compensates the material to produce an insulating layer and the conductivity reaches its optimum value when the doping level in the bath is about 150 ppb level.Further addition of Ga produces n^+-ZnSe making the PEC signal zero again. Addition of $Ga_2(SO_4)_3$ into the electrolyte reduces the p-signal due to compensation and when the doping level was 40 ppb (C), the signal was zero again meaning fully compensated, insulating material. Further doping increases the n-type conductivity due to having appropriate doping suitable for Schottky type devices and when the doping level was 150 ppb (D), the n-signal showed an optimum value. The photo-voltage however went on decreasing for doping of over 150 ppb levels, due to heavy n-doping causing the depletion region to diminish (DE). This demonstrates the possibility of doping ZnSe to both n- and p-types. This flexible behaviour of ZnSe indicates the presence of low background impurities in ECD-ZnSe layers. The as grown material did not show any photo response and the sample showed a signal only after annealing at 250°C for 15 minutes. As observed from XRD results, annealing improves the crystallinity hence it improves the photo-voltage. It must be noted that post annealing of electrodeposited samples is an essential step for improved electrical and optical properties.

As shown in figure 5.9 (a), the single crystal ZnSe sample, which is about 3 mm thick shows a clear absorption edge at 460 nm which corresponds to 2.7 eV, the accepted band gap of ZnSe, whereas the electrodeposited layers have a gradual change in absorption with a maximum at ~460 nm. The gradual change in absorption of the electrodeposited layer can be due to the presence of impurity levels within the band gap and the gradual fall of the absorption below 460 nm in the spectrum [figure 5.20 (a)] may be due to photoluminescence of the material. However, it has been found utilising

the other techniques that these samples are of low impurity concentrations. Therefore it can be suggested that the gradual change in absorption may be due to the very small layer thickness which is ~ 0.3 mm in comparison with 3 mm of the commercial sample.

5.3 Electrodeposition of thin CdSe layers

The three electrode cell which consisted of a cathode, Pt or C anode and Ag/AgCl reference electrode was used for deposition of CdSe. This set up was almost same to the set up used for ZnSe deposition. Electrodeposition of CdSe in an aqueous electrolytic medium has been reported by several other groups in the past. Among them are, Mishra and Rajeshwar in (1989) who employed a Cd:Se ratio $0.01:4x10^{-3}$.

$CdSO_4$ was used as the Cd source in the electrolyte and SeO_2 or H_2SeO_3 as the Se source. The pH was set to 2.5 and the temperature to 65°C. Pourbaix diagram [figure 3.1 (b)] and cyclic voltammograms were used to determine the deposition potential. Chemicals used were analytical grade at the beginning but 99% pure $CdSO_4$ and 99.99% pure H_2SeO_3 were used in the end. The pH value was adjusted using diluted H_2SO_4, to have the values between 2 and 3. The deposition was a success in the range pH = 2-3.

5.3.1 Cyclic voltammometry

Cyclic voltammograms were obtained to determine the most suitable deposition voltage range. Figures 5.10 (a) and (b) show a slow and a fast scan of a typical voltammogram for the deposition of CdSe. A cathodic current onset at -0.3 V and -0.75 V and a plateau region between them and an anodic peak at potential -0.70 V were observed.

5.3.2 XRD results

The layers which were electrodeposited at high negative (-0.60 to -0.70 V) potentials showed ITO peaks, Se peaks and all the peaks relevant to polycrystalline CdSe in almost all spectra [figure 5.11.1 (a)]. The spectra of annealed samples at 350°C for 15 minutes contained only those peaks which correspond to hexagonal CdSe with exact matchings to standard PDF data [figure 5.11.1 (b)]. The drop in negative deposition voltage and careful purification of the electrolyte system turned the hexagonal layer into a highly preferentially oriented cubic CdSe layer in (111) direction [figure 5.11.2 (a)]. The annealing at 400° for 40 minutes sharpened the (111) peak leading to a FWHM value of 0.05° [figure 5.11.2 (b)].

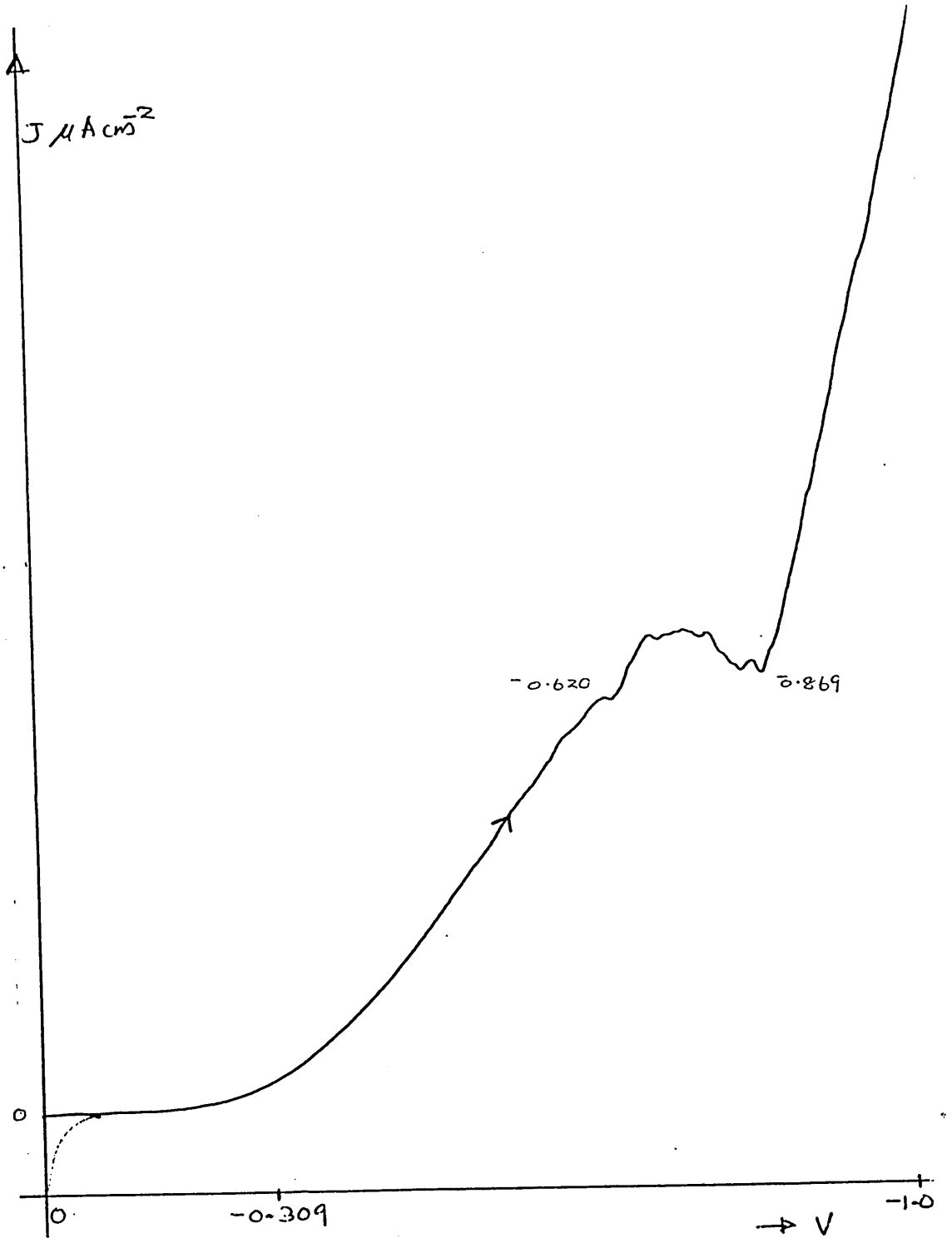

Figure 5.10 (a) A typical cyclic voltammogram for the electrodeposition of CdSe. Only a slow (50 mV/s) forward sweep showing the CdSe deposition region which is -0.62 V to -0.869 V.

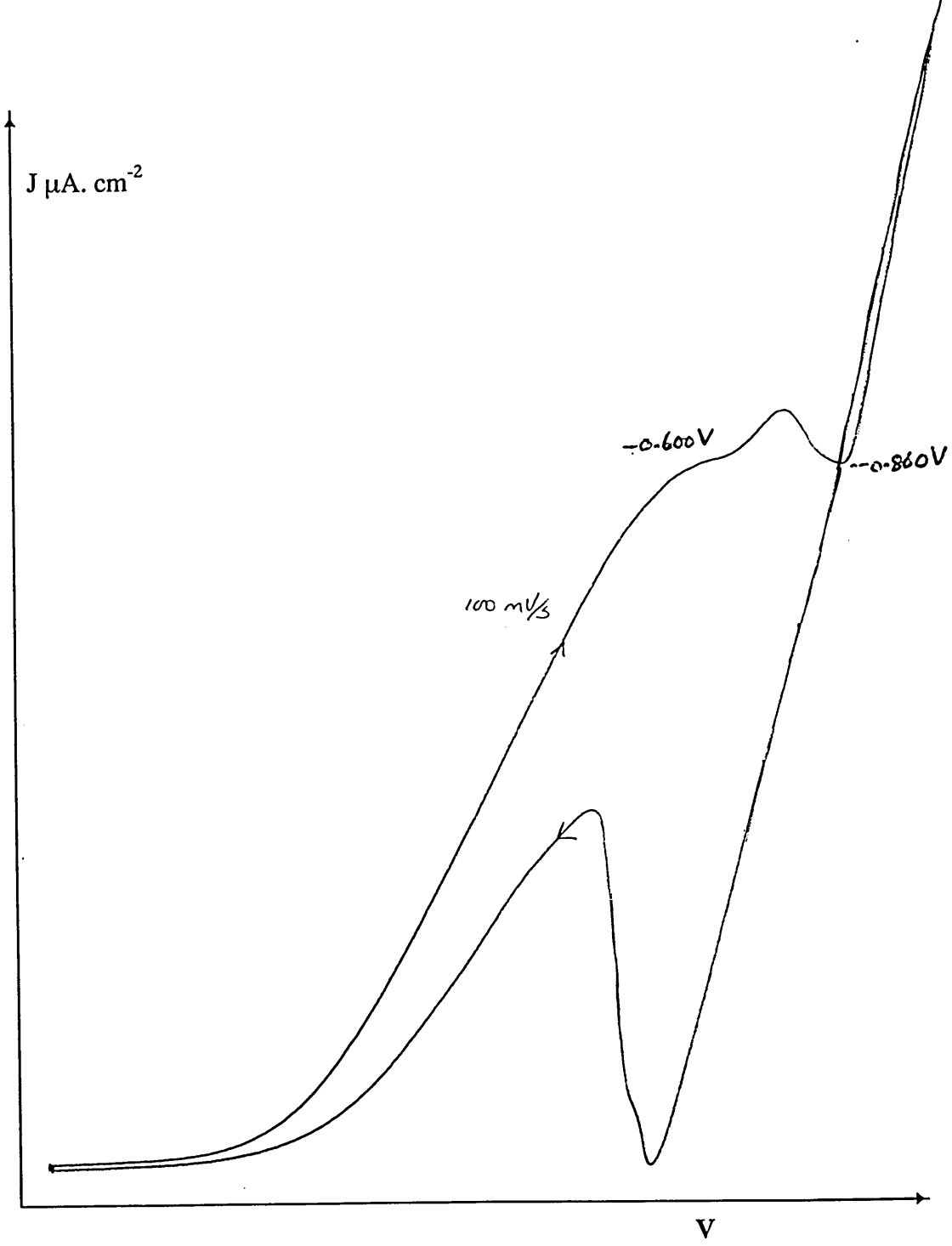

Figure 5.10 (b) Cyclic voltammograms for the electrodeposition of CdSe. A fast scanned (100 mV/s) complete cycle . The onset of cathodic currents above -0.6 V and below -0.86 V indicate the deposition of Se and Cd respectively. The anodic wave in the reverse sweep indicates the corrosion of unstable Cd deposited at more negative potentials in the forward scan.

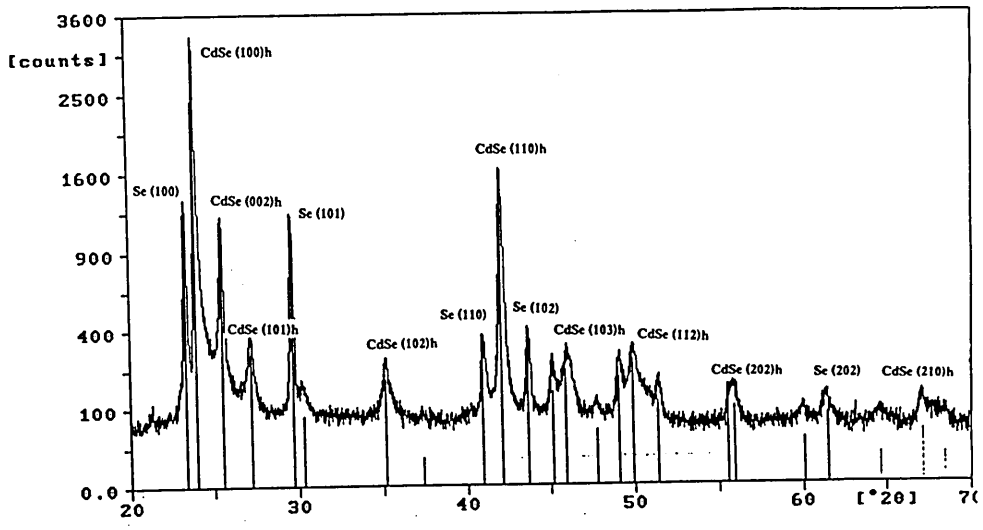

(a)

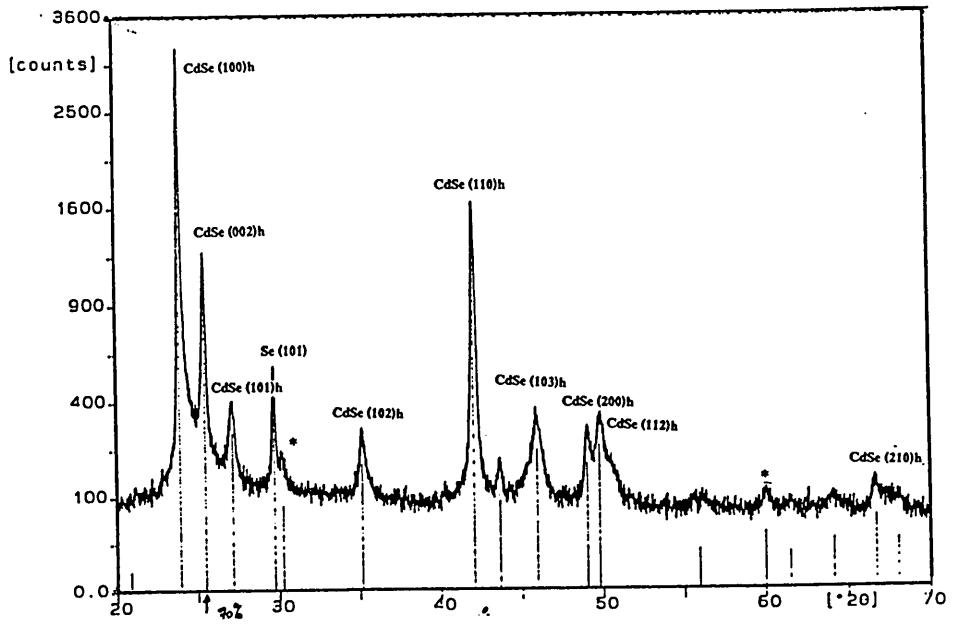

(b)

Figure 5.11.1 (a) The XRD spectrum of a sample (13CS10S1) grown at the voltage -0.68 V. Many of the major peaks correspond to hexagonal CdSe but there are few peaks due to the reflections from 0Se. (b) The XRD spectrum of the annealed sample shows sharper CdSe peaks.

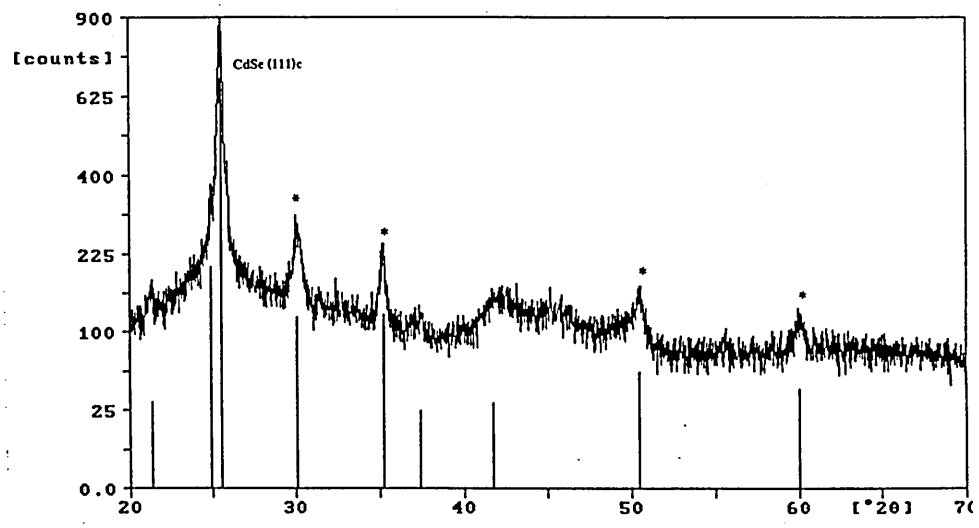

(a)

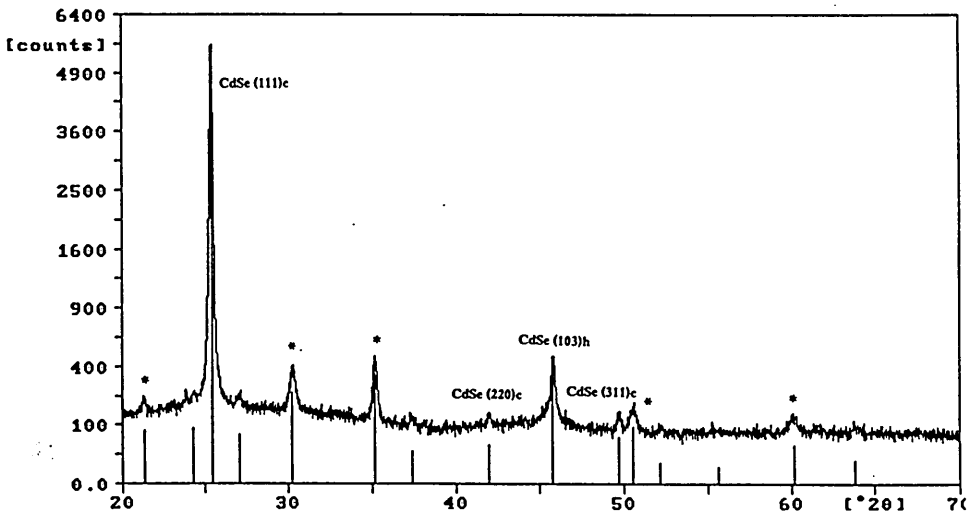

(b)

Figure 5.11.2 (a) A typical spectrum of a sample grown at -0.58 V. The broad peaks marked with * are arising from the substrate ITO and the peak at 25.2° is due to the reflections from (111) plane of Cubic CdSe. (b) Annealing at 400°C for 40 minutes sharpened the (111) peak improving the crystallinity of the layer.

5.3.3 XPS results

Strong Cd peaks and Se peaks were observed in XPS spectra for CdSe samples grown under the conditions which showed the presence of only a (111) peak. As shown in figure 5.12.1, carbon and oxygen peaks were also observed in the spectra for air exposed chemically etched samples. The two peaks Cd $4d_{3/2}$ and $Se3d_{3/2}$ were selected to estimate the stoichiometry of samples as they are only ~40 eV apart, so that the escape depths should be similar. The samples grown at -0.44 V were nearly stoichiometric with Cd:Se = 57:43 (figure 5.12.2).

5.3.4 SEM results

Figure 5.13 is a typical scanning electron micrograph for an electrodeposited CdSe layer grown at -0.44 V and annealed at 400°C for 40 minutes. The grain sizes were about 100Å. The films were uniform, and no cracks or holes could be observed.

5.3.5 GDOES results

Preliminary studies of GDOES showed the presence of Na in the samples grown in glass beakers. The presence in Cd and Se of the CdSe samples were also observed (Figure 5.14) and the two elements Cd and Se are fairly uniform. The presence of Na diminishes with depth but the presence of In and O appears from the substrate, ITO. This observation can arise due to interface roughness at the CdSe/ITO junction.

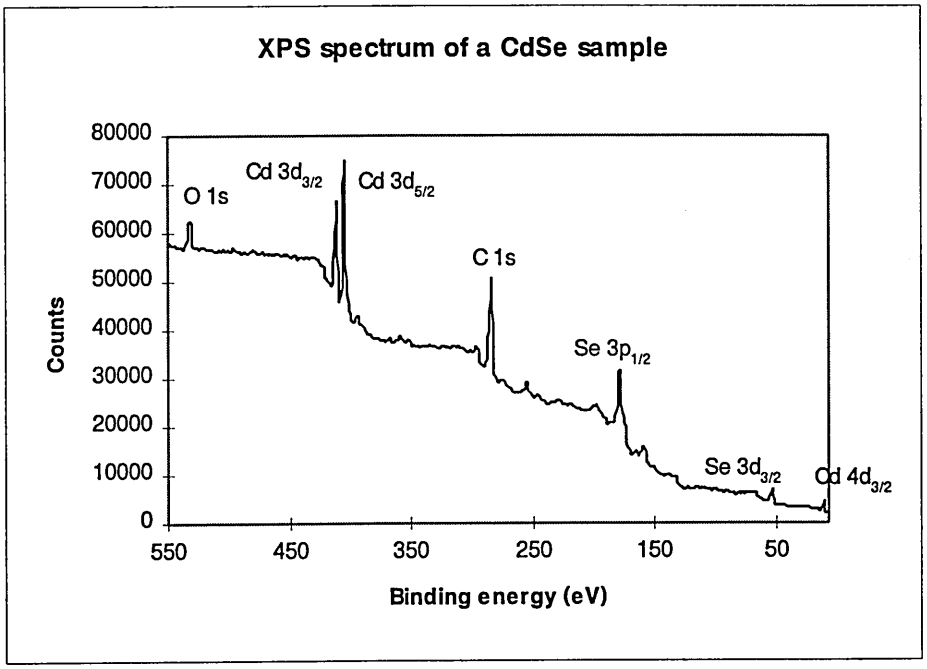

Figure 5.12.1 A typical XPS spectrum of electrodeposited CdSe. Except carbon and oxygen, the spectrum consists only of Cd and Se peaks.

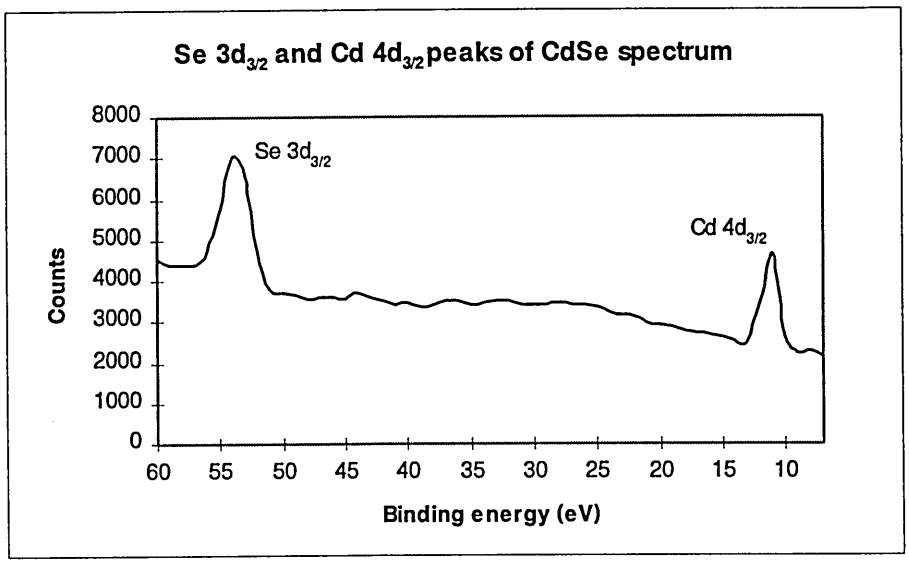

Figure 5.12.2 Se $3d_{3/2}$ and Cd $3d_{3/2}$ peaks of CdSe spectrum. The two peaks are only ~40 eV apart from each other and the stoichiometric ratio Cd:Se = 57:43.

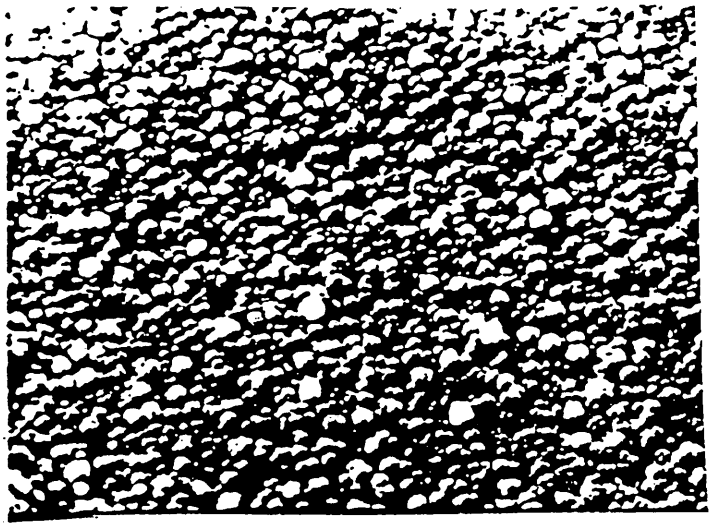

Figure 5.13 A typical SEM micrograph of an electrodeposited CdSe layer. Films were uniform and the grain sizes were 100Å.

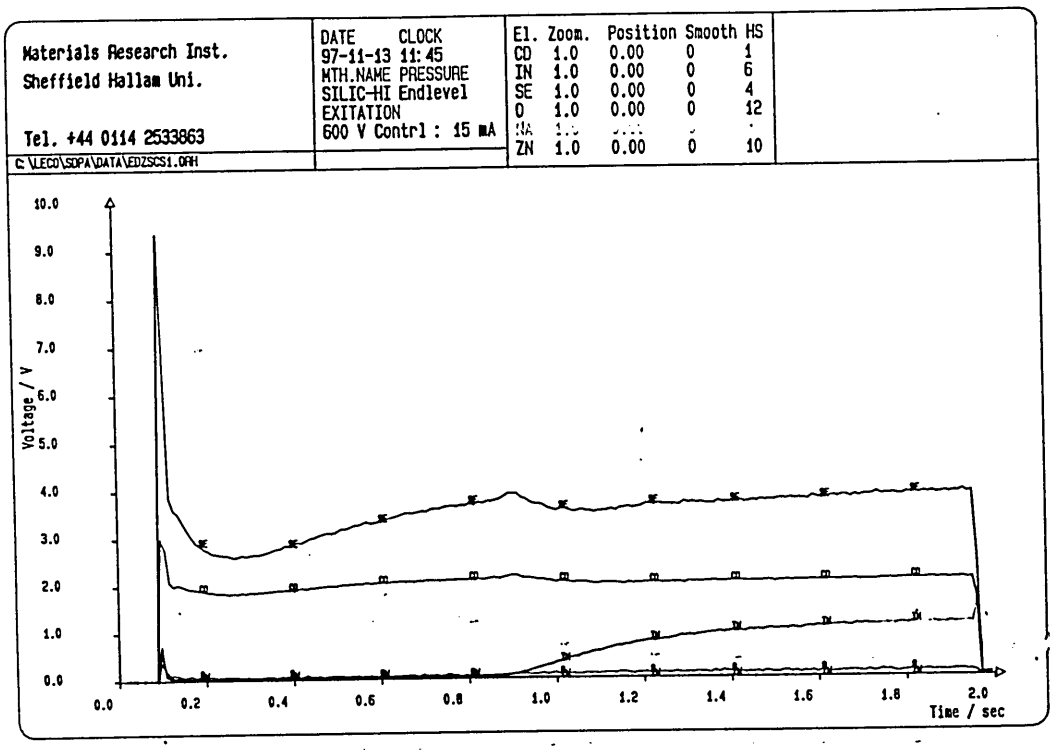

Figure 5.14 A GDOES profile of an electrodeposited CdSe layer. Cd and Se are evenly distributed but the presence of Na on the top of the sample is evident. Merging of In and O can arise due to rough ITO surface filled with CdSe.

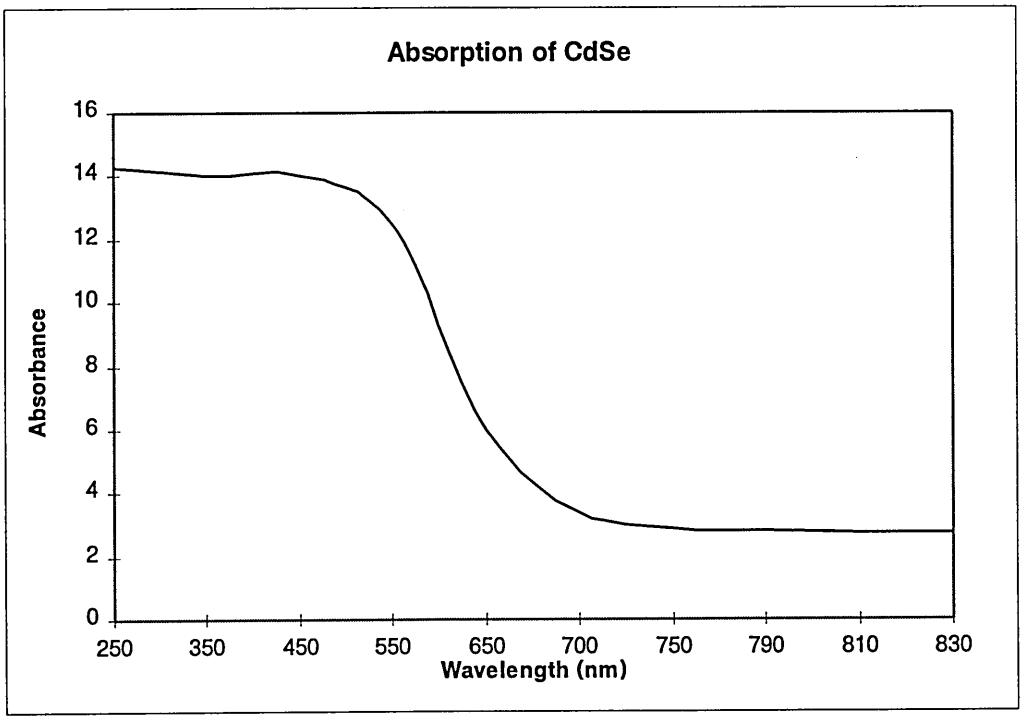

Figure 5.15 Optical absorption of electrodeposited CdSe. Even though the absorption does not show a sharp change, the high absorption near 730 nm indicates the band gap of about 1.7 eV of the material.

5.3.5 Optical absorption

A change in optical absorption near 730 nm can be observed in the absorption spectra of electrodeposited CdSe samples (figure 5.15). This value corresponds to 1.7 eV, which is the band gap of CdSe reported in the literature. However, the curve does not show any sharp change in absorption but a gradual change in the region 1.5 eV to 1.8 eV. This is an indication of the presence of energy states in the band gap and should disappear with purification and optimisation of the growth of the material.

5.3.6 Discussion of the electrodeposition of CdSe

Similar to the formation of ZnSe, the low temperature deposition gives amorphous CdSe and the deposition temperature had to be elevated to 65°C for crystalline layers to be deposited overcoming the kinetic barrier. The reduction of Se^{4+} to Se for CdSe deposition occurs via the reactions 3.3 (a), 5.2 (a) and 5.2 (b). However, there is a competition between the formation of H_2Se and Se that passivates the cathode, which is the ITO electrode. As observed from XRD results, similar to ZnSe deposition, the formation of H_2Se at positive voltages than -0.3 V can be expected via the following reaction.

$$H_2SeO_3 + 6H^+ + 6e^- \rightarrow H_2Se + 3H_2O \qquad [5.4\ (a)]$$

followed by the formation of Se;

$$H_2SeO_3 + 2\ H_2Se \rightarrow 3Se + 3H_2O \qquad [5.5]$$

When the H_2SeO_3 concentration is high enough, these reactions may occur in the forward direction and the overall process can be given by;

$$H_2SeO_3 + 4H^+ + 4e^- \rightarrow Se + 3H_2O. \qquad [5.7]$$

Even though it has not been reported to what extent the production of Se along this route makes the CdSe layer unstable, this could be the reason for some XRD (figure 5.11.1) spectra of electrodeposited layers showing a CdSe structure with Se and substrate (ITO) peaks. The formation of crystalline CdSe on active metallic substrate as described by Lokhande and Pawar (1989) occurs through the reactions 3.3 (a), 3.3 (b) and 3.3 at -0.60 V. However, the depletion of Cd, the potential determining species for any Se concentration in the bath, with the formation of CdSe would increase the relative concentration of Se allowing the reactions 5.1 (a), 5.1 (b) and 5.1 to occur, leaving excess Se formed on the surface of the deposit.

Even though CdSe is reported to be more stable with a hexagonal crystal structure, almost all II-VI compounds tend to form zinc blende structure with the deposition at low negative voltages. The preferential orientation in a (111) plane can be understood as (111) is the close packing direction of the zinc blende form. Lade et al (1997) deposited CdSe on stainless steel with similar deposition conditions. The Cd:Se ratio in the bath was 0.05:0.01 and the standard reference electrode was SCE but the precursors were the same as those used in this project. The XRD analysis shows that their layers were hexagonal polycrystalline in phase but preferentially oriented in a (002) crystal plane. The information currently available is not enough to conclude whether the crystal structure would depend on the substrate. However, the structure depends on the deposition conditions. Figure 5.11.1 (b) shows that excess Se contained in the samples grown at -0.68 V could be removed by annealing at 400°C for 40 minutes. This may perhaps be due to CdSe becoming more crystalline after annealing and reflection from

Se are therefore less prominent or with high temperature, Se can be expected to combine with excess Cd to form CdSe. The excess Cd may come from the disintegrated CdO or $Cd(OH)_2$ molecules after annealing. During annealing the material can also lose excess Se leaving more stoichiometric CdSe. Mishra and Rajeshwar (1989) proposed an alternate mechanism for indirect deposition of CdSe.

$$3Cd + H_2SeO_3 + 4H^+ \rightarrow CdSe + 3H_2O + 2Cd^{2+} \qquad [5.8]$$

Even though Cd^{2+} ions produced in this reaction were attributed to react with H_2SeO_3 forming CdSe in another side reaction, we can expect them to react with H_2O when in the presence of a depleted H_2SeO_3 concentration, forming $Cd(OH)_2$ or CdO. Either of them would produce excess Cd in the sample when annealed at high temperature releasing oxygen or H_2O.

As the applied voltage moves down to -0.58 V keeping temperature and concentration ratio the same, the deposition of Se becomes less significant, because the production of Se via side reactions [equation 5.7] may not be possible at this potential and only the set of reactions mentioned in section 3 (equations 3.3, 3.3 (a) and 3.3 (b)) may be taking place. Thin CdSe films are preferentially oriented in a (111) crystal plane in this growth.

Even though the two standard potentials of Cd and Se have a gap of about 1.148 eV, the gain in free energy (-136.4 $kJ.mol^{-1}$) upon compound formation appears to be adequate for the reduction of Cd^{2+} making the deposition of CdSe possible as described in section 3.1.

The possibility of growing uniform CdSe layers is shown by the SEM studies (figure 5.13). As shown in figure 5.12.2, the electrodeposition at 65°C with an applied cathodic voltage of -0.58 V gives nearly stoichiometric CdSe layers. Also the layers grown at -0.58 V are free of impurities and contain only carbon and oxygen as observed from XPS (figure 5.12.1) and GDOES (figure 5.12.2) studies. The deposition bath contains Cl (or S), also Cl infiltrates ZnSe layers very easily but the deposition rate of CdSe appear to be fast enough not to contain Cl or other impurities from the electrolyte. However the rate of deposition is slower in comparison with Na atoms which are being released from the glass beaker as shown in GDOES studies (Figure 5.14). The amount of Na in CdSe is comparatively lower than the considerable amount of Na observed in some ZnSe layers. This can be attributed to the deposition time, ZnSe is deposited for 3 - 4 hours whereas the current density of CdSe growth is high enough to grow a 0.25 μm thick layer in 30 minutes. For this reason, CdSe contains only a small amount of Na whereas some ZnSe layers contain a large amount of Na.

However, optical absorption studies (figure 5.15) indicate that the samples contain some impurities, perhaps on a very small scale even though they are not detectable utilising the techniques used in the project. The absorption curve doesn't show a very sharp change in absorption but it does indicate the change in absorption around the wavelength 730 nm, which corresponds to the accepted band gap of CdSe (1.70 eV).

5.4 Electrodeposition of thin CdTe layers

Unlike the rest of II-VI compounds, many reports with regard to the electrodeposition of CdTe can be found in the literature, among them are Panicker et al (1978), Lokhande et

al (1989) and Meulenkamp (1996). However, there have been no reports published on whether CdTe can be grown epitaxially or in a preferred crystal plane utilising an electrochemical deposition technique, except the attempt by Stickney et al utilising an electrochemical atomic layer epitaxy process, which is practically highly complicated.

Electrodeposition of CdTe involves cathodic co-deposition of Cd and Te. Low pH solutions and deposits often contain substantial amounts of elemental Te and in practice it is difficult to obtain stoichiometric CdTe particularly in low pH solutions.

5.4.1 Effect of deposition parameters

Poor dissolution of TeO_2 in aqueous solutions does not help the stoichiometric deposition of CdTe. However, the deposition prefers lowest possible TeO_2 concentration similar to ZnSe and CdSe deposition. Therefore, 0.1 M TeO_2 solution, which could effectively be expected to be a millimolar solution in a 0.1 M $CdSO_4$ solution, was used for experiments. The pH was adjusted using H_2SO_4 to be 2.25 and the deposition voltage range was decided to be -0.20 V to -0.70 V using Pourbaix diagram (figure 1.1 (c)). Experiments were carried out for a temperature range from 30°C to 70°C.

5.4.2 Cyclic voltammometry

A typical voltammogram for CdTe is shown in figure 5.16. Very often, onset of three cathodic waves at ~-0.13 V, ~ -0.25 V, ~ -0.49 V and a plateau region between -0.30 V and -0.49 V were observed. Two anodic waves at -0.30 V and -0.1135 V were also observed. The deposition potential range was wider (-0.30 V to -0.49 V) compared to that of ZnSe. The current density was as high as 10 times that of the deposition of ZnSe.

The current density varied from 300 μA to 800 μA for very small changes in deposition parameters.

5.4.3 XRD results

The XRD pattern for CdTe layers deposited at room temperature with -0.5 V applied voltage, showed only the substrate peaks, even though the layers were dark in appearance. The spectra did not show any difference even after annealing at 450°C for 30 minutes. Only the spectra of the samples grown at elevated temperature, ~50°C to 70°C contained peaks corresponding to polycrystalline CdTe. The layers deposited at 65°C showed good results in XRD analysis with some peaks exactly matching with the standard PDF data corresponding to polycrystalline CdTe (figure 5.17.1 (a)) but containing Te and ITO peaks as well. Annealing at 450°C for 20 minutes increased the intensity keeping the ratios the same and reducing the intensities of ITO and Te peaks (5.17.1 (b)). When the applied potential moved towards less negative potentials, the (111) peak of cubic CdTe became dominant. Annealing increased the intensity of the (111) layer narrowing peak width and making the layer almost entirely oriented in (111) plane (5.17.2). Optimum results were obtained for the samples grown under an applied voltage of -0.39 V at 65°C in an electrolyte solution containing 0.1M $CdSO_4$ and millimolar solution of H_2SeO_3 and pH value of 2.25.

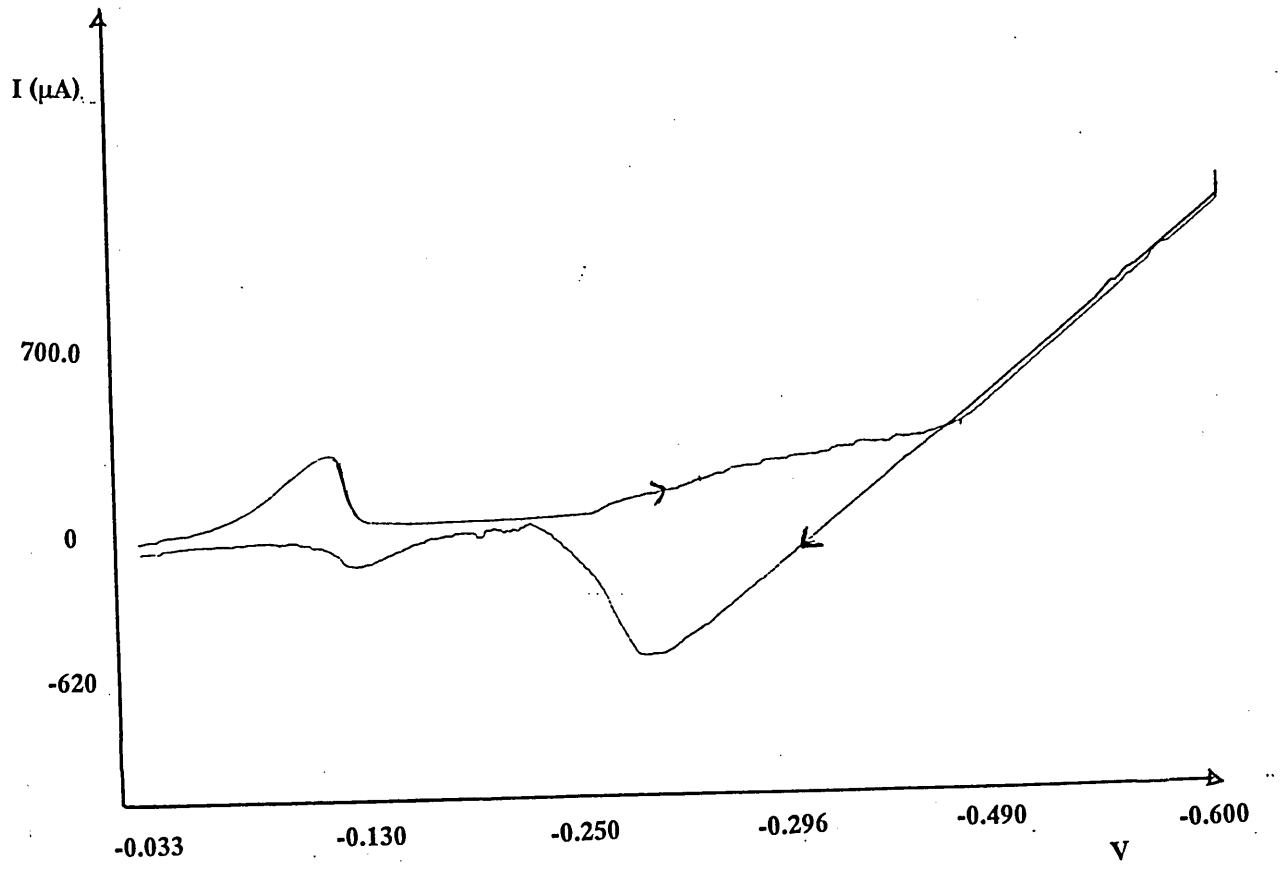

Figure 5.16 Cyclic voltammogram of the electrodeposition of CdTe. The onset of three cathodic waves at ~-0.13 V, ~ -0.25, ~ -0.49 V and a plateau region between -0.30 V and -0.49 V can be seen. Two anodic waves are also observed at -0.30 V and -0.1135 V. The deposition potential range (-0.30 V to -0.49 V) is wider in comparison with ZnSe and CdSe meaning a wide range of possible deposition potentials of CdTe

5.4.4 SEM results

The samples which were highly preferentially oriented in a (111) crystal plane showed a columnar growth (figure 5.18) similar to those published in the literature. It was observed that the films were homogeneous and uniform surfaces with grain sizes of ~ 0.3 μm. Those samples grown at ~ -0.5 V, which did not show any peaks arising from CdTe in XRD patterns did not show any grains. The thin films were uniform and crystallinity was improved with annealing.

5.4.5 XPS results

All the XPS spectra for CdTe thin layers contained Cd and Te peaks, regardless of the deposition temperature or the potential of the deposit (figure 5.19.1). Similar to the other two materials, C and O were present in all air exposed chemically etched surfaces. The two strongest Cd $3d_{3/2}$ and Te $3d_{5/2}$ peaks (figure 5.18.2) were selected to determine the stoichiometry of the layers. The surfaces were nearly stoichiometric with the ratio Cd:Te = 54:46 in the optimised material.

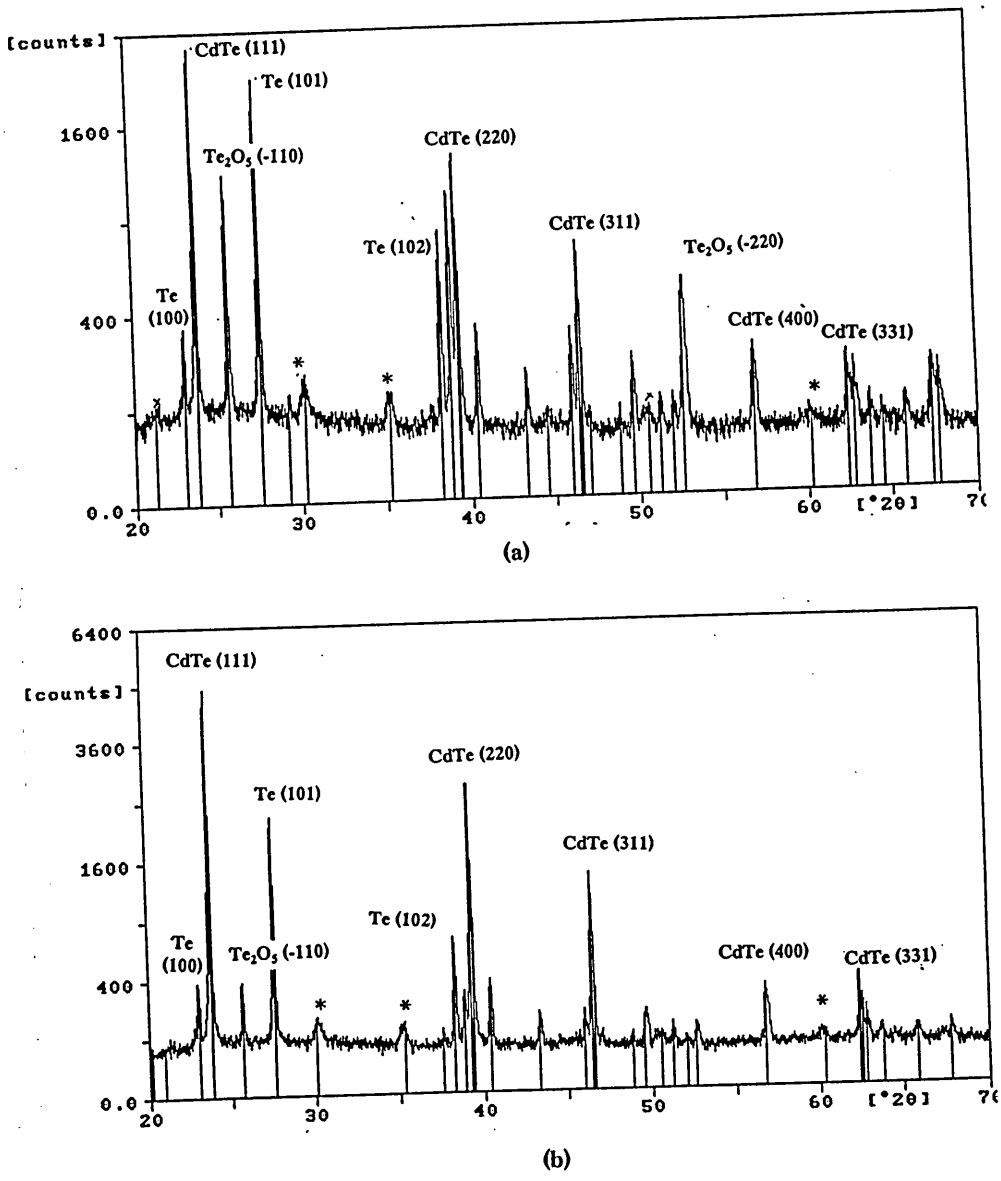

Figure 5.17.1 (a) XRD spectrum of the sample 15CT12S2 grown at 65°C under an applied voltage of -0.5 V. Some peaks are exactly matching with the standard PDF data corresponding to hexagonal CdTe but containing Te, Te_2O_5 and ITO peaks as well. (b) Annealing at 450°C for 20 minutes increased the intensity keeping the ratios the same and reducing the intensities of ITO, Te_2O_5 and Te peaks. The intensity ratio of CdTe peaks remains the same with annealing, (111):(220):(311) = 100:55:27.

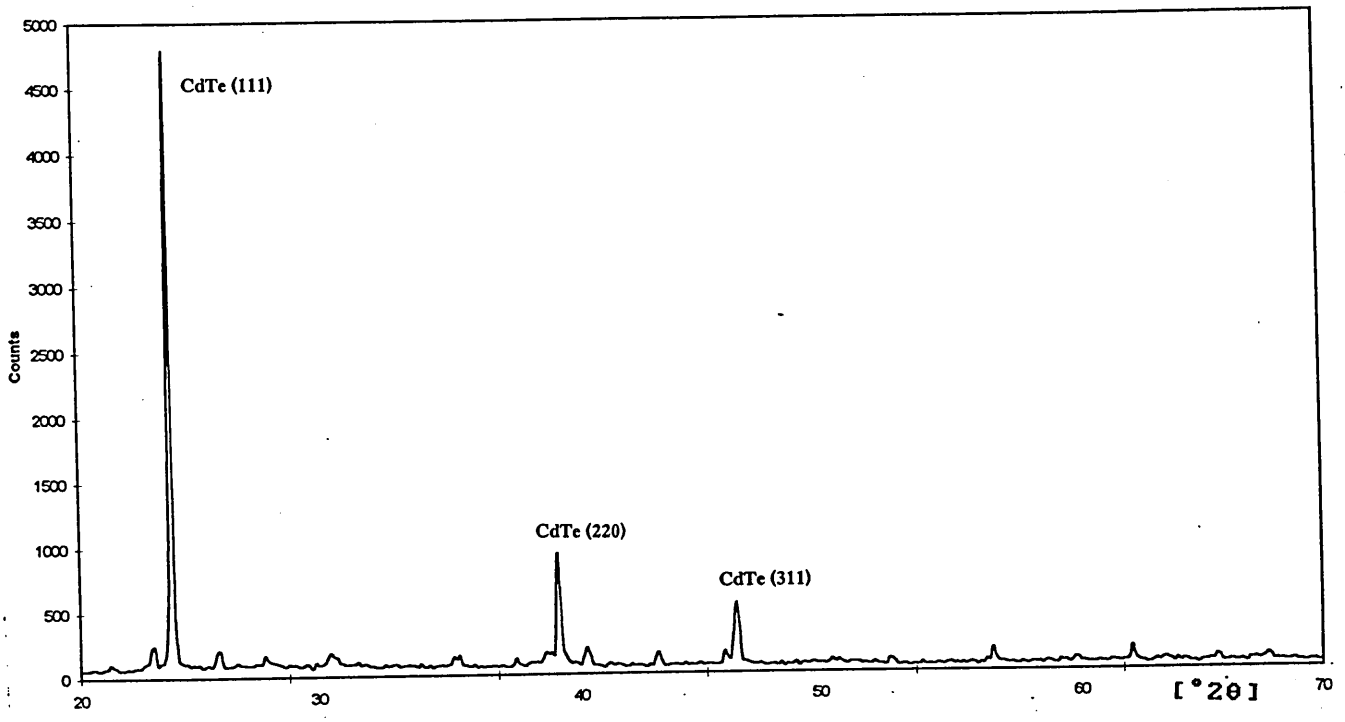

Figure 5.17.2 An XRD spectrum of a sample grown at -0.39 V and 65°C. The intensity ratios of the three major peaks are 100:23:4.

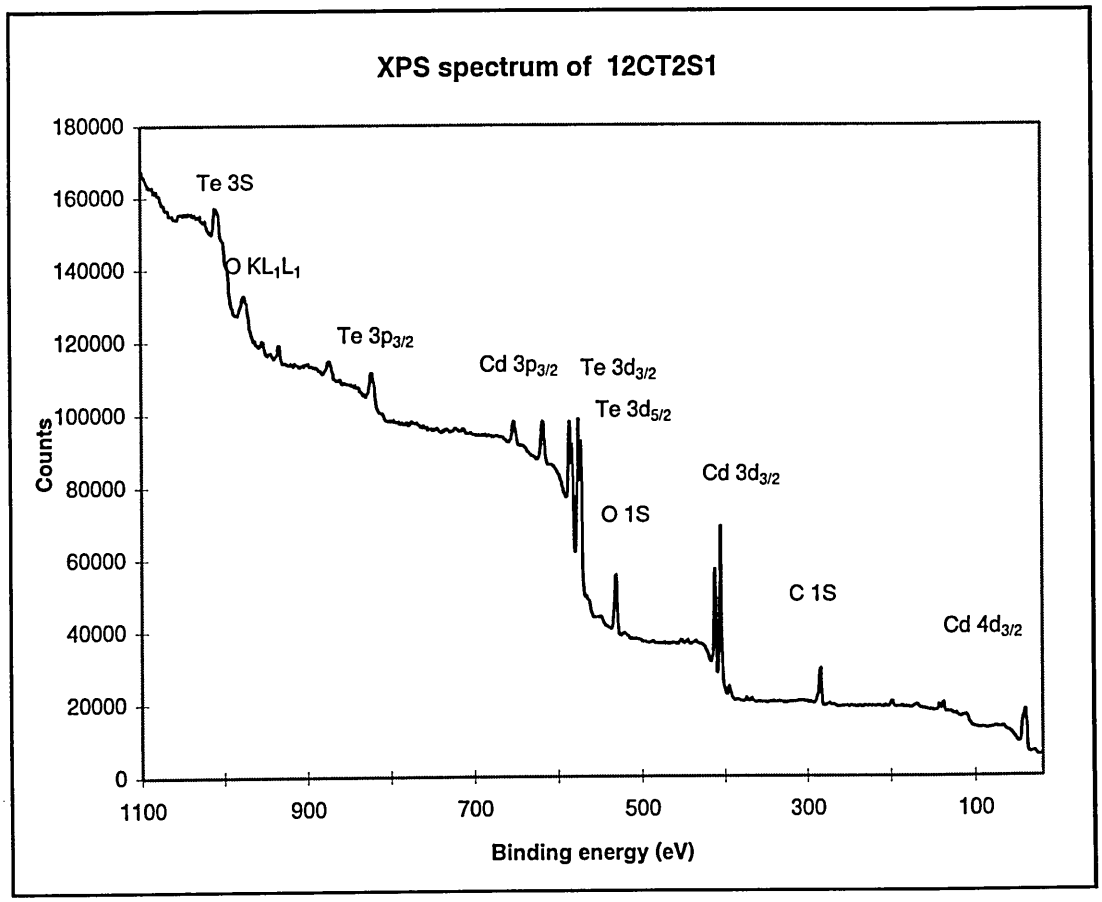

Figure 5.18.1 A typical XPS spectrum of an electrodeposited CdTe layer. A few peaks are arising from C 1S , O 1S and O Auger peak and, all the other peaks are due to either Cd or Te.

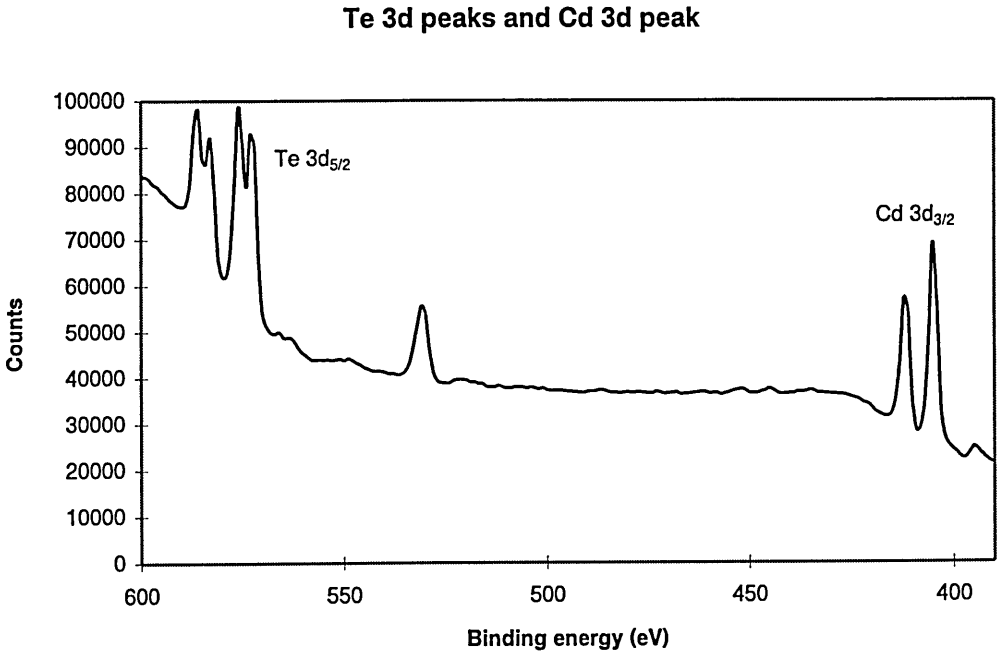

Figure 5.18.2 The strongest peaks of CdTe spectrum, Cd $3d_{3/2}$ and Te $3d_{5/2}$ peaks. The stoichiometric ratio determined using these two peaks is, Cd:Te = 54:46.

5.4.6 Discussion of electrodeposition of CdTe

The range of CdTe deposition potentials is found to be wider in the voltammogram (figure 5.16) indicating the wider range of possible deposition potentials. The layers deposited at room temperature were amorphous, even though the layers were dark in appearance, no CdTe peaks could be found but all the peaks were arising from ITO. The layers may contain some CdTe leaving the layer dark in colour but a satisfactory deposition at room temperature can not be expected for two reasons. Firstly, room temperature deposition may not be capable of overcoming the kinetic barrier from the precursors to the CdTe product and secondly, the deposition of Te could well be expected at lower temperatures forming an amorphous layer. It can also be suggested that the deposition of a thin amorphous layer on top of the CdTe crystalline layer denies any reflections in the XRD studies.

However, the electrochemical deposition of CdTe at a slightly higher elevated temperature is thermodynamically not impossible due mainly to two reasons. As shown in the XRD spectrum of a sample grown at -0.5 V at 65°C (figure 5.17.1 (a)), Te rich CdTe can be grown. Firstly, the difference between the standard redox potentials of the constituents of CdTe, which are Cd and Te, is small enough so that not much activation energy is needed for a successful deposition. Secondly, the gain in free energy upon compound formation which is, $\Delta G°$=-93 kJ mol^{-1}, Mishra and Rajeshwar (1989) is adequate enough for the reduction of Cd^{2+} at more positive potentials. Similar to CdSe, annealing at a higher temperature, would improve the crystallinity of the structure (figure 5.17.1 (b)).

As shown in figure 5.17.2, the XRD spectrum of a sample grown at 65°C under an applied potential of -0.39 V shows a preferential growth of CdTe along a (111) crystal plane. Figure 5.19.2 is an XPS spectrum showing the nearly stoichiometric nature of the layer. For a stoichiometric deposition, the rate of production of Te and CdTe through reactions 3.4 (a) and 3.4 respectively, must be equal. However, the indirect production of Te via the side reaction forming H_2Te (equation 5.9) may be expected to play a less significant role in the electrodeposition of CdTe relative to CdSe for the reason that Te reduction occurs at much more positive potentials than Se. Yet, the production of H_2Te is inevitable in an acidic bath.

$$CdTe + 2H^+ + 2e^- \rightarrow Cd + H_2Te \qquad [5.9]$$

Many published reports describe the use of a slightly acidic aqueous electrolyte for the deposition of CdTe, Sella et al (1986), Sugimoto (1995). In fact Sella et al found that CdTe layers deposited in an alkaline bath were powdery whereas those formed in an acidic bath were bright and adhesive.

As discussed by Mishra and Rajeshwar (1989), this reaction will follow the formation of a small quantity of Te via the reaction aside from the reaction 3.4 (a);

$$2\,H_2Te + HTeO_2^+ \rightarrow 3Te + 2H_2O + H^+ \qquad [5.10]$$

The significance of H_2Te appear to become almost negligible at more positive potentials, specifically at 65°C under the bias of -0.39 V. Figure 5.17.2 shows a highly

crystalline and preferentially oriented layer in (111) crystal plane when grown under those conditions.

The XPS spectrum (figure 5.18.1) of a CdTe layer, similar to CdSe and ZnSe, contains only semiconductor elements (Cd and Te), oxygen and carbon peaks. XPS technique may not be capable of tracing any Na or Cl impurities but their presence is unlikely in the material due to the short deposition time resulting from a high current density. The current density was about 300 - 800 $\mu m/cm^2$ so a layer of the thickness 1 μm could be deposited in a 30 minute period. The deposition time is far too short in comparison to those of CdSe and ZnSe. Thus, the contamination due to the deposition of impurities simultaneously with CdTe from the glass beaker may be negligible.

5.5 General discussion

The electrochemical deposition of ZnSe, CdSe and CdTe on ITO depends on the composition, temperature, pH and applied voltage. Crystallinity can be improved by annealing the samples. The optimum annealing conditions found in this work are ZnSe at 250°C for 15 minutes, CdSe at 400°C for 40 minutes and CdTe at 450°C for 20 minutes.

All three materials can be grown in cubic phase with preferential orientation along (111) planes. XPS shows that all materials contain carbon and oxygen on the surfaces as expected. Optical absorption studies reveal that the band gap of ZnSe and CdSe are 2.7 eV and 1.7 eV respectively.

By varying mainly the potential, the deposition can be switched in general from M (Cd or Zn) rich to X (Se or Te) rich material. The deposition potential for one of these particular materials takes place in between the standard potentials of the constituents. Out of all three materials, the deposition of CdTe is far more easier mainly due to the smaller potential difference between Cd and Te standard reduction potentials. Inclusion of Na and Si from the glass beaker is more likely in ZnSe as the deposition current density is much lower and the time required for the deposition is comparatively higher. High current density resulting in a short deposition time helps deposition of CdTe with lower impurity levels.

CHAPTER SIX:

FABRICATION OF DEVICES USING ELECTRODEPOSITED THIN FILMS OF ZnSe, CdSe AND CdTe.

6.1 Introduction

This chapter presents the preliminary results of the homojunction and heterojunction device structures fabricated using electrochemically deposited thin layers on ITO/glass substrates. ZnSe layers were deposited to produce p-n and n-p junction devices. Also CdSe layers were deposited on ZnSe layers and CdTe layers were deposited finally on CdSe to form the multi-layer solar cell structure, glass/ITO/ZnSe/CdSe/CdTe. The multi-layer surfaces were characterised using XRD and optical absorption techniques for the texture and optical properties respectively. Completed solar cells after metallisation with Au or Ag were characterised mainly using the I-V technique.

6.2 Electrodeposition and characterisation of ZnSe homo-junctions

The initial p or n type ZnSe layer which was deposited on glass/ITO substrate was annealed at 250°C for 15 minutes and the second layer was deposited on top of the first layer. The exposed surface of the first layer was chemically etched with the etchant 4 of the table 3.2 in order to remove any surface oxides prior to deposition of the second layer. Each layer was deposited for three hours under the optimum deposition conditions described in the previous chapter. The top layer was annealed under the same annealing conditions prior to deposition of the heavily doped layer and

metallisation. These types of devices (n-p and p-n) produced are shown in figures 6.1.1 and 6.1.2 respectively. Heavily doped p^+ or n^+ layers were deposited on top of p and n surfaces respectively, prior to metallisation to establish good ohmic contacts to the material.

6.2.1 Material characterisation

Even though the thin films grown on conducting glass substrates were characterised for their material properties, the device structures were characterised again to understand the properties of the thin films grown on semiconducting substrates. The films were grown for six hours and the estimated thickness is about 0.6 μm. However, the layers were not adhesive enough or thick enough to do GDOES profiling studies. The PEC cell did not produce any photovoltage under illumination and this was expected due to the existence of two junctions in a situation prohibiting easy flow of charge carriers. The two major peaks (111) and (222) of XRD spectra of ZnSe p-n junctions in general showed an improved intensity in comparison with single p or n ZnSe layers. The optical absorption spectra were not different from those of single layers grown on ITO substrates.

6.2.2 Device characterisation

A heavily doped n layer (n^+-layer) was formed on the n-ZnSe layer of the structure ITO/p-ZnSe/n-ZnSe and a heavily doped p layer (p^+-layer) was formed on the p-ZnSe layer of the ITO/n-ZnSe/p-ZnSe structure and etched using the etchant 4 of the table 3.2 (0.6g NaOH, 1.0g $Na_2S_2O_7$ and 75 ml H_2O) expecting a stoichiometric surface before the metallisation was expected. The formation of ohmic contacts was

established using these heavily doped layers and energy band diagrams of the two devices are shown in figures 6.1.1 and 6.1.2. Au or Ag metal contacts were then made on those preliminary stage devices and they were characterised mainly using the I-V technique.

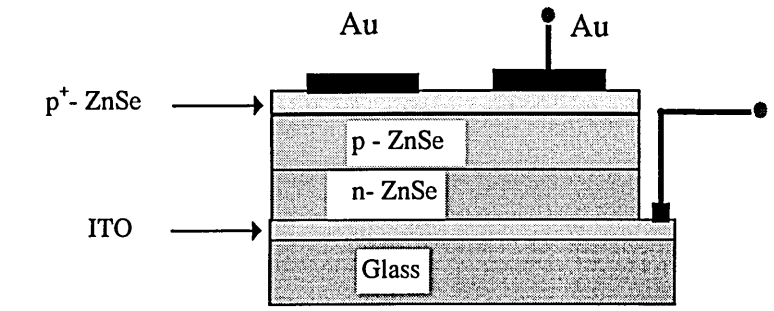

(a)

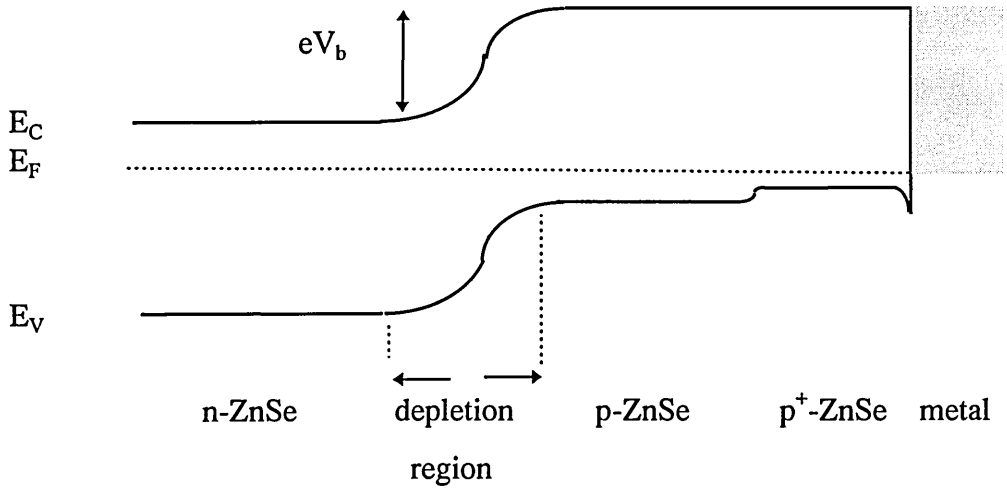

(b)

Figure 6.1.1 (a) A Schematic of Glass/ITO/n-ZnSe/p-ZnSe/p^+-ZnSe/Au device structure and (b) the corresponding energy band diagram.

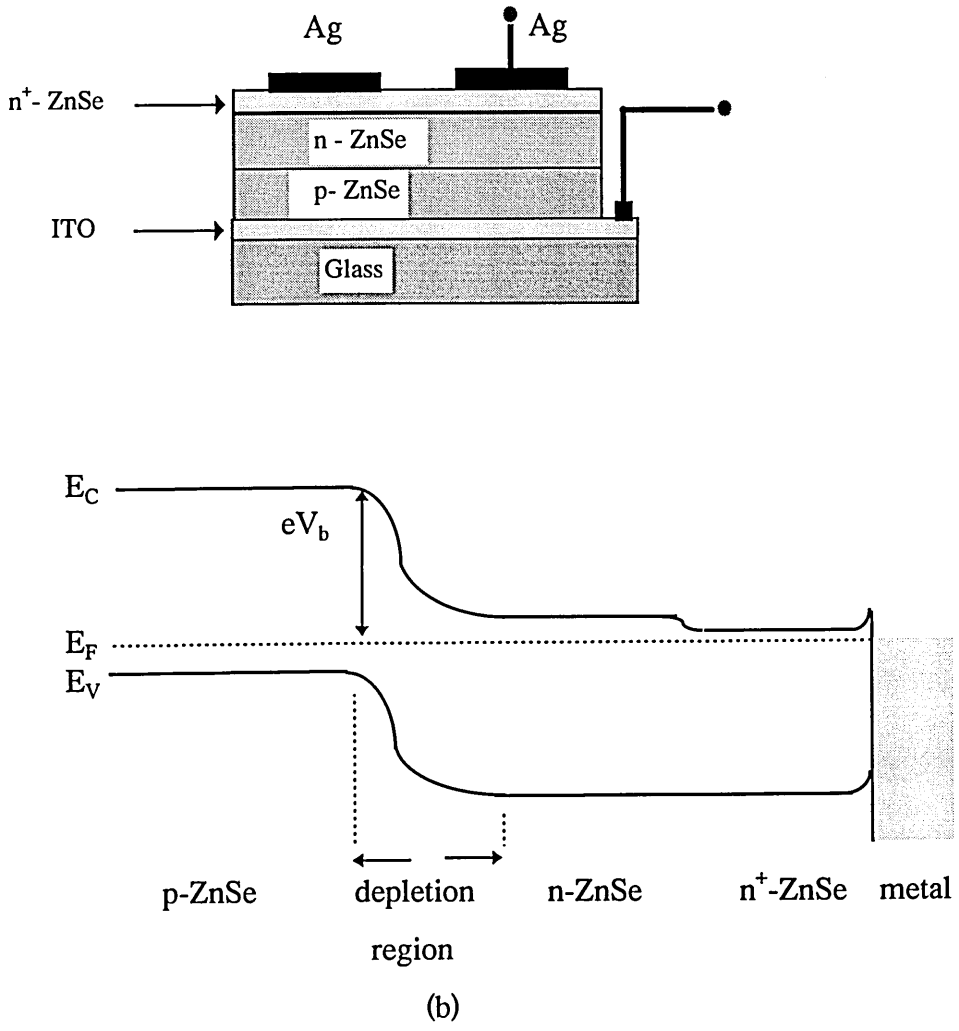

Figure 6.1.2 (a) A Schematic of Glass/ITO/p-ZnSe/n-ZnSe/n^+-ZnSe/Ag device structure and (b) the corresponding energy band diagram.

(a) I-V results

Figure 6.2.1 shows I-V curves of these initial stage devices in both log-linear and linear-linear scales. The devices show a slight rectification but it was a very soft device indicating a low shunt resistance. The threshold voltage was zero and the device was nearly ohmic. Figure 6.2.2 is an I-V result of a device fabricated after thorough purification of the electrolyte and also using high purity chemicals. The rectification factor of the device is considerably higher (~5 orders of magnitude) and the breakdown voltage has been increased to a considerably higher value and the threshold voltage has been extended to about +0.15 V.

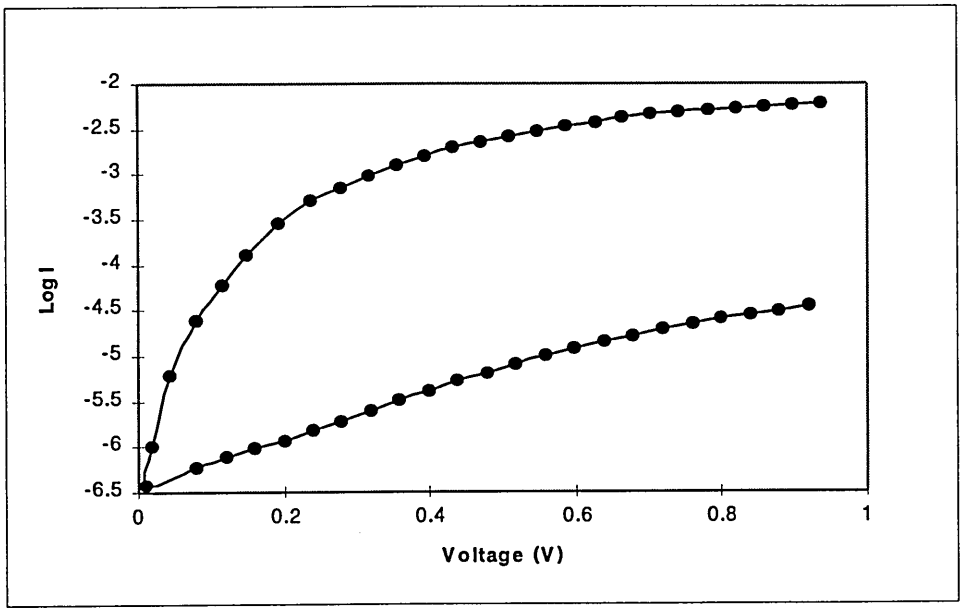

(a)

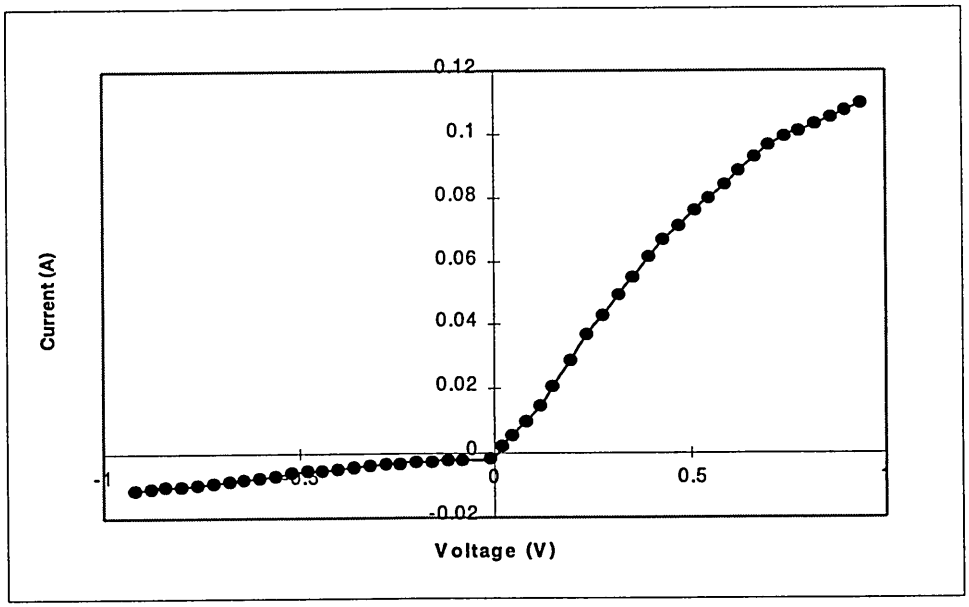

(b)

Figure 6.2.1 I-V characteristics of an early stage ZnSe p-n junction diode, (a) Log I vs V and (b) linear I-V curve. The rectification factor is about 3 but the diode shows a soft breakdown.

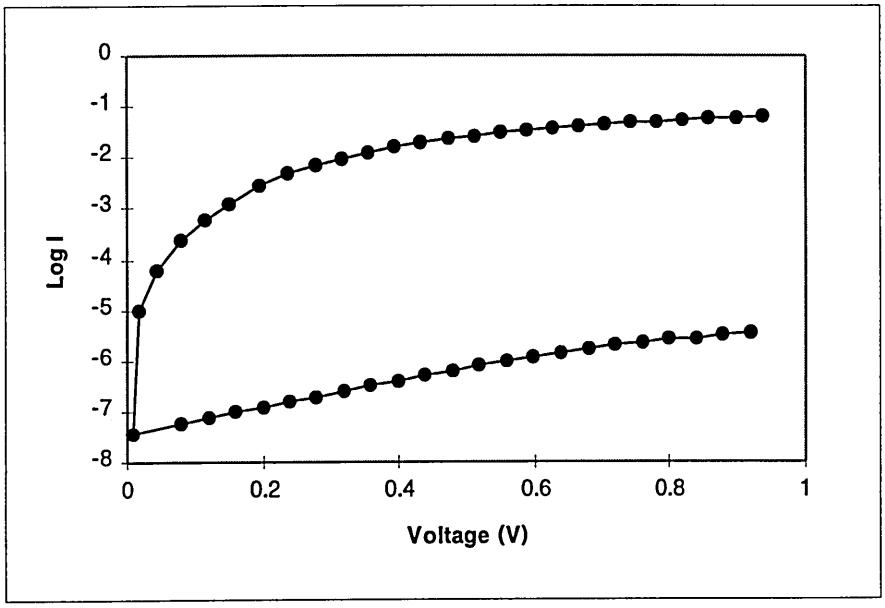

(a)

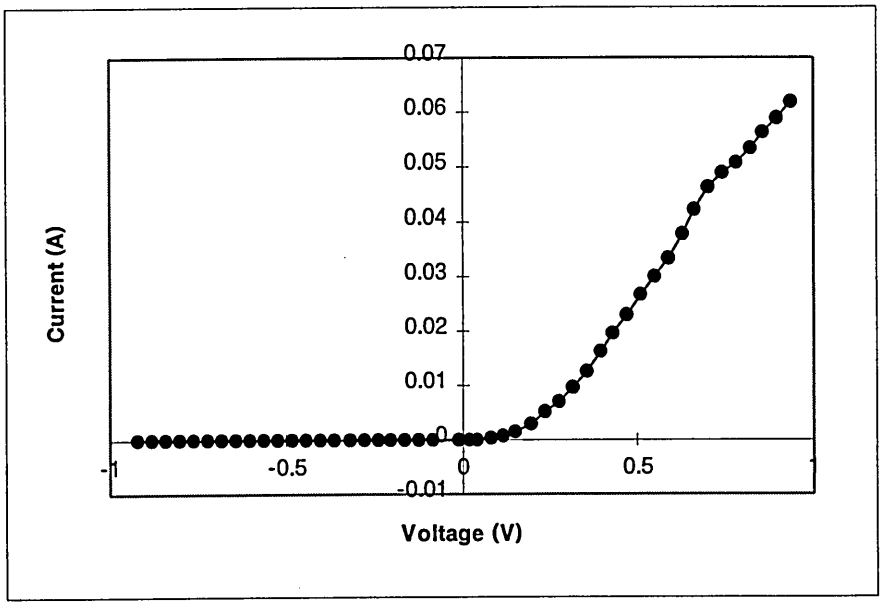

(b)

Figure 6.2.2 An I-V curve of a p-n junction fabricated after purification of the electrolyte, (a) Log I vs V and (b) linear I-V curves. The breakdown voltage has been increased and the threshold voltage has improved up to 0.15 V. The rectification factor has improved to ~ 5 orders of magnitude.

The reverse current has been decreased to give a saturated current indicating a required high shunt resistance. The built in voltages measured for optimised devices were ~ 0.84 eV (with n~ 1.30) and the values were consistent for a range of devices. The rectification factor has gone up from zero to about 5 within a few months due to material purification. The above electrical properties together with a high potential barrier at the junction indicate the possibility of fabrication of high quality devices from these layers.

6.2.3 Discussion

The PEC cell did not produce any measurable photo-voltage for p-n or n-p junctions when compared to single p or n ZnSe layers. The built-in-voltage of the p-n junction structure and the barrier height of the liquid/solid junction might have nullified each other's effect producing no significant photovoltage in the circuit. The adhesion of thin films to the polycrystalline substrate may be highly dependent on the cleanliness of the substrate. At the elevated temperature, the ITO layer may not have been stable in the presence of a low current density and it may have had an impact on the adhesion as well. Natarajan et al (1994) reported a decrease in the plating efficiency of ZnSe by the complicated nature of the electrochemistry of Se. This may have limited the applicability of Faraday's relationship for the estimation of the film thickness and therefore the layer thickness may be much less than the estimated value of 0.6 μm. If the layers are very thin, they may not be suitable for GDOES studies. The XRD spectra of p-n junctions however indicate an improved crystallinity and thicker layers.

As shown in figures 6.1.1 and 6.1.2, metal contacts made on the device structures could be expected to be ohmic due to the heavily doped ZnSe layer. The measured built in voltage therefore may not have a contribution from the metal/semiconductor junction. The estimated minimum value of 0.84 eV with n~1.30 should therefore be the energy step present at the p-n junction. This may perhaps be due not to an impurity level but a defect level, as that value has been consistent for a series of diodes fabricated under different levels of purification. The rectification factor however has gone up with purification of the electrolyte. Also the breakdown voltage and the threshold voltage have been increased with purification of the electrolyte. This evidence indicates the improvement of the quality of the device performance with purification. However, there may have a limit to the purifying process and then other changes such as processing and doping should be considered in further development.

6.3 Electrodeposition and characterisation of glass/ITO/ZnSe/CdSe/CdTe/metal solar cells.

In order to fabricate the device, the second CdSe layer was deposited on top of the ZnSe layer. The initial n-type ZnSe layer was deposited for ~2.5 hours on the glass/ITO substrate. The CdSe layer was deposited for nearly an hour and the third CdTe layer was deposited for 30 minutes. The estimated individual layer thicknesses of the 2 μm thick device structure were ZnSe:CdSe:CdTe=0.25 μm:0.25 μm:1.5 μm. The three layer structures as shown in figure 6.3.1 were characterised using XRD and optical absorption techniques. They were annealed in air at 350°C for 40 minutes and etched using etchant 4 of table 3.2 (0.6g NaOH, 1.0g $Na_2S_2O_7$ and 75 ml H_2O) prior to

metallisation. Au was used to make metal contacts and the devices were characterised using the I-V technique.

6.3.1 Material characterisation

Although the individual thin layers deposited on glass/ITO substrates were characterised for their material properties, these layers were characterised again to explore any differences as they were grown on different (semiconducting) substrates. The substrate used for semiconductor material growth has a great influence on the bulk, electrical and optical properties of the subsequent layers, Dharmadasa et al (1998). All semiconductor layers were annealed at 350°C for 30 minutes prior to material characterisation.

(a) XRD results

XRD studies were performed on ZnSe layers grown on glass/ITO substrates, CdSe layers grown on ZnSe substrates and CdTe layers grown on CdSe substrates. The spectra as shown in figures 5.3.6 (b), 6.3.2 (a) and 6.3.2 (b) of ZnSe on ITO, CdSe on ZnSe and CdTe on CdSe respectively, show better crystalline surfaces with high count rates. As shown in figure 6.3.2 (a), the spectrum of CdSe grown on ZnSe, the peaks arising from (111) layers of ZnSe and CdSe are present but the intensity of the (222) peak of ZnSe is very low, which is almost indistinguishable from the noise. However, there are no other peaks except those arising from (111) crystal planes of ZnSe, CdSe and CdTe present in the spectrum of the three layer structure, and is Glass/ITO/ZnSe/CdSe/CdTe (figure 6.3.2 (b)). This clearly shows the effect of the substrates provided for the growth of CdSe and CdTe. Although both CdSe and CdTe

grown on ITO substrates are polycrystalline, both materials in this structure are highly crystalline with (111) preferred orientation.

(b) Optical absorption

The optical absorption technique was employed to study the band gap variation within the glass/ITO/ZnSe/CdSe structure. CdTe whose band gap is 1.4 eV, was not subjected to optical absorption studies as it does not show any absorption edge within the visible spectrum and in fact it lies in the near IR spectrum. The spectrum as shown in figure 6.3.3 for the above structure, indicates two absorption edges at ~730 nm and ~575 nm indicating band gap values of 1.70 eV and 2.16 eV. The value 1.70 eV corresponds to the band gap of CdSe and the other value 2.16 eV, is in between the band gaps of ZnSe (2.70 eV) and CdSe. This is a strong indication of the formation of alloys of the two compounds such as $Zn_{(1-x)}Cd_xSe$. There may be a more stable alloy with a composition corresponding to the 2.16 eV band gap. It is also interesting to note the gradual change of absorption indicating a whole range of composition of the above alloy. This alloy formation is in fact desirable to fabricate these types of graded band gap solar cell structures.

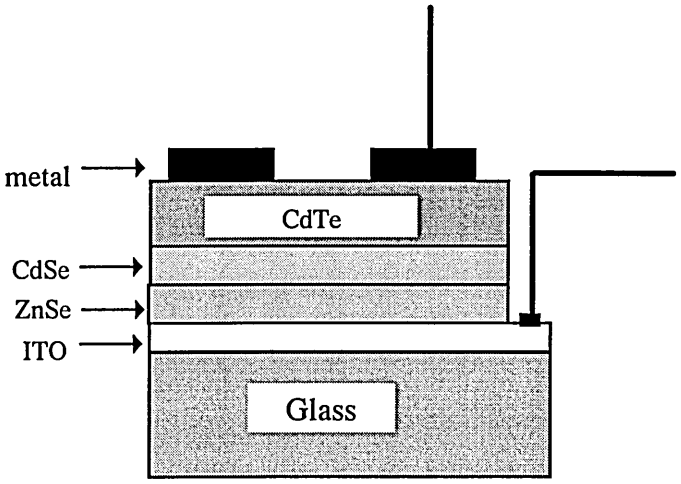

Figure 6.3.1 Schematic of the Glass/ITO/ZnSe/CdSe/CdTe/metal device structure.

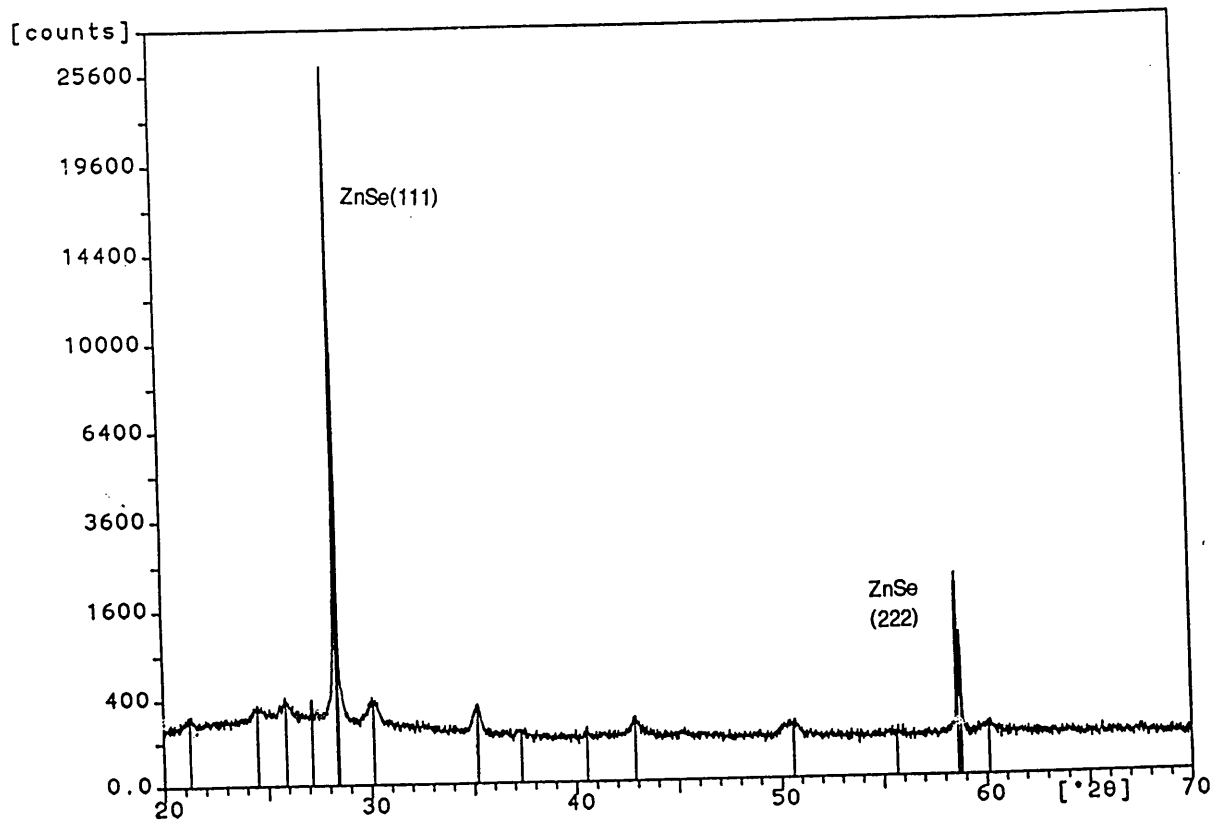

Figure 5.3.6 (b) A typical spectrum of an annealed ZnSe sample grown on ITO substrate and annealed at 250°C for 15 minutes.

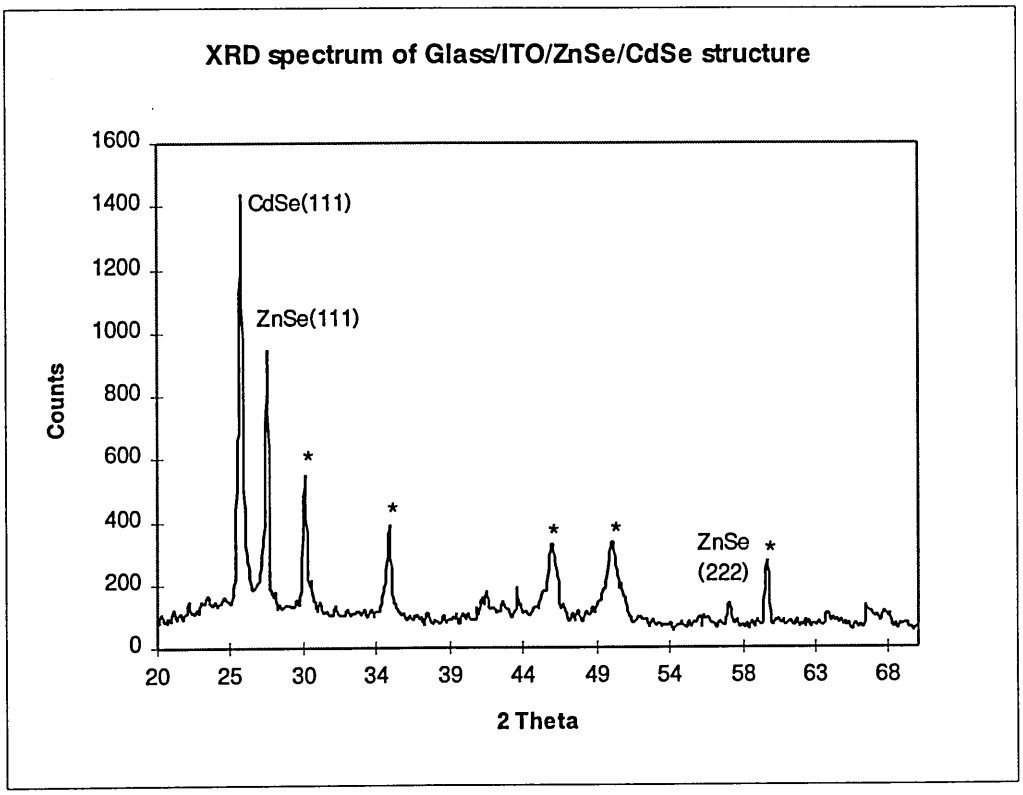

Figure 6.3.2 (a) XRD spectrum of Glass/ITO/ZnSe/CdSe structure. The major peaks are arising from (111) planes of ZnSe and CdSe as labelled and a smaller peak at 57.2 is arising from the crystal plane (222) of ZnSe. The peaks marked with * are due to the substrate ITO.

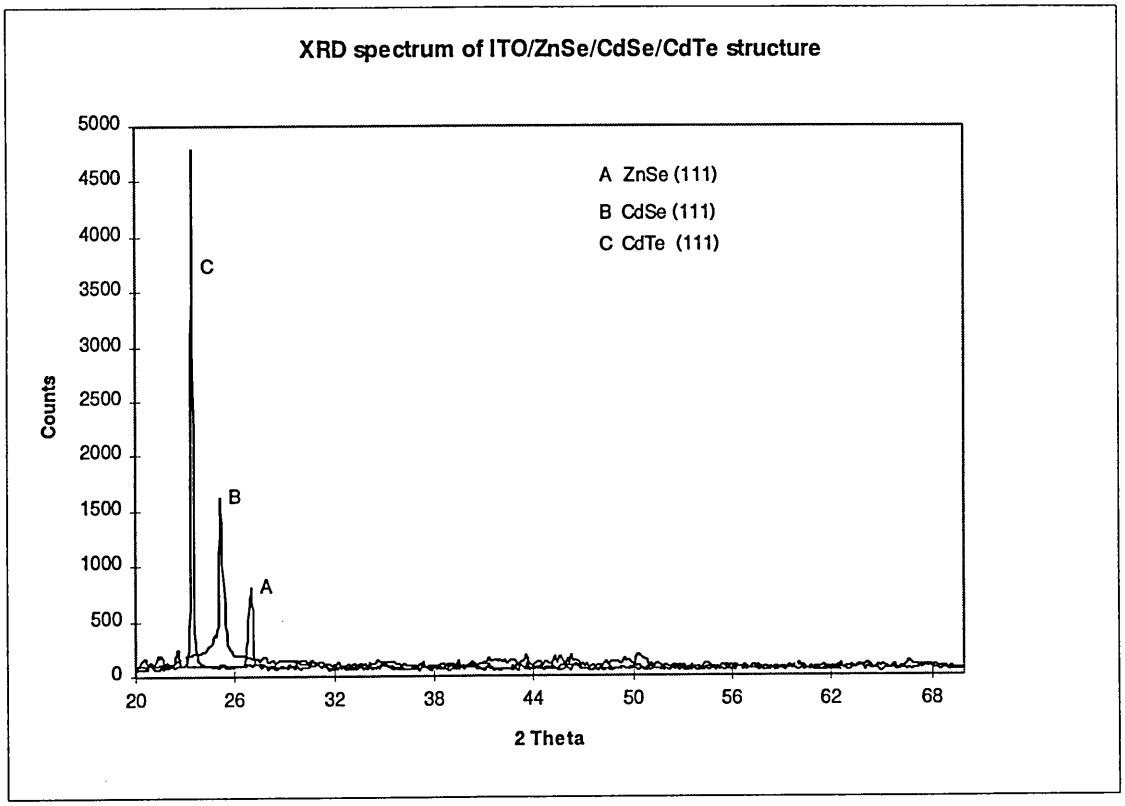

Figure 6.3.2 (b) An XRD spectrum of Glass/ITO/ZnSe/CdSe/CdTe structure. A, B and C are (111) peaks of ZnSe, CdSe and CdTe respectively.

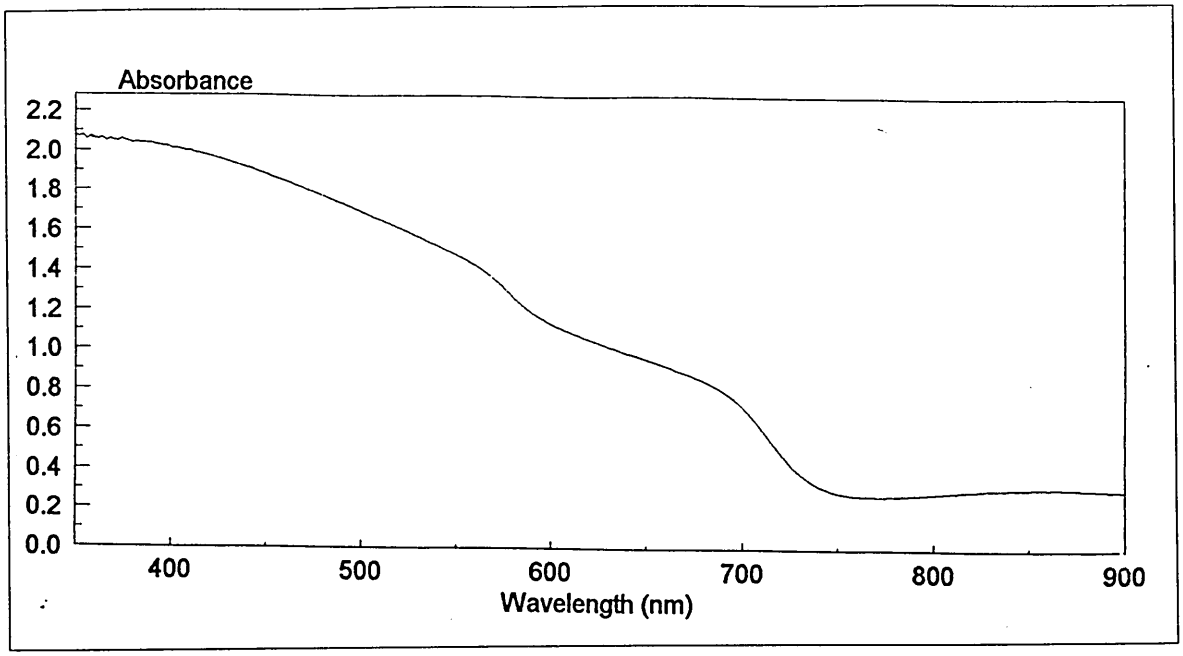

Figure 6.3.3 Absorption spectrum of a CdSe layer grown on ZnSe substrate. Two absorption edges are present at 730 nm and 575 nm indicating the band gap of CdSe (1.7 eV) and of an intermediate $Zn_{(1-x)}Cd_xSe$ layer. Gradual variation of the absorption indicates the presence of a range of alloys with varying band gaps.

6.3.2 Device characterisation

The tandem type solar cell structure Glass/ITO/ZnSe/CdSe/CdTe, was annealed at 350°C for 40 minutes in air and etched using the etchant 4 of the table 3.2 and metallised in order to complete the device structure. Au was used as the contact metal for these preliminary stage devices.

(a) I-V characteristics

Figures 6.4.1 (a) and (b) are I-V characteristics measured under dark and illuminated conditions respectively, of a device fabricated at the beginning. The dark I-V characteristics show reasonable rectification with good saturated reverse current up to ~1 V. To test the photovoltaic activity of the devices, I-V measurements were repeated under illumination. The open circuit voltage of the device (V_{OC}) is ~200 mV and the short circuit current density, J_{SC} is 10 $\mu A\ cm^{-2}$. The estimated fill factor was about 0.36 and the efficiency was about 0.2%. Figure 6.4.2 (a) and (b) are I-V characteristics of improved devices fabricated recently with more purified materials. The devices have shown a gradual improvement in all parameters indicating the possibility of development with device optimisation. The latest devices have shown values such as V_{OC} ~ 250mV, J_{SC} ~ 15 $mA\ cm^{-2}$, FF ~ 0.6 and η ~ 0.9%.

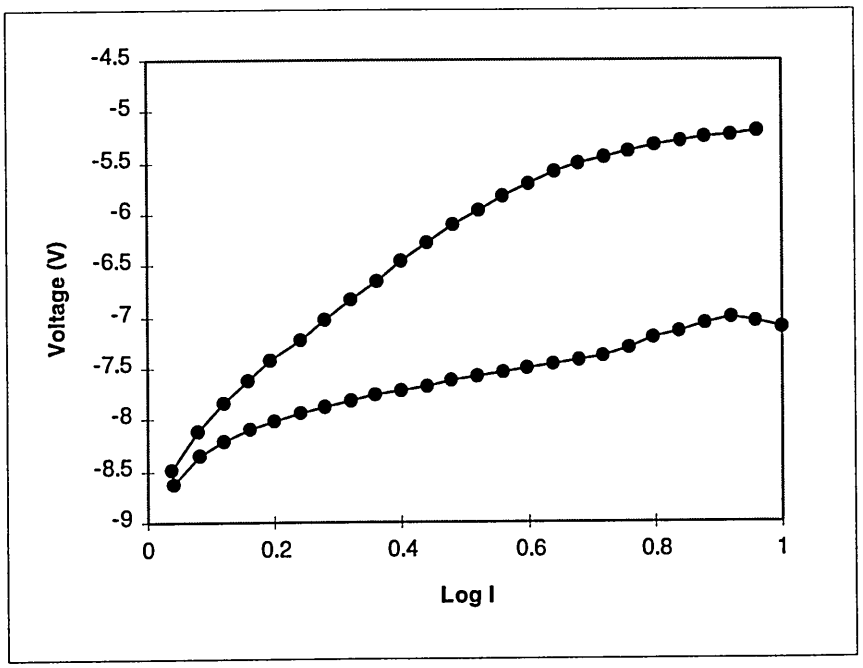

(i)

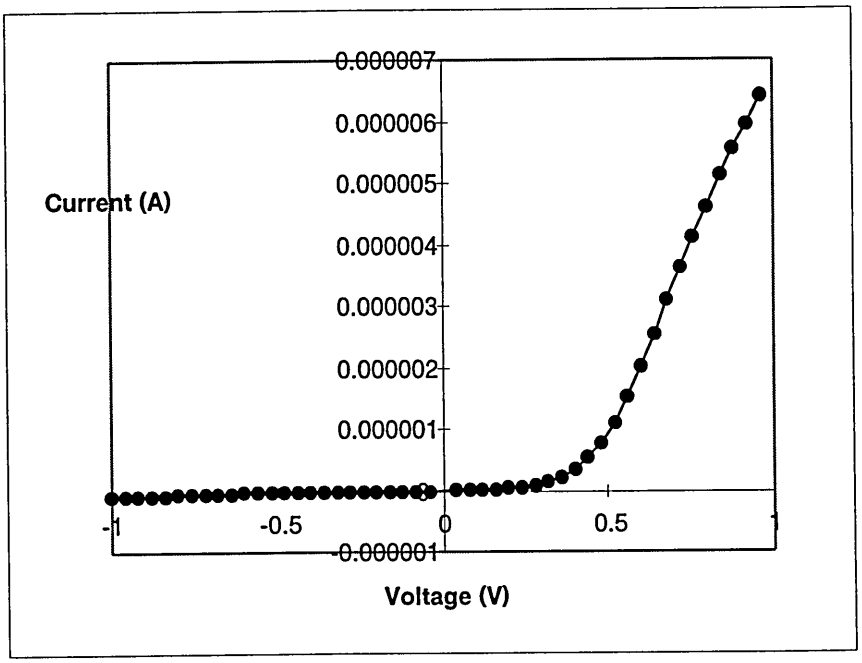

(ii)

Figure 6.4.1 (a) The dark I-V characteristics of an early stage solar cell structure plotted in , (i) Log - linear and (ii) linear - linear scales.

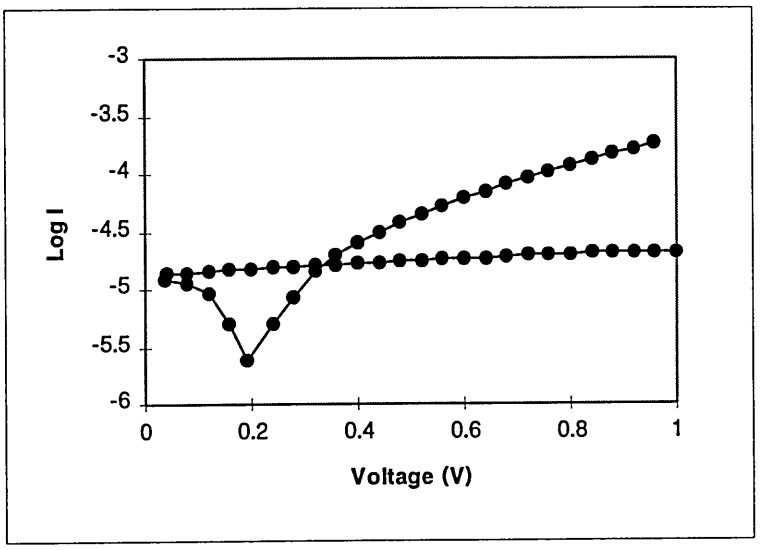

(i)

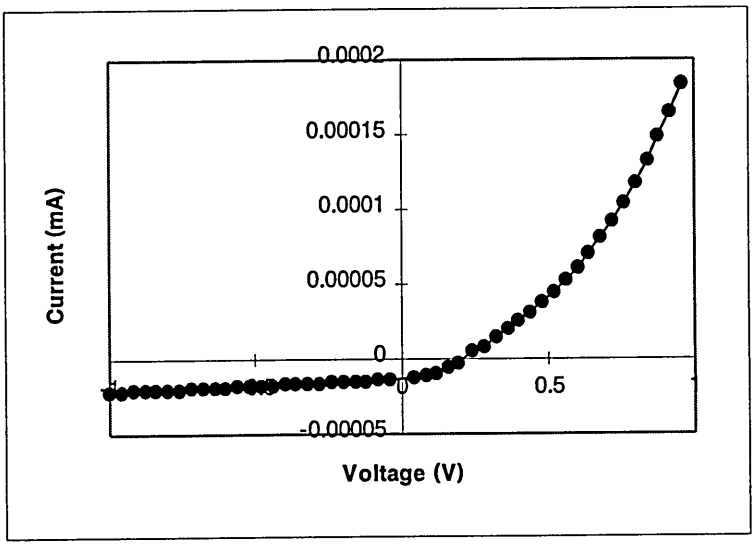

(ii)

Figure 6.4.1 (b) I-V characteristics of the above solar cell structure under illumination, (i) Log - linear and (ii) linear - linear scales. The V_{OC} is ~200 mV and the J_{SC} is ~10 μA cm^{-2}. The fill factor estimated was about 0.36 and the efficiency was about 0.2% for this device.

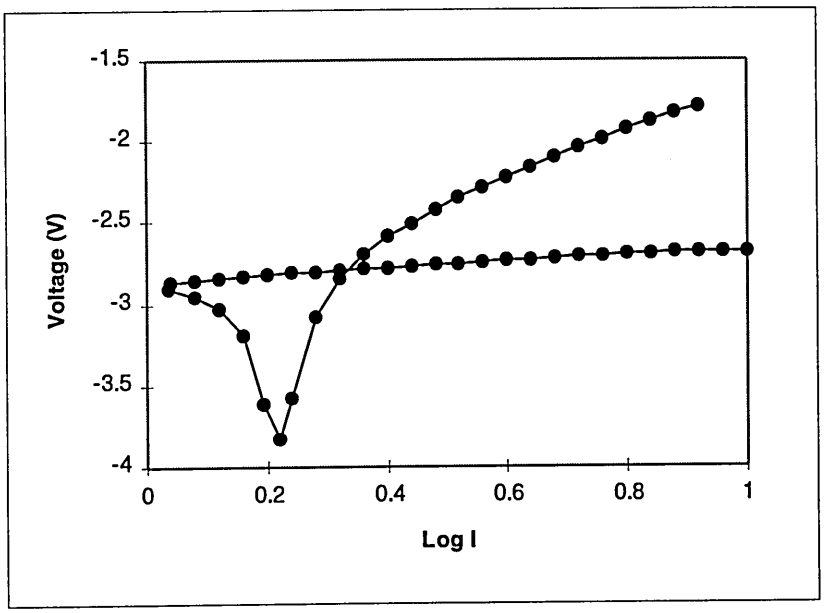

(a)

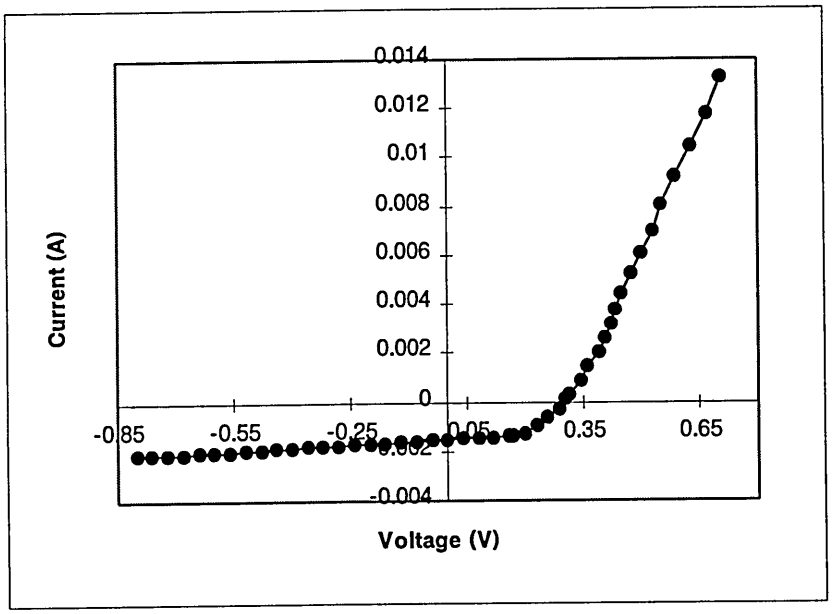

(b)

Figure 6.4.2 I-V characteristics of an optimised devices fabricated recently, (a) Log - linear and (b) linear - linear scales. I_{SC} has gone up to 15 mA cm^{-2} but V_{OC} has been increased only up to 250 mV giving a fill factor 0.6 and an efficiency 0.9%.

6.3.3 Discussion

The device, Glass/ITO/ZnSe/CdSe/CdTe/metal, as shown in figure 6.3.1 is a multi-layer double hetero-junction structure. In figure 6.3.2 (a), low intensity (222) peak of ZnSe could not be observed clearly due to attenuation from the preferentially oriented CdSe overlayer. This fact is justified in the spectrum of CdTe layer grown on CdSe (figure 6.3.2 (b)) as the (222) peak of ZnSe has completely disappeared. However, the multi-layer structure displays a highly crystalline nature and preferential growth along the <111> direction. Among others Lockhande et al (1989) reported the growth of CdTe in the <111> orientation but not CdSe or ZnSe, eventhough they had electrochemically grown all three layers. Natarajan et al (1995) electrodeposited $Zn_{(1-x)}Cd_xSe$ layers with preferential orientation in the <111> direction, but their layers were very thin and the spectrum contained substrate peaks with higher intensities. This evidence has shown that growth of both CdSe and CdTe materials is highly preferential when provided with a (111) oriented ZnSe substrate.

The optical absorption results show that there are two absorption edges and one of them which is 1.7 eV, corresponds to CdSe but the other one which is, 2.16 eV appears to be an intermediate layer in between ZnSe and CdSe layers. The ZnSe absorption edge could not be observed in the spectrum. The reason may be high transparency of visible light through ZnSe in comparison with that of CdSe as shown in sections 5.2.9 and 5.3.5. The CdSe and ZnSe layers might react at the interface, especially during annealing and form an intermediate alloy showing an absorption of 2.16 eV. In fact, Natarajan et al (1995) also reported a band gap of about 2.1 eV for $Zn_{0.5}Cd_{0.5}Se$ layers. They observed an increase in the band gap with decrease in Cd

atomic percentage. Therefore it can be concluded that the intermediate layer has the composition $Zn_{(1-x)}Cd_xSe$ and 'x' varies along the structure from ZnSe to CdSe regions. This was indicated by the varying amount of absorption (figure 6.3.3) across the device structure.

The early stage device showed a J_{SC} of only 0.4 mA cm^{-2}, but purification gave a remarkable increase. This clearly shows the significance of the purification step. Also the competition between the impurity ions that deposit at relatively low negative voltages and Te or Se metal ions, slows down the deposition rate. The deposition of pure semiconductors only occurs in a purified electrolyte. Unlike J_{SC}, the increase in V_{OC} has not been very significant. However, the fill factor and the efficiency have gone up from 0.36 to 0.6 and 0.2% to 0.9% respectively. Further purification and optimisation of device processing steps would improve the efficiency of the devices. The significance of the window layer has been shown by many researchers in the literature. However, Das and Morris (1993) found that there was no improvement of the performance of an ITO/CdTe solar cell with the introduction of the CdS intermediate window layer.

6.4 Summary of results.

ZnSe p-n junction structures are highly crystalline and show (111) preferred growth orientation. The thin layers are not thick enough to show an improvement in the optical absorption or GDOES profiling studies. Thin n and p type films can be grown on ITO and also on top of either type layer. The p-n junction devices produced during

the project show a maximum ~ 5 orders of magnitude rectification factor at ~1 V and a built-in-voltage of about 0.84 eV. The diode quality factors observed (~1.30) indicate the possibility of further improvement.

The glass/ITO/ZnSe/CdSe/CdTe/metal multi-layer solar cell structure again shows a highly crystalline structure for all three materials used. The optical absorption studies indicate an existence of an intermediate $Zn_{(1-x)}Cd_xSe$ layer due to interactions within the device producing a graded band gap structure. The optimum V_{OC}, J_{SC} and η are 250 mV, 16 mA cm^{-2} and 0.9%. The ability to grow highly crystalline ZnSe layers with (111) preferred orientation leads to the possibility of producing high efficiency multi-layer solar cell structures and devices based on these p-n junctions. The growth of all three materials involved in the (111) orientation is extremely attractive and important for thin film device development.

CHAPTER SEVEN:

CONCLUDING REMARKS AND FURTHER WORK.

Electrical contacts to MBE grown n-ZnSe on GaAs show two major problems. One is the existence of a large series resistance of the order of 10^6-10^9 Ω in the device structure. GDOES and C-V profiling studies indicate the existence of a resistive layer at the ZnSe/GaAs interface. In order to decrease the threshold voltage of blue-green light emitting technology based on ZnSe, the formation of this layer has to be avoided during growth. The second significant observation is the multi Fermi level pinning at the metal/n-ZnSe interface. Almost all metals studied produce high Schottky barriers and the barrier heights are independent of the metal work function contrary to the Schottky model. There is a relationship between discrete barrier heights and deep levels observed in the band gap due to native defects or defect-impurity complexes. As suggested by Blomfield et al (1996), deep levels due to these defects can influence the pinning of E_F to a unique position which is independent of the metal used. Extrinsic modulation of these deep levels has to be studied further through semiconductor surface preparation techniques to enable better understanding of the device design and development.

The successful electrodeposition ZnSe, CdSe and CdTe was demonstrated in this project and the materials were grown in a preferential <111> direction with a single phase and with a highly crystalline structure. Although, the devices fabricated utilising the electrochemical technique are still in an early stage the results observed during the project are encouraging. The growth of all three materials has to be optimised for best device performance. Among many of the researchers, Natarajan et al (1994) and

Meulenkamp et al (1996) observed better layers for all three materials at 85°C- 90°C, therefore temperature is still an issue to be considered. In fact, almost all the other deposition parameters have to be studied carefully for further optimisation. Although, Natarajan et al (1994) and many others reported that the best results in terms of crystallinity, uniformity of the deposits and composition were given by the potentiostatically deposited films, the suitability of galvanostatic deposition of CdSe was observed by Tomkiewicz et al (1982). The ability to control current density is an advantage in the galvanostatic technique, as it can be maintained at a low value during the deposition of semiconductors which prefer deposition under low current densities.

Even though the layers grown utilising cathodic co-deposition were found to exhibit better performance over galvanostatically grown semiconductors, one of the common difficulties that cathodic co-deposition of CdSe and ZnSe undergoes is the deposition of Se together with material layers. Lokhande et al (1989) used alkaline selenosulfite electrolytic baths to solve such problems associated with the acidic media. An organised series of experiments needs to be performed with different deposition combinations to determine the suitability of galvanostic growth.

Both ZnSe and CdTe were grown at voltages close to the standard redox potentials of Se and Te respectively. It has however been found that the devices based on these materials display better results when grown at voltages closer to Zn and Cd. It was also found in this work that CdSe and ZnSe are hexagonal if grown under high negative potentials (closer to Cd and Zn standard potentials) and it has been reported that the most stable structure for CdSe is the hexagonal structure. Therefore, the deposition of

thin layers at higher negative potentials producing hexagonal structures may have a useful impact on device performance.

Although glass/ITO was used for electrodeposition in this project, the suitability of other substrates was not studied in detail. Substrates such as Cu and Sb proved not to be suitable for ZnSe deposition in an acidic medium. The results of electrodeposited ZnSe layers can be compared directly with MBE and MOCVD grown layers if GaAs substrates are used for the growth. Meulenkamp (1996) reported that CdS is a better substrate for CdTe deposition. Different conducting or semiconducting substrates have to be studied thoroughly for improved device structures.

In addition to the points that have been suggested so far, replacing Se and Te precursors with complexes such as selenosulfite might loosen the complexity of the reaction mechanism in electrolytes. Se chemistry has to be studied thoroughly and thick layers have to be grown in order to perform GDOES and optical absorption techniques on the layers. XPS results did not indicate the presence of Na but GDOES did in ZnSe and CdSe layers grown in glass beakers. Also GDOES has been identified as a good technique within limits for impurity trace analysis in semiconductors. Therefore, the GDOES technique should be employed to examine elemental distribution within the crystal structure and material uniformity. Further, XRF studies would provide information about impurity sources within these thin film structures.

Another important step for device development is the optimisation of processing steps. The determinations of the optimum post growth annealing temperature, more suitable

etchants, etching conditions and also the best metal for electrical contacting will be the next few steps in the development of devices.

As Natarajan et al (1995) reported, a change in Cd concentration can vary the band gap of the intermediate layer making a well graded device structure. A continuous layer with different Cd concentrations may produce a graded structure with very small steps within and increase the efficiency of the device. The significance of the window layer is however to be assessed. Das and Morris (1993) have observed that there was no significant improvement in device performance by inserting a window layer of CdS in a CdS/CdTe solar cell.

The control of impurities and doping of ZnSe, CdSe and CdTe play an important role in the final device performance. The use of high purity chemicals, identifying the impurities which could not be traced by means of the techniques that have already been used, using ICPMS and purifying the bath to minimise background impurities are a few steps to be taken in the future to ensure better device performance. When the background impurity levels are low, useful dopants should be added to the electrolyte for growth of more suitable materials.

The most important material of this solar cell structure is CdTe. Metal contacts to n-CdTe exhibited five discrete barrier heights, Dharmadasa et al (1996) and this is very similar to the behaviour of metal/n-ZnSe junction. Thus, the Fermi level pinning, the role of native defects and impurities will have to be examined closely. These investigations could be done utilising BEEM, DLTS and PL techniques.

The carrier concentration of the semiconductor layers has to be maintained within a region between 5×10^{15} cm^{-3} and 5×10^{17} cm^{-3} in order to fabricate highly efficient devices. The required doping conditions for the three materials should therefore be established in the future.

REFERENCES.

Allen JW, Livingston AW, Turvey K, Solid State Electeronics, 1972 Vol 15 pp1363.

Bardeen J, Physical Review, 1947 Vol 71 pp717.

Basol BM, Journal of Applied Physics, 1984 Vol 55 No 2 pp601-603.

Berezovskii MM, Makhnii VP, Melnik VV, Inorganic Materials, 1997 Vol 33 No 2 pp136-138.

Bhattacharya RN and Carter MJ, Thin Solid Films, 1996 Vol 288 pp176-181.

Blomfield CJ, Dharmadasa IM, Prior KA and Cavenett BC. Journal of Crystal Growth, 1996 Vol 159 pp 727-731.

Blomfield CJ, Dharmadasa IM, Prior KA, Cavenett BC, Journal of Crystal Growth, 1995 Vol 4589 pp1-5.

Briggs D and Seah MP, Practical Surface Analysis, (John Wiley and sons, 1984).

Brillson LJ, Journal of Vacuum Science and Technology, 1978 Vol 15 No 4 pp 1378-1383.

Brillson LJ, Journal of Vacuum Science and Technology, 1979 Vol 16 No 5 pp1137-1142.

Brillson LJ, Surface Science, 1994 Vol 299/300 pp909-927.

Card HC and Rhoderick EH, Journal of Applied Physics, 1971 Vol 4 pp1589-1601.

Chou HC, Rohatgi A, Thomas EW, Kamra S, Bhat AK, Journal of Electrochemical Society, 1995 Vol 142 No 1 pp254-259.

Chu TL, Proc. Of 11th European Photovoltaic Solar Energy Conference,1992 pp1165-1168.

Colak S, Marshall T and Cammack D, Solid State Electronics, 1989 Vol 32 No 8 pp647-653.

Coratger R, Ajustron F, Beauvillain J, Dharmadasa IM, Blomfield CJ, Prior K, Cavenett BC, 1995 Physical Review B Vol 15 pp 2357.

Coratger R, Giradin C, Beauvillain J, Dharmadasa IM, Samantilleke AP, Frost JEF, Prior K, Cavenett BC, 1997 Journal of Applied Physics Vol 81 No 12 pp7870-7875.

Cowache P, Lincot D and Vedel J, Journal of Electrochemical Society, 1989 Vol 136 No 6 pp 1646-1650.

Cowley AM, Journal of Applied Physics, 1966 Vol 37 No 8 pp3024-3032.

Crowell CR and Sze SM, Solid State Electronics, 1966 Vol 9 pp1035.

Cullity BD, Elements of X-ray diffraction, (Addison Wesley Publishing Co.Inc, 1978)

Das SK, Morris GC, Journal of Applied Physics, 1993 Vol 73 No2 pp782-786.

David Wood, (Prentice Hall International limited, 1994).

Dawar AL, Shishoda PK and Mathur PC, Journal of Materials Science Letters, 1989 Vol 8 pp561-562.

Dharmadasa IM, Blomfield CJ, Gregory GE and Young J, International Journal of Electronics, 1994 Vol 76 No 5 pp961-967.

Dharmadasa IM, Blomfield CJ, Gregory GE, Cavenett BC, Prior KA and Simpson J, Surface and Interface Analysis, 1994 Vol 21 pp718-723.

Dharmadasa IM, Blomfield CJ, Coratger R, Ajustron E, Beauvillain J, Simpson J, Prior KA and Cavenett BC, Materials Science and Technology, Jan.1996, Vol.12, pp.86-89.

Dharmadasa IM, Blomfield CJ, Scott CG, Coratger R, Ajustron F and Beauvillain J, Solid State Electronics, 1998 Vol 42 No 4 pp595-604.

Dharmadasa IM, Ives M, Breen C, Hill G, Button CC and Hopkinson M, in press.

Dharmadasa IM, Ives M, Brooks JS, Breen C. Chapter 14.2, Glow Discharge Optical Emission Spectroscopy,(John Willey publications, 1996).

Dharmadasa IM, McLean AB, Patterson MH, Williams RH, Semiconductor Science and Technology, 1987 Vol 2 pp404-405.

Dharmadasa IM, Review Article, in press.

Dharmadasa IM, Thornton JM, Williams RH, Applied Physics Letters, 1989 Vol 54 pp137-139.

Edamura T and Muto J, Thin Solid Films, 1993 Vol 226 pp135-139.

Engelken RD and Van Doren TP, Journal of Electrochemical Society, 1985 Vol 132 No 12 pp 2910-2919.

Engelken RD, Journal of Electrochemical Society, 1987 Vol 134 No4 pp832-836.

Engelken RD, Van Doren TP, Journal of Electrochemical Society, 1985 Vol 132 No12 pp2904-2909.

Ferekides C and Britt J, Solar Energy Materials and Solar Cells, 1994 Vol 35 pp255-262.

Fowell AE, Williams RH, Richardson BE and Shen TH, Semiconductor Science and Technology, 1990 Vol 5 pp348-350.

Freeouf JL and Woodall JM, Applied Physics Letters, 1981 Vol 39 No 9 pp727-729.

Freeouf JL, Jackson TN, Laux SE, Woodall JM, Applied Physics Letters, 1982 Vol 40 No 7 pp634-636.

Fulop GF and Taylor RM, Annual Review of Materials Science, 1985 Vol 15 pp197.

Grill C, Bastide G, sagnes G, Rouzeyre M, Journal of Applied Physics, 1979 Vol 50 No 3 pp1375-1380.

Gunshor RL and Nurmiko AV, Semiconductors and Semimetals, Vol 44 (Academic press, 1997).

Haase MA, Qiu J, Deuydt JM and Cheng H, Applied Physics Letters, 1991 Vol 59 pp1272.

Hasegawa H and Ohno H, Journal of Vacuum Science and Technology B, 1986 Vol 4 No 4 pp1130-1138.

Heine V, Physical Review, 1965 Vol 138 No 6A ppA1689-1696.

Hoffmann V, Fresenius Journal of Analytical Chemistry, 1993 Vol 346 pp165-168.

Isett LC and Raychudhuri PK, Journal of Applied Physics, 1984 Vol 55 No10 pp3605-3612.

Islam R, Rao DR, Optical Materials, 1997 Vol 7 No1-2 pp47-50.

Itoh S, Nakayama N, Ohata T, Ozawa M, Okuyama H, Nakano K, Ishibashi A, Ikeda M, Mori Y, Japanese Journal of Applied Physics; part 2-Letters, 1993 Vol 32 No 10B ppL1530-L1532.

Ives DJG and Janz GJ, Chapter 4, Ref. Electrodes, Theory and practice, (Academic Press, 1961).

Jeon H, Ding J, Patterson W, Nurmikko AV, Xie W, Grillo DC, Kobayashi M, Gunshor RL, Applied Physics Letters, 1991 Vol 59 pp3619.

Kaiser WJ and Bell LD, Physics Review Letters, 1988 Vol 60 No 14 pp1406.

Kröger FA, Journal of Electrochemical Society, 1978 Vol 125 No12 pp2028-2034.

Krishnan V, Ham D, Mishra KK and Rajeshwar K, Journal of Electrochemical Society, 1992 Vol 139 No1 pp23-27.

Kröger FA, Journal of Electrochemical Society, 1978 Vol 125 pp 2028-2034.

Kurtin S, McGill TC, Mead CA, Physical Review Letters, 1969 Vol 22 No 26 pp1433-1436.

Lade SJ, Uplane MD, Uplane MM and Lokhande CD, in press

Lee WI, Taskar NR, Ghandhi SK and Borrego JM, Solar Cells, 1988 Vol 24 pp279-286.

Lee WI, Heiang TC, Guo JD, Feng MS, Applied Physics Letters, 1995 Vol 67 No 12 pp1721-1723.

Lide DR, CRC Handbook of Chemistry and Physics, 79th edition, (CRC press, 1998).

Livingstone AW, Turvey K, Allen JW, Solid State Electronics, 1973 Vol 16 pp351-356.

Lokhande CD and Pawar SH, Physica Status Solidi (a), 1989 Vol 111 No 17 pp 18-39.

Mane RS and Lokhande CD, The Solid Films, 1997 Vol 304 pp56-60.

Pourbaix M, Atlas of Electrochemical Equilibria in Aqueous Solutions, 1st English edition(Pergamon press, 1966).

McGregor SM, Dharmadasa IM, Wadsworth I, Care CM, Optical Materials, 1996 Vol 6 pp75-81.

Meulenkamp EA and Peter LM, Journal of Chemical Society-Faraday Trans., 1996, Vol.92, No.20, pp.4077-4082.

Mishra KK and Rajeshwar K, Journal of Electroanalytical Chemistry 1989 Vol 273 pp169-182.

Miyajima T, Akimoto K, Mori Y, Journal of Applied Physics, 1990 Vol 67 No 3 pp1389-1392.

Mondal A, McCandless BE, Birkmire RW, Solar Energy Materials and Solar Cells,1992 Vol 26 No 3 pp181-187.

Morgan BA, Ring KM, Kavanagh KL, Talin AA, Williams RS, Yasuda T, Yasui T and Segawa Y. Journal of Applied Physics, 1996 Vol 79 pp 1532-1535.

Morkoc H, Strite S, Gao GB, Lin ME, Sverdlov B, Burns M, Journal of Applied Physics, 1994 Vol 76 No 3 pp1363-1398.

Morris GC and Vanderveen RJ, Applied Surface Science, 1996 Vol 92 pp630-634.

Nakamura S, Physics World, February 1998 pp31-35.

Nakayama N, Itoh S, Ohata T, Nakano K, Okuyama H, Ozawa M, Ishibashi A, Ikeda M, Mori Y, Electronics Letters, 1993 Vol 29 No 16 pp1488-1489.

Natarajan C, Nogami G, Sharon M, Thin Solid Films, 1995 Vol 261 pp44-51.

Natarajan C, Sharon M, Levy-Clement C and Neumann-Spallart M, Thin Solid Films, 1994 Vol 237 pp118-123.

Nedeoglo DD, Lam DH, Simashkevich AV, Physica Status Solidi (a), 1977 Vol 44 No 83 pp83-89.

Neumann-Spallart M, Konigstein C, Thin solid Films, 1995 Vol 265 pp33-39.

Nishitani M, Ikeda M, Wada T, Solar Energy Materials and Solar Cells, 1994 Vol 35 pp279-284.

O'Connor DJ, Sexton BA and St.C.Smart R, Surface Analysis Methods in Materials Science, (Springer-Verlag publishers, 1991).

Ohdomari I and Tu KN, Journal of Applied Physics, 1980 Vol 51 pp3735-3738.

Ohtsuka T, Yoshimura M, Morita K and Koyama M, Applied Physics Letters, 1995 Vol 67 No 9 pp1277-1279.

Omkiewicz M, Ling I and Parson WS, Journal of Electrochemical Society, 1982 Vol 129 pp2017.

Ozawa M, Itoh S, Okuyama H, Nakano K, Nakyama N, Hiei F, Ohata T, Akimoto K, Ikeda M, Ishibashi A, Mori Y, Optoelectronics-Devices and Technolgies, 1994 Vol 9 No 2 pp193-204.

Panicker MPR, Knaster M, Kroger FA, Journal of Electrochemical Society, 1978 Vol 125 pp566.

Perkowitz S, Optical characterisation of semiconductors:Infra Red, Raman and photoluminescence spectroscopy (Academic press, 1993).

Premaratne K, Akuranthilake SN, Dharmadasa IM, Samantilleke AP, in press.

Prior KA, Contemporary Physics, 1996 Vol37 No 5 pp345-358.

Rai JP, Solar Energy Materials and Solar Cells, 1993 Vol 30 pp119-126.

Rhoderick EH and Williams RH, Metal-Semiconductor Contacts, second edition (Oxford press, 1988).

Robinson RJ, Kun ZK, Applied Physics Letters, 1975 Vol 27 No 2.

Ruda HE, Wide gap II-VI compounds for opto-electronic applications, (Chapman & Hall, 1992).

Schottky W, Z. Physics, 1939 Vol 113 pp367.

Samantilleke AP, Boyle MH, Young J and Dharmadasa IM, Journal of Materials Science: Materials in Electronics, 1998 Vol 9 pp 231-235.

Saraby-Reintjes A, Peter LM, Özsan ME, Dennison S and Webster S, Journal of Electrochemical Society, 1993 Vol140 No10 pp2880-2888.

Schull K, Spahn W, Hock V, Lunz U, Ehinger M, Faschinger W and Landwehr G. 1997Semiconductor Science and technology Vol 12 pp 485-489.

Sella C, Boncorps P and Vedel J, Journal of Electrochemical Society, 1986 Vol 133 No10 pp2043-2047.

Singh K and Rai JP, Indian Journal of Chemistry, 1989 Vol 28A pp557-560.

Singh K and Rai JP, Physica Status Solidi (a), 1987 Vol 99 pp257-265.

Singh VB and Sarabi RS, Materials Science and Technology, 1995 Vol 11 pp317-321.

Spicer WE, Chye PW, Skeath PR, Su CY, Lindau I, Journal of Vacuum Science and Technology, 1979 Vol 15 No 5 pp1422-1433.

Spicer WE, Kendelewicz T, Newman N, Chin KK, Lindau I, Surface Science, 1986 Vol 168 pp240-259.

Spicer WE, Liliental-Weber Z, Weber E, Newman N, Journal of Vacuum Science and Technology B, 1988 Vol 6 No 4 pp1245-1251.

Sugimoto Y and Peter LM, Journal of Electroanalytical Society, 1995 Vol 381 pp 251-255.

Sze SM, Physics of Semiconductor Devices, (John Wiley and sons, 1981).

Taniguchi S, Hino T, Itoh S, Nakano K, Nakayama N, Ishibashi A, Ikeda M, Electronic Letters, 1996 Vol 32 No 6 pp552-553.

Tarricone L, 1980, Revue physique Applications, Vol.15, pp.1617-1623.

Tejedor C, Flores F and Louis E, Journal of Physics C:Solid State Physics, 1977 Vol 10 pp2163-2164.

Tersoff J, Physical Review Letters, 1984 Vol 52 No 6 pp465-468.

Tomitori M, Kuriki M and Hayakawa S, Japanese Journal of Applied Physics, 1987 Vol 26 No 4 pp588-591.

Tung RT, Physical Review B, 1992 Vol 45 No 23 pp13509-13523.

Tyagi MS and Arora SN, Physica Status Solidi (a), 1975 Vol 32 No 165 pp165-172.

Uda H, Ikegami S, Sonomura H, Solar Energy Materials and Solar Cells, 1994 Vol 35 pp293-298.

Vos M, Xu F, Anderson SG, Weaver JH and Cheng H, 1989, Physical Review B, Vol. 39, No.15, pp.10744-10752.

Wang AZ and Anderson WA, Applied Physics Letters, 1995 Vol 66 No 15.

Wei C and Rajeshwar K, Journal of Electrochemical Society, 1992 Vol 139 No 4 ppL40- L41.

Wei C, Rajashwar K, Journal of Electrochemical Society,1992 Vol 139 No 4 ppL40-L41.

Williams RH, Dharmadasa IM, Patterson MH, Maani C and Forsyth NM, Surface Science, 1986 Vol 168 pp323-335.

Williams RH, Surface Science, 1991 Vol 251/252 pp12-21.

Wolfframm D, Gnoth DN, Evans M, Prince K, Westwood D and Evans DA, Applied Surface Science, 1998 Vol 123/124 pp 575-579.

Wolverson D. Inorganic Materials, 1997 Vol 33 No 2 pp 139-147.

Wood D, Optoelectronic Semiconductor Devices (Prentice Hall, 1994).

Verdeyen JJ, Laser Electronics, second edition, (Prentice Hall, 1981).

Zweibel K, 1997, National Renewable Energy Laboratory, Golden, CO 80401.

A1 List of refereed publications.

1. Growth of n-type and p-type ZnSe thin films using an electrochemical technique for applications in large area optoelectronic devices., **AP Samantilleke,** MH Boyle, J Young and IM Dharmadasa., J.Materials Science: Materials in Electronics. 1998 Vol 9 pp 231-235.

2. Schottky barrier formation at metal/n-ZnSe interfaces and characterisation of Au/n-ZnSe by ballistic electron emission microscopy., R Coratger, C Girardin, J Beauvillain, IM Dharmadasa, **AP Samantilleke**, JEF Frost, KA Prior, BC Cavenett., Journal of Applied Physics, 1997 Vol 81 No 12 pp 7870-7875.

3. Ballistic Electron Emission Microscopy; A new Technique using a Scanning Tunnelling Microscope for Solar Cell Characterisation., IM Dharmadasa, CJ Blomfield, **AP Samantilleke**, R Coratger, C Giradin, J Beauvillain.

4. Growth and Characterisation of $CdS_xSe_{(1-x)}$ Ternary Compounds for Utilisation in Liquid/Solid Junction and Solid State Solar Cells., K Premaratne, SN Akuranthilake, IM Dharmadasa, **AP Samantilleke.**

5. Electrodeposition of n-type and p-type ZnSe thin films for applications in Large area Optoelectronic devices., **AP Samantilleke,** MH Boyle, J Young and IM Dharmadasa., A letter submitted to J. Materials Science: Materials in Electronics.

6. Air ballistic emission microscopy of n-ZnSe and local density of states spectroscopy., A Chahboun, R Coratger, F Ajustron, J Beauvillain, IM Dharmadasa, **AP Samantilleke.**, paper in final preparation.

A2 Contributions in conferences.

1. Growth of n-type and p-type ZnSe thin films using an electrochemical technique for applications in large area optoelectronic devices., **AP Samantilleke,** MH Boyle, J Young and IM Dharmadasa., BACG conference, York, UK, 1997.

2. Ballistic electron emission microscopy; A new technique using Scanning Tunnelling Microscope for solar cell characterisation., IM Dharmadasa, CJ Blomfield, **AP Samantilleke**, R Coratger, C Girardin, J Beauvillain., Proceedings of workshop held in Colombo, Sri Lanka, February 1997.

3. Electrodeposited ZnSe layers for development of high efficiency multi-layer solar cells., IM Dharmadasa, **AP Samantilleke,** MH Boyle and J Young., Proceedings of workshop on "Renewable Energy Sources", Colombo, Sri Lanka, 10-11 February 1998.

4. **Poster:** Growth, Characterisation and Doping of ZnSe and Fabrication of Blue-Green Light emitting Devices., **AP Samantilleke,** MH Boyle and J Young, IM Dharmadasa., Conference on "Highlights of Physics Research and R&D in 1997 by Young Physicists from University, Industrial and Government Laboratories.", 2 October 1997, Rutherford Appleton Laboratory, Chilton, Didcot, Oxfordshire OX11 0QX, UK.

5. Electrodeposited p-type and n-type ZnSe layers for light emitting devices and multi-layer tandem solar cells., IM Dharmadasa, **AP Samantilleke**, J Young, MH Boyle, R Bacewicz and A Wolska., ICMM2 conference proceedings, Bordeaux, France, 14-15 Sep 1998.

A3 Other research meetings attended.

1. II-VI Semiconductor Interaction meeting, UK-1996., 18-19 March 1996, University of Durham, Durham , UK.

2. II-VI Semiconductor Interaction meeting, UK- 1997., University of East Anglia, Norwich, UK.

3. II-VI Semiconductor Interaction meeting, UK-1998. 2-3 April 1998., Herriot Watt University, Edinburgh, UK.